CRANFIELD INSTITUTE OF TECHNOLOGY

SCHOOL OF MECHANICAL ENGINEERING

DEPARTMENT OF FLUID ENGINEERING & INSTRUMENTATION

PhD

Academic Year 1991-2

J. HANNON

Mixing and chemical reaction in tubular reactors and stirred tanks

Supervisor: M. Sanderson

November 1992

ABSTRACT

Fluid flow patterns and turbulence levels are instrumental in determining chemical reactor performance. Parameters such as stirrer type and size, fluid physical properties, chemical species concentrations and flowrates can strongly influence the safety, efficiency and reliability of reactors, with consequent cost implications.

In this project, Computational Fluid Dynamics has been used to obtain insight into the characteristics of tubular and stirred tank chemical reactors. Attention is focused on single-phase liquid isothermal turbulent flows. Turbulence theory is used to select and develop appropriate physical models for both fluid flow and chemical reaction rates. Many previously-used models are shown to be of limited validity.

Results of simulations are compared with experimental measurements of the flow field and progress of both simple and complex chemical reactions. Comparisons are generally favourable. Limitations of the present approach are highlighted and future refinements and extensions suggested.

ACKNOWLEDGEMENTS

This thesis is dedicated to Bernadette & Eamon Hannon and Deirdre Foley.

Many thanks to my colleagues at BHR Group for their assistance and encouragement, notably Dr. Nick Fawcett, Dr. Richard Grenville, Dr. Steve Ruszkowski, Mr. Steve Hearn, Mr. Trevor Sparks, Mr. Mike Musgrove, Mr. Andrew Green and Dr. Roger King. Thanks are also due to Ms. Suzanne Simcox and Dr. Nigel Wilkes of CFDS.

Support from my Total Technology PhD Panel: Prof. Mike Sanderson, Dr. John Hemp and Prof. Paul Burns is gratefully acknowledged.

Discussions with members of BHR Group's FMP and HILINE Steering Committees, particularly Dr. John Middleton of ICI, Dr. Art Etchells of Du Pont and Professor John Bourne of ETH Zurich are much appreciated.

CONTENTS

Page Number

ABSTRACT

ACKNOWLEDGEMENTS

CONTENTS

FIGURES

NOTATION

Chapter 1 INTRODUCTION 1

1.1 BACKGROUND 1

1.2 METHODS FOR PROCESS PREDICTION 1

1.3 COMPUTATIONAL FLUID DYNAMICS (CFD) 2

1.4 CONTRIBUTIONS OF THIS WORK 2

1.5 LAYOUT OF THE THESIS 4

Chapter 2 FLUID FLOW MODELLING 5

2.1 INTRODUCTION & OBJECTIVES 5

2.2 GOVERNING EQUATIONS 5

2.3 TURBULENCE MODELLING 7

2.3.1 Objectives & Criteria 7
2.3.2 The Reynolds Stress Equations 7
2.3.3 Second Moment Closure 8
2.3.4 Wall Effects 11
2.3.5 Use of Second Moment Closure 12
2.3.6 Algebraic Stress Model 12
2.3.7 Two Equation Models 13

2.4 DISCRETISATION 14

2.5 SUMMARY OF RELEVANT LITERATURE ON MIXING VESSEL FLOWS 17

2.5.1 Tubular Reactors 17
2.5.2 Stirred Tank Reactors 17

2.6 CONCLUSIONS 20

Chapter 3 CHEMICAL REACTION MODELLING 21

3.1 INTRODUCTION & OBJECTIVES 21

3.2 MIXING EFFECTS ON REACTIONS 21

3.3 MIXING MECHANISMS 22

3.4 DESIRABLE ATTRIBUTES OF A MIXING-REACTION MODEL 27

3.5 INTERPRETATION OF CONCENTRATION COVARIANCE 28

3.5.1 Balance Equation 28
3.5.2 Modelling Approaches 29
3.5.3 Asymptotic Behaviour 31

3.6 SINGLE TIMESCALE MODELS 31

3.6.1 Laminar Model 31
3.6.2 Toor's Model 31
3.6.3 Patterson's Model 32
3.6.4 Dutta & Tarbell's Models 35
3.6.5 Ziman's Model 36
3.6.6 Ranade & Bourne's Model 37

3.7 MULTIPLE TIMESCALE MODELS 39

3.7.1 Pohorecki & Baldyga's Model 39
3.7.2 Micromixing Models 40
3.7.3 Baldyga's Model 43

3.8 DIRECT NUMERICAL SIMULATIONS 43

3.9 NEW REACTIVE MIXING MODEL 44

3.9.1 Introduction & Objectives 44
3.9.2 Assumed structure of the concentration field 46
3.9.3 Calculation of segregated volume fraction 48
3.9.4 Calculation of reaction zone volume fraction 49
3.9.5 Calculation of concentration distribution 50
3.9.6 Calculation of reaction rate 51
3.9.7 Asymptotic behaviour of new closure 52
3.9.8 Discussion 53

3.10 CONCLUSIONS 55

Chapter 4	TUBULAR REACTORS		56
	4.1	INTRODUCTION & OBJECTIVES	56
	4.2	DESCRIPTION OF SIMULATED GEOMETRIES AND REACTIONS	56
	4.2.1	Tubular reactors	56
	4.2.2	Dimensions, reaction schemes and measurements	56
	4.2.3	Experiments of Tovstiga (1986)	60
	4.2.4	Experiments of Li & Toor (1986)	60
	4.3	FLOW FIELD PREDICTION	62
	4.4	CHEMICAL REACTION PREDICTION	64
	4.4.1	MTPDF implementation in FLOW3D	64
	4.4.2	Calculation procedure	65
	4.5	NEUTRALISATION EXPERIMENTS OF TOVSTIGA (1986)	65
	4.6	AZO-COUPLING EXPERIMENTS OF LI & TOOR (1986)	75
	4.7	SENSITIVITY TESTS	80
	4.7.1	Neutralisations	80
	4.7.2	Azo-couplings	85
	4.8	COMPARISON OF MODELS	88
	4.9	CONCLUSIONS	91
Chapter 5	STIRRED TANK REACTORS		92
	5.1	INTRODUCTION & OBJECTIVES	92
	5.2	DESCRIPTION OF SIMULATED STIRRED TANK	93
	5.3	FLOW FIELD MEASUREMENTS	93
	5.3.1	Measuring system	93
	5.3.2	Results	95

5.4	FLOW FIELD PREDICTIONS		102
	5.4.1	Boundary conditions	102
	5.4.2	Grid-dependence and differencing scheme	105
	5.4.3	Turbulence model	107
5.5	FLOW FIELD VALIDATION		113
	5.5.1	Integral validation	113
	5.5.2	Point validation	117
5.6	CHEMICAL REACTION MEASUREMENTS		122
	5.6.1	Details of test reaction	122
	5.6.2	Experimental design	124
	5.6.3	Experimental procedure	127
	5.6.4	Results	130
5.7	CHEMICAL REACTION PREDICTIONS		134
	5.7.1	Assumptions	134
	5.7.2	Boundary & Initial Conditions	139
	5.7.3	Timestep selection	139
	5.7.4	Special considerations for complex geometry simulations	140
5.8	CHEMICAL REACTION VALIDATION		140
	5.8.1	Effect of feed time	142
	5.8.2	Effect of feed position	145
	5.8.3	X_Q and X_S during batch time	145
	5.8.4	Effect of timestep size	147
5.9	DISCUSSION OF RESULTS		150
	5.9.1	Flow field	150
	5.9.2	Chemical reaction	152
5.10	CONCLUSIONS		153
Chapter 6	COST-BENEFIT ANALYSIS OF CFD IN REACTOR SCALE-UP		154
6.1	INTRODUCTION & OBJECTIVES		154
6.2	BACKGROUND		154
6.3	INVESTMENT APPRAISAL METHODS		154
	6.3.1	Net present value	156
	6.3.2	Internal rate of return	157

6.4 COST-BENEFIT ANALYSIS OF CFD 157

6.4.1 Factors taken into account 158
6.4.2 Results for base case 161
6.4.3 Effect of scale-up uncertainty 161
6.4.4 Sensitivity analysis 162

6.5 CONCLUSIONS 164

Chapter 7 CONCLUSIONS AND RECOMMENDATIONS 165

7.1 ADVANCES IN PREDICTIVE MODELS AND VALIDATION 165

7.2 INSIGHTS GAINED 166

7.3 RECOMMENDATIONS FOR FUTURE WORK 167

REFERENCES 169

APPENDIX A: SIMPLIFIED VERSIONS OF MTPDF 174

APPENDIX B: MTPDF IN NON-ISOTHERMAL FLOWS 175

APPENDIX C: EQUATIONS USED IN COST-BENEFIT ANALYSIS 176

APPENDIX D: COMPARATIVE PLOTS FROM LDA AND CFD 179

FIGURES

2.1 Comparison of finite difference (discretisation) schemes for capturing the value of a function at the cell face.

2.2 Schematic of a coaxial jet tubular reactor

2.3 Schematic of a stirred tank reactor with four baffles

3.1 Destruction of large feed eddies by turbulent mixing.

3.2 The spectrum of turbulent concentration fluctuations in liquids (adapted from Baldyga & Bourne, 1984)

3.3 Schematic square-wave response of a concentration probe in an incompletely-mixed solution.

3.4 Some probability density functions commonly used in reaction modelling (adapted from Patterson, 1981)

3.5 Concentration versus time profile and probability density function used in Patterson's closure

3.6 Micromixing stages (adapted from Baldyga & Bourne, 1984):

3.7 Evolution of the joint single-point probability density functions for initially segregated reactant concentrations obtained from Direct Numerical Simulations (adapted from Leonard & Hill, 1989)

3.8 Ratio of approximate covariances of Toor's and Patterson's closures to data from Direct Numerical Simulations

3.9 Concentration distribution in a reacting mixture consisting locally of three zones

3.10 Explanation of modelled form of local three-zone concentration distribution

3.11 Probability density function assumed for the MTPDF model.

4.1 Coaxial jet tubular reactor, showing the confluence zone

4.2 Photograph of neutralisation reactions in a coaxial jet reactor (adapted from Tovstiga, 1986)

4.3 Computational grid used for BN flow and reaction simulations.

4.4 Predicted velocity vectors near the feed tube for BN

4.5 Predicted turbulent kinetic energy distribution between the axis and the wall of BN.

4.6 Effect of grid density on conversion versus distance profile for simulation BN1 (using MTPDF model).

4.7 Effect of acid/base concentration ratio on conversion-distance profiles for BN using MTPDF model.

4.8 Regions where the reaction zone volume fraction (α_r) exceeds 1% for simulation BN1.

4.9 Predicted conversion-distance profiles for experiment BN1 using various chemical reaction closure models.

4.10 Predicted core region turbulent energy dissipation rates as a function of distance downstream of feed tube for two levels of viscosity (BN).

4.11 Predicted velocity vectors in the initial region of the tubular reactor of Li & Toor (1986).

4.12 Predicted radial profile of turbulent energy dissipation rate 1.0 mm downstream from the feed tube in TA.

4.13 Predicted conversion-distance profile for sulfanilic acid (B) in the azo-coupling experiments of Li & Toor (1986) using MTPDF model.

4.14 Predicted side-product (S) formation versus distance downstream of feed tube showing the effect of increasing initial B concentration.

4.15 MTPDF predicted radially-averaged correlation coefficients (R_{ij}) between covariances and mean concentrations for the multiple reactions of Li & Toor (1986), plotted against distance downstream from the feed tube.

4.16 Side-product (S) formation predicted by various models for TA1.

4.17 Sensitivity of MTPDF conversion-distance predictions for BN1 to values of the model constants.

4.18 Sensitivity of MTPDF predictions to acid/base concentration ratio at raised viscosity (0.0025 Pa.s)

4.19 Sensitivity of MTPDF predictions of side-product formation in TA1 to model constants

4.20 Predicted ZIM product concentrations in TA1 as a function of distance downstream from the feed tube

4.21 Predicted MTPDF product concentrations in TA1 as a function of distance downstream of the feed tube

5.1 Details of stirred tank reactor used for simulations and experimental measurements

5.2 Coordinate system for stirred tank calculations

5.3 Average velocities in the impeller discharge

5.4 Fluctuating velocities in the impeller discharge

5.5 Estimated turbulent energy dissipation rate ε in the impeller discharge

5.6 Average velocities in the impeller stream

5.7 Fluctuating velocities in the impeller stream

5.8 Schematic of types of approximate impeller boundary conditions

5.9 24,000 cell computational grid used for flow field calculations

5.10 Grid sensitivity of average axial velocity at r=64 mm

5.11 Grid sensitivity of fluctuating velocities at r=64 mm

5.12 Predicted k-ε velocity vectors in a vertical slice between baffles (θ=0 degrees) and in a horizontal slice at x/T =0.025. No baffle-wall spacing

5.13 Predicted DSM velocity vectors in vertical slices at θ=0 degrees (between baffles), 46 (upstream of baffle) and 44 (downstream of baffle). No baffle-wall spacing

5.14 Predicted DSM velocity vectors in horizontal slices at x/T=0.025, 0.167 and 0.51. No baffle-wall spacing

5.15 Predicted DSM velocity vectors in vertical slices at θ=0 degrees (between baffles), 46 (upstream of baffle) and 44 (downstream of baffle). T/60 baffle-wall spacing

5.16 Predicted DSM velocity vectors in horizontal slices at x/T=0.025 0.167 and 0.51. T/60 baffle-wall spacing

5.17 DSM predictions compared to LDA measurements in the impeller stream.

5.18 DSM predictions compared to LDA measurements in the impeller stream.

5.19 DSM predictions compared to LDA measurements at r=64 mm.

5.20 DSM predictions compared to LDA measurements at r=64 mm.

5.21 Flowsheet for chemical reaction experiments

5.22 Comparison of timed and weighed B volumes as a function of B velocity.

5.23 Effect of feed time on side-product (Q and S) formation. Feed point at liquid surface.

5.24 Effect of feed time on side-product (Q and S) formation. Feed point in impeller suction.

5.25 Effect of impeller speed on side-product (Q and S) formation. Feed point at liquid surface.

5.26 Effect of feed position on side-product (Q and S) formation for various feed times.

5.27 Predicted DSM velocity vectors from a two-dimensional flow field simulation.

5.28 Comparison between feed pipe geometries in three- and two-dimensional situations.

5.29 Predicted development of the reaction plume in the impeller discharge (t_B=5.5s)

5.30 DSM and MTPDF two-dimensional model predictions of the effect of feed time on side-product formation compared with measurements.

5.31 DSM and MTPDF two-dimensional model predictions of the development of X_S during the batch time.

5.32 DSM and MTPDF two-dimensional model predictions of the development of X_Q during the batch time.

5.33 Effect of computational timestep on predicted X_Q and X_S

6.1 Schematic of stages in typical chemical production process

D.1 Mean velocities on the impeller top surface (x=0.190 m)

D.2 Mean velocities on the impeller bottom surface (x=0.203 m)

D.3 Mean velocities at x=0.238 m

D.4 Mean velocities at x=0.263 m

D.5 Fluctuating velocities on the impeller top surface (x=0.190 m)

D.6 Fluctuating velocities on the impeller bottom surface (x=0.203 m)

D.7 Fluctuating velocities at x=0.238 m

D.8 Fluctuating velocities at x=0.263 m

D.9 Mean velocities at r=0.054 m

D.10 Mean velocities at r=0.064 m

D.11 Fluctuating velocities at r=0.054 m

D.12 Fluctuating velocities at r=0.064 m

NOTATION

Symbol	Meaning	Units
A	species A	
A	proportionality constant of order 1.0	-
	proportionality constant in Arrhenius equation	m^3/mol.s
A_m	convection and diffusion fluxes	kg/s
B	species B	
C	species C	
C	impeller clearance from tank bottom	m
C_{Ai}	concentration of species A in zone i	mol/m^3
C_{A0}	initial concentration of A	mol/m^3
C_{B0}	initial concentration of B	mol/m^3
C_{C0}	initial concentration of C	mol/m^3
C_{CONi}	costs of modifications to pilot plant i	£
C_{cov}	convection of covariance	mol^2/m^6.s
C_{EX}	running costs of experiments in pilot plant	£
C_i	mean concentration of species i	mol/m^3
C_{ib}	concentration of species i in the bulk	mol/m^3
C_{ie}	concentration of species i in the environment	mol/m^3
C_{ij}	convection of Reynolds stress component ij	m^2/s^3
	concentration of species i in subgroup/zone j	mol/m^3
C_{INSTi}	cost of instrumentation for pilot plant stage i	£
C_{ir}	concentration of species i in the reaction zone	mol/m^3
C_{is}	concentration of species i in the segregated zone	mol/m^3
C_k	convection of turbulent kinetic energy	m^2/s^3
C_{MH}	cost per man-hour	£
$C_{MP,i}$	cost penalty for plant start-up n years late	£
C_n	cash flow arising in year n	£
C_{PR}	cost of lost profits per year of pilot-plant work	£
C_{RM}	cost of raw materials	£
C_{RMV}	cost of raw materials per unit volume	£/m^3
C_W	cost of waste treatment	£
C_{WV}	cost of waste treatment per unit volume	£/m^3
C_γ	constant used by Rosensweig (1964)	-
$\hat{C}_i$	instantaneous concentration of species i	mol/m^3
c_i	fluctuating concentration of species i	mol/m^3
c_{ij}	fluctuating concentration of species i in zone j	mol/m^3
C_p	specific heat capacity at constant pressure	J/kg.K
c_s	diffusion constant in transport equations	-
c_ε	constant in ε transport equation	-
$c_{\varepsilon 1}$	constant in ε transport equation	-
$c_{\varepsilon 2}$	constant in ε transport equation	-
c_μ	constant in eddy viscosity formula	-
c_1	constant in pressure-strain model	-
c_2	constant in pressure-strain model	-
D	impeller diameter	m
	molecular diffusion coefficient	m^2/s
D_A	diameter of pipe containing A	m
D_B	diameter of pipe containing B	m

D_{cov}	diffusion of covariance	$mol^2/m^6.s$
D_H	impeller hub diameter	mm
D_{ij}	diffusion of Reynolds stress component *ij*	m^2/s^3
D_k	diffusion of turbulent kinetic energy	m^2/s^3
D_n	discounting multiplier for year *n* cash flows	-
E	engulfment parameter	1/s
	relative roughness of wall (in wall law)	-
	activation energy (in Arrhenius equation)	J/mol
E^*	modified Engulfment parameter	1/s
e_i	volume fraction of subgroup *i*	-
G	rate of viscous-diffusive mixing	1/s
$G(\kappa)$	concentration spectrum function	mol^2/m^5
H	liquid depth	m
	enthalpy	J/m^3
H_e	enthalpy in the environment zone	J/m^3
H_r	enthalpy in the reaction zone	J/m^3
H_s	enthalpy in the segregated zone	J/m^3
I_s	intensity of segregation	-
IRR	internal rate of return	-
k	turbulent kinetic energy	m^2/s^2
	reaction velocity constant	$m^3/mol.s$
k_i	velocity constant of reaction *i*	$m^3/mol.s$
k_{ij}	reaction velocity constant between components *i* and *j*	$m^3/mol.s$
k_{md}	molecular mixing rate of Pohorecki & Baldyga (1983)	1/s
L_c	integral scale of concentration fluctuations	m
l_e	characteristic eddy size	m
L_v	integral scale of velocity fluctuations	m
L_{95}	95% neutralisation length	m
M	impeller torque	N.m
MB	mass balance ratio	-
MPF_i	penalty factor for plant start-up *i* years late	-
m	flow ratio of Mehta & Tarbell (1989)	-
min()	minimum value of arguments in brackets	
N	number of subgroups in model of Ranade & Bourne (1991)	-
	impeller rotational speed	1/s
N_{A0}	initial number of moles of A	mol
N_{B0}	initial number of moles of B	mol
N_{C0}	initial number of moles of C	mol
N_{MHi}	number of man-hours required for pilot plant stage *i*	-
NPV	net present value	£
$NPV_{CFD,c}$	net present value of CFD costs neglecting uncertainty	£
$NPV_{CFD,uc}$	net present value of CFD costs, accounting for uncertainty	£
NPV_n	net present value of (costs of) *n* stages of development	£
$NPV_{n,c}$	NPV_n neglecting uncertainty	£
$NPV_{n,uc}$	NPV_n accounting for uncertainty	£
N_{RPi}	number of runs in pilot plant stage *i*	-
n	unit normal vector	m
P	mean pressure	Pa
	impeller power	W
	production of turbulent kinetic energy	m^2/s^3
P_{cov}	production of covariance	$mol^2/m^6.s$

P_{ij}	production of Reynolds stress component *ij*	m^2/s^3
P_M	power based on torque	W
Po	impeller power number	-
PRF_i	penalty factor for failure of scale-up after *i* stages of development	-
PR_v	profit per unit volume	£/m^3
PV	present value	£
PV_n	present value of a cash flow in year *n*	£
$PV_{PR,i}$	present value of profits lost in year *i*	£
P_ε	power based on ε	W
$\hat{p}$	instantaneous pressure	Pa
p	fluctuating pressure	Pa
$p()$	probability density function of argument in brackets	-
Q	species Q	
Q_B	flowrate of B stream	m^3/s
Q_P	Production rate	m^3/day
Q_1,Q_2	component flow rates of Mehta & Tarbell (1989)	m^3/s
R	species R	
R	discount rate	-
	main pipe radius in Chapter 4	m
R_B	radial position of B feed pipe	m
R_c	cost ratio of pilot plant to CFD under conditions of certainty	-
Re_A	Reynolds number of stream containing species A	-
Re_B	Reynolds number of stream containing species B	-
Re_i	impeller Reynolds number	-
R_{ij}	correlation coefficient for covariance *ij*	-
R_1	cost ratio of 1 stage of pilot studies to CFD, including uncertainty	-
R_2	cost ratio of 2 stages of pilot studies to CFD, including uncertainty	-
R_3	cost ratio of 3 stages of pilot studies to CFD, including uncertainty	-
r	radial coordinate	m
S	species S	
S	area vector	m^2
S_B	source associated with the feed stream	ϕ units.kg/s
Sc	Schmidt number	-
S_j	area normal to direction *j*	m^2
S_P	source term coefficient of ϕ_P	kg/s
S_u	source term for ϕ	ϕ units.kg/s
S_ϕ	source of ϕ	ϕ units/s
T	species T	
T	tank diameter	m
	temperature	K
T_i	diameter of pilot plant vessel *i*	m
T_r	temperature in the reaction zone	K
t	time	s
	impeller blade thickness	mm
t_B	batch (or feed) time	s
t_{DM}	diffusive mixing time	s
t_{ic}	inertial-convective mixing timescale	s
t_M	sum of t_{macro} and t_{micro}	s
t_{macro}	macromixing time used by Ziman (1990)	s
t_{mi}	timescale for mixing stage *i*	s
t_{micro}	micromixing time used by Ziman (1990)	s

t_{ms}	inertial-convective mixing time of Rosensweig (1964)	s
t_R	intrinsic reaction time	s
t_{95}	95% mixing time	s
U	mean axial velocity (cylindrical coordinates)	m/s
	velocity vector (in vector equations)	m/s
	velocity parallel to a wall (in wall laws)	m/s
U_A	average velocity of stream containing species A	m/s
U_B	average velocity of stream containing species B	m/s
U_{CFD}	uncertainty of successful scale-up after CFD calculations	-
U_i	mean velocity in direction i	m/s
	uncertainty of successful scale-up after i stages of pilot-plant work	-
U^+	dimensionless velocity parallel to a wall	-
$\hat{u}_i$	instantaneous velocity in direction i	m/s
u	thinning velocity of Baldyga & Bourne (1984)	m/s
	fluctuating axial velocity (cylindrical coordinates)	m/s
u_i	fluctuating velocity in direction i	m/s
V	volume	m^3
	mean radial velocity (cylindrical coordinates)	m/s
	volume of reaction zone (Baldyga & Bourne, 1989)	m^3
V_i	initial volume of stream containing species i	m^3
V_{RM}	volume of raw materials	m^3
V_s	volume of segregated zone	m^3
V_{TIP}	impeller tip speed	m/s
v	fluctuating radial velocity (cylindrical coordinates)	m/s
W	mean tangential velocity (cylindrical coordinates)	m/s
	impeller blade width	mm
w	fluctuating tangential velocity (cylindrical coordinates)	m/s
X_Q	Yield of species Q	-
X_{R+T}	Yield of R and T	-
X_S	Yield of S	-
x	axial coordinate	m
x_i	cartesian coordinate in the i direction	m
y	wall distance	m
y^+	dimensionless wall distance	-
y_0^+	y^+ at intersection between viscous sub-layer and log layer (wall law)	-
α	local A concentration divided by initial mean value	-
	impeller blade angle	degrees
α_e	volume fraction of environment	-
α_{eng}	volume fraction engulfed	-
α_i	volume fraction of stream/zone i	-
α_r	volume fraction of reaction zone	-
α_s	volume fraction of segregated zone	-
β	local B concentration divided by initial mean value	-
Γ	Gamma function	-
Γ_ϕ	Diffusivity of ϕ	m^2/s
ΔH_r	heat of reaction	J/mol
Δt_i	time spent by stream i at a point	s
δ_{ij}	Kronecker delta component ij	-
ε	dissipation of turbulent kinetic energy	m^2/s^3 (or W/kg)
ε_{cov}	dissipation of covariance	$mol^2/m^6.s$

ε_{ij}	dissipation of Reynolds stress component *ij*	m^2/s^3
θ	tangential coordinate	radians or degrees
κ	wavenumber	1/m
	von Karman constant (in wall law)	-
κ_c	wavenumber of the integral concentration scale	1/m
λ_B	Batchelor microscale	m
λ_K	Kolmogoroff microscale	m
μ	dynamic viscosity	Pa.s
μ_t	eddy viscosity	Pa.s
ν	molecular kinematic viscosity	m^2/s
ν_t	eddy diffusivity of momentum	m^2/s
ϱ	density	kg/m^3
σ_k	turbulent Prandtl number for *k*	-
σ_ε	turbulent Prandtl number for ε	-
τ_k	wall shear stress	Pa
τ_M	mixing time in Mehta & Tarbell's (1989) model	s
τ_ω	vortex lifetime	s
ϕ	transported quantity	ϕ units
ϕ_B	ϕ in the feed stream	ϕ units
ϕ_E	ϕ at point *E* (east cell centre)	ϕ units
ϕ_e	ϕ at east cell face	ϕ units
ϕ_i	volume fraction of stream *i* (Mehta & Tarbell, 1989)	-
ϕ_{ij}	pressure-strain rate correlation component *ij*	m^2/s^3
ϕ_m	ϕ in cell *m*	ϕ units
ϕ_P	ϕ at point *P* (cell centre)	ϕ units
ϕ_W	ϕ at point *W* (west cell centre)	ϕ units
$\hat{\Omega}_A$	instantaneous rate of reaction of species A	$mol/m^3.s$
Ω_A	average rate of reaction of species A	$mol/m^3.s$
Ω_i	average rate of reaction of species *i*	$mol/m^3.s$
Ω_{ij}	average rate of reaction of species *i* in zone *j*	$mol/m^3.s$

Chapter 1

INTRODUCTION

1.1 BACKGROUND

Operation of processes in a safe and profitable manner poses significant challenges for the Chemical and Process industries. In recent times, increased public pressure to be environmentally friendly and legislative pressure to comply with pollution regulations have placed greater importance on the ability to understand processes and predict their behaviour in detail.

This thesis is concerned with prediction of chemical reactor performance, with a view to improving design procedures. The reactor is where raw materials are converted chemically to products and waste and as such is the nucleus of the process plant. Product quality, waste volumes, raw material and utilities requirements are dictated to a large degree by reactor performance. Understanding, prediction and optimisation are thus of major interest.

1.2 METHODS FOR PROCESS PREDICTION

Ideally, reactor design would start with a knowledge of the reaction kinetics (e.g. fast or slow), mechanism (simple or complex) and fluid properties (such as density and viscosity) and the task of the engineer would be to select the appropriate fluid flow pattern and equipment design. In practice, this is rarely possible for the following reasons:

i) sufficiently detailed information, particularly relating to kinetics, is rarely available, being expensive and difficult to generate

ii) flow patterns of mixtures in reactors of different types and in different flow regimes are rarely predictable with sufficient accuracy

iii) Even if i) and ii) are available, there are few fundamental, rigorously tested and robust models to allow chemical kinetic and fluid dynamic information to be combined correctly

In practice, reactor design is achieved through pilot-scale testing of various ideas, followed by scale-up to commercial plant using rules of thumb (ROT). For example, a new liquid-phase reaction process might be carried out in several small vessels of different sizes, varying stirrer speed, reagent addition point, temperature, species concentrations and any other factors which are believed to influence the process. Performance might then be correlated statistically with some parameter, for example, power dissipated per unit mass. The commercial plant would be designed to achieve the same power input per unit mass as the pilot plant.

Disadvantages with ROT include:

i) safety and cost implications of pilot-plant work
ii) inability to deal confidently with new, complex reaction schemes
iii) long delays between product development and commercialisation
iv) risk of costly under- or over-design of full-scale equipment

It is desirable to improve methods for process prediction. One potential long-term solution is to work within the framework of Computational Fluid Dynamics.

1.3 COMPUTATIONAL FLUID DYNAMICS (CFD)

CFD is a semi-fundamental computer-based method for predicting fluid flows and their consequences. It works as follows:

i) The reactor geometry is split into a large number of small segments (called "cells")
ii) Boundary conditions (such as impeller type and speed, chemical species concentrations, temperatures) and fluid physical properties (e,g, density, viscosity) are input
iii) A computer program solves mass, energy, momentum and chemical species conservation equations throughout the reactor volume
iv) Output is converted into graphical or some other form suitable for analysis and decision-making

Many of the basic equations required for CFD have been known for a long time. However, to apply CFD requires a very large number of arithmetic operations and its emergence as a potential predictive tool for chemical reactors is the result of recent advances in computer power.

Despite its complexity, CFD is an inexact science and involves substantial modelling approximations, particularly for turbulent, non-isothermal, multi-phase and chemically-reacting flows. These are the subjects of most interest for reactor performance prediction. Progress towards improving the ability of CFD requires improved models for each of these phenomena to be developed, programmed and tested against experimental data. Once the models have been validated, they can be used with confidence for process design.

1.4 CONTRIBUTIONS OF THIS WORK

This work concentrates on advancing the capability of CFD for strongly three-dimensional and chemically-reacting flows in single-phase liquids. This is an essential building block for further progress to multi-phase applications. All of the simulations presented employed the Harwell FLOW3D Version 2.4 CFD program.

It is shown that Second Moment Closure of the Reynolds-averaged momentum equations is required to describe in sufficient detail the complex flow structure in a stirred reactor. Three-dimensional flow simulations using the Differential Stress turbulence model (DSM) are compared with the traditionally used k-ε model. Laser Doppler Anemometry is used to measure the flow field and validate the CFD predictions. The DSM proves to be superior to k-ε, and is recommended for use in these applications.

For chemical reactions, the principal difficulty lies in correct formulation of sources and sinks in the species conservation equations. These are affected by both fluid flow and process chemistry. Methods previously available are shown to be restricted to certain simplified operating conditions, or inaccurate.

A new method, the Multiple Timescale Probability Density Function (MTPDF) model, is devised based on turbulence theory. It reflects the influences of all scales of motion (including inertial-convective, viscous-convective and viscous-diffusive) on chemical reaction rates. It reduces to the correct asymptotic forms for instantaneous and infinitely slow reactions and to the models of some previous authors under simplified circumstances. The framework of the model is sufficiently flexible for extension to more complicated situations, such as non-isothermal flows.

The MTPDF model, which uses flow field predictions as input, is tested against experimental data for simple and complex (multi-step) fast reactions in tubular reactors. Agreement is satisfactory. The model is used to gain insight into the behaviour of multi-step reactions in multi-dimensional reactors. It is recommended for use as a predictive tool.

A fast multi-step reaction was conducted experimentally in a stirred vessel under varied operating conditions in order to validate MTPDF for this complex flow. The effects of feed time and feed position on yield are illustrated. Complete validation proved impossible due to the magnitude of the computational task (transient three-dimensional flow with five chemical reactions). Even simplification to two dimensions still required very substantial CPU time on a Cray 2 supercomputer. However, some qualitative validation was possible.

A cost-benefit analysis has been carried out on alternative routes of scale-up of new chemical processes. This shows that CFD, when technically applicable, tends to be more cost-effective than pilot-plant trials, particularly for high end-value products.

1.5 LAYOUT OF THE THESIS

Chapter 2 presents the governing equations of the fluid flow problem and details the assumptions required by turbulence models in order to close the equation set.

Chapter 3 reviews the theory of mixing and chemical reaction and the models proposed in the chemical engineering and combustion literature. The applicability of these models is appraised against stringent criteria. Finally, a new model, MTPDF, is developed, incorporating and generalising many concepts from existing models.

Chapter 4 presents application of the fluid flow and chemical reaction models to tubular reactors. Two reactor geometries and two types of chemical reaction are considered. Experimental results are compared with predictions by a range of models.

In Chapter 5, the fluid flow and reaction models are applied to three-dimensional, swirling flow in stirred tank reactors. Results are compared with Laser Doppler measurements of all three average and fluctuating velocity components. As expected, increased predictive accuracy is obtained for the flow field when a Differential Stress turbulence model is used.

Also in Chapter 5, experimental data on the yield of a complex reaction is presented. Results illustrate the effects of feed rate, feed position and stirrer speed on performance. A simplified model of the stirred tank flow field is used to predict the chemical reaction yield under various conditions. Computational restrictions prevented a complete assessment of the reaction model. Qualitative agreement is satisfactory.

Chapter 6 presents a Cost-Benefit Analysis of CFD applied to development and scale-up of new chemical processes. Investment appraisal methods are used to compare the costs of CFD with those of pilot plant work. The effect of uncertainty in the final design is illustrated. For certain types of application, it appears that CFD is more economical than pilot plant work.

Chapter 7 contains conclusions of this project and recommendations for future work.

Chapter 2

FLUID FLOW MODELLING

2.1 INTRODUCTION & OBJECTIVES

Chemical reactor performance is strongly linked to fluid motion. The objective of this chapter is to identify methods for predicting flow patterns in turbulent liquid-phase reactors. Equations describing turbulent flow are presented and the assumptions made in solving them listed. The basic hydrodynamic model is general for any turbulent flow of a Newtonian liquid.

The governing fluid flow equations are ensemble-averaged, resulting in extra terms: "Reynolds stresses". Models for calculating the latter vary in accuracy and contain a number of empirical (fitted) parameters. Two of these models are applied in later chapters to tubular reactors and stirred tanks.

Equations are discretised in three dimensions for numerical solution. The choice of discretisation method is important for convection-dominated flows, where "numerical diffusion" can lead to errors. Some techniques are available for minimising this effect.

Previous work on modelling the hydrodynamics of pipe reactors and stirred tanks is summarised.

2.2 GOVERNING EQUATIONS

For a constant viscosity isothermal incompressible fluid, the equation describing conservation of mass, i.e. "Continuity" is:

$$\frac{\partial \hat{u}_i}{\partial x_i} = 0 \qquad (2.2.1)$$

$\hat{u}_i$ denotes a component of the instantaneous velocity of fluid and x_i any of the three cartesian coordinate directions. Cartesian tensor notation is used throughout this thesis. Wherever the same subscript is repeated within one term of an equation, summation over all possible values of that subscript is implied, i.e.

$$\frac{\partial \hat{u}_i}{\partial x_i} = \frac{\partial \hat{u}_1}{\partial x_1} + \frac{\partial \hat{u}_2}{\partial x_2} + \frac{\partial \hat{u}_3}{\partial x_3} \qquad (2.2.2)$$

The equation for conservation of momentum in the x_i direction is:

$$\frac{\partial \hat{u}_i}{\partial t} + \hat{u}_j \frac{\partial \hat{u}_i}{\partial x_j} = -\frac{1}{\varrho}\frac{\partial \hat{p}}{\partial x_i} + \frac{1}{\varrho}\frac{\partial}{\partial x_j}\left(\frac{\mu \partial \hat{u}_i}{\partial x_j}\right) \qquad (2.2.3)$$

Equations 2.2.1 and 2.2.3 are derived from mass and momentum balances over small control volumes within the flow. Their derivation is available in standard fluid dynamics textbooks (see for example, Bird, Stewart & Lightfoot, 1960).

There are four unknown quantities (instantaneous values of three velocity components and pressure) and four equations, one for continuity and three for momentum transfer; the equation set is therefore closed and the unknowns can be found by integration with suitable boundary conditions.

A ratio of inertial to viscous forces or "Reynolds number" can be defined and is of the order of the ratio of terms 2 and 4 in equation 2.2.3. Low Reynolds numbers (e.g. <10) indicate "laminar" flow, i.e. relatively streamlined and slow-moving. It is possible to divide a laminar flow domain into small enough "cells" to capture the variations of velocities and pressures with good accuracy. Even time-dependent flows can be solved economically, due to relatively long characteristic times for changes in the flow.

High Reynolds numbers (e.g. $>10^4$) indicate "turbulence", i.e. rapidly varying velocities and pressures and almost chaotic behaviour. High Reynolds numbers are of interest in the present context. In turbulent flow, velocities and pressures vary so rapidly in both space and time that accurate resolution of instantaneous values is beyond the scope of today's most powerful computers. For example, approximate calculations (Gibson et al., 1990) suggest that 10^9 computational cells would be needed for a Reynolds number of 50,000. 10^5 cells is the practical maximum at the present state of hardware and software development.

Fortunately, the fine details of instantaneous turbulence are not often required in industrial applications, and calculation of the average situation over a period of seconds, minutes or hours is usually sufficient. Equations 2.2.1 and 2.2.3 can be recast into equations for average velocities and pressures by expressing the variables as the sum of mean and fluctuating parts ("the Reynolds decomposition"):

$$\hat{u}_i = U_i + u_i \tag{2.2.4}$$

$$\hat{p} = P + p \tag{2.2.5}$$

The averaged continuity equation becomes:

$$\frac{\partial U_i}{\partial x_i} = 0 \tag{2.2.6}$$

and the averaged momentum equation in the x_i direction:

$$\frac{\partial U_i}{\partial t} + U_j \frac{\partial U_i}{\partial x_j} = -\frac{1}{\varrho}\frac{\partial P}{\partial x_i} + \frac{1}{\varrho}\frac{\partial}{\partial x_j}\left(\frac{\mu \partial U_i}{\partial x_j}\right) - \frac{\partial \overline{u_i u_j}}{\partial x_j} \tag{2.2.7}$$

With the exception of the last term in 2.2.7, the equations still form a closed set from which average velocities and pressures can be obtained by integration. This extra term, the product of two fluctuating components of velocity at the same point, is called the "Reynolds stress" and is a measure of the extra momentum transfer which takes place in turbulent flows but is absent in the laminar case.

There are nine Reynolds stresses, reduced to six by symmetry, three shear (i not equal to j) and three normal (i equal to j). Each shear stress appears in two momentum equations; normal stresses appear in one equation each. Three Reynolds stresses appear in each momentum equation, one normal and two shear.

Six new variables have therefore been introduced by the averaging process. To calculate the hydrodynamics of turbulent flows, the number of equations must be increased to again equal the number of unknowns. This is the focus of turbulence modelling.

2.3 TURBULENCE MODELLING

2.3.1 Objectives & Criteria

To make use of equations 2.2.6 and 2.2.7, a turbulence model must be selected. In the following sub-sections, the main alternatives are reviewed, with advantages and disadvantages. Finally, choices are made for simulations in subsequent chapters.

The turbulence model(s) selected for practical use should satisfy certain criteria. Important for this work is that the model should:

1. Be based on physically plausible concepts
2. Reproduce experimentally observed flow field data to sufficient accuracy
3. Not involve excessive computational cost

Criterion 1 is satisfied by all common turbulence models, since physical intuition is their main foundation. Satisfying criterion 2 depends on the complexity of the flow field under examination; since stirred tank reactors are characterised by complex, swirling flow patterns, only the more sophisticated turbulence models satisfy this criterion. Tubular reactors are simpler, so less complex models suffice. Criterion 3 is dependent on the size of computer used. For modern workstations, all turbulence models of the type described here meet this criterion to a greater or lesser extent for computing steady-state flows. Computational cost is more a function of the number of cells employed in the calculation than of the turbulence model.

2.3.2 The Reynolds Stress Equations

Transport equations for the Reynolds stresses can be obtained from the momentum transfer equations (see Hanjalic & Launder, 1972; Launder, Reece & Rodi, 1975). They take the form:

$$C_{ij} = P_{ij} + \phi_{ij} + D_{ij} - \varepsilon_{ij} \tag{2.3.1}$$

where:

$$C_{ij} = \frac{\partial}{\partial x_k}(U_k \, \overline{u_i u_j}) \tag{2.3.2}$$

$$P_{ij} = -(\overline{u_j u_k}\frac{\partial U_i}{\partial x_k} + \overline{u_i u_k}\frac{\partial U_j}{\partial x_k}) \tag{2.3.3}$$

$$\phi_{ij} = \overline{\frac{p}{\varrho}\left(\frac{\partial u_i}{\partial x_j} + \frac{\partial u_j}{\partial x_i}\right)} \tag{2.3.4}$$

$$D_{ij} = -\frac{\partial}{\partial x_k}\left(\overline{u_i u_j u_k} + \overline{\frac{p}{\varrho}u_i}\delta_{jk} + \overline{\frac{p}{\varrho}u_j}\,\delta_{ik} - \nu\frac{\partial \overline{u_i u_j}}{\partial x_k}\right) \tag{2.3.5}$$

$$\varepsilon_{ij} = 2\nu\,\overline{\frac{\partial u_i}{\partial x_k}\frac{\partial u_j}{\partial x_k}} \tag{2.3.6}$$

Terms in equation 2.3.1 describe convection, C_{ij}, production, P_{ij}, redistribution by pressure strain, ϕ_{ij}, diffusion, D_{ij} and dissipation, ε_{ij} of turbulent stress. Six such equations can be formed, one for each independent Reynolds stress. The equations as written have dimensions of m^2/s^3 (or W/kg) and represent the rate of transport, generation and dissipation of turbulent energy. The first two terms (C_{ij} and P_{ij}) are made up of Reynolds stresses and average velocity gradients. Remaining terms consist of new, unknown correlations between fluctuating velocities and their derivatives and fluctuating pressure.

Further transport equations for these new unknowns can also be derived but these equations too contain further unknowns. In order to calculate turbulent flows, the unknown terms must be approximated at some level.

The origins of all common models can be traced back to Equation 2.3.1. Those which attempt closure by estimating pressure-strain, diffusion and dissipation terms directly are termed "Second Moment Closures". These are generally regarded as the most reliable practical models for complex turbulent flows (Gibson et al, 1990; Launder, 1989), such as those in stirred tank reactors. The essential features of this method are now described.

2.3.3 Second Moment Closure

C_{ij} and P_{ij} in the Reynolds stress transport equation can be calculated exactly if equations for the six Reynolds stresses and three average velocities are solved. P_{ij} represents generation of turbulence energy by gradients of average velocity. This implies that accurate predictions of turbulence generation require accurate velocity gradients. ε_{ij}, ϕ_{ij} and D_{ij} require modelling.

ε_{ij} (Dissipation)

ε_{ij} is responsible for destruction of turbulent stresses by the action of viscosity on fine-scale fluctuating velocity gradients. Kolmogoroff (1941) defined the concept of a locally isotropic turbulence, which has the following consequences:

1. Turbulent motion on a fine scale is completely random. There is no correlation between fluctuating components of velocity in different directions. Hence the Reynolds shear stresses are zero.

2. If the fluctuating velocities themselves are uncorrelated, their spatial derivatives are also uncorrelated.

With these assumptions:

$$\varepsilon_{ij} = \frac{2}{3}\,\delta_{ij}\,\nu\,\overline{\frac{\partial u_i}{\partial x_k}\frac{\partial u_i}{\partial x_k}} \tag{2.3.7}$$

This expression is used in equations where $i=j$, i.e. for the turbulent normal stresses, since viscous destruction of the shear stresses is zero. Dissipation is assumed to be equally distributed between the three normal stress transport equations, i.e.

$$\varepsilon_{11} = \varepsilon_{22} = \varepsilon_{33} = \frac{2}{3}\,\varepsilon \tag{2.3.8}$$

Total dissipation from the three equations is then 2ε, because the sum of the turbulent normal stresses is twice the turbulent kinetic energy:

$$k = \frac{1}{2}\,\overline{u_i^2} \tag{2.3.9}$$

An important consequence of isotropy in the fine scale motion is that energy exchange among Reynolds stress components cannot be accomplished by this term. Dissipation in the shear stress equations is zero and each normal stress is dissipated at an equal rate. This concept is later used to help model the pressure-strain rate correlation.

Modelling requires that ε be approximated in terms of known quantities. An exact transport equation for ε can be written, but it is of little use (Hanjalic & Launder, 1972); terms contain only (unknown) interactions among the finest scales of motion. Turbulence theory (e.g. Kolmogoroff, 1941) suggests that the rate of energy dissipation is not determined by these motions, rather that energy cascades from large to small eddies. The interactions producing the energy and taking part in the transfer process are large-scale and unaffected by viscosity. Once ε is determined by the large scale motions, the finer scales simply adjust to consistent behaviour. Modelling of the ε equation is therefore based not on the details of each term in the exact equation, but on intuition primarily related to the behaviour of large eddies.

The form adopted is:

$$\frac{\partial}{\partial x_k}\,U_k\,\varepsilon = c_\varepsilon\,\frac{\partial}{\partial x_k}\left(\frac{\overline{u_k u_l}}{\varepsilon}\,k\,\frac{\partial \varepsilon}{\partial x_l}\right) - c_{\varepsilon 1}\,\frac{\varepsilon}{k}\,\overline{u_k u_l}\,\frac{\partial U_k}{\partial x_l} - c_{\varepsilon 2}\frac{\varepsilon^2}{k} \tag{2.3.10}$$

The three terms on the right hand side represent diffusion, generation and dissipation of ε. Predictions made using this equation are sensitive to the values of $c_{\varepsilon 1}$ and $c_{\varepsilon 2}$. The most widely used and generally applicable set of constants are those in Table 2.1.

Table 2.1 Differential Stress model constants

$c_{\varepsilon 1}$	$c_{\varepsilon 2}$	c_ε	c_1	c_2	c_s	E	κ
1.44	1.92	0.16	1.8	0.6	0.22	9.793	0.4187

ϕ_{ij} (Pressure-strain rate correlation)

Because of isotropy in the fine scale motion the pressure-strain correlation is believed to be solely responsible for energy transfer amongst Reynolds stress components. This allows fitted constants in the pressure-strain model to be determined by comparison with measured flows in which inter-component energy transfer takes place.

An equation for the pressure-strain correlation can be obtained by manipulation of the momentum transfer equation (Chou, 1945) and has two types of term, one containing fluctuating turbulence quantities, the other, mean velocity gradients. The turbulent term is assumed to be responsible for the return to isotropy of an anisotropic shear field. It is modelled as a first-order function of the anisotropy. The mean velocity gradient term is modelled as a function of the anisotropy of stress production. The complete model, incorporating both terms is then (Launder, Reece & Rodi, 1975):

$$\phi_{ij} = -c_1 \frac{\varepsilon}{k} \left(\overline{u_i u_j} - \frac{2}{3}\delta_{ij}\, k\right) - c_2 \left(P_{ij} - \frac{2}{3}\delta_{ij}\, P\right) \qquad (2.3.11)$$

The model is intuitive and only loosely connected with the real processes that are taking place (Launder, 1989). An analogy to explain the two terms is that the turbulent part can be considered a wealth tax and the mean-strain part an income tax. The overall pressure strain is responsible for a re-distribution of wealth (turbulence) within the flow, while not affecting the overall income (turbulent energy) level.

There is some disagreement over the most appropriate values of c_1 and c_2. c_1 generally takes a value in the region 1.5-1.8 and c_2, 0.6 (Launder, 1989). One proposal of c_1=3.0 and c_2=0.3 was reported to work well for some swirling flows (Younis, 1984).

D_{ij} (Diffusion)

Diffusional transport of Reynolds stress is regarded as much less important than redistribution by pressure-strain or dissipation (Launder, 1989) and has received correspondingly less attention. The contributions arising from the triple velocity products, pressure diffusion and viscous diffusion are lumped together in a gradient diffusion term (Daly & Harlow, 1970):

$$D_{ij} = c_s \frac{\partial}{\partial x_k} \left(\frac{k}{\varepsilon}\, \overline{u_k u_l}\, \frac{\partial \overline{u_i u_j}}{\partial x_l}\right) \qquad (2.3.12)$$

where c_s=0.22. Although originally advanced as a model for the triple velocity correlation component of diffusion only, where the pressure component was neglected completely, this model is now regarded as a composite of both effects. Diffusion of stress through the molecular viscosity is neglected.

2.3.4 Wall Effects

The no-slip boundary condition applied at walls means that both average and fluctuating velocities vary rapidly as the wall is approached. The fluctuating velocity normal to the wall is reduced and one or both of the other components increased. Such effects are not catered for in the models presented so far.

Neither diffusion nor dissipation are believed to be responsible for wall effects on the velocity fluctuations. Attention is focused on the pressure-strain correlation, which redistributes energy amongst the Reynolds stress components. The influence of the wall extends to a distance of the order of the size of the largest eddies. Models adopt a correction to the pressure-strain correlation whose magnitude varies with the ratio of the eddy size to wall distance. Constants used are not well established for flows with even moderately complex geometries, such as cylindrical walls, for example. The result is that wall effects on the Reynolds stresses are often neglected (Clarke et al., 1989).

Very near a wall, mean velocity and turbulence structure appear to follow near-universal behaviour, the so-called "law of the wall" (e.g. Launder, 1989). Flow within the viscous sublayer, adjacent to the wall, is directly affected by viscosity. Outside this region, in the "buffer region", both viscous and turbulent effects are important. Beyond this layer, the flow is assumed to be fully turbulent. Wall law equations are used to bridge the gap between the wall and the main body of the flow.

A characteristic shear stress can be defined as:

$$\tau_k = c_\mu^{1/2} \varrho\, k \tag{2.3.13}$$

Scaled velocities and distances can be defined by:

$$U^+ = \frac{(\varrho\, \tau_k)^{1/2}\, U}{\tau_k} \tag{2.3.14}$$

$$y^+ = \frac{(\varrho\, \tau_k)^{1/2}\, y}{\mu} \tag{2.3.15}$$

The intersection between the viscous sublayer and the logarithmic wall region is given by the upper root of:

$$y_o^+ = \frac{1}{\kappa} \log(E\, y_o^+) \tag{2.3.16}$$

The average velocity parallel to the wall is then given by:

$$U^+ = y^+ \quad (\text{if } y^+ < y_o^+) \tag{2.3.17}$$

$$U^+ = \frac{1}{\kappa} \log(E\, y^+) \quad (\text{if } y^+ > y_o^+) \tag{2.3.18}$$

To define τ_k, the turbulent kinetic energy is required. This is obtained from solution of the normal Reynolds stress equations in the cell adjacent to the wall. From this, the velocities can be determined. Production terms follow from the velocity gradients. The turbulent energy dissipation rate is given by (see Table 1):

$$\varepsilon = \frac{c_\mu^{3/4}\, k^{3/2}}{\kappa\, y} \tag{2.3.19}$$

2.3.5 Use of Second Moment Closure

Second moment closure represents the highest level of complexity of the closures that can be practically used for complex geometries. The complete model requires simultaneous solution of the continuity and momentum equations with up to seven extra transport equations for the turbulence (six Reynolds stresses and the rate of turbulent energy dissipation). This represents a substantial computational task in three-dimensional flows but offers the best hope of a generally accurate solution. In Chapter 5, second moment closure is applied to predict the flow field in a stirred tank reactor.

Because of computational cost, efforts have been made by many workers to simplify turbulence modelling, while not sacrificing too much generality. Two common simplifications are the Algebraic Stress Models and the widely-used k-ε model. These are now described.

2.3.6 Algebraic Stress Model

The Algebraic Stress model (ASM) assumes that convection and diffusion of each turbulent stress component is proportional to the corresponding rate of transport of the turbulent kinetic energy. A transport equation for k is obtained by summing the equations for the turbulent normal stresses and dividing by two:

$$U_k \frac{\partial k}{\partial x_k} = -\overline{u_i u_k} \frac{\partial U_i}{\partial x_k} - \frac{\partial}{\partial x_k}\left(\frac{1}{2}\overline{u_k u_i^2} - \nu \frac{\partial k}{\partial x_k} + \overline{\frac{p}{\varrho} u_k}\right) - \nu \overline{\frac{\partial u_i}{\partial x_k} \frac{\partial u_i}{\partial x_k}} \tag{2.3.20}$$

The k equation contains the following terms: rate of change by advection, production by interaction with the mean strain rate, diffusion and viscous dissipation. The pressure strain rate correlation is absent on summation of the normal stress equations. The effect of this term is to redistribute energy between components (see Section 2.3.3).

If equations for Reynolds stresses and ε are provided, the only term requiring modelling in 2.3.20 is diffusion. This is accomplished by a gradient diffusion term:

$$D_{ij} = c_s \frac{\partial}{\partial x_k}\left(\frac{k}{\varepsilon} \overline{u_k u_l} \frac{\partial k}{\partial x_l}\right) \tag{2.3.21}$$

where c_s=0.22. The essence of the ASM formulation is that convection and diffusion of each Reynolds stress are assumed to follow:

$$C_{ij} = \frac{\overline{u_i u_j}}{k} C_k \tag{2.3.22}$$

$$D_{ij} = \frac{\overline{u_i u_j}}{k} D_k \tag{2.3.23}$$

so that the Reynolds stress transport equations are now algebraic rather then differential. However, there are some pitfalls inherent in these assumptions. For example, near a symmetry axis, the turbulent kinetic energy has a zero gradient, but the Reynolds shear stresses are antisymmetric. Furthermore, convergence to a stable numerical solution is often difficult to achieve with this formulation (Clarke et al., 1989; Launder, 1989). The Algebraic Stress model is not used in this project.

2.3.7 Two Equation Models

If P_{ij} and ε_{ij} in equation 2.3.1 are equal, transport effects on the Reynolds stresses can be neglected (ie. the left hand side of Equation 2.3.1 is zero). Flows in which this occurs are said to be in "local equilibrium". Examples are thin shear layers and flow near walls. With this simplification, the turbulent stress at any point depends only on conditions at that point, and is independent of its surroundings. This results in an algebraic equation for the Reynolds stresses, analogous to Newton's Law of Viscosity for a laminar flow:

$$\tau_{laminar} = \mu \left(\frac{\partial U_i}{\partial x_j} + \frac{\partial U_j}{\partial x_i}\right) \tag{2.3.24}$$

For turbulent flow, the molecular viscosity is replaced by a fictitious "eddy viscosity" or eddy diffusivity of momentum:

$$-\overline{u_i u_j} = \nu_t \left(\frac{\partial U_i}{\partial x_j} + \frac{\partial U_j}{\partial x_i}\right) - \frac{2}{3} k \delta_{ij} \tag{2.3.25}$$

Closure then requires specification of the eddy viscosity. The most commonly used method is to solve two transport equations, one for the turbulent kinetic energy, k and one for its rate of dissipation, ε. The equation for k is obtained by summing the equations for the three turbulent normal stresses and dividing by two (equation 2.3.20 above). Terms that involve Reynolds stresses are modelled using Equation 2.3.25. The ε equation is similar to the one used in second moment closure, but again uses Equation 2.3.25 wherever a turbulent stress term is needed. The resulting equations are:

$$U_i \frac{\partial k}{\partial x_i} = \frac{\partial}{\partial x_i} \left(\frac{\mu_t}{\varrho \sigma_k} + \nu \frac{\partial k}{\partial x_i}\right) + P - \varepsilon \tag{2.3.26}$$

$$U_i \frac{\partial \varepsilon}{\partial x_i} = \frac{\partial}{\partial x_i} \left(\frac{\mu_t}{\varrho \sigma_\varepsilon} + \nu \frac{\partial \varepsilon}{\partial x_i} \right) + \frac{\varepsilon}{k} \left(c_{\varepsilon 1} P - c_{\varepsilon 2} \varepsilon \right) \tag{2.3.27}$$

$$P = \frac{\mu_t}{\varrho} \frac{\partial U_i}{\partial x_j} \left(\frac{\partial U_i}{\partial x_j} + \frac{\partial U_j}{\partial x_i} \right) \tag{2.3.28}$$

$$\mu_t = c_\mu \varrho \frac{k^2}{\varepsilon} \qquad (2.3.29)$$

The k-ε model is based on approximations to terms appearing in the exact Reynolds stress, turbulent kinetic energy and dissipation transport equations. Empirical constants are extensively used, whose numerical values are based mainly on comparison with experimental data for decay of grid turbulence and near-wall turbulence (see Table 2.2).

k-ε has been criticised for two main reasons. Firstly equation 2.3.29 suggests that eddy viscosity should always be positive and isotropic (the same in all directions). However, measurements demonstrate that this is not so. Furthermore, turbulent shear stress does not always have the opposite sign to mean velocity gradients. As a result, different values of μ_t result from different combinations of i and j (e.g. Fawcett, 1992).

The Boussinesq hypothesis, equation 2.3.25, suggests that the effects on the turbulence of both longitudinal and lateral strain rates are equal. However, experimental data shows that the effects of two strain rates have different stabilising or destabilising effects on the flow, which can either enhance or reduce turbulent shear stress relative to equation 2.3.25 (Bradshaw, 1973). Equation 2.3.25 also predicts that the effect of strain is felt immediately the strain is applied, but in fact flow history, or turbulence transport effects, can be important.

As a result, k-ε is not expected to accurately predict turbulence in complex (e.g. swirling) flows. Ad-hoc corrections are available (Bolour-Froushan, 1986) which improve matters somewhat, but it appears that for a generally applicable model, ASM and DSM, which take account of non-isotropic diffusion and transport effects, are preferable.

The k-ε model is used in Chapter 4 to predict the flow fields in tubular reactors and in Chapter 5 for a stirred tank reactor.

Table 2.2 k-ε model constants

$c_{\varepsilon 1}$	$c_{\varepsilon 2}$	σ_ε	σ_k	c_μ	κ	E
1.44	1.92	1.22	1.0	0.09	0.4187	9.793

2.4 DISCRETISATION

All of the differential equations described above are intractable by analytical methods, except in very simplified flows. Numerical methods are required to calculate particular solutions for a given set of boundary conditions. The equations are discretised so that they become algebraic rather than differential and can be solved by matrix methods. This works as follows.

The solution domain is divided into a large number of cells. This is called "the grid". Discrete equations are formed by integrating over the surface area and volume of each grid cell:

$$\int_V \varrho \frac{\partial \phi}{\partial t}\, dV + \int_S \varrho \phi\ U \,.\, n\, dS - \int_S \varrho \Gamma_\phi\ \nabla \phi \,.\, n\, dS = \int_V \varrho S_\phi\, dV \quad (2.4.1)$$

The resulting large set of simultaneous equations is passed to a matrix solver, which performs iterations based on updated guesses for each variable until it arrives at the converged solution. The solution is a set of values of each variable, evaluated at the centre of each cell. Values at other points, if required, are obtained by interpolation.

Convective and diffusive fluxes are evaluated at cell boundaries. Convection of any quantity (e.g. a concentration) is the product of density, velocity, concentration and cell frontal area. Diffusion is the product of density, diffusion coefficient, concentration gradient and area. Sources and sinks are evaluated at cell centres as the products of density, a rate (e.g. of chemical reaction) and the cell volume.

To evaluate a quantity at the boundary between two cells requires interpolation. This is necessary for calculating convection and diffusion.

For the diffusion terms, central differencing (CD) is used. This corresponds to linear interpolation between cell centres to obtain the value at the boundary. When used for the convection terms, however, CD causes instability in most flows. The reason is that convection is a one-way effect, i.e. in a convection-dominated flow, the value of a variable at any point should depend on its upstream values but not on those downstream. CD leads to a strong unphysical dependence on downstream quantities, which makes the equations unstable.

The simplest method for calculating convective fluxes is UPWIND differencing, see Figure 2.1. This sets the interpolated value equal to the value at the centre of the upstream cell. However, in flows where the grid lines are not aligned with the streamlines, UPWIND differencing can lead to an error called "Numerical Diffusion". This is a diffusive effect introduced by the differencing scheme, which transports material that would not be transported in reality. The largest error occurs when the grid lines are at 45 degrees to the flow. Numerical diffusion has an important effect on turbulence predictions, as will be shown in Chapter 5, where it tends to flatten velocity profiles, which in turn reduces turbulence generation.

Intuitively, numerical diffusion can be overcome by forming an average value at the cell boundary based on the values of all upstream neighbours. Such schemes exist and are called "flow-oriented". However, these are difficult to implement in three dimensions (Ziman, 1990).

Alternatively, a higher order of interpolation can be used in an UPWIND-type scheme. Higher UPWIND differencing (HUD) for example passes a line through two upstream values and interpolates linearly to the cell face, see Figure 2.1. Quadratic UPWIND differencing (QUICK) uses two upstream cells and one downstream to fit a quadratic function which then interpolates to the cell face. Both methods should lead to improved accuracy, but at increased computational cost, and without guaranteed stability. Use of high order differencing is equivalent to passing a polynomial through experimental data. Unless the data itself is of good quality and sufficiently well spatially resolved, incorrect results can be obtained. This can happen during the course of a CFD calculation at stages when the solution is still far from converged.

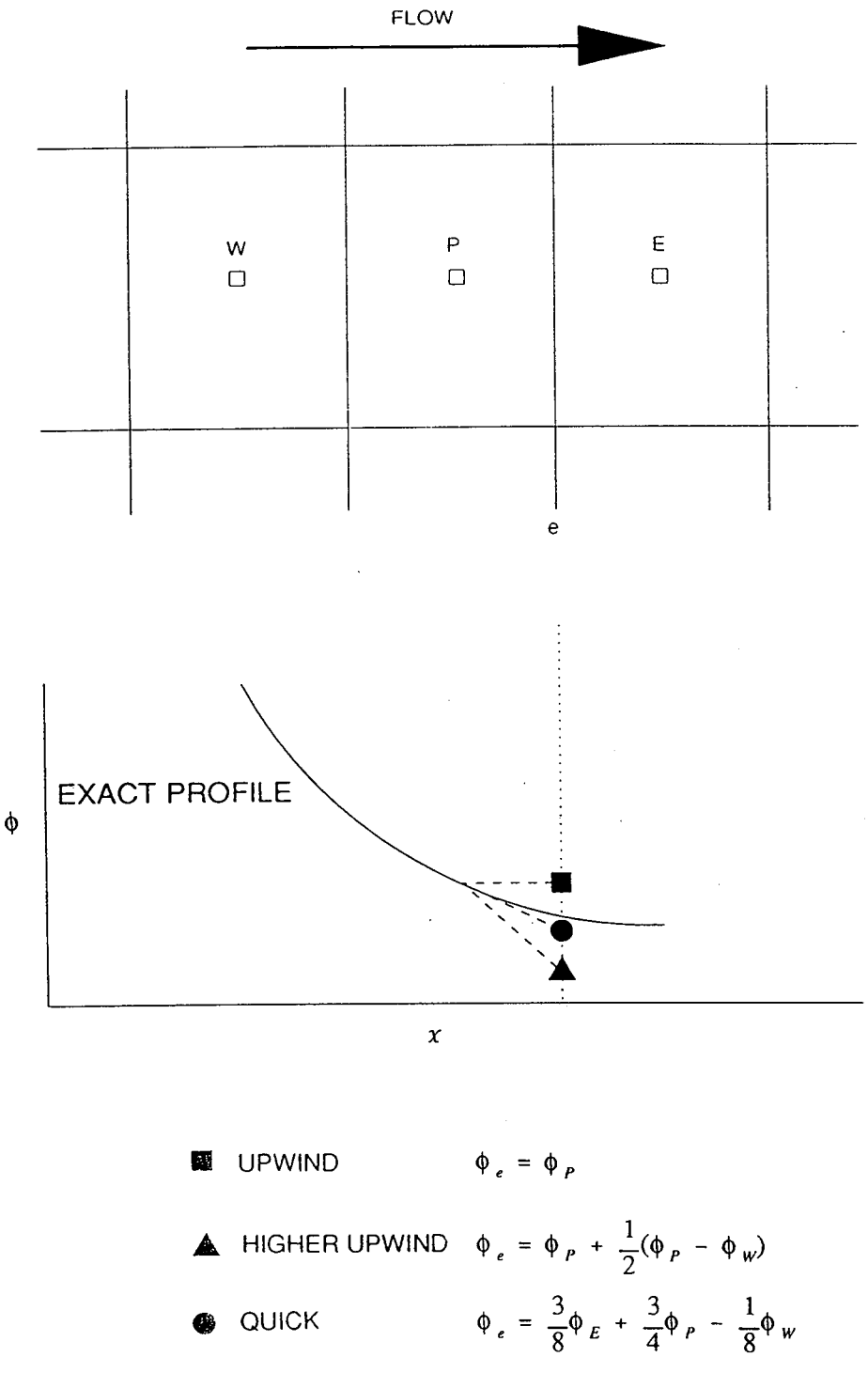

Figure 2.1 Comparison of finite difference (discretisation) schemes for capturing the value of a function at the cell face. UPWIND is stable but tends to overestimate convective fluxes. HIGHER UPWIND and QUICK are potentially more accurate but less stable.

In much of this thesis, UPWIND is used despite its deficiencies. Some mathematical models (e.g. the Differential Stress turbulence model) are so inherently unstable that it is often only practical to use UPWIND. Where possible and advantageous, higher order schemes are employed.

2.5 SUMMARY OF RELEVANT LITERATURE ON MIXING VESSEL FLOWS

In Chapters 4 and 5, simulations of tubular and stirred tank reactors are presented which used the models described in this chapter. Relevant previous measurements and calculations by other workers are described below.

2.5.1 Tubular reactors

Tubular reactors are applied in industry for mixing and reaction applications which do not require long residence times (see Figure 2.2). Motionless mixing elements or baffles are sometimes employed to increase the mixing intensity relative to an empty pipe. In Chapter 4, coaxial jet tubular reactors are simulated.

Although calculations of jet flows are plentiful in the literature, there are few calculations available of coaxial jet mixing in tubular reactors. This type of flow was measured by Oosthuizen & Wu (1978) and Guiraud et al. (1991) and computations using the k-ε model made by Oosthuizen & Wu. Tovstiga (1986) made some calculations using a simple flow model and a one-dimensional reaction model. Most computational work on these devices assumes that the flow is essentially one-dimensional (e.g. Li & Toor, 1986; Mao & Toor, 1970).

2.5.2 Stirred tank reactors

Simulation of the flow field inside tank mixers and chemical reactors (see Figure 2.3) has received considerable attention in recent years. The first published Navier-Stokes simulations of mixing tanks were performed by Harvey (1980) who studied Rushton (six flat-bladed) turbines. Middleton et al. (1986) and co-workers at ICI (e.g. Bolour-Froushan, 1986; Ziman, 1990) have modelled turbulent mixing and in some cases chemical reaction for Rushton turbines and some multiple impeller combinations in three dimensions.

Hutchings et al. (1989) calculated the flow patterns for both radial and axial flow impellers in two and three dimensions. Ranade et al. (1989) simulated both Rushton and six-bladed pitched-blade impellers, Bakker (1992) simulated Rushton, axial flow and six-bladed pitched blade impellers. Brucato et al. (1989), Placek & Tavlarides (1986) and Kresta & Wood (1991) studied Rushton turbines. Ziman (1990) developed a novel discretisation scheme, called Self-Filtered Central Differencing (SFCD), which improved flow calculations for Rushton turbines.

Although Fawcett (1992) and Jaworski et al. (1991) made flow measurements of four-bladed pitched-blade turbines, there appear to be no computational studies available for this impeller, which is amongst the most common in industrial use.

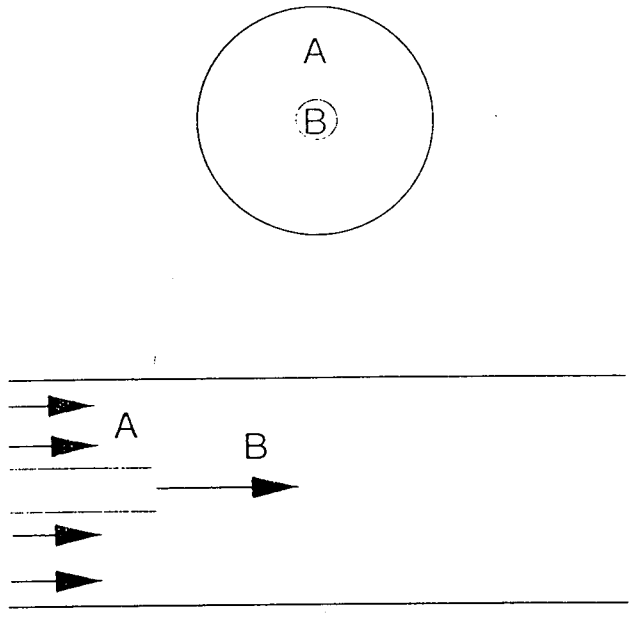

Figure 2.2 Schematic of a coaxial jet tubular reactor

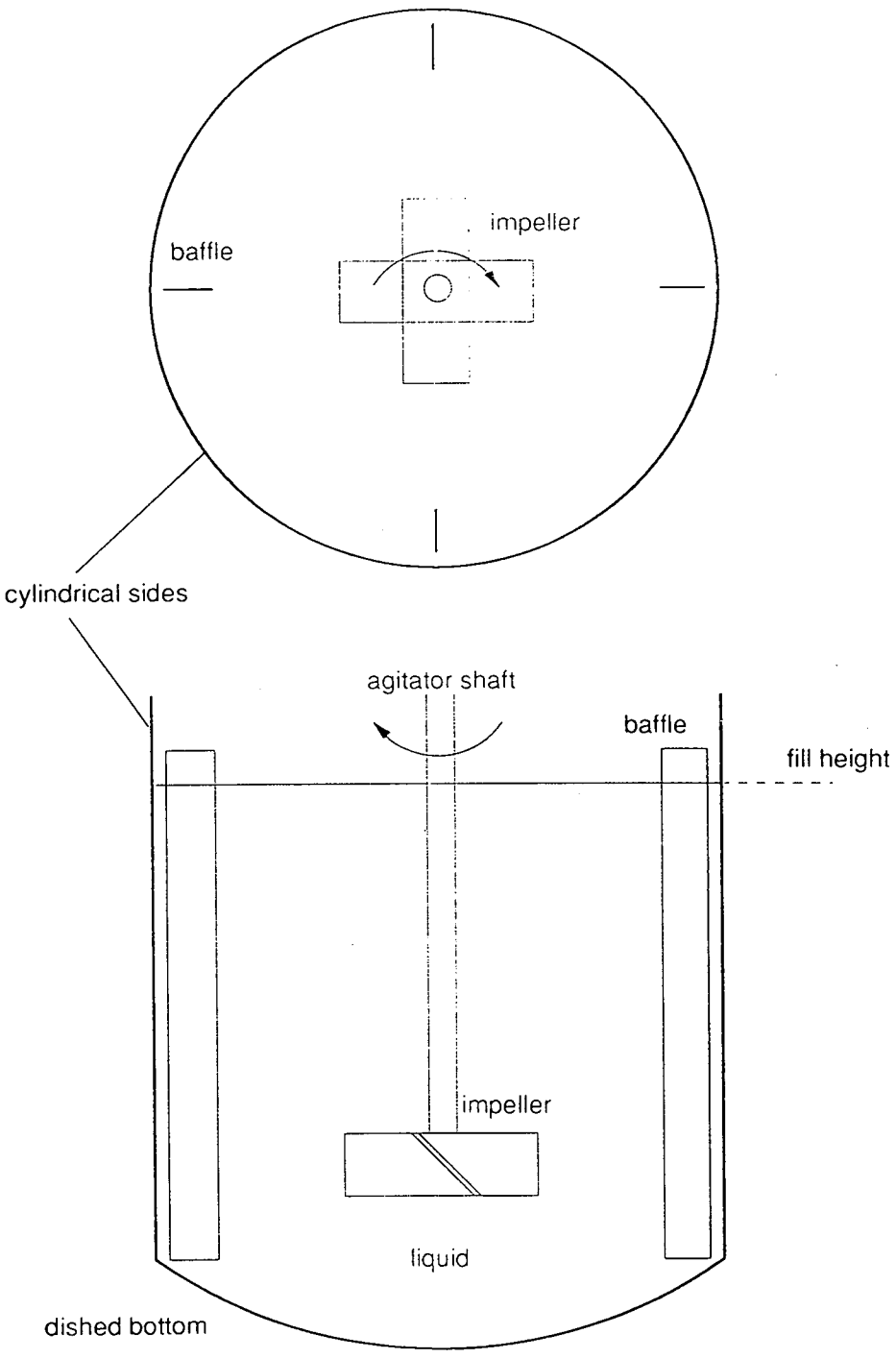

Figure 2.3 Schematic of a stirred tank reactor with four baffles

All of the above authors used the k-ε model of turbulence and found reasonable quantitative agreement between measurements and computations for bulk flow patterns. Bakker (1992) also used the Algebraic Stress turbulence model (ASM), which yielded better predictions than k-ε. The Differential Stress model (DSM) has not previously been applied to stirred reactors.

Predictions of turbulence quantities (such as k and ε) and of swirl velocity were least accurate in all cases. Most simulations (e.g. Middleton et al., 1986; Ranade et al., 1989; Ziman, 1990) have failed to reproduce correctly the direction of the average flow pattern in the upper half of the tank, where swirl in the opposite direction to the impeller rotation has been predicted.

In all simulations of baffled tanks, the impeller has been treated as a time-averaged source of flow, turbulence and momentum. Calculation of the flow relative to each blade in a rotating frame of reference is computationally prohibitive at the present time. Boundary conditions on the impeller periphery were obtained from experimental data. Some efforts have been made to develop more general boundary conditions (e.g. Pericleous & Patel, 1987). The effects of grid dependence were evaluated by Ziman, who found that k-ε solutions with 80,000 cells were still not fully grid-independent.

Simulations of the flow field generated by a four-bladed pitched blade turbine using both k-ε and Differential Stress models are presented in Chapter 5 and compared with measurements by Laser Doppler Anemometry.

2.6 CONCLUSIONS

Suitability of different turbulence modelling approaches for stirred tanks and tubular reactors has been assessed. From a review of the turbulence modelling literature, it appears that the Differential Stress turbulence model should be applied to predict the three-dimensional flow patterns and turbulence distribution in stirred vessels. The k-ε model should be adequate for non-swirling flow in a coaxial jet tubular reactor. These flow simulations are presented in Chapters 4 and 5.

Chapter 3

CHEMICAL REACTION MODELLING

3.1 INTRODUCTION & OBJECTIVES

In this chapter, effects of flow pattern and turbulence on chemical reactions are described. The objective is to identify an accurate method for linking CFD flow predictions with chemical reaction rates.

Reactions can be characterised according to their speed relative to mixing. Design for slow reactions does not require flow computations. For intrinsically fast reactions, the rate at which species are brought together can retard the reaction and cause unwanted byproducts to be formed. Desirable attributes of a dual flow-reaction modelling method are presented and the various methods available reviewed. A new closure is proposed. This and some other models are tested for reactive mixing predictions in subsequent chapters.

3.2 MIXING EFFECTS ON REACTIONS

Chemical reactions can be classified according to whether their intrinsic speed is faster or slower then mixing:

$$t_R \ll t_{mi} \quad \text{instantaneous} \tag{3.2.1}$$

$$t_R \propto t_{mi} \quad \text{fast} \tag{3.2.2}$$

$$t_R \gg t_{mi} \quad \text{slow} \tag{3.2.3}$$

Reaction time much shorter than mixing time indicates the instantaneous regime, where the kinetics of the reaction are irrelevant and mixing alone determines the rate. Reaction time similar to mixing time indicates the fast regime, where both mixing and kinetics influence the rate. Reaction much slower than mixing indicates the slow regime, where only kinetics are important.

Reactors can be designed for slow reactions based on kinetics alone (Levenspiel, 1972). Mixing rate calculations are necessary to predict both instantaneous and fast reactions, which occur in many common processes: polymerisation, neutralisation, organic oxidation and precipitation reactions are a few examples. Fast is preferable to slow for productivity reasons: at a given level of production, equipment can have a shorter residence time, or for a given equipment size, throughput can be higher. Methods for predicting rates and yields of these reactions are needed.

Some reactions exhibit complex pathways involving several species consecutively or in parallel. Depending on the relative speeds of different steps, mixing can affect not only the rate of product formation, but also which product is formed. Successful scale-up

for these situations requires detailed fluid dynamic data (see for example, Middleton et al., 1986; Ziman, 1990).

In much of what follows, the following single-step reaction scheme will be used as an illustration:

$$A + B \rightarrow R$$

Results will later be generalised, where possible, to multi-step reactions. The instantaneous local concentration of chemical species can be obtained from the following transport equation:

$$\frac{D\hat{c}_A}{Dt} = \hat{\Omega}_A = k\,\hat{c}_A\,\hat{c}_B \tag{3.2.4}$$

where:

$$\frac{D\phi}{Dt} = \frac{\partial\phi}{\partial t} + U_i\frac{\partial\phi}{\partial x_i} - \frac{\partial}{\partial x_i}\Gamma_\phi\frac{\partial\phi}{\partial x_i} \tag{3.2.5}$$

In turbulent flows, it is necessary to average 3.2.4 (see Chapter 2). The average reaction rate, in the absence of temperature fluctuations, is:

$$\Omega_A = k\,(\,C_A\,C_B + \overline{c_A\,c_B}\,) \tag{3.2.6}$$

The second term on the right-hand side of equation 3.2.6 is the covariance of concentration fluctuations and is analogous to the Reynolds stresses for fluctuating velocities (Chapter 2). It needs to be calculated to determine the average reaction rate. Because of fluctuations (which occur when mixing is incomplete), A and B can be present at the same point but fail to react because they arrive at different times (Spalding, 1971). In other words, the second term in equation 3.2.6 can be large and negative, thereby reducing the reaction rate (Bourne & Toor, 1977). Mixing is the process by which the magnitude of the second term is reduced, eventually tending towards zero; when the fluctuations are zero, the reaction proceeds at its intrinsic rate, according to kinetics.

Estimation of the covariance is the crux of chemical reaction modelling. To shed light on how this might be achieved, the various stages of mixing in turbulent liquids are now described.

3.3 MIXING MECHANISMS

When a feed stream enters a chemical reactor, it mixes with the surrounding fluid by means of convection and diffusion over a range of spatial and time scales. During mixing, the feed changes from a coherent structure of a given composition and size to smaller, less coherent eddies (Figure 3.1). In this way, the distances over which molecules need to travel in order to meet are reduced. When perfect mixing is approached, intermingled fluid layers are indistinguishable except at the molecular level.

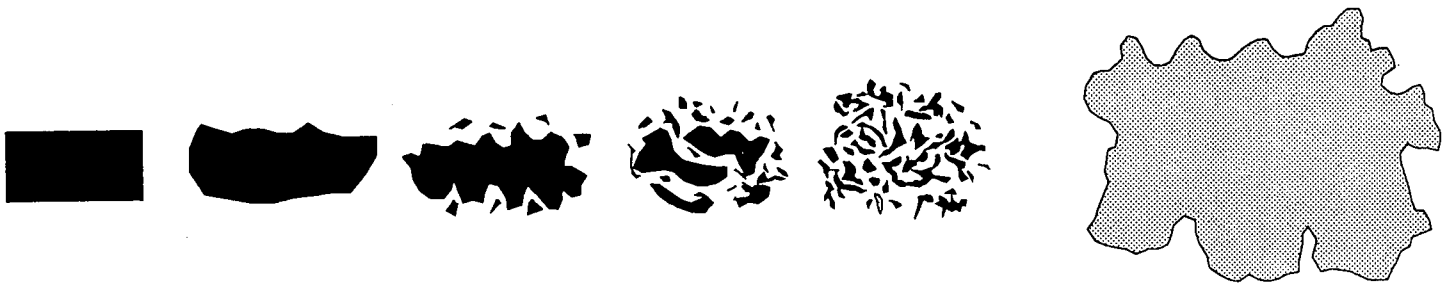

Figure 3.1 Destruction of large feed eddies by turbulent mixing. Feed fluid changes from a coherent structure into many smaller eddies.

There are five types of mixing in turbulent liquids:

i) Large-scale convection patterns
ii) Large-scale (turbulent) diffusion
iii) Inertial-convective strain
iv) Viscous-convective strain
v) Molecular diffusion

These are active at different scales, as can be understood from the spectrum of turbulent concentration fluctuations, Figure 3.2 (Tennekes and Lumley, 1972; Baldyga & Bourne, 1984; Baldyga, 1989). The spectrum indicates the contributions of eddies of different sizes to the overall level of concentration fluctuations (or "unmixedness"). The total fluctuation is the integral of the spectrum function over all eddy sizes or wavenumbers:

$$\frac{1}{2}\,\overline{c'^2} = \int_0^\infty G\,(\kappa)\,d\kappa \qquad (3.3.1)$$

Wavenumber (κ) is inversely proportional to eddy size: large eddies have low wavenumbers and contribute most to the concentration fluctuations; small eddies have high wavenumbers and contribute least. As mixing proceeds, concentration fluctuations are passed down the spectrum from large to small eddies.

Large-scale convection is accomplished by the average velocities, which transport fluid elements around the mixer. This mechanism is active at the low end of the wavenumber range. Turbulent diffusion is also active mainly on the large scale and is a measure of the mixing produced by large-scale fluctuating velocity components. Convection and turbulent diffusion are adequately described by terms 2 and 3 on the left-hand side of equation 3.2.5. Characteristic rates of both these mechanisms are determined by initial and boundary conditions (such as equipment geometry) and vary from flow to flow.

The remaining mechanisms are postulated to have a certain "universal" nature (Kolmogoroff, 1941; Tennekes & Lumley, 1972), i.e. their basic characteristics are the same for any flow with a sufficiently high Reynolds number. The universal part of the spectrum can be thought of as consisting of three regions:

- Inertial-convective, where eddy size ranges from L_c to λ_K
- Viscous convective, where eddy size varies from λ_K to λ_B
- Viscous-diffusive, where eddies are smaller than λ_B

Inertial-convective mixing describes the breakdown of large-scale inhomogeneities (such as blobs of fresh reagents) into smaller ones, whose lower bound size is near the Kolmogoroff microscale:

$$\lambda_K = \left(\frac{\nu^3}{\varepsilon}\right)^{1/4} \qquad (3.3.4)$$

Its rate is determined by the sizes of the eddies and the turbulent energy dissipation rate; a characteristic timescale is (Corrsin, 1964):

$$t_{ic} = \frac{1}{2}\frac{3}{\varepsilon^{1/3}\,\kappa_c^{2/3}} \qquad (3.3.5)$$

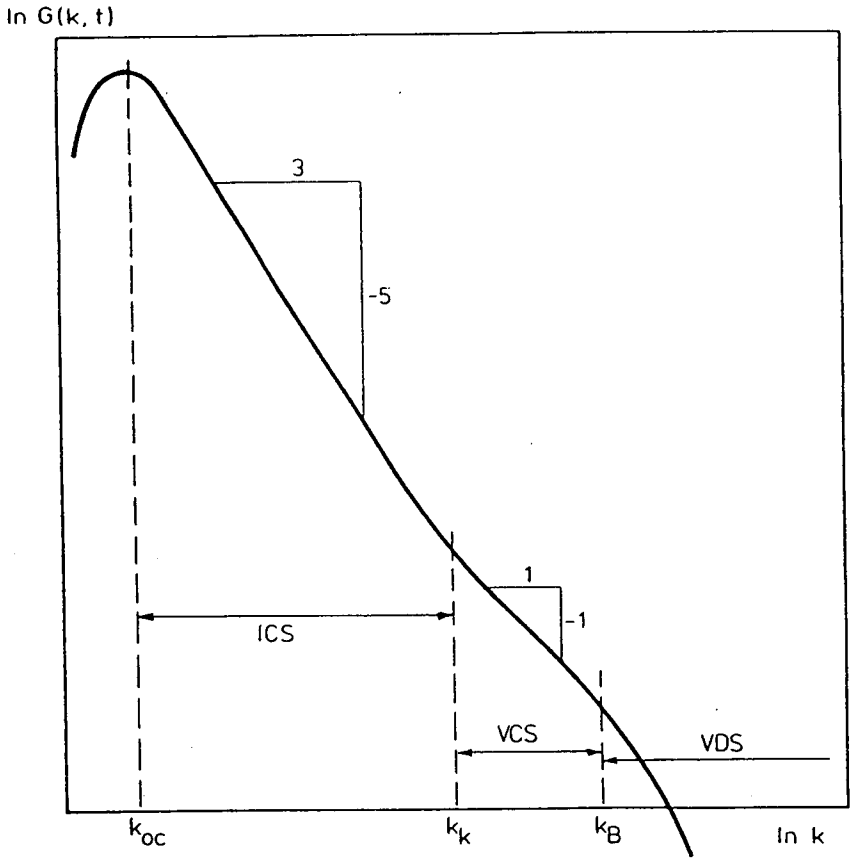

FIGURE 1a Concentration spectrum for liquid mixtures having $Sc \gg 1$.
ICS — Inertial-convective subrange
VCS — Viscous-convective subrange
VDS — Viscous-diffusive subrange.

Figure 3.2 The spectrum of turbulent concentration fluctuations in liquids (adapted from Baldyga & Bourne, 1984)

where κ_c denotes the wavenumber of the large-scale concentration eddies. Equation 3.3.5 is valid for the decay of inertial-convective concentration fluctuations in fully-developed, isotropic, homogeneous, turbulence.

During and following inertial-convective mixing, micromixing takes place. This describes viscous-convection followed by molecular diffusion within thinning fluid elements. Micromixing acts between the Kolmogoroff microscale and the Batchelor microscale:

$$\lambda_B = \frac{\lambda_K}{\sqrt{Sc}} \tag{3.3.6}$$

where Sc denotes the Schmidt number:

$$Sc = \frac{\nu}{D} \tag{3.3.7}$$

Micromixing is affected by viscosity and turbulent energy dissipation rate. A characteristic time constant is (Baldyga & Bourne, 1989):

$$E^{-1} = 17.3 \left(\frac{\nu}{\varepsilon}\right)^{\frac{1}{2}} \tag{3.3.8}$$

Molecular diffusion within the fine-scale laminae produced by micromixing is affected by viscosity, temperature and chemical kinetics. An approximate time-constant is (Baldyga, 1989):

$$G^{-1} = \frac{1}{0.303 + 17051/Sc} \tag{3.3.9}$$

Mixing therefore has several characteristic times and the term "mixing-limited" should be qualified depending on which stage it refers to. The chemical engineering literature frequently describes convection patterns as "macromixing" and other stages as micromixing. Baldyga & Bourne (1992) coined the term "mesomixing" for the turbulent diffusion stage. Micromixing is also sometimes used to describe the general field of mixing with chemical reaction, presumably because reaction requires mixing down to the molecular scale. Here, macromixing will be used to describe stages (i) to (iii) above and micromixing (iv) and (v), the distinction being the influence of viscosity.

Some comparisons and contrasts between modelling fluctuating velocities and fluctuating concentrations are in order. ε and k can be modelled using quantities related only to the large-scale motion (Chapter 2) because these motions are responsible for generating the velocity fluctuations and determining the shape of the velocity spectrum (e.g. size of largest eddies, see Chapter 2). In the concentration field, this is not necessarily the case. The integral scale of concentration fluctuations depends primarily on the manner of reactant injection. Large blobs of reactants (large concentration eddies) cause slower dissipation of concentration fluctuations (Warhaft & Lumley, 1978; Warhaft, 1984), even if the integral scale of the velocity fluctuations remains constant. Dissipation rates therefore depend on the initial length scale of the reactants (equation 3.3.5). Large-scale inhomogeneities lengthen the mixing time since

they need to be passed further down the spectrum before molecular mixing can take place. Small scale inhomogeneities lead to rapid mixing.

Reactions tend to be limited by macromixing when volumetric feed rates are high and in large-scale equipment (large integral scale of concentration fluctuations). Micromixing tends to limit when feed rates are low, viscosities are high and in smaller scale equipment (small integral scale). Diffusive mixing can limit when the viscosity (or Schmidt number) is high. Low stoichiometric excesses tend to favour macromixing.

3.4 DESIRABLE ATTRIBUTES OF A MIXING-REACTION MODEL

A model for predicting mixing effects on reactions should for the present purposes ideally be:

1. Predictive, rather than an empirical best-fit or composed of arbitrary parameters
2. Based on local rather than global effects within the reactor
3. Able to predict all stages of mixing
4. General for isothermal (including multi-step) reaction schemes
5. Economical to calculate in terms of computer time
6. Capable of interfacing with Computational Fluid Dynamics programs

A predictive model is desirable so that it can be generalised to arbitrary mixing and reaction conditions. Local effects must be calculated because intrinsically fast reactions sometimes occupy only a fraction of the reactor volume; in general, therefore, models should be capable of adaptation to three-dimensional flows. The ability to predict all stages of mixing allows for generality in reaction conditions. Since macromixing and micromixing effects are closely related, it is desirable for both to be calculated.

The model should be applicable to arbitrary reaction kinetics, pathways or stoichiometric ratios (i.e. relative amounts of reactants). It should reduce to certain well-known relationships for asymptotic cases, e.g. infinitely fast and infinitely slow reactions (see Section 3.5.3). Model parameters should not depend on assumptions about the particular characteristics of any of the reaction steps. Restriction to isothermal flows is a necessary first step, but the model structure should allow greater complexity to be added incrementally.

Economy in computing the model is desirable. In particular, the number of differential transport equations required should be as small as possible, in view of the inbuilt complexity of practical reaction schemes. The ability to interface with CFD programs is vital in view of criterion 2 and the increasing use of CFD in both industry and academia.

3.5 INTERPRETATION OF CONCENTRATION COVARIANCE

3.5.1 Balance Equation

Equation 3.2.6 states that the rate of chemical reaction in a turbulent fluid is slowed relative to the intrinsic rate if the covariance is negative; if the magnitude of this effect can be determined, the reaction rate can be predicted.

A balance equation for covariance can be derived from the transport equation for chemical species as follows:

1. Multiply the C_A equation by c_B
2. Multiply the C_B equation by c_A
3. Reynolds-average the equations and add them together

The result is, after manipulation:

$$\frac{\partial \overline{c_A c_B}}{\partial t} + C_{cov} = D_{cov} + P_{cov} - \varepsilon_{cov} + \left(\frac{D}{Dt}\right)_{chem} \tag{3.5.1}$$

where C_{cov} denotes convection:

$$C_{cov} = U_i \frac{\partial \overline{c_A c_B}}{\partial x_i} \tag{3.5.2}$$

D_{cov} denotes diffusion and is given by:

$$D_{cov} = -\left(\frac{\partial\, \overline{u_i c_A c_B}}{\partial x_i} - D\, \frac{\partial^2\, \overline{c_A c_B}}{\partial x_i^2}\right) \tag{3.5.3}$$

P_{cov} denotes production and is given by:

$$P_{cov} = -\left(\overline{c_B\, u_i} \frac{\partial C_A}{\partial x_i} + \overline{c_A\, u_i} \frac{\partial C_B}{\partial x_i}\right) \tag{3.5.4}$$

ε_{cov} denotes dissipation:

$$\varepsilon_{cov} = 2\, D\, \overline{\frac{\partial c_A}{\partial x_i} \frac{\partial c_B}{\partial x_i}} \tag{3.5.5}$$

The rate of change due to chemical effects (consumption or production) is:

$$\left(\frac{D}{Dt}\right)_{chem} = k\, \overline{(c_A c_B + C_A c_A + C_B c_B)\, (c_B + c_A)} \tag{3.5.6}$$

Covariance is produced by gradients in mean concentrations, transported by convection and turbulent diffusion and dissipated by fine-scale gradients of concentration fluctuations.

3.5.2 Modelling Approaches

The local value of covariance is determined by the fractions of time spent by fluid elements of different compositions at any point and the relative concentrations during those times. Consider the schematic response of a concentration probe in an incompletely-mixed solution of A and B (Figure 3.3). At any instant, the probe reads high A (& low B), intermediate A (and intermediate B) or low A (and high B) concentrations. The time-averaged correlation between fluctuations of A and B is given by:

$$\overline{c_A c_B} = \frac{\sum_i (c_A c_B)_i \, \Delta t_i}{\sum_i \Delta t_i} \tag{3.5.7}$$

Alternatively, the volume averaged correlation is:

$$\overline{c_A c_B} = \sum_i (c_A c_B)_i \, \alpha_i \tag{3.5.8}$$

where α_i denotes the volume fraction of fluid with each level of correlation, which is equivalent to the probability of finding fluid of composition i. This concept has previously been used in various forms by Patterson (1981), Donaldson (1975), Dutta & Tarbell (1989) and Ranade & Bourne (1991), amongst others.

Two methods suggest themselves for modelling the covariance. One is to start with equation 3.5.1 and model its terms (e.g. using the turbulence model approach) so that the approximated equation can be solved in conjunction with the flow field equations. Equation 3.5.1 has been derived previously but is rarely used directly (Donaldson, 1975). Diffusion, production, dissipation and chemical terms require modelling, as they contain correlations between fluctuating velocities, concentrations and their derivatives. Equation 3.5.1 is analogous to the transport equation for Reynolds stress in Chapter 2.

An equation for the mean squared concentration fluctuation of single species (analogous to the turbulent normal stress) can be obtained in a similar way and is a little easier to model. This has been used by Patterson (1981), Baldyga (1989) and others.

An alternative is to formulate a description of concentration fluctuations on a fine-scale, e.g. using concepts from the spectral theory of turbulence described above. This route is attractive because dissipation of concentration fluctuations is accomplished in the main by fine-scale fluid structures. Once a model for these has been developed, it can be embedded in a description of the large-scale flow. This type of approach has been taken in the development of micromixing models (Harada et al., 1962; Mao & Toor, 1970; Villermaux & Devillon, 1972; Pohorecki & Baldyga, 1983; Baldyga & Bourne, 1984; Baldyga & Bourne, 1989).

All reactive mixing models are substitutes for equation 3.5.1. In Sections 3.6 and 3.7, a representative sample of models of both the above types are described. A distinction is made between models employing a single mixing timescale for dissipation of concentration fluctuations and those employing multiple timescales. The former provide useful information on individual mixing stages, whereas the latter are more likely to fulfil the criteria set out above.

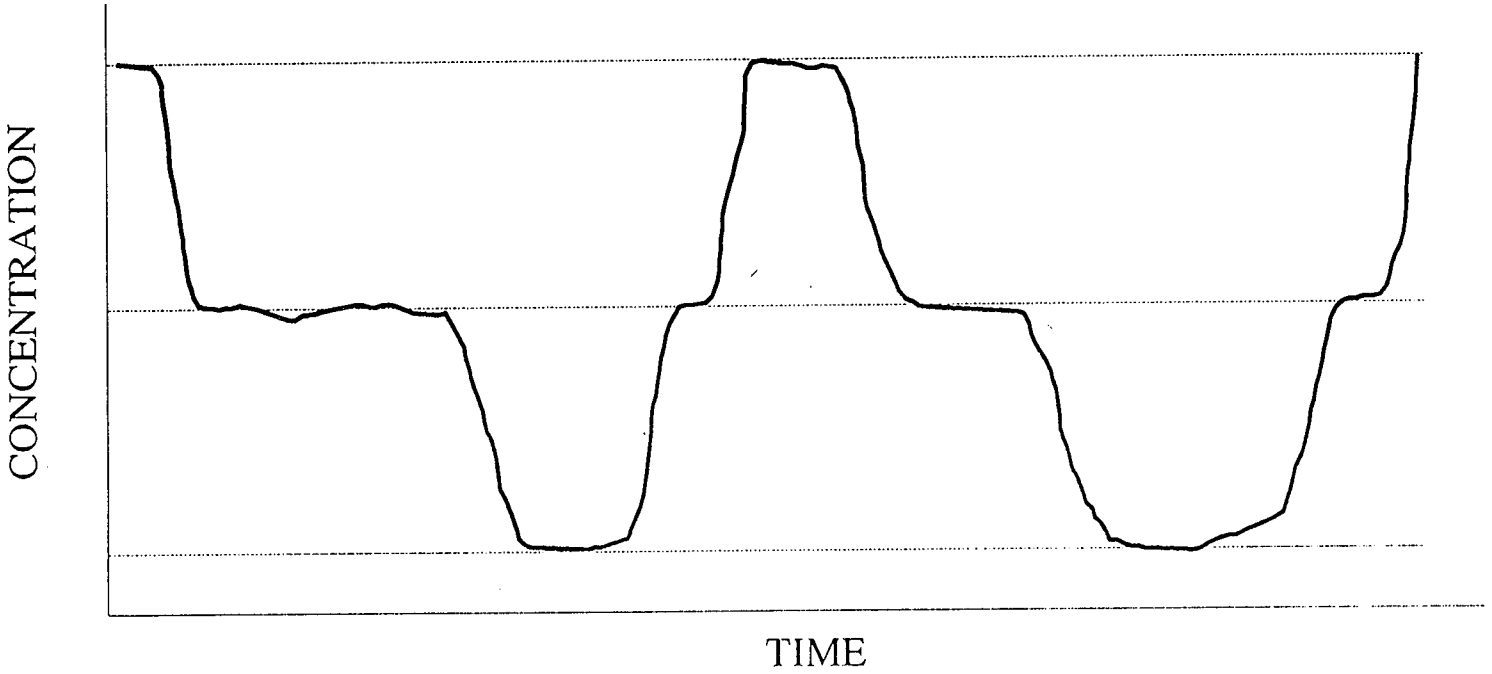

Figure 3.3 Schematic square-wave response of a concentration probe in an incompletely-mixed solution. Peaks and troughs represent passage of fluid elements of different composition.

3.5.3 Asymptotic Behaviour

Prior to mixing, reagents A and B are said to be "completely segregated". In the instantaneous reaction regime, reaction is infinitely fast relative to mixing and is confined to surfaces separating A-rich and B-rich regions. During reaction, therefore, the mixture remains almost completely segregated and:

$$\overline{c_A c_B} = - C_A C_B \tag{3.5.9}$$

At the other extreme, when reaction is infinitely slow relative to mixing, e.g. $k \rightarrow 0$, covariance decay is as for pure mixing without reaction:

$$\overline{(c_A c_B)_0} = - C_{A0} C_{B0} \tag{3.5.10}$$

$$\overline{(c_A c_B)_\infty} = 0 \tag{3.5.11}$$

The "intensity of segregation" can be defined as:

$$I_s = \frac{\overline{c_A c_B}}{\overline{(c_A c_B)_0}} = - \frac{\overline{c_A c_B}}{C_{A0} C_{B0}} \tag{3.5.12}$$

so covariance for pure mixing is given by:

$$\overline{c_A c_B} = - I_s \, C_{A0} C_{B0} \tag{3.5.13}$$

3.6 SINGLE TIMESCALE MODELS

3.6.1 Laminar Model

The simplest model of equation 3.5.1 is to assume that the correlation between fluctuating concentrations is zero everywhere. This is sometimes called the "laminar flow approximation" and has been used by Liu & Barkelew (1986) and Middleton et al. (1986), among others. It meets all criteria except for number 3, by ignoring the effects of turbulence felt through inertial-convective and micromixing. As such it is not generally applicable. This model is tested in Chapter 4.

3.6.2 Toor's Model

Toor (Vassilatos & Toor, 1965; Toor, 1969; McKelvey et al, 1975) proposed a direct model for the covariance, by hypothesising that:

$$c_A = -c_B \tag{3.6.1}$$

Hence:

$$I_s = \frac{\overline{c_A'^2}}{\overline{c_{A0}'^2}} \tag{3.6.2}$$

Equation 3.6.2 holds exactly for rapid reactions in macroscopically uniform stoichiometric mixtures. The modified I_s could be determined from non-reacting tracer experiments or solution of a transport equation for fluctuating concentration. Covariance is then given by equation 3.5.13 above.

Conversion for single-step reactions of various speeds was predicted in one-dimensional tubular reactors using this model (Vassilatos & Toor, 1965; Mao & Toor, 1971). Quality of agreement with experimental data depended on the stoichiometric ratio.

In non-stoichiometric mixtures, equation 3.6.1 is invalid. Toor's model does not account for micromixing effects and is applicable only to single-step reactions. Therefore it does not fulfil the required criteria.

3.6.3 Patterson's Model

Probability density functions can be used to describe the average probability of finding fluid of a particular composition at any point in space. Figure 3.4 shows some pdfs that have been used for reacting flows. If the pdf is known, any moments of concentration fluctuations can be determined for single-step and multi-step reactions. For example, the covariance can be found from:

$$\overline{c_A c_B} = \int p\ (c_A c_B)\ c_A c_B\ \mathrm{d}c_A c_B \tag{3.6.3}$$

With this approach, the problem of estimating the covariance is reduced to determining the pdf. There have been several attempts to do this.

Patterson (1981) proposed the "interdiffusion model", which corresponds to the conjectured pdf and concentration history in Figure 3.5. From the assumed pdf, the covariance is given by a straightforward closure equation:

$$\overline{c_A c_B} = \frac{-\overline{c_A'^2}\ \overline{c_B'^2}}{C_A\ C_B} \tag{3.6.4}$$

The model requires solution of the mean squared fluctuating concentration balance for each species (analogous to the turbulent normal stress equations) and is therefore a second-order closure. The modelled equations are highly approximate because of the numerous unknown quantities arising in the exact transport equations (see equation 3.5.1). This is a problem also shared by Toor's model above if experimental I_s data are unavailable. Modelling the unknown terms is complicated by the existence of several mixing mechanisms over a range of spatial and time scales.

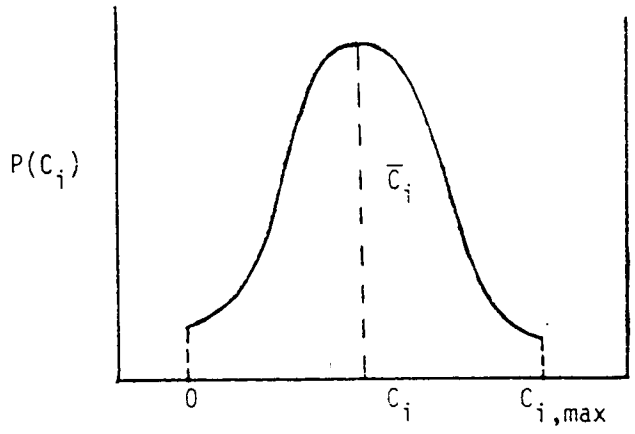

(a) Clipped-normal distribution function.

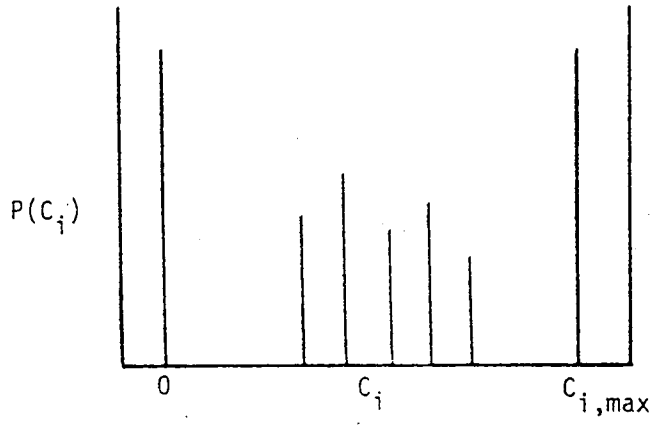

(b) Spiked distribution function.

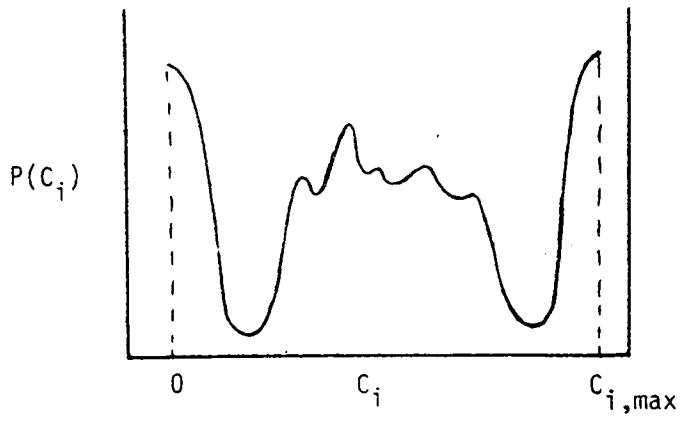

(c) Typical real distribution function.

Figure 3.4 Some probability density functions commonly used in reaction modelling (adapted from Patterson, 1981)

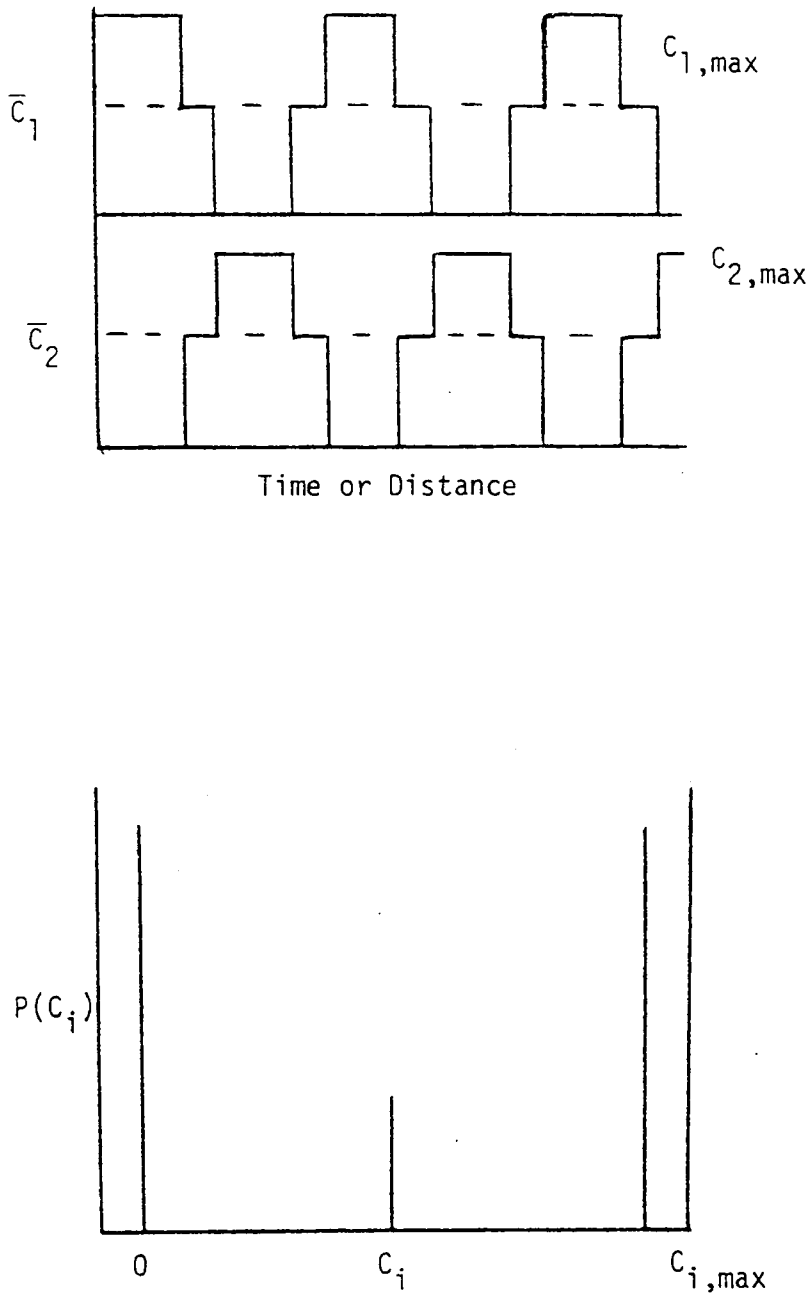

Figure 3.5 Concentration versus time profile and probability density function used in Patterson's closure

Patterson's model assumes that the concentration in the reaction zone is equal to the mean (volume-averaged) value, which is unrealistic. All stages of dissipation of concentration fluctuations are modelled using a single time-scale, based on Corrsin's (1964) analysis and similar to that used by Ziman (1990), see Section 3.6.5. Direct effects of molecular diffusion and micromixing on the pdf are ignored. Patterson's model satisfies all criteria except 1, 3 and 5.

PDFs are also used in combustion modelling (e.g. Jones and Whitelaw, 1981). Applications in combustion also tend to ignore micromixing effects. PDFs that are symmetric about the local average value (e.g. normal and clipped-normal distributions, Figure 3.4) are often used for conserved scalars. Symmetric pdfs will not adequately represent individual species concentrations in reacting systems, particularly in non-stoichiometric mixtures.

3.6.4 Dutta & Tarbell's Models

Dutta & Tarbell (1989) used some existing mechanistic micromixing models to derive algebraic closure expressions for covariance in simple flows. Each closure was assessed against the asymptotic cases of pure mixing and instantaneous reaction (see Section 3.5.3 above).

The most promising models in this light were forms of so-called three- and four-environment models (Ritchie & Tobgy, 1979; Mehta & Tarbell, 1983), which satisfied both asymptotes. The three-environment model assumes that the reactor volume is divided into three zones, two entering environments (EEs), which contain the initially separate streams, and one leaving environment (LE), in which reaction occurs. The LE is at the mean concentration. If the flowrate fraction is given by:

$$m = \frac{Q_1}{Q_1 + Q_2} \tag{3.6.5}$$

the volume fractions of each environment are given by:

$$\phi_1 = m\, I_s \tag{3.6.6}$$

$$\phi_2 = (1-m)\, I_s \tag{3.6.7}$$

$$\phi_3 = 1-I_s \tag{3.6.8}$$

where:

$$I_s = \exp\left(-\frac{t}{\tau_M}\right) \tag{3.6.9}$$

The single time-constant τ_M is assumed to describe all stages of mixing and can be obtained by fitting the model with experimental data. Closure models were derived on the basis of volume-averaging concentration fluctuations within the three zones:

$$\overline{c_A c_B} = \Sigma\ \phi_i\ (C_{Ai}-C_A)(C_{Bi}-C_B) \tag{3.6.10}$$

A closure based on the 3E model produced reasonably good agreement with experimental data for one-dimensional tubular reactors:

$$\overline{c_A c_B} = -I_s \left(C_A C_{B0} + C_{A0} C_B - C_A C_B \right)$$

The connection between unmixed fluid volume fractions (equivalent to probabilities) and concentration covariance allows closure equations for multi-step reactions to be formulated. However, Dutta & Tarbell's model is unable to describe situations with incomplete macroscopic mixing. Furthermore, all mixing stages cannot be adequately described by a single time-constant. Release of EE material is assumed to be symmetric, i.e. the LE contains the same percentage of both EEs (equations 3.6.6 to 3.6.8) and the reaction zone is at the mean concentration. These conditions are unlikely to be fulfilled for widely different flow ratios. Dutta & Tarbell's type of model meets all criteria except 1, 2 and 3.

3.6.5 Ziman's Model

Ziman (1990) proposed a modification to the laminar model which takes account of some mixing effects, but retains the simplicity and computational economy of the laminar model. The covariance term is not directly calculated; instead the reaction rate is assumed to depend on mean (volume-averaged) concentrations but with reduced kinetics reflecting incomplete mixing. Drawing on the work of Corrsin (1964), the timescale for the disintegration of inertial-convective concentration eddies was calculated from:

$$t_{macro} = 2 \frac{k}{\varepsilon} \qquad (3.6.11)$$

Equation 3.6.11 assumes that the wavenumber of the large concentration eddies is given by Corrsin's (1964) formula:

$$\kappa_c = \frac{\pi}{5L_c} \qquad (3.6.12)$$

and that the integral scale of the concentration fluctuations is equal to that of the velocity fluctuations:

$$L_c = L_v = \frac{k^{\frac{3}{2}}}{\varepsilon} \qquad (3.6.13)$$

Alternative proposals for both equations 3.6.12 and 3.6.13 have been made (Pohorecki & Baldyga, 1983; Rosensweig, 1964). In particular, the integral scale of the concentration fluctuations is more closely related with the diameter of the inlet port than that of the velocity field (Section 3.3 above).

Viscous-convective and viscous-diffusive mixing within eddies smaller than the Kolmogoroff microscale is described in Ziman's model by:

$$t_{micro} = 1.54 \left(\frac{\nu}{\varepsilon}\right)^{\frac{1}{2}} \ln Sc \qquad (3.6.14)$$

The sum of these time constants gives the overall mixing time, t_M. The rate of a chemical reaction occurring in the liquid is then calculated as either the intrinsic rate or the rate at which the least abundant reactant is mixed:

$$\Omega_A = \min\left(k_{AB} C_A C_B \ , \ \frac{1}{t_M} \min\left(C_A \ , \ C_B\right) \right) \tag{3.6.15}$$

This model was applied to predict the yield of a competitive-consecutive azo-coupling reaction in a stirred batch reactor:

$$A + B \rightarrow R$$

$$R + B \rightarrow S$$

and gave results in reasonable quantitative agreement with experimental measurements at three scales of operation (Ziman, 1990). However, experimental conditions were insensitive to micromixing (very short feed times).

Ziman's model satisfies all six criteria to an extent, but does not simulate in sufficient detail the macromixing or micromixing processes felt through the covariance term. To illustrate, consider the large concentration eddy moving through the flow in Figure 3.1. Initially, no reaction occurs because the eddy is completely segregated from its surroundings. After a time, when the eddy has passed through sufficient turbulent regions, its constituents begins to react. The reaction rate is now no longer dependent on local macromixing, but on micromixing and chemical kinetics, but Ziman's model retains an inertial-convective timescale ($2k/\varepsilon$) in the reaction rate calculation throughout the flow. As a consequence, fully mixed streams are forced by the computations to "mix again" repeatedly before being allowed to react; this artificially retards the reaction rate (see Chapter 4).

Furthermore, micromixing involves laminar strain and deformation with simultaneous molecular diffusion and chemical reaction within fine-scale eddies (Baldyga & Bourne, 1984; Chella & Ottino, 1984). It cannot be accurately described using the single time-constant, t_{micro}. Thus some details of the micromixing process, which affect the reaction rate and yield, are also obscured in Ziman's model (see Chapter 4).

3.6.6 Ranade & Bourne's Model

While this thesis was in preparation, Ranade & Bourne (1991) published a new model combining CFD predictions of the velocity and turbulence field with a modified version of the micromixing model of Baldyga & Bourne (1989).

Within each computational cell, the concentrations of each species are divided between a number of subgroups (N). Effectively, this amounts to a pdf with N spikes. The covariance is given by:

$$\overline{C_A C_B} = \Sigma\ e_i\ (C_{Ai}-C_A)(C_{Bi}-C_B) \tag{3.6.16}$$

where e_i denotes the volume fraction of each subgroup.

Initially, feed fluid is assumed to occupy subgroup 1, while bulk fluid occupies subgroup N. Mass exchange between subgroups takes place by viscous-convective engulfment. Reaction takes place in all but the Nth subgroup. Ultimately, all fluid is engulfed into subgroup 1. For the case N=2, growth of the reaction zone is given by:

$$\frac{De_1}{Dt} = E\ e_1 e_2 \tag{3.6.17}$$

where E, the viscous-convective engulfment frequency, is given by:

$$E = 0.058\ (\frac{\varepsilon}{\nu})^{1/2} \tag{3.6.18}$$

The amount of species i in each subgroup is given by:

$$\frac{De_1 C_{i1}}{Dt} = E\ e_1 e_2 C_{i2} + e_1 \Omega_{i1} \tag{3.6.19}$$

$$\frac{De_2 C_{i2}}{Dt} = -E\ e_1 e_2 C_{i2} \tag{3.6.20}$$

More complex but analogous expressions apply when N>2. The model does not explicitly account for inertial-convective decay of concentration fluctuations. It ignores viscous-diffusive mixing (and therefore molecular diffusion) as a limiting factor, which is valid when Sc<<4000 and the feed stream is much more highly concentrated than the bulk fluid (see Section 3.7.2 below).

This model was tested against experimental data for a competitive-consecutive reaction in a semi-batch stirred tank reactor (Ranade & Bourne, 1991). It was possible to vary the rate-limiting mixing step by varying the feed time. Using one subgroup (i.e. no sub-grid modelling), data for short feed times was well predicted. This would be expected, as only the largest scales of motion are influential under these conditions. Predictions for longer feed times gave poorer results, which gained in accuracy as the number of subgroups increased. This may reflect incomplete modelling of intermediate stages of mixing, such as inertial-convective. Ranade & Bourne's model satisfies all criteria except 3. It is tested in Chapter 4.

3.7 MULTIPLE TIMESCALE MODELS

3.7.1 Pohorecki & Baldyga's Model

The concentration fluctuations in Equations (3.2.6) and (3.5.1) are made up of contributions from all eddy sizes. Fluctuations can be dissipated by inertial-convective, viscous-convective and viscous-diffusive mixing, see Figure 3.2. For fast reactions in liquids, the latter two variances can determine the reaction rate and selectivity. These considerations have led workers to model stages of dissipation separately. Pohorecki and Baldyga (1983), for example, used separate models of the large and fine-scale mixing. They described inertial-convective mixing by:

$$\frac{dV_s}{dt} = -\frac{V_s}{t_{ms}} \tag{3.7.1}$$

or

$$\frac{d\overline{c_{il}^2}}{dt} = -\frac{\overline{c_{il}^2}}{t_{ms}} \tag{3.7.2}$$

and viscous-convective and diffusive mixing as:

$$\frac{d\overline{c_{i2}^2}}{dt} = -k_{md}\,\overline{c_{i2}^2} \tag{3.7.3}$$

where:

$$t_{ms} = 0.694\ \kappa_c^{-2/3}\ \varepsilon^{-1/3} \tag{3.7.4}$$

$$\kappa_c = \frac{2\pi}{d_B} \tag{3.7.5}$$

$$k_{md} = 0.162\ \left(\frac{\varepsilon}{\nu}\right)^{\frac{1}{2}}\ (\ln Sc - 1.27)^{-1} \tag{3.7.6}$$

They adapted Mao and Toor's (1971) model:

$$\Omega_A = k\ (C_A\ C_B - I_s\ C_{A0}\ C_{B0}) \tag{3.7.8}$$

with

$$I_s = \frac{1}{1 + 2k_{md}\ t} \tag{3.7.9}$$

Segregation in the viscous-convective and viscous-diffusive subranges was used to determine I_s, whereas dissipation of inertial-convective variance caused a time-lag between feeding and the start of reaction, rather than directly affecting the reaction.

Pohorecki & Baldyga applied this model to the experimental data of Bourne et al. (1977) for competitive-consecutive azo-coupling reactions in a continuous stirred tank reactor under micromixing-controlled conditions:

$$A + B \rightarrow R$$

$$R + B \rightarrow S$$

The first reaction was assumed to be instantaneous and the second, being relatively slow, to be free from the effects of segregation (Mao & Toor's model does not provide a closure equation for multi-step reactions, see Section 3.6.2). Agreement between model and measurements was good. This model meets all criteria apart from 2 and 4.

3.7.2 Micromixing Models

Several models have been proposed which concentrate only on micromixing, (Baldyga & Bourne, 1984; Chella & Ottino, 1984; Mao & Toor, 1970). These simulate simultaneous convection, molecular diffusion and chemical reaction in one dimension within stationary or deforming fine-scale laminae. The initial thicknesses of the laminae are related to turbulence levels and physical properties.

Micromixing (Baldyga & Bourne, 1984) is currently believed to occur by three mechanisms (Figure 3.6):

1. Engulfment (E) of surrounding fluid into the reaction zone
2. Laminar shear and deformation (D) within the resulting fine-scale eddy
3. Molecular diffusion (D)

The initial thickness of A and B laminae is assumed to be near the Kolmogoroff microscale (see Figure 3.6). Vortical structures with lifetime τ_ω incorporate these laminae, where:

$$\tau_\omega = 12 \left(\frac{\nu}{\varepsilon}\right)^{\frac{1}{2}} \tag{3.7.10}$$

Within each vortex, partial differential equations describing simultaneous thinning accompanied by molecular diffusion and reaction apply:

$$\frac{\partial C_i}{\partial t} + u \frac{\partial C_i}{\partial x} = D \frac{\partial^2 C_i}{\partial x^2} + \Omega_i \tag{3.7.11}$$

The thinning velocity depends on kinematic viscosity and turbulent energy dissipation rate:

$$u = - \frac{(\varepsilon/\nu)^{1/2}\, x}{(4 + \varepsilon\, t^2/\nu)^{1/2}} \tag{3.7.12}$$

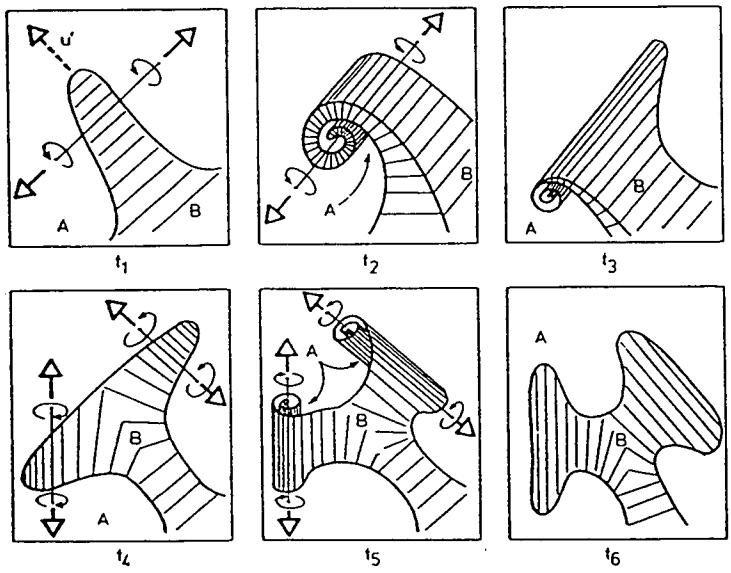

a) Formation of laminated structures by viscous-convective engulfment with subsequent laminar shear and deformation. t_1 to t_3 shows first vortex generation; t_4 to t_6 shows second generation.

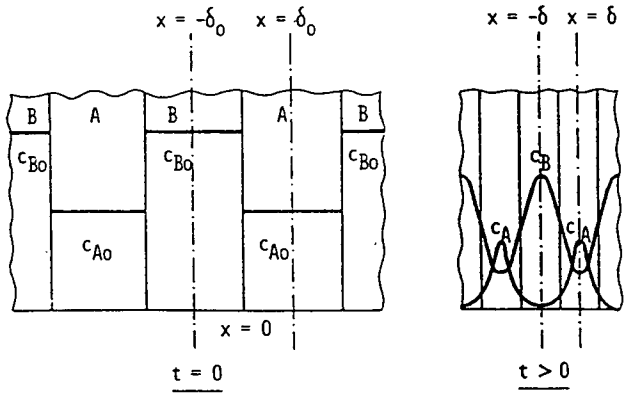

b) Steepening of concentration gradients by laminar shear, accelerating molecular diffusion and chemical reaction.

Figure 3.6 Micromixing stages (adapted from Baldyga & Bourne, 1984):

Each vortex generation allows fresh bulk fluid to enter the reaction zone, whose volume is assumed to double. This model has been successfully used to predict rates of micromixing-controlled reactions in a range of mixing equipment and at different viscosities and diffusivities. It appears to provide an excellent description of fine-scale mixing and is not intended to simulate large-scale inhomogeneity. A disadvantage of the model is that it is computationally intensive. This prevents its use at present as a sub-grid model within already compute-intensive CFD programs (criterion 6 above).

Baldyga & Bourne (1989) showed that the above "EDD" model of micromixing could be simplified under certain circumstances to a model describing "points" mixing with their environment. The simplified "E" model assumes that viscous-convective engulfment is the rate-determining step and was used by Ranade & Bourne (1991) for sub-grid modelling in a CFD program, see Section 3.6.6 above.

A timescale for mixing by laminar shear and molecular diffusion within a fine-scale eddy in the absence of reaction is (Baldyga & Bourne, 1984):

$$t_{DM} = 2 \left(\frac{\nu}{\varepsilon}\right)^{\frac{1}{2}} \sinh^{-1} (0.05\ Sc) \tag{3.7.13}$$

Equation 3.7.13 gives numerically similar results to Ziman's t_{micro} (equation 3.6.14) . If t_{DM} is small compared to τ_ω, mixing within the eddies is much faster than engulfment and engulfment is rate-controlling. This result is exact for situations where micromixing is rate-limiting, Sc<4000 and the additive (B) stream is much more highly concentrated than the bulk liquid.

In the E model, the initial volume of the reaction zone is assumed to be equal to the volume of fresh feed added. This volume grows by viscous-convective engulfment of its surroundings, according to:

$$\frac{dV}{dt} = E\ V \tag{3.7.14}$$

The frequency of engulfment is:

$$E = \frac{\ln 2}{\tau_\omega} \tag{3.7.15}$$

Baldyga and Bourne (1989) used equation 3.7.14 to derive a mass balance on the growing reaction zone which leads to:

$$\frac{dC_{ir}}{dt} = E\ (C_{ie} - C_{ir}) + k_{ij}\ C_{ir}C_{jr} \tag{3.7.16}$$

The E model (equations 3.7.14 and 3.7.16) accurately predicts reactions which are controlled by viscous-convective mixing, i.e. when macromixing and molecular diffusion are very rapid. This simplified form can be incorporated into a CFD program, but the complete EDD model would be prohibitively expensive at present.

Global models for micromixing do not meet criteria 2 and 3.

3.7.3 Baldyga's Model

Baldyga (1989) proposed a multiple timescale model for instantaneous reactions in a one-dimensional reactor. A Beta pdf was assumed for the concentration distribution, which required as an input the solution of the concentration fluctuation balance. All three important subranges of the concentration spectrum were modelled by separate equations. This is a plausible model for transport of concentration fluctuations, which cascade down the spectrum from inertial-convective through viscous convective into viscous diffusive. Balance equations for each stage are (Baldyga, 1989):

$$\frac{D\overline{c_{i1}^{z}}}{Dt} = -\frac{\overline{c_{i1}^{z}}}{t_{ms}} \tag{3.7.17}$$

$$\frac{D\overline{c_{i2}^{z}}}{Dt} = \frac{\overline{c_{i1}^{z}}}{t_{ms}} - E\,\overline{c_{i2}^{z}} \tag{3.7.18}$$

$$\frac{D\overline{c_{i3}^{z}}}{Dt} = E\,\overline{c_{i2}^{z}} - G\,\overline{c_{i3}^{z}} \tag{3.7.19}$$

where t_{ms} and E are given by equations 3.7.4 and 3.7.15 respectively and:

$$G = E\,(0.303 + \frac{17051}{Sc}) \tag{3.7.20}$$

Equations 3.7.17 to 3.7.19 can be normalised to predict intensity of segregation in all three subranges. The fluctuations can be used together with mean values of concentration to calculate the form of the Beta pdf for species concentrations. The Beta pdf has the advantage that it is not necessarily symmetric about the mean value and therefore is potentially a good description of the early stages of mixing. Baldyga (1989) accurately predicted Vassilatos & Toor's (1965) data for fast single-step reactions.

This model requires three transport equations for the concentration fluctuations of each species, which would be computationally intensive for complex reaction systems. Unlike earlier pdf models, it takes account of micromixing in determining the pdf shape. However, it is applicable only to single-step reactions and thus does not meet criterion 4.

3.8 DIRECT NUMERICAL SIMULATIONS

In recent years, it has become possible with the most powerful computers (e.g. Cray 2) to calculate in detail turbulent motion on a fine-scale in very simple geometries. These methods are unlikely to see common usage for many years, but their results can be used to guide the development of the simplified models presented above. Leonard & Hill (1989) have been active in simulating chemical reactions. They calculated the rate of the elementary reaction:

under mixing-sensitive conditions in a square box with periodic boundary conditions. The mixture was stoichiometric and the reactants initially completely segregated. The Schmidt number was low ($Sc < 1$). Pdfs for reactant concentrations were calculated as a function of time (Figure 3.7). A and B are initially highly-segregated, with delta functions at $\alpha=\beta=2.0$ (local concentrations of A and B divided by initial mean concentrations). As time progresses, the delta functions persist, but their heights are reduced. The pdf for each reactant is asymmetric. At intermediate stages in the course of reaction, there is no distinct peak in concentrations. The reaction did not go to completion in these simulations, presumably for reasons of computational cost. The pdfs at completion would consist of delta functions at $\alpha=\beta=0.0$.

The pdfs are not of the idealised shape used in Patterson's closure. The closure schemes of both Toor (1969) and Patterson (1981) were tested against the direct simulation results by Leonard & Hill (1989). Figure 3.8 shows the ratios between covariances predicted by the closure theories and those from direct simulations. The symbol shapes indicate different relative rates of mixing and reaction. Toor's model performs better than Patterson's and is less sensitive to the mixing/reaction regime. Both closures diverge from the direct simulations increasingly with time.

The direct simulations did not test the closures in liquids, where $Sc>>1$: under these conditions, viscous-convective and viscous-diffusive mixing would play a greater role and Toor's and Patterson's closures would diverge further from reality.

Eswaran & Pope (1988) conducted direct simulations of non-reactive mixing to investigate the influence of the integral scale of concentration fluctuations on their decay. Fluctuations with a large integral scale (i.e. large eddies) were dissipated more slowly than smaller eddies. This effect is in agreement with equation 3.3.5 of Corrsin (1964) and 3.7.4 of Rosensweig (1964), but not equation 3.6.11 (Ziman, 1990). It could not be predicted by the model of Ranade & Bourne (1991).

3.9 NEW REACTIVE MIXING MODEL

3.9.1 Introduction & Objectives

Development of a new model is motivated by the need for a more general description of interactions between mixing and chemical reaction than provided by previous models. None of the models described above meets all the criteria in Section 3.4. However, some provide useful tools for developing such a general model.

Presentation of the new model is structured as follows. Sections 3.9.2 to 3.9.5 concentrate on the interaction between mixing and kinetics. This requires estimation of the covariance term in equation 3.2.6 through assumptions about the structure of the concentration field (Section 3.9.2). Transport equations associated with the model are derived in Sections 3.9.3 to 3.9.5. In Section 3.9.6, the final expression for the reaction rate is given. Section 3.9.7 analyses the behaviour of the closure under asymptotic conditions and Section 3.9.8 contains a summary and discussion of the model.

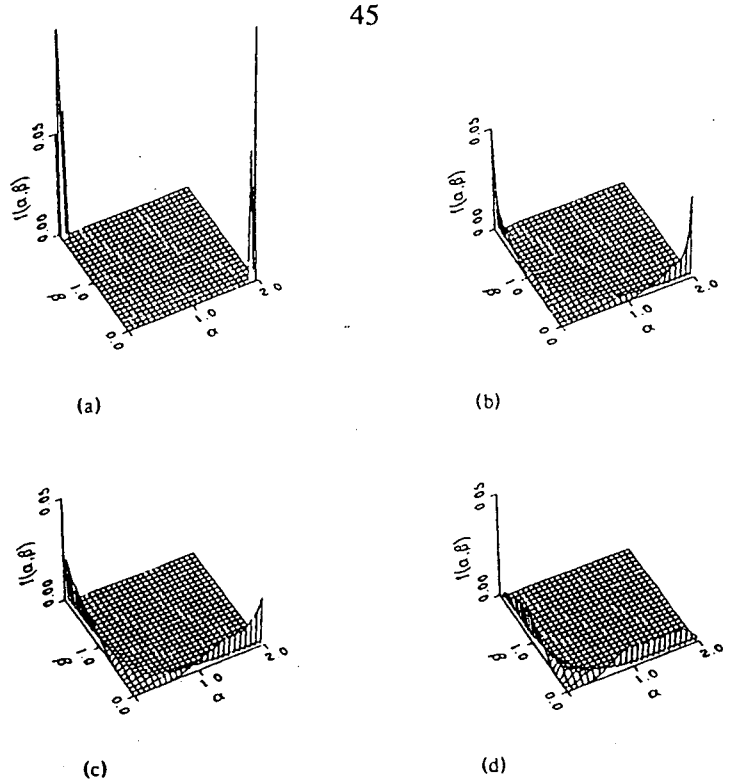

Figure 3.7 Evolution of the joint single-point probability density functions for initially segregated reactant concentrations obtained from Direct Numerical Simulations (adapted from Leonard & Hill, 1989)

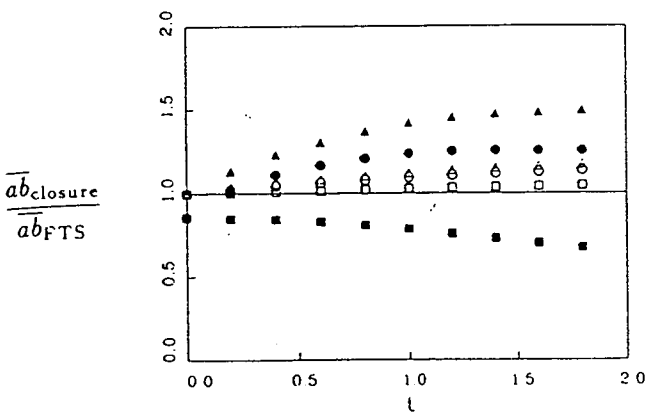

▪, •, ▲ Patterson's form (*i.e.*, $-\overline{a^2}\,\overline{b^2}/(\bar{A}\bar{B}\overline{ab})$)

□, o, △ Toor's form (*i.e.*, $(\overline{ab}_0/\overline{ab})(\overline{a^2}/\overline{a_0^2})_m$)

Figure 3.8 Ratio of approximate covariances of Toor's and Patterson's closures to data from Direct Numerical Simulations (or "Full Turbulent Simulations (FTS)", from Leonard & Hill, 1989) for low Schmidt number reactions.

3.9.2 Assumed structure of the concentration field

The scales of motion influencing reaction are finer in liquids than the scales of turbulence ($Sc>>1$). Three stages of covariance dissipation have to be considered: inertial-convective, viscous-convective and viscous-diffusive. Covariance is related to volume fractions and concentrations of each fluid element, and the timescales of mixing in the three subranges of the concentration spectrum.

If the local concentration field within any segment of the reactor can be thought of as consisting of three zones, these are (Figures 3.9 and 3.10):

1. The unmixed (or segregated) region (volume fraction α_s)
2. The reaction zone (volume fraction α_r)
3. The bulk region (or environment) (volume fraction α_e or $1-\alpha_r-\alpha_s$)

The unmixed region contains fresh feed (additive) material, which has not yet mixed with its surroundings. The reaction zone contains both feed and bulk fluid, and is the region where mixing has taken place. The bulk region contains only bulk fluid, with no fresh feed fluid present.

The average correlation between concentration fluctuations within this volume is dependent on the volume fractions of each of the three regions and the relative concentrations of the species. The volume fractions determine the fraction of time for which each region persists and the relative concentrations determine the magnitudes of the fluctuations.

A general equation for covariance between reactants is:

$$\overline{c_i c_j} = \sum_k \alpha_k \, (C_{ik} - C_i) \, (C_{jk} - C_j) \qquad (3.9.1)$$

There are 11 unknowns in equation 3.9.1, when applied to just one pair of reactants. These comprise:

- segregated volume fraction
- reaction zone volume fraction
- environment volume fraction
- volume-averaged concentrations (2)
- reaction zone concentrations (2)
- segregated zone concentrations (2)
- environment concentrations (2)

Since the sum of volume fractions equals 1, it is only necessary to calculate two of these. As shown below in Section 3.9.5, segregated and environment concentrations are related to volume-averaged and reaction zone concentrations, so that four equations are sufficient to calculate the remaining eight unknowns in equation 3.9.1 for each pair of species.

Once this is done, the covariance and hence the reaction rate can be evaluated. Methods for achieving this are the subject of the following three sections.

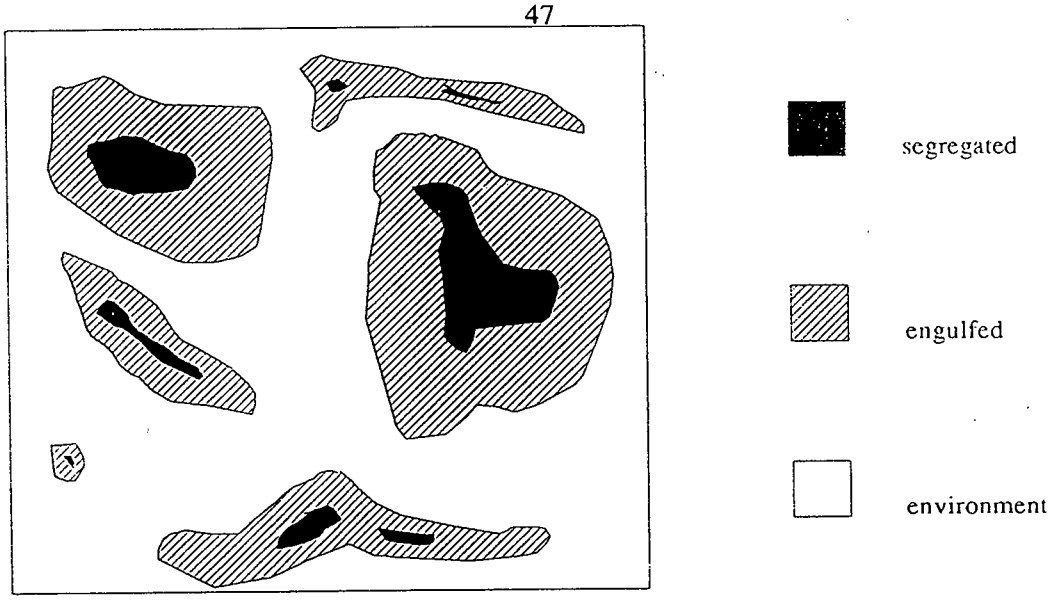

Figure 3.9 Concentration distribution in a reacting mixture consisting locally of three zones

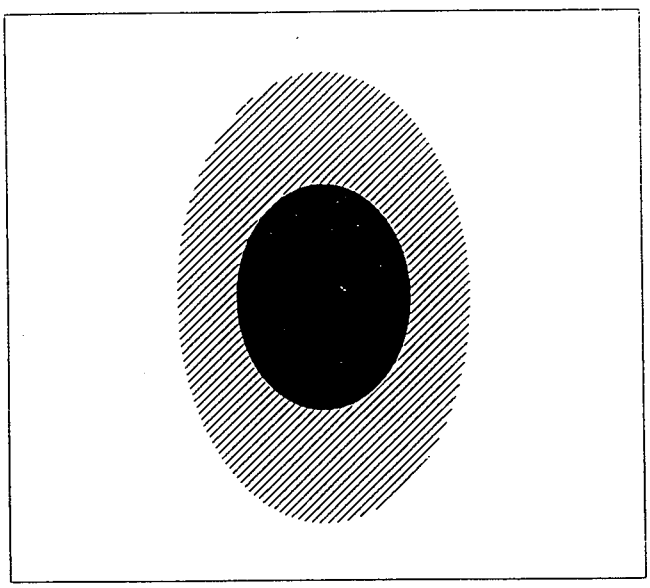

Figure 3.10 Explanation of modelled form of local three-zone concentration distribution

3.9.3 Calculation of segregated volume fraction

Segregated volume originates in the fresh feed stream. In order for reaction to take place, this volume should be dissipated (passed down the concentration spectrum) as rapidly as possible. It consists of large eddies of unmixed feed, and corresponds to concentration fluctuations in the inertial-convective subrange. Dissipation of α_s can be visualised as the breaking down of large clumps of feed into smaller clumps (Figure 3.1).

A transport equation for segregated volume fraction can be written and is similar to that of Pohorecki & Baldyga (1983) for segregated volume (Equation 3.7.1 above):

$$\frac{D\alpha_s}{Dt} = - \frac{\alpha_s(1-\alpha_s)}{t_{ic}} \tag{3.9.2}$$

The sink term models reduction in α_s by turbulent strain. The factor $(1-\alpha_s)$ ensures that dissipation of segregated volume commences only after feed contacts bulk fluid. Dissipation due to turbulence can be modelled by analogy with Corrsin's expression for the decay of concentration fluctuations, with time-constant t_{ic}.

There are several methods of estimating t_{ic}. Corrsin's formula is equation 3.3.5, where κ_c is the characteristic wavenumber of the large concentration eddies. If L_c is assumed to be equal to the characteristic dimension of the large-scale velocity field (as per Ziman, 1990 and Patterson, 1981):

$$L_v = \frac{k^{3/2}}{\varepsilon} \tag{3.9.3}$$

t_{ic} can be calculated from the turbulent kinetic energy and dissipation rate using equation 3.6.2 for κ_c:

$$t_{ic} = 2 \frac{k}{\varepsilon} \tag{3.9.4}$$

Alternatively, κ_c may be given by (Pohorecki & Baldyga, 1983; Tennekes & Lumley, 1972):

$$\kappa_c = \frac{2\pi}{d_B} \tag{3.9.5}$$

which results in:

$$t_{ic} = 0.44 \, d_B^{2/3} \varepsilon^{-1/3} \tag{3.9.6}$$

Both experiments (Warhaft & Lumley, 1978) and direct numerical simulations (Eswaran & Pope, 1988) support the intuitive view that the characteristic dimension used to calculate t_{ic} should reflect the initial scale of segregation of the feed stream. Equation 3.9.6 then seems more physically realistic. Note that the coefficient 0.44 is based on Corrsin's (1964) analysis whereas 0.2 results from equation 3.7.4 above due to

Rosensweig (1964). Sensitivity of predictions to this parameter is explored in Chapter 4.

Boundary conditions are α_s=1.0 in the feed stream and zero elsewhere. Qualitative analysis of equation 3.9.2 shows that the volume fraction of unmixed material near the feed inlet remains close to 1.0. Downstream of the injection point, some unmixedness has decayed, so some fluid is now available for the next stage of mixing (i.e. viscous-convective) but the majority is not. At a sufficient distance downstream, α_s approaches zero. Most fluid is now available for further mixing and reaction. Reduction in unmixed volume fraction is assumed to be a purely hydrodynamic process and is independent of the compositions of the streams being mixed.

Equation 3.9.2 with time constant t_{ic} is valid for inertial-convective mixing only. It describes the reduction in unmixed volume fraction due to the action of inertial-convective turbulent eddies. It is unable to describe mixing effects at a finer scale than the order of the Kolmogoroff microscale (Baldyga & Bourne, 1984),

$$\lambda_K = \left(\frac{\nu^3}{\varepsilon}\right)^{1/4} \tag{3.9.7}$$

Below this scale, viscous-convective and viscous-diffusive mixing predominate.

3.9.4 Calculation of reaction zone volume fraction

The reaction zone volume fraction is initially zero, but as mixing proceeds, it is generated from bulk and segregated volume. For the situation where a small stream of B is added to a large stream of A, all A is initially contained in bulk volume and all B in segregated volume. These do not intersect. The rate of decrease in segregated volume is modelled in Section 3.9.3. This determines the rate of addition of B to the reaction zone. Inertial-convective mixing within the B added is complete, i.e. it consists of small eddies. The rate of addition of A to the reaction zone is determined by the rate at which small eddies of fresh feed mix with bulk fluid. The reaction zone is therefore defined by the presence of small eddies of both A and B.

Let α_{eng} be the local volume fraction of fluid containing B (Figure 3.8). α_s is a subset of α_{eng}. Following Baldyga & Bourne (1984), α_{eng} grows by engulfing surrounding fluid. The rate of growth of α_{eng} is determined by the rate of viscous-convective mixing of small feed eddies with small bulk eddies. The transport equation for α_{eng} is similar to equation 3.7.14:

$$\frac{D\alpha_{eng}}{Dt} = E^* (\alpha_{eng} - \alpha_s) \tag{3.9.8}$$

In the model of Baldyga & Bourne (1989), α_s is zero because their model accounts only for the viscous-convective stage of mixing. Here, the rate of growth of α_{eng} is restricted by the presence of α_s. Only eddies that are mixed on an inertial-convective scale can partake in engulfment.

Initially, both α_s and α_{eng} are 1.0 in the feed stream. As soon as α_{eng} and α_s differ, α_{eng} begins to engulf its surroundings. The volume fraction of fluid able to react is the engulfed volume less the segregated volume, i.e. the reaction zone volume:

$$\alpha_r = \alpha_{eng} - \alpha_s \tag{3.9.9}$$

α_{eng} has a maximum value of 1.0, attained when the whole reactor volume has been engulfed by eddies originating in the feed stream. By this time, α_s is reduced significantly and α_r also tends towards 1.0.

As α_{eng} approaches 1.0, its rate of growth is slowed, because it becomes more difficult to find fresh material to engulf. The rate constant for growth of α_{eng} given by Baldyga & Bourne (1989) is therefore modified to:

$$E^* = E\,(1 - \alpha_{eng}) \tag{3.9.10}$$

This retards growth of α_{eng} as it approaches 1.0, which is physically realistic. Baldyga & Bourne (1989) use a similar concept to describe "self-engulfment" amongst fresh feed eddies when feed volume fractions are high. Ranade & Bourne (1991) also use this approach.

Finally, a transport equation for the reaction zone volume fraction is obtained by subtracting equation 3.9.2 from equation 3.9.8:

$$\frac{D\alpha_r}{Dt} = E^*\,\alpha_r + \frac{\alpha_s\,(1-\alpha_s)}{t_{ic}} \tag{3.9.11}$$

The first term on the right-hand side represents the rate of addition of bulk fluid to the reaction zone. The second term represents addition of feed fluid. Boundary conditions for equation 3.9.11 are α_r=0 in both feed and bulk streams prior to mixing.

3.9.5 Calculation of concentration distribution

Volume-averaged concentrations of species are subject to equations of form:

$$\frac{DC_i}{Dt} = \Omega_i \tag{3.9.12}$$

One such equation can be solved for each species. It is often possible in practice to reduce the number of equations required by manipulation of the reaction pathways; however the manipulation depends on the specific reaction scheme and cannot be generally programmed. A more general technique based on the concepts of stream fraction and reaction extent was proposed by Ziman (1990) which is useful if the number of species greatly exceeds the number of reactions. This was not the case in the present work.

Reaction zone concentrations for each species are obtained by a mass balance on the growing reaction zone. For a species originating in the bulk stream:

$$\frac{D\alpha_r C_{ir}}{Dt} = E^*\,\alpha_r\,C_{ie} + \Omega_i\,\alpha_r \tag{3.9.13}$$

where the first term on the right-hand side represents the rate of addition of material to the reaction zone by viscous-convective engulfment and the second the rate of consumption or generation by reaction. The bulk (environment) concentration is also given by the mass balance on species *i*:

$$C_{ie} = \frac{C_i - \alpha_r C_{ir}}{1-\alpha_{eng}} \tag{3.9.14}$$

Substitution of equation 3.9.14 into 3.9.13 to eliminate C_{ie} gives:

$$\frac{D\alpha_r C_{ir}}{Dt} = E\ \alpha_r(C_i-\alpha_r C_{ir}) + \Omega_i \alpha_r \tag{3.9.15}$$

For a species originating in the segregated (additive) stream a mass balance on the growing reaction zone gives:

$$\frac{D\alpha_r C_{ir}}{Dt} = \frac{1}{t_{ic}}\ \alpha_s\ (1-\alpha_s)\ C_{is} + \Omega_i\ \alpha_r \tag{3.9.16}$$

The segregated concentration is obtained from a mass balance on species *i*:

$$C_{is} = \frac{C_i - \alpha_r C_{ir}}{\alpha_s} \tag{3.9.17}$$

Combining 3.9.17 and 3.9.16 to eliminate C_{is}:

$$\frac{D\alpha_r C_{ir}}{Dt} = \frac{1}{t_{ic}}\ (1-\alpha_s)\ (C_i-\alpha_r C_{ir}) + \Omega_i \alpha_r \tag{3.9.18}$$

The first term on the right-hand side now represents addition of material to the reaction zone by disintegration of large eddies.

3.9.6 Calculation of reaction rate

Solution of equations 3.9.2 and 3.9.11 yields the distribution of α_s and α_r. Equation set 3.9.12 yields volume-averaged concentrations and equation sets 3.9.15 and 3.9.18 yield reaction zone concentrations for each reactant. From these, environment volume fraction and both environment and segregated zone concentrations can be obtained for substitution into equation 3.9.1 for covariance. The reaction rate is then given by:

$$\Omega_i = k_{ij}\ (C_i C_j + \overline{c_i c_j}) \tag{3.9.19}$$

The above procedure can be simplified by noting that reaction only occurs in the reaction zone. Therefore equation 3.9.19 can be replaced by:

$$\Omega_i = k_{ij}\ C_{ir}\ C_{jr}\ \alpha_r \tag{3.9.20}$$

To use this equation it is necessary only to know the reaction zone volume fraction and concentrations.

The model so far described accounts for all stages of mixing except viscous-diffusive. As described in Section 3.3, molecular diffusion and chemical reaction can sometimes be limited by very fine-scale mixing within small eddies. If this mixing is rapid relative to kinetics, the reaction rate is given by equation 3.9.20, without modification.

However, if the rate of diffusive mixing is less than the kinetic reaction rate, the reaction may be limited by diffusive mixing. These two effects can be strongly coupled and to resolve the reaction rate precisely requires solution of partial differential equations within each fine-scale eddy (Baldyga & Bourne, 1984). An approximate formula for the rate can be obtained by equating it with the speed of the rate-limiting step. Thus, if the kinetics are faster than mixing, mixing determines the rate; if mixing is faster than kinetics, kinetics determine the rate. The approximate rate of viscous-diffusive mixing, G, is given by equation 3.7.20 due to Baldyga (1989). The final expression for reaction rate is then:

$$\Omega_i = \min (k_{ij} C_{ir} C_{jr}, GC_{ir}, GC_{jr}) \alpha_r \qquad (3.9.21)$$

Approximations based on a rate-limiting step are common in chemical engineering and are used in a similar context by Ziman (1990) and in combustion modelling (Jones & Whitelaw, 1981).

3.9.7 Asymptotic behaviour of new closure

It is of interest as a preliminary test to determine the asymptotic behaviour of the proposed new covariance closure. For instantaneous reactions species i and j cannot co-exist and the covariance is given by equation 3.5.9. In the present model, from equations 3.9.19 and 3.9.20, the covariance is given by:

$$\overline{c_i c_j} = C_{ir} C_{jr} \alpha_r - C_i C_j \qquad (3.9.22)$$

and since the reaction zone concentrations cannot simultaneously be greater than zero, the correct asymptote is produced. However, equation 3.9.20 is strictly not applicable to instantaneous reactions, since, by definition, these will be affected by viscous-diffusive mixing. Equation 3.9.21 should be used in this case, from which:

$$\overline{c_i c_j} = \frac{\Omega_i}{k_{ij}} - C_i C_j = - C_i C_j \qquad (3.9.23)$$

which is still the correct asymptote. For very slow reaction, or pure mixing, the correct limiting expression is equation 3.5.13. Volume averaged concentrations are constant in this case and equation 3.9.22 becomes:

$$\overline{c_i c_j} = C_i C_j \left(\frac{(\alpha_1 - (1 - \alpha_{eng}))\ (\alpha_2 - \alpha_s)}{\alpha_r \alpha_1 \alpha_2} - 1 \right) \qquad (3.9.24)$$

where α_1 and α_2 denote the volume fractions of streams *1* and *2* prior to mixing. The term in brackets is $-I_s$ and initially equals 1. Thus the correct limiting expression is also obtained for slow reactions.

3.9.8 Discussion

The proposed new model achieves closure of the time-averaged chemical reaction rate by sub-division of reactor segments into three zones. This corresponds to a three-spike pdf within each segment (see Figures 3.10 and 3.11). The reaction rate is obtained by means of equations for the following variables:

Fluid flow (U_i, P + turbulence quantities), see Chapter 2
Segregated volume fraction (α_s)
Reaction zone volume fraction (α_r)
Volume-averaged concentrations (C_i)
Reaction zone concentrations (C_{ir})

The last four sets of equations describe motion of fluid elements into the reaction zone and the rates of reactions occurring within it; collectively these can be described as a "Multiple Timescale Probability Density Function (MTPDF) Model". MTPDF can be applied to multi-dimensional reactors by linking it to CFD predictions of the flow field.

Like the models described above, MTPDF can be applied to single-step reactions; a total of 6 MTPDF equations are needed to calculate acid/base neutralisation in a coaxial jet mixer (Chapter 4). Description of mixing using volume fractions allows closure equations for multi-step reactions to be formulated. 11 equations are needed for a four-step reaction simulated in Chapter 4 and 12 for a five-step scheme in Chapter 5.

The MTPDF model is based on similar concepts to the turbulent mixer model of Baldyga (1989): cascading of segregation down the spectrum of turbulent eddy sizes prior to chemical reaction. Local volume fractions of each fluid type are equated to probabilities. Unlike earlier models (Patterson, 1981, Donaldson, 1975, Ranade & Bourne, 1991), effects of inertial-convective, viscous-convective and viscous-diffusive mixing are taken into account here in determining dissipation of concentration fluctuations. Species concentrations in the reaction zone are not necessarily equal to the mean concentration, meaning greater realism. The single-point joint pdf of reactant concentrations is calculated locally from transport equations, assuming a three delta-function distribution.

Fluctuating concentrations are not calculated; this is unnecessary in view of the definitions of α_s and α_r. Relative computational economy is achieved in this way and some of the uncertainties associated with fluctuation modelling in the large-scale flow are avoided. However, solution of the model equations for multi-dimensional flows remains a substantial computational task (see Chapters 4 and 5).

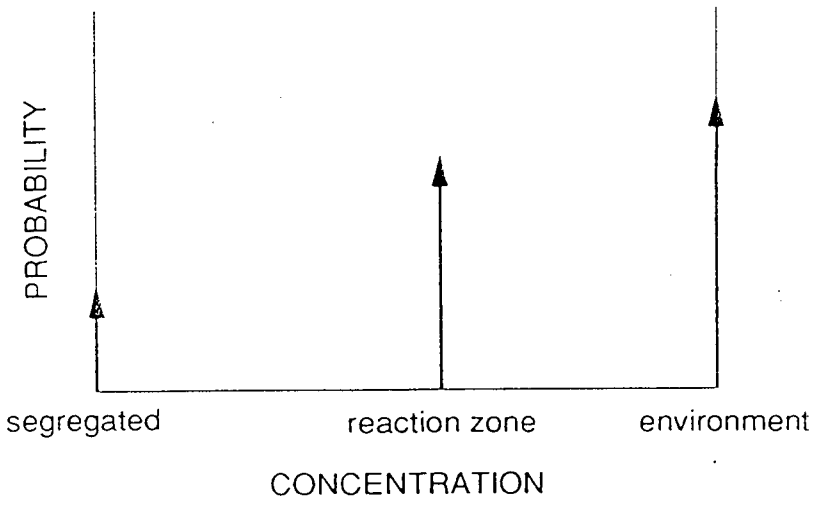

Figure 3.11 Probability density function assumed for the MTPDF model. This applies to all species: reactants and products.

In practice, multi-dimensional reactor simulation with MTPDF is split into two parts for reasons of computational economy. This implicitly assumes that the flow field is unaffected by the reaction, which is justified for isothermal mixing of fluids with similar densities and viscosities. First, the flow field is computed; then the results are recalled by a second program which solves only the MTPDF equations. This can be done time-dependently for a batch or semi-batch reactor or in steady-state for a continuous reactor. Time-dependent calculations in three-dimensional flows are computationally very intensive (see Chapter 5). Some possible simplifications are described in Appendix A.

MTPDF does not require complicated boundary conditions and contains no arbitrary fitted constants. It meets the criteria laid out in Section 3.4. Its principal assumptions are:

- validity of Corrsin's mixing time-constant (t_{ic})
- validity of Baldyga & Bourne's micromixing model (E)
- a locally well-mixed reaction zone (G)

The model formulation is sufficiently flexible to allow extra features to be added, once confidence is obtained in its basic form. Appendix B describes a possible extension to non-isothermal flows.

3.10 CONCLUSIONS

Closure of the time-averaged species transport equations in isothermal chemically reacting flows has been considered in the light of turbulence theory. Existing closure theories have been reviewed and it was found that no completely general model exists. A new model, MTPDF, has been proposed, which builds on elements of previous models, and is applicable to complex reactions in multi-dimensional reactors.

Experience with using the new model will be gained in Chapter 4 by applying it to tubular reactors. Sensitivity of predictions to changes in model parameters will be explored. Results will be compared with experimental data and predictions of previous models.

In Chapter 5, the new model will be applied to the complex flow in a stirred tank semi-batch reactor, for which reliable experimental data for the flow field and chemical reaction rates are available.

Chapter 4

TUBULAR REACTORS

4.1 INTRODUCTION & OBJECTIVES

The fluid flow and chemical reaction models described in Chapters 2 and 3 are applied to two tubular reactor geometries and two kinds of chemical reaction. Results are compared with experimental measurements from the published literature. This provides an initial test of the proposed models before application to the more complicated stirred tank reactor in Chapter 5. The objectives of the tubular reactor simulations are:

1. To test and validate the modelling method in a simplified flow geometry
2. To determine the sensitivity of predictions to model parameters
3. To compare the MTPDF model with other available reaction models

4.2 DESCRIPTION OF SIMULATED GEOMETRIES & REACTIONS

4.2.1 Tubular Reactors

Continuous flow tubular reactors are used for reactions that require only a short residence time, i.e. shorter than the time taken for the fluid to flow through the tube. If additional residence time is required, this can be provided by a recycle loop. Feeding can be coaxial, or at an angle to the main flow. In the present case studies, coaxial feeds are used (Figure 4.1).

One reactant (A) flows in the main pipe and the second (B) is introduced concentrically through a feed tube. The secondary jet expands and mixes with the primary fluid in an initially highly turbulent "confluence zone". Far downstream from the injector, the mixing intensity tends toward that of fully-developed turbulent pipe flow. Recirculation can occur in this geometry, just downstream of the jet (Schetz, 1980; Tovstiga, 1986), but does not occur under the conditions of the studies presented here.

4.2.2 Dimensions, reaction schemes and measurements

There have been a large number of investigations of fast reactions in tubular reactors (e.g. Vassilatos & Toor, 1965; Mao & Toor, 1971; McKelvey et al., 1975). Many investigations focused on nearly one-dimensional reactors. For example, the above workers all used multi-jet reactors, which inhibit radial concentration gradients. More recently, there have been some investigations in single-jet reactors (Pohorecki & Baldyga, 1983; Li & Toor, 1986; Tovstiga, 1986).

Criteria for selecting a sample of experimental data to test the present models are as follows:

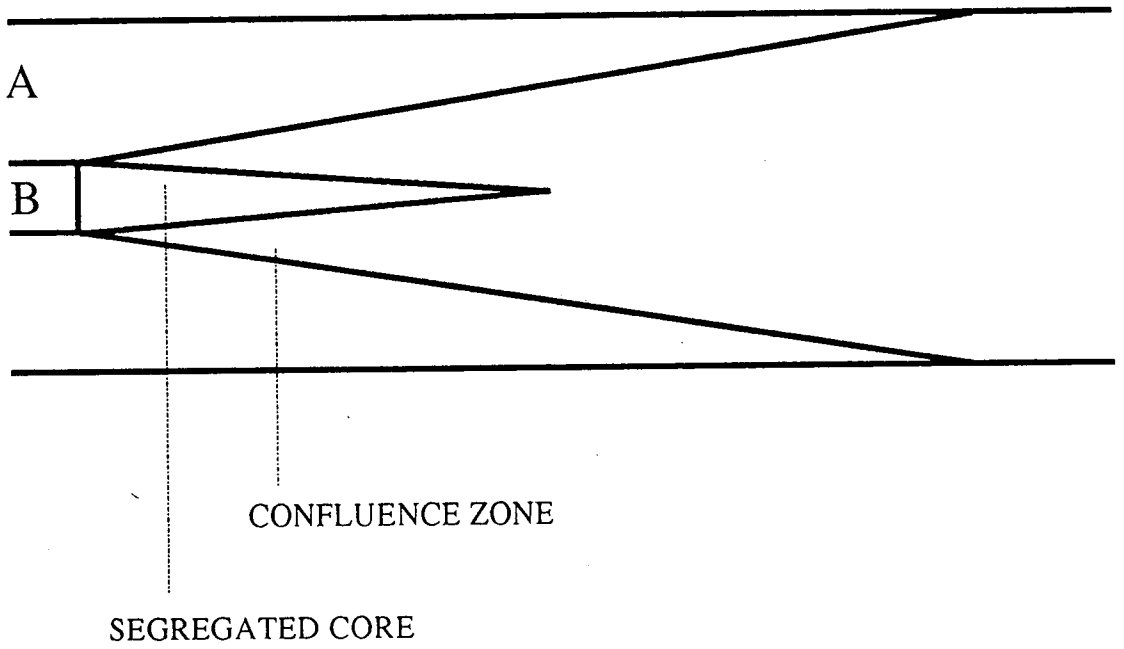

Figure 4.1 Coaxial jet tubular reactor, showing the confluence zone

1. Reactor should be multi-dimensional (i.e. single jet)
2. Reaction schemes should be well characterised
3. Examples should test suspected modelling weak points
4. The amount of computation required should not be excessive

The acid/base neutralisation experiments of Bourne & Tovstiga (1988) were chosen as the first case study. These were made under similar chemical and hydrodynamic conditions to those of Pohorecki & Baldyga (1983), so that similar factors were likely to limit in both cases. These experiments were sensitive to viscous-diffusive mixing, a potential modelling weak-point. They were preferred to the azo coupling reactions conducted by the same authors, which were likely to be less sensitive to molecular diffusion effects (Bourne & Tovstiga, 1988) and, being semi-batch rather than continuous, would be computationally more intensive.

The second case study was the experiments of Li & Toor (1986). These employed an azo-coupling reaction under conditions unusual amongst experimenters with this system. Equal flowrates of reagents were used, with only slight stoichiometric excess. Kinetic reaction speeds varied over four orders of magnitude, so that each mixing stage was potentially limiting.

Table 4.1 lists details of the two sets of experiments simulated, with pipe dimensions, reaction velocity constants, concentrations, volume and velocity ratios and Reynolds numbers, defined as:

$$Re = \frac{\varrho\, U\, D}{\mu} = \frac{U\, D}{\nu} \tag{4.1}$$

All experiments were carried out with turbulent flow in the main pipe (Re_A>>2000). In the feed tube the flow was either transitional or turbulent. Isokinetic (i.e. equal velocity) feed conditions applied to the experiments of Bourne & Tovstiga (1988). In the experiments of Li & Toor (1986), the velocity ratio was 1.28.

The two case studies selected for testing of the simulations provide an initial test of the ability to predict macromixing and micromixing effects. Validation against these case studies would establish confidence in the proposed model for application to both simple and complex reactions.

Table 4.1 Details of experiments simulated

Run	D_A (mm)	D_B (mm)	μ (Pa.s)	Sc	k_i (m^3/mol.s)	C_{A0} (mol/m^3)	C_{B0} (mol/m^3)	U (m/s)	Re_A	Re_B	V_A/V_B	U_B/U_A
BN1	26.5	0.8	0.001	400	1.0×10^8	0.01	2×10^{-4}	1.0	26500	800	1096	1.0
BN2	26.5	0.8	0.001	400	1.0×10^8	0.01	0.001	1.0	26500	800	1096	1.0
BN3	26.5	0.8	0.001	400	1.0×10^8	0.01	0.01	1.0	26500	800	1096	1.0
BN4	26.5	0.8	0.0025	1000	1.0×10^8	0.01	0.001	1.0	10600	320	1096	1.0
BN5	26.5	0.8	0.0025	1000	1.0×10^8	0.01	0.01	1.0	10600	320	1096	1.0
TA1	6.6	4.0	0.001	1425	12238 921 1.835 22.25	1.0042	0.964	1.144	7552	6230	1.0	1.28
TA2	6.6	4.0	0.001	1425	12238 921 1.835 22.25	2.9792	2.86	1.144	7552	6230	1.0	1.28

4.2.3 Experiments of Tovstiga (1986)

These are denoted "BN" and employed acid-base neutralisation, an instantaneous single-step reaction with pathway:

$$A + B \rightarrow R \tag{4.2}$$

Modelling requires one covariance to be determined. Reaction length and time was determined experimentally from the decolorisation of the base (secondary) stream as neutralisation was completed (Figure 4.2). These measurements form the basis for comparison between model calculations and experimental data.

A very large excess of A meant that complete radial mixing was unnecessary for complete conversion of B. The reaction zone was normally highly-localised near the feed tube (Tovstiga, 1986). However, it was reported experimentally that reaction did not commence until a short distance downstream of the feed tube, indicating some influence of large-scale inhomogeneities.

4.2.4 Experiments of Li & Toor (1986)

These are denoted "TA" and used azo-coupling competitive-consecutive reactions of the form:

$$A + B \rightarrow R \tag{4.3.1}$$

$$A + B \rightarrow T \tag{4.3.2}$$

$$R + B \rightarrow S \tag{4.3.3}$$

$$T + B \rightarrow S \tag{4.3.4}$$

The velocity constants (Table 4.1) are sufficiently high for the product distribution (or yield of each dyestuff) to be mixing-sensitive. Rapid mixing leads to production of R and T, poor mixing leads to production of S. Modelling requires estimation of four covariance terms. Product concentrations were determined experimentally by spectrophotometric analysis of the final reaction mixture. This measurement forms the basis for comparison between simulations and experimental data.

The reactant mixture is initially colourless, but becomes dark red after reaction begins. Thus it is not possible to visually determine the end point. However, the composition of the product mixture reflects an integrated history of the mixing rates in the reaction zone. Reactions with mixing-sensitive product distributions allow investigation of mixing effects without having to follow the progress of the reaction, which is a major experimental advantage over acid/base methods.

Experiments TA were carried out with a large diameter ratio and equal flowrates of A and B with A in small stoichiometric excess (<5%). Almost complete radial mixing was needed for conversion of B.

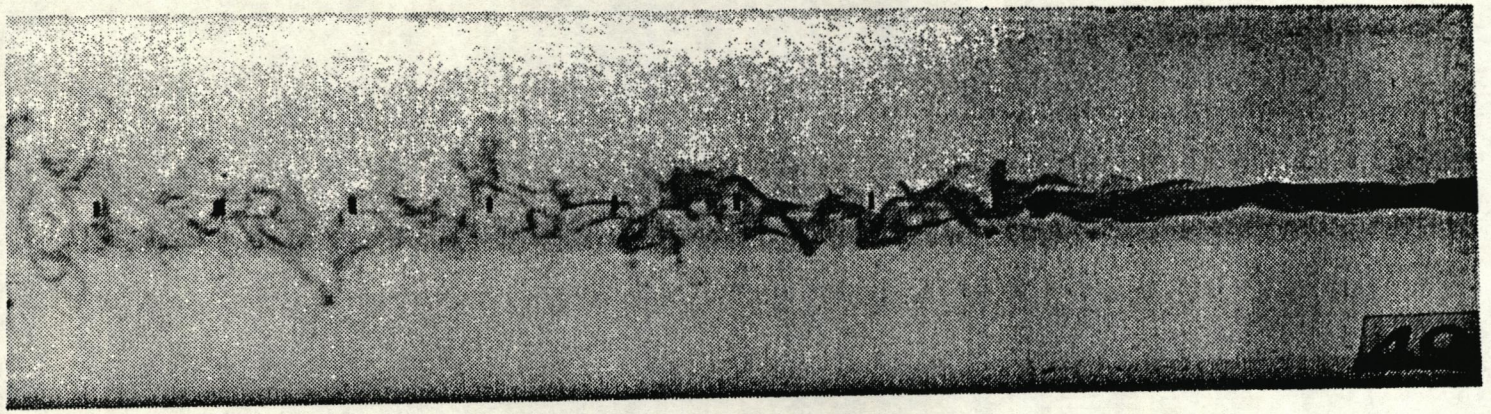

(a)

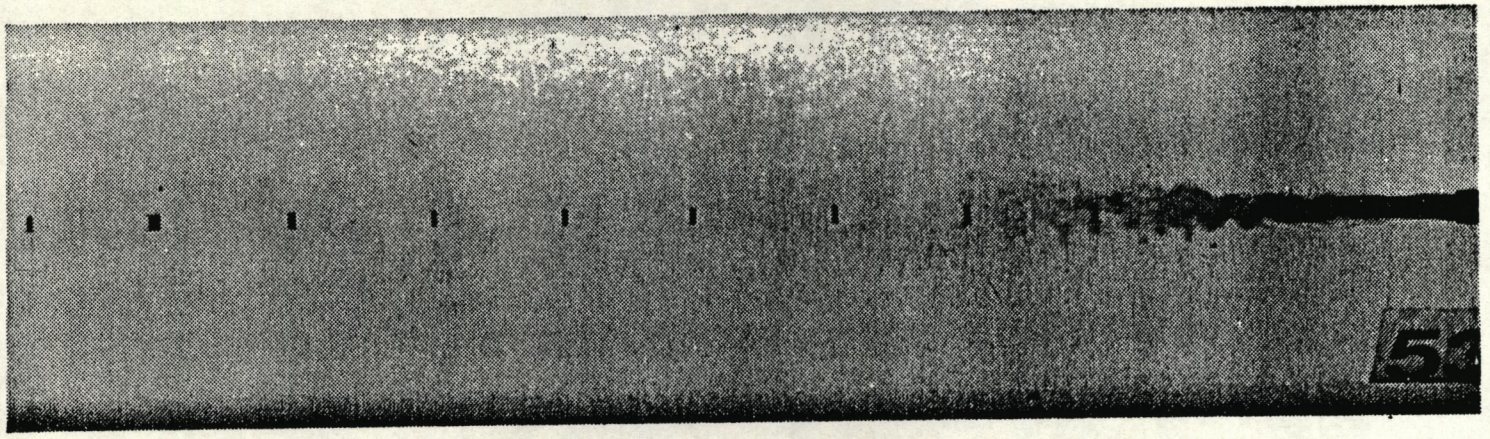

(b)

Figure 4.2 Photograph of neutralisation reactions in a coaxial jet reactor. Experimental conditions correspond to experiments BN5 (a) & BN2 (b); (adapted from Tovstiga, 1986)

4.3 FLOW FIELD PREDICTION

Flow field measurements for confined jets are relatively scarce in the published literature. Some recent measurements have been made using Laser Doppler Anemometry (Guiraud et al. 1991), but at much higher velocity ratios than in the present case studies. One set of applicable measurements were made by Oosthuizen & Wu (1978), who also simulated the flow using the k-ε turbulence model (see Chapter 2). Good agreement was obtained for average velocities and reasonable agreement for the turbulence quantities. Straight pipe flows without swirl are generally quite well represented by the k-ε model (Clarke et al., 1989).

The standard k-ε model in Harwell FLOW3D Version 2.4 was thus used for all of the present tubular reactor simulations. Since the flow patterns were neither swirling nor recirculating, use of the Differential Stress model was not justified.

For each reactor, an axi-symmetric section of pipe with a concentric feed tube was modelled. The length chosen had to be sufficient to allow the reactions to go to completion. Identification of this length required some iteration and was guided by the experimental results. For BN the simulated length was $5D_A$, compared to $75D_A$ for TA.

A typical computational mesh is shown in Figure 4.3. This was constructed by placing a fine grid across the feed tube and the shear layer between the feed tube wall and the centre of the main tube, then gradually increasing cell size approaching the main tube wall. UPWIND interpolation was used for convection terms (see Chapter 2). In the axial direction, the feed tube protruded a few diameters into the grid. Towards the confluence zone, the grid was refined in both directions. Downstream cells were gradually increased in length. The number of cells used for each geometry is shown in Table 4.2.

Table 4.2 Number of grid cells used

	Axially	Radially
BN	80	30
TA	110	25

Grid density in the radial direction is most important, since this is where the largest gradients exist: 30 cells gave acceptable resolution. In the axial direction, gradients are smaller, except near the confluence zone, where a fine grid was used.

Boundary conditions for velocities and turbulence levels were required upstream. The jet velocity profile was assumed to be flat for BN, where flow in the inner pipe was transitional between laminar and turbulent. Near-zero turbulence levels were also specified. In these simulations, the predominant mixing mechanism was diffusion of turbulence energy from the outer annulus into the core region. Predictions would therefore not be sensitive to the details of the feed tube boundary conditions.

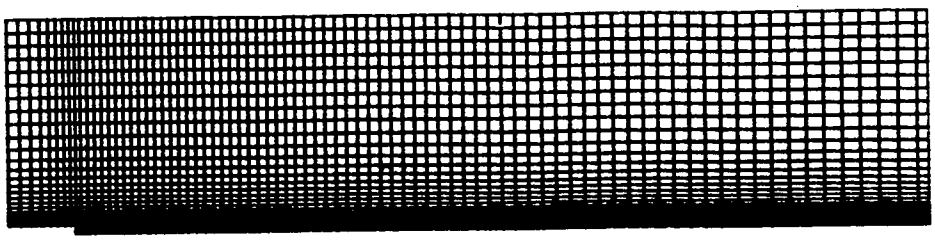

a) complete grid

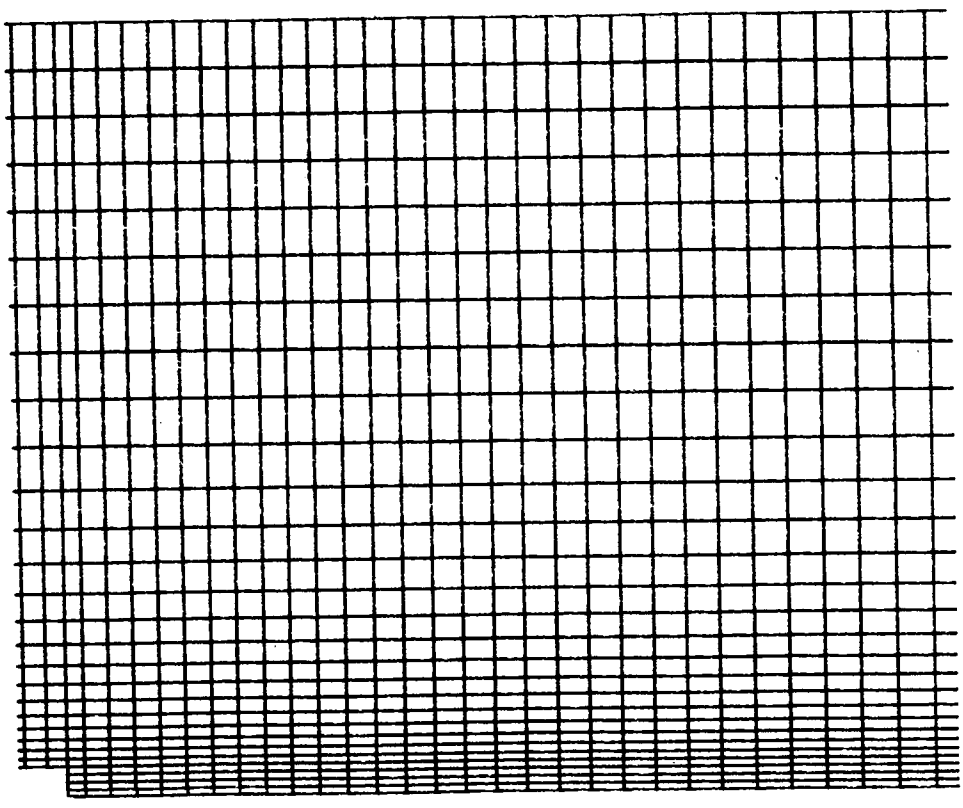

b) close-up of initial region

Figure 4.3 Computational grid used for BN flow and reaction simulations. Due to symmetry, it is sufficient to model one half-section of the reactor.

In the outer annulus, which was highly-turbulent, boundary conditions for fully-developed annular flow were obtained from separate simulations and used as input.

For TA, the feed tube was more than half the diameter of the main tube and its Reynolds number indicated turbulence (Table 4.1). Boundary conditions for the feed tube were thus more critical than for BN. In this case, both the inner tube and the annulus were specified from simulations of the upstream geometry assuming fully-developed turbulence.

4.4 CHEMICAL REACTION PREDICTION

4.4.1 Model implementation in FLOW3D

The MTPDF model (see Chapter 3) with default parameters (Table 4.3) was used for all the reactive mixing simulations. This was compared with the laminar model, "LAM", Ziman's (1990) model, "ZIM" and a 2 subgroup version of the model of Ranade & Bourne (1991), "R&B".

Table 4.3 MTPDF default parameters

t_{ic}	$0.44\ d_B^{2/3}\ \varepsilon^{-1/3}$
E	$0.05776\ (\varepsilon/\nu)^{1/2}$
G	$E(0.303 + 17051/Sc)$

FLOW3D Version 2.4 has a facility for solving transport equations for user-defined variables of form:

$$\frac{D\phi}{Dt} = \frac{\partial\phi}{\partial t} + U_i\frac{\partial\phi}{\partial x_i} - \frac{\partial}{\partial x_i}\Gamma_\phi\frac{\partial\phi}{\partial x_i} = S_\phi \qquad (4.4)$$

The left hand sides denote total rate of change of ϕ in time, by convection and diffusion. The right hand side denotes sources and sinks of ϕ. Each equation is solved in discretised form:

$$\sum_m A_m(\phi_m - \phi_P) = S_P\phi_P + S_u \qquad (4.5)$$

where ϕ_P denotes the value of ϕ at the centroid of the current cell and A_m denotes contributions of convection and diffusion of ϕ from neighbouring cells. It is normal practise to put sources and sinks which are functions of ϕ into S_P and those that are not into S_u. However, if sources are placed in S_P, diagonal dominance of the coefficient matrix can be violated, which can lead to divergence of the solution. To expedite convergence, only sinks are placed in S_P and only sources in S_u.

Equation 4.5 was used for all MTPDF equations, which only differed from each other in the specification of sources and sinks. Six such equations were needed for the neutralisation simulations and 11 for the azo-couplings. For tests of LAM and ZIM, only volume-averaged species concentration equations were needed. For R&B, the full set of MTPDF equations minus the α_s equation were solved.

Physically unrealistic results were obtained with LAM and R&B models for neutralisation because the reaction kinetics appear directly in sink terms. This is discussed further in Section 4.5.

Due to the high rates of reaction which resulted from rapid mixing and fast kinetics, and the strong coupling between variables, certain equations required under-relaxation to secure convergence. Under-relaxation is a method for reducing the rate of change of ϕ with each iteration of a numerical solution to secure better convergence. The degree of under-relaxation varied from case to case, but a factor of 0.4 to 0.6 was usual. In FLOW3D it was not possible to selectively under-relax certain equations, so all were under-relaxed by the same amount. As a result, CPU times (typically 2-3 hours on a Silicon Graphics 2-10 Server) were somewhat longer than necessary.

4.4.2 Calculation Procedure

Reactive mixing simulations used the same grids and boundary conditions as the velocity field predictions. The flow field was not recalculated, but read from a previous solution. Only the reaction model equations were solved, making calculations faster. Splitting the problem in this way is acceptable for low concentration isothermal flows, where the progress of the reaction does not influence the flow field.

Additional boundary conditions for segregated and reaction zone volume fractions and species concentrations were needed. These together with the stoichiometric coefficients and the reaction velocity constants completed the required input (see Table 4.4).

Insight into the robustness of models and the physical rate-controlling processes could be obtained by testing the sensitivity of predictions to the values of model constants (e.g. t_{ic}, E and G). This was done extensively (Section 4.7).

4.5 NEUTRALISATION EXPERIMENTS OF TOVSTIGA (1986)

Tovstiga (1986; Bourne & Tovstiga, 1988) used a rapid decolorisation reaction between dilute streams of sodium hydroxide (in feed tube) and hydrochloric acid (in main pipe) to study micromixing. Under mainly isokinetic feed conditions, they varied velocity, viscosity, feed tube diameters and concentration ratios. 95% decolorisation length was estimated by eye.

Table 4.4 MTPDF inlet boundary conditions for neutralisations

	Main pipe	Feed tube
α_s	0	1.0
α_r	0	0
$\alpha_r C_{Ar}$	0	0
$\alpha_r C_{Br}$	0	0
C_A	C_{A0}	0
C_B	0	C_{B0}
C_R	0	0

The acid concentration was always greater than or equal to the base concentration, so the acid was in very large stoichiometric excess. Under these conditions, only a small amount of mixing is required before reaction goes to completion. Once the segregated volume has decayed and a small quantity of bulk fluid has been engulfed into the reaction zone, molecular diffusion rapidly completes the mixing process. Results of simulations are thus a test of how well diffusive mixing is modelled.

Experiments with a 0.8 mm feed in a 26.5 mm pipe at an average velocity of 1.0 m/s have been simulated here. Predicted velocity vectors in the confluence zone are shown in Figure 4.4. There is no recirculation. A characteristic velocity profile for pipe flow is developing downstream. Radial profiles of turbulent kinetic energy show high levels from the feed tube boundary layer diffusing into the core region, giving rise to an increase in the turbulent energy dissipation rate (Figure 4.5). This accelerates mixing on the molecular scale.

The MTPDF model was used to calculate 95% neutralisation lengths as a function of concentration ratio and viscosity. The effect of grid dependence on reaction results was checked and 30 cells in the radial direction gave good accuracy (Figure 4.6).

Predicted conversion (i.e. fraction of B consumed) versus distance profiles for three concentration ratios are shown in Figure 4.7. Conversion is radially-averaged in these graphs, although most of the reaction takes place along the centre of the tube. The gradient is an indication of the reaction rate. Initially, the gradient is small, reflecting the effects of segregation near the feed inlet, but increases as segregated volume decreases and A and B meet in the reaction zone. The curves flatten near complete conversion.

Tovstiga measured the distance required for 95% conversion, which is compared with MTPDF predictions in Table 4.5. Reduced concentration ratio and increased viscosity should increase reaction length. Quantitative agreement between model and experiment appears to be better for the lower (0.001 Pa.s) viscosity data and at lower concentration ratios of acid to base. This observation is discussed further in Section 4.7.

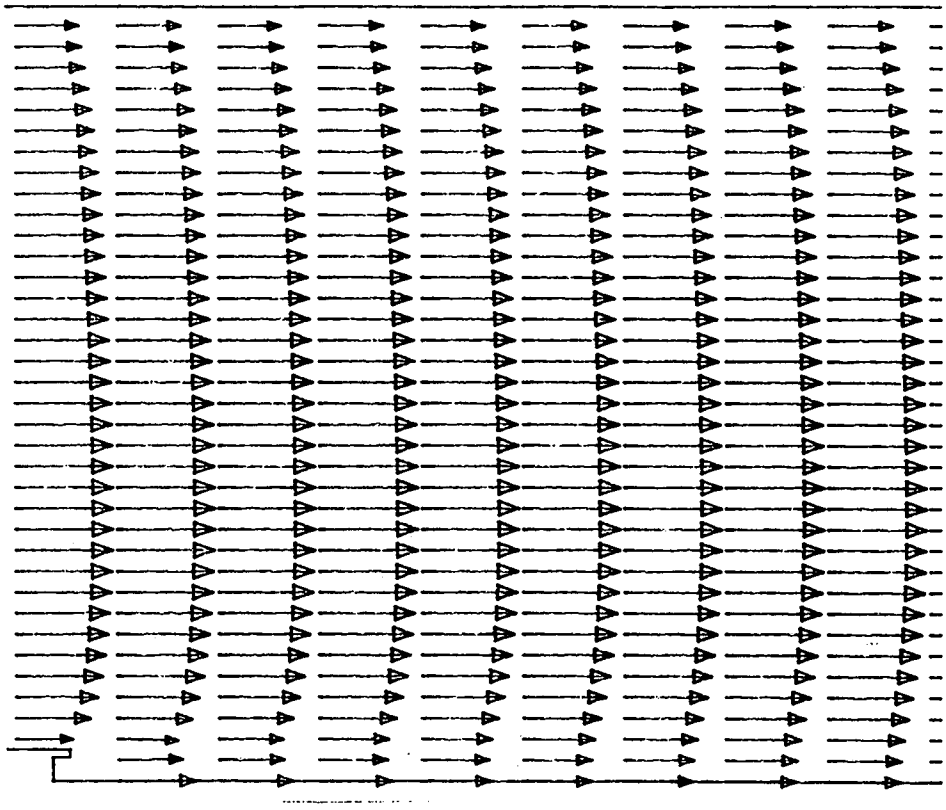

Figure 4.4 Predicted velocity vectors near the feed tube for BN

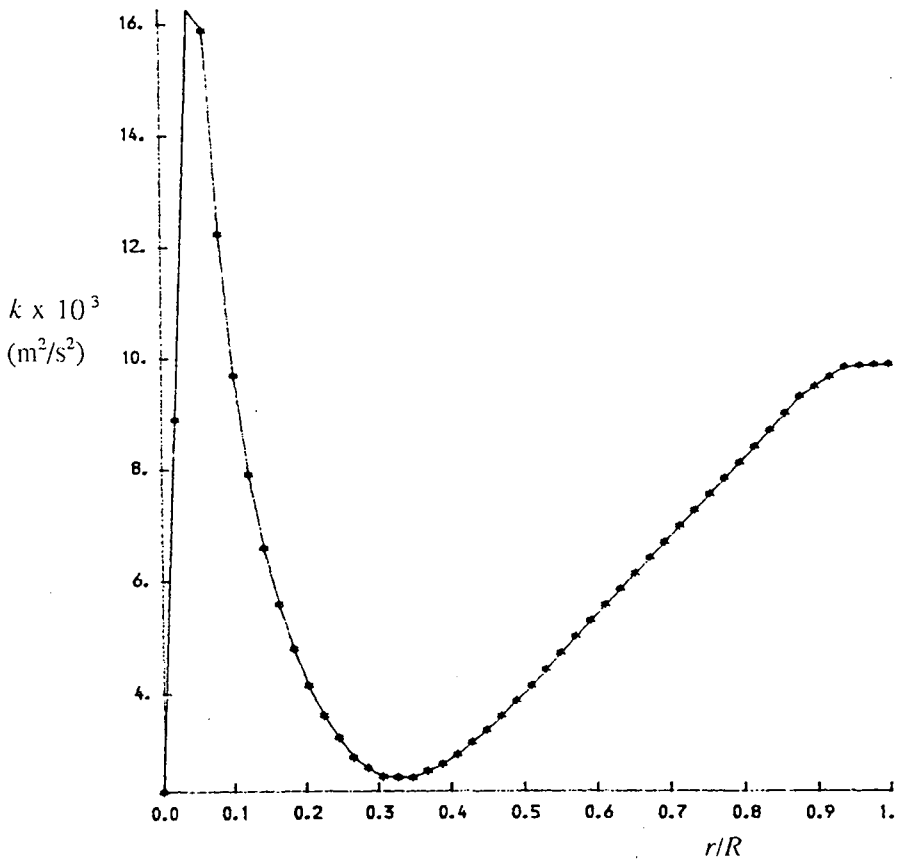

Figure 4.5 Predicted turbulent kinetic energy distribution between the axis and the wall of BN. Traverse position is 1.0 mm downstream of feed tube.

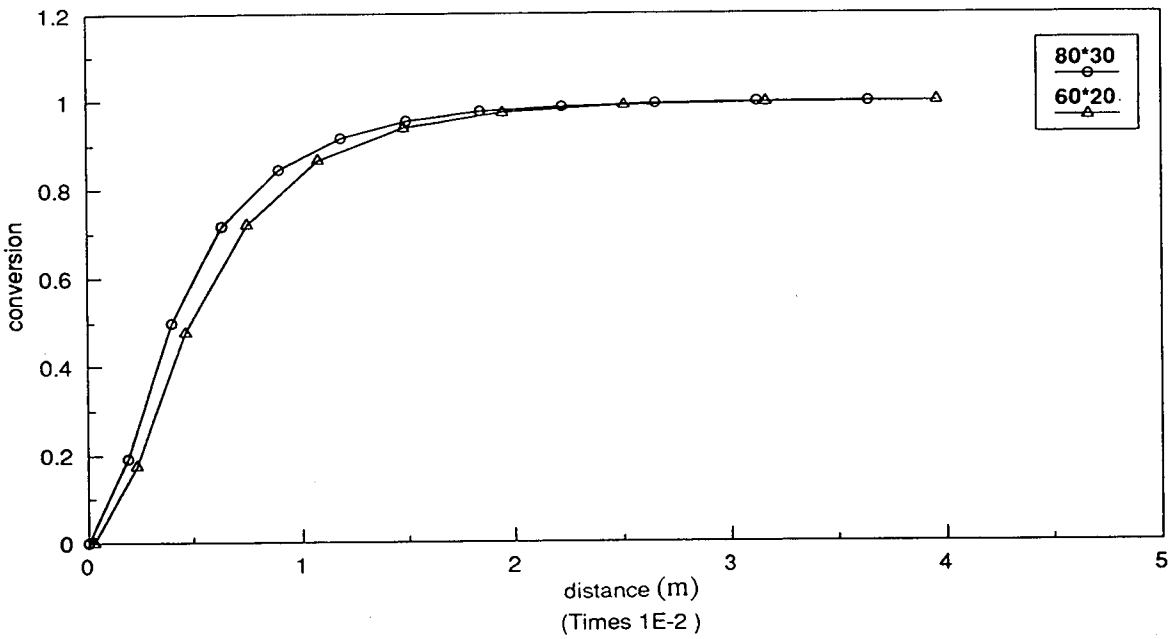

Figure 4.6 Effect of grid density on conversion versus distance profile for simulation BN1 (using MTPDF model).

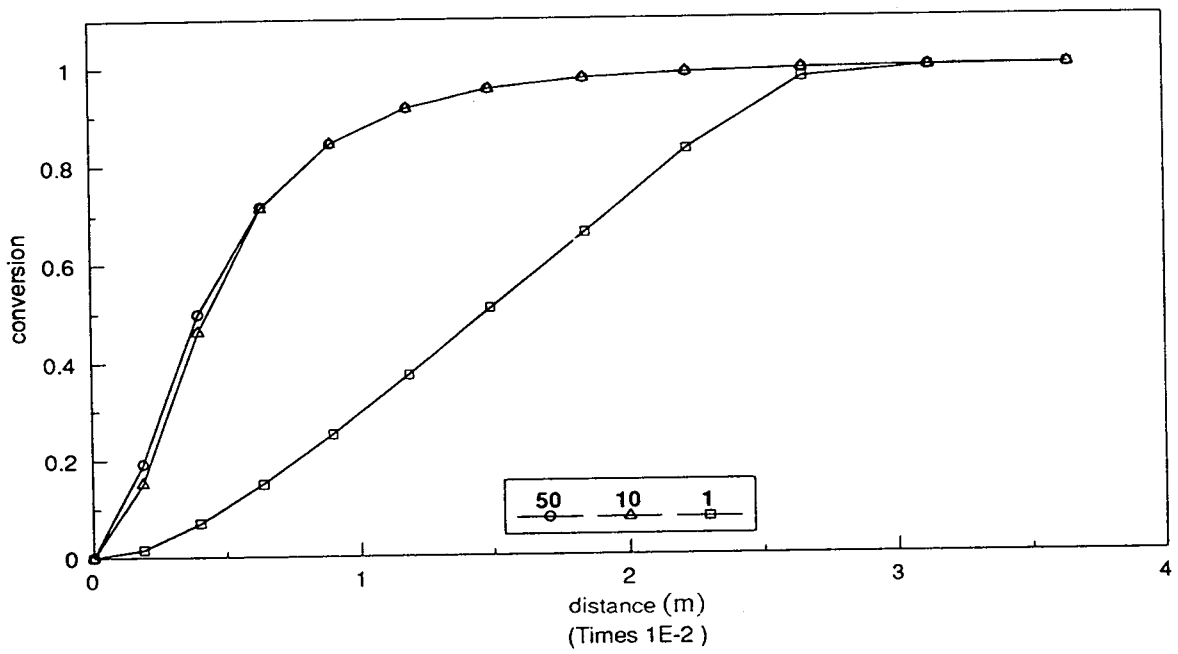

Figure 4.7 Effect of acid/base concentration ratio on conversion-distance profiles for BN using MTPDF model. Conversion at a given position decreases with concentration ratio.

Contours of reaction zone volume fraction (Figure 4.8) predicted with the MTPDF model show that reaction was confined to the central region of the pipe. There was insufficient time for B to travel outwards towards the wall. This is in agreement with experiments (Tovstiga, 1986 and Figure 4.1).

Table 4.5 MTPDF predictions of reaction length compared with measurements

μ (Pa.s)	C_{A0}/C_{B0}	Predicted L_{95} (cm)	Measured L_{95} (cm)
0.001	50	1.5	1.3
0.001	10	1.5	1.7
0.001	1	2.6	2.7
0.0025	10	1.5	2.8
0.0025	1	3.5	4.6

Correlation coefficients between the predicted covariance and mean reactant concentrations were close to 1.0. Thus the reactants remained almost completely segregated. This is in agreement with theory for instantaneous reactions (see Chapter 3).

The LAM model could not be applied to these experiments because of numerical difficulties arising from the use of kinetic sink terms for neutralisation. These lead to impractically high rates of reaction, which cause numerical instability. ZIM gave reduced conversion compared to MTPDF, which was anticipated in Chapter 3 (Figure 4.9).

R&B (Figure 4.9) as defined in Chapter 3 gives unphysical results for the same reason as LAM: use of kinetic sinks. The conditions of the present case study are outside the range of its applicability, with $C_{A0}>>C_{B0}$ (Chapter 3). A modified version of R&B using equation 3.9.21 instead of kinetic sinks was also tried here with two subgroups (N=2) which predicts shorter reaction lengths than MTPDF (Figure 4.9). This actually corresponds to a limiting version of MTPDF with t_{ic}=0.0 and can therefore be seen as a test of sensitivity of MTPDF to t_{ic}. Clearly, the more rapid the disintegration of large B eddies, the shorter the reaction zone length.

The micromixing model of Baldyga & Bourne (1984) predicts the correct conversion (Tovstiga, 1986) based on an estimated average ε in the reaction zone of 0.1 W/kg at 0.001 Pa.s and 0.16 W/kg at 0.0025 Pa.s. Simulated ε values in the core region from the present work are shown in Figure 4.10. These indicate strong axial turbulence inhomogeneity induced by the presence of the feed tube. ε values tend towards an asymptotic value, characteristic of pipe flow, within a few pipe diameters of the injector, but are predicted to be substantially higher in the initial region. This agrees with the conclusions of Bourne & Tovstiga (1988).

Figure 4.8 Regions where the reaction zone volume fraction (α_r) exceeds 1% for simulation BN1. Reaction is confined to the core of the tube. Conclusion is similar to experiment (see Figure 4.2)

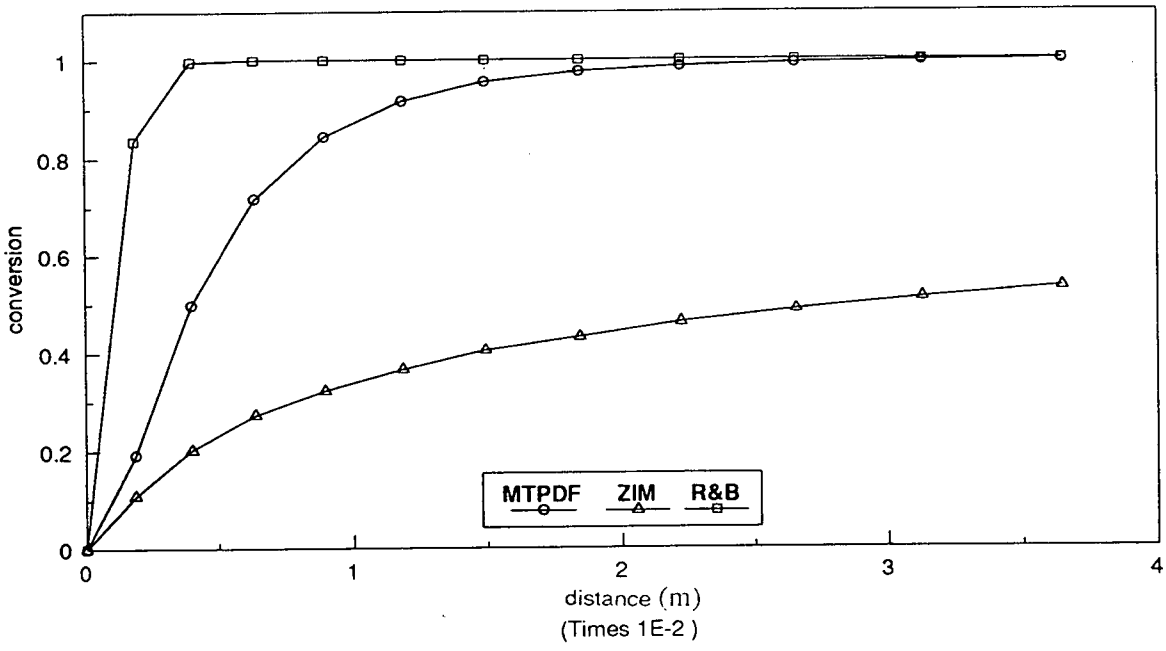

Figure 4.9 Predicted conversion-distance profiles for experiment BN1 using various chemical reaction closure models. R&B underestimates and ZIM overestimates the required reactor length.

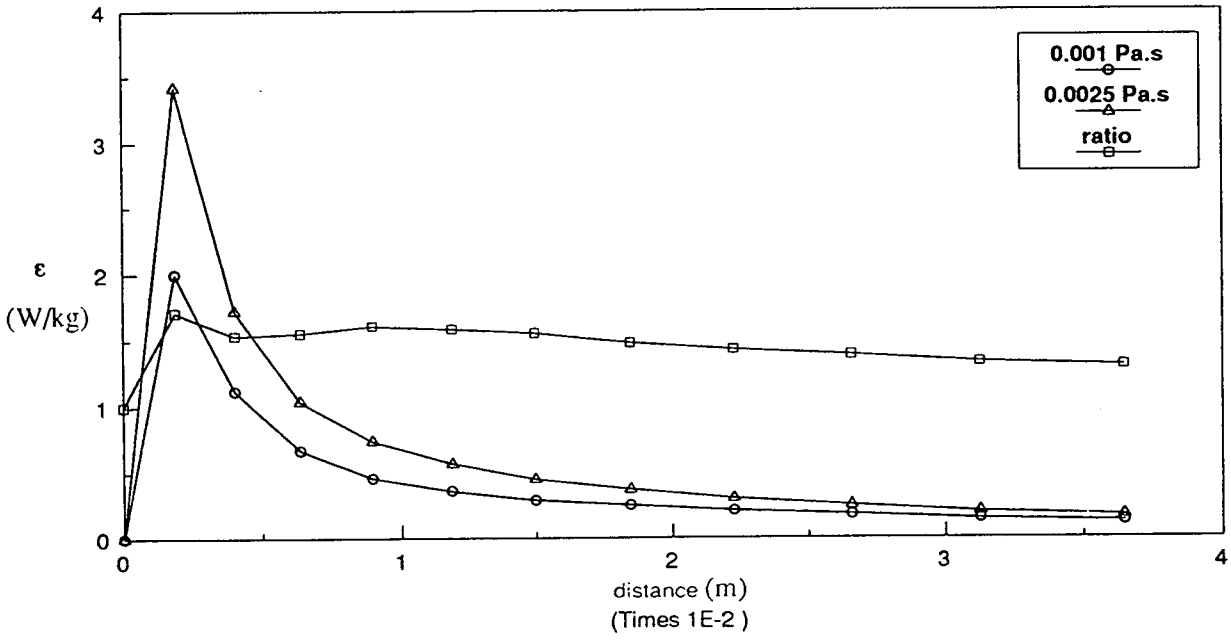

Figure 4.10 Predicted core region turbulent energy dissipation rates as a function of distance downstream of feed tube for two levels of viscosity (BN). Calculations used the k-ε model. The ratio of ε values at the two viscosities is approximately 1.5.

Overall, MTPDF makes reasonable quantitative predictions for experiments BN and is better than the other closure models tested. However, in light of comparisons with experimental data, predictions are least accurate for the effect of viscosity and at high concentration ratios. This will be further discussed after simulations of the second case study are described.

4.6 AZO-COUPLING EXPERIMENTS OF LI & TOOR (1986)

Li & Toor (1986) conducted azo-coupling reactions according to equation set 4.3 under conditions likely to require near-complete macromixing (small excess of A) for complete conversion and give a high yield of intermediates (R and T). Their experiment was unusual amongst research papers on this subject in that both streams carried the same flowrate and the feed tube was relatively large. They varied velocity (Reynolds number) and feed concentrations with a constant 4% excess of A.

Experiments in a 6.6 mm tube with a 4.0 mm feed nozzle are simulated here. Velocity vectors are shown in Figure 4.11. Turbulence levels are high (Figure 4.12), indicating potential for rapid mixing.

The MTPDF model was used to predict yield of R & T as a function of feed concentration:

$$X_{R+T} = \frac{C_R+C_T}{C_B+C_R+C_T+2C_S} \tag{4.6}$$

X_{R+T} is the fraction of reacted B which forms desired products R & T. The fraction of side product is:

$$X_S = 1-X_{R+T} \tag{4.7}$$

Boundary conditions for the simulations were analogous to those for the neutralisations (Table 4.4). Experimental and computed results using MTPDF are given in Table 4.6. Raising the inlet concentrations makes the reactions intrinsically faster and leads to a reduced yield. Reaction was virtually complete within a few diameters of the inlet. Yield of intermediates R and T was high. Simulations over-predict the yield compared to experiments by a few per cent for both levels of concentration. A conversion-distance profile is given in Figure 4.13 and side-product formation, X_S as a function of distance for both levels of concentration in Figure 4.14.

Table 4.6 MTPDF predictions and experimental measurements for TA

	Predicted X_{R+T}	Measured X_{R+T}
TA1	97.6%	93.5%
TA2	90.9%	88.3%

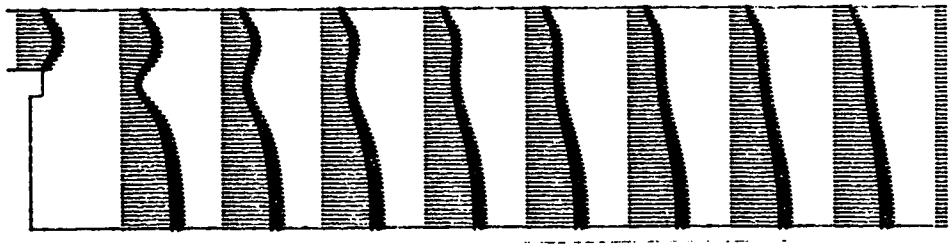

Figure 4.11 Predicted velocity vectors in the initial region of the tubular reactor of Li & Toor (1986).

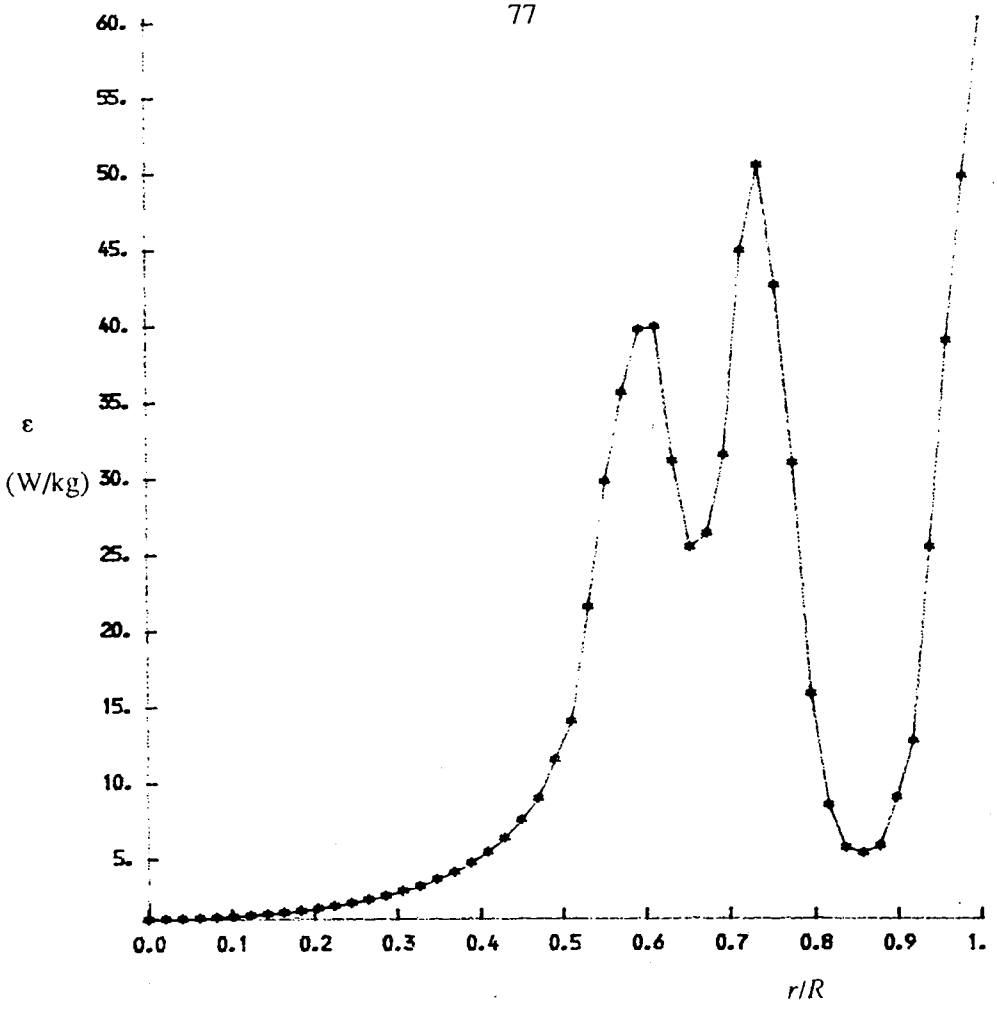

Figure 4.12 Predicted radial profile of turbulent energy dissipation rate 1.0 mm downstream from the feed tube in TA.

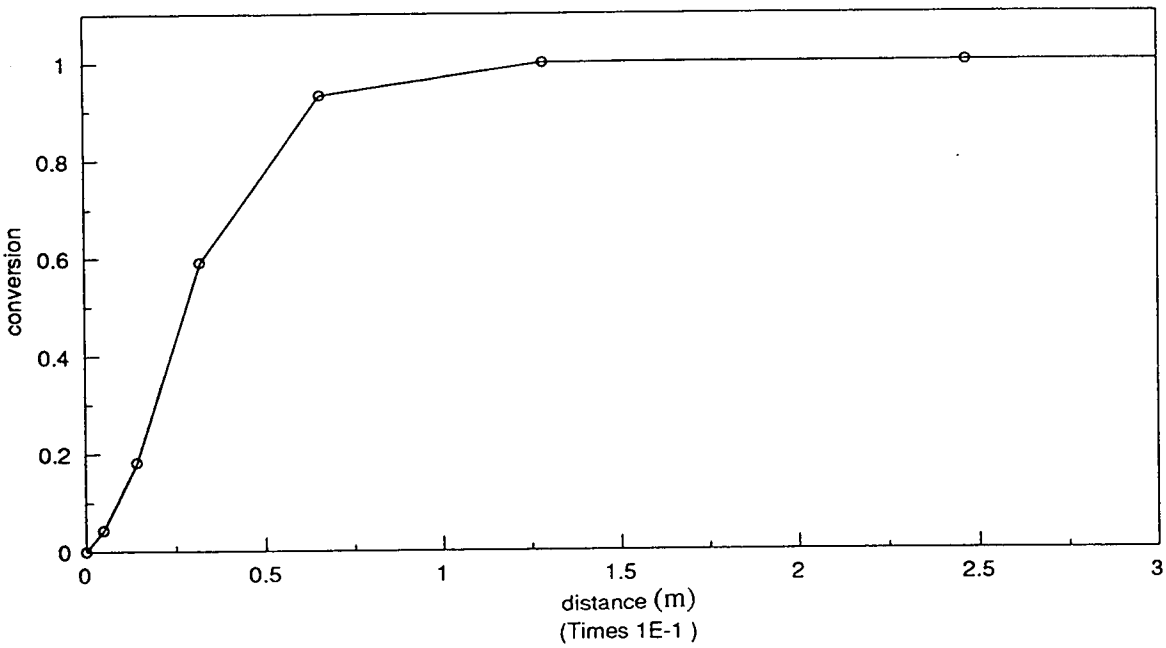

Figure 4.13 Predicted conversion-distance profile for sulfanilic acid (B) in the azo-coupling experiments of Li & Toor (1986) using MTPDF model.

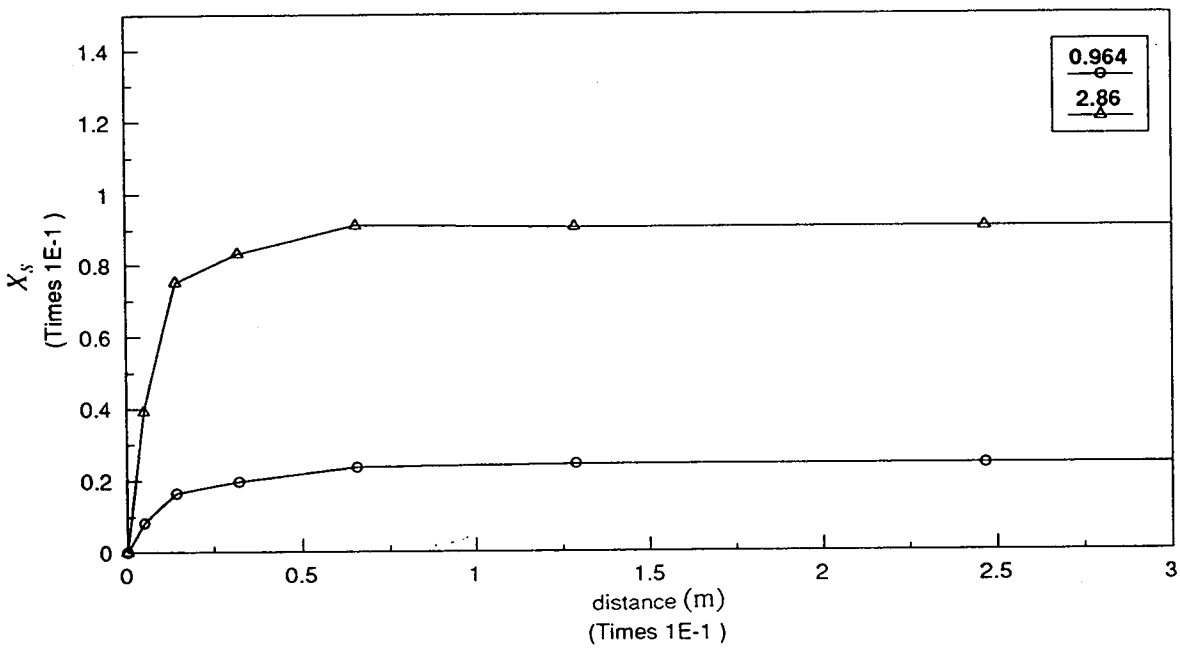

Figure 4.14 Predicted side-product (S) formation versus distance downstream of feed tube showing the effect of increasing initial B concentration. This raises side-product formation by raising the intrinsic speed of the reactions.

Four covariances were calculated by MTPDF. These are qualitatively plotted for TA1 in Figure 4.15 as correlation coefficients. By definition:

$$R_{ij} = \frac{\overline{c_i c_j}}{C_i C_j} \tag{4.8}$$

R_{ij} in Figure 4.15 is radially-averaged. Initially, covariance is low, because at any point in the cross-section the product of mean concentrations is also low (reactants are fed in separate streams). As soon as the product of means departs from zero, R_{ij} for reactions 1 and 2 rapidly increases to almost -1.0, indicating almost complete segregation. This is the expected behaviour for fast single-step reactions.

R_{ij} for reactions 3 and 4 shows different behaviour. Staring from zero, it becomes positive as soon as reaction begins and remains so for some distance downstream, before becoming negative. Positive R_{ij} means the reaction rate exceeds the intrinsic rate based on kinetics and the volume-averaged i and j concentrations. Such behaviour is more characteristic of reactions in premixed streams. Physically, it indicates that reaction zone concentrations of B, R and T temporarily exceed local volume-averaged concentrations, leading to positive correlation. Such effects are to be expected with multi-step reactions.

R_{ij} for all four reaction steps ultimately decreases towards zero as the end of the reactor is approached. This indicates the approach of complete homogeneity. The non-monotonic behaviour of the axial profiles of R_{ij} is due to simultaneous changes in concentrations in the radial direction. This underlines the requirement of multi-dimensional flow models to describe such a reactor accurately.

ZIM applied to TA1 under-predicts yield of R & T and requires a longer distance for complete conversion compared to MTPDF (Figure 4.16); this is in agreement with the theoretical arguments in Section 3.6.5. R&B over-predicts yield by slightly more than MTPDF. This is due to two competing factors: R&B neglects the initial inertial-convective disintegration stage and thus releases B into the reaction zone immediately, which tends to depress yield of R and T. On the other hand, R&B uses kinetics directly as source terms, which tends to increase yield.

4.7 SENSITIVITY TESTS

4.7.1 Neutralisation

Sensitivity of MTPDF predictions to values of t_{ic}, E and G was investigated for both reactors under various conditions. Some results at high concentration ratio for BN are given in Figure 4.17. These are insensitive to doubling of E and G but doubling the rate of inertial-convective mixing (halving t_{ic}) produces a 50% reduction in reaction length. Halving E slightly lengthens the reaction zone for higher concentration ratios, and substantially lengthens it for lower ratios and higher viscosity.

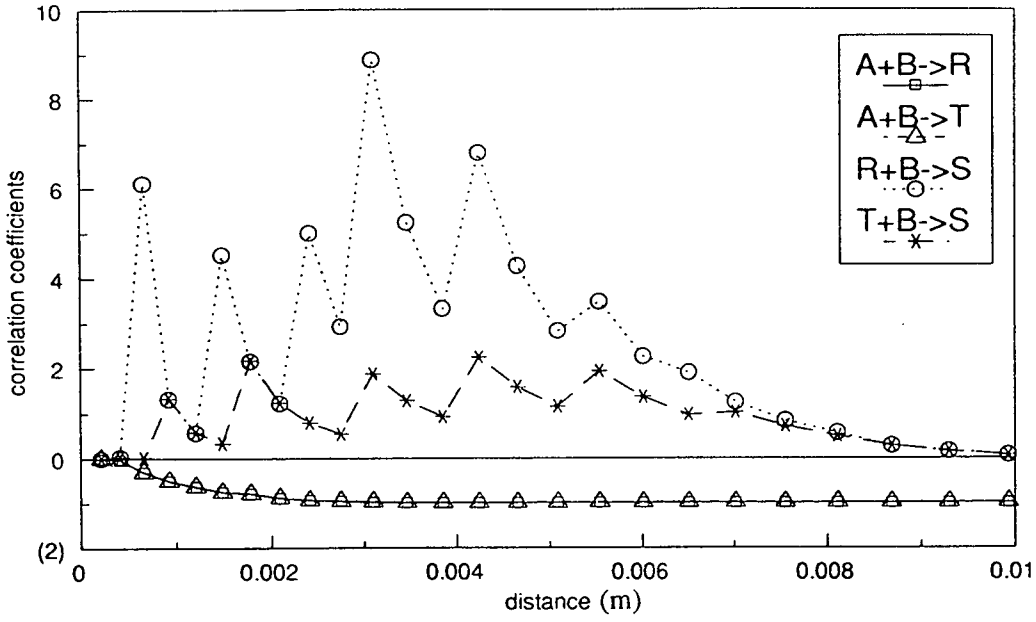

a) the initial region of the reactor, where R_{ij} for the primary reactions rapidly becomes -1 and becomes positive for the secondary reactions.

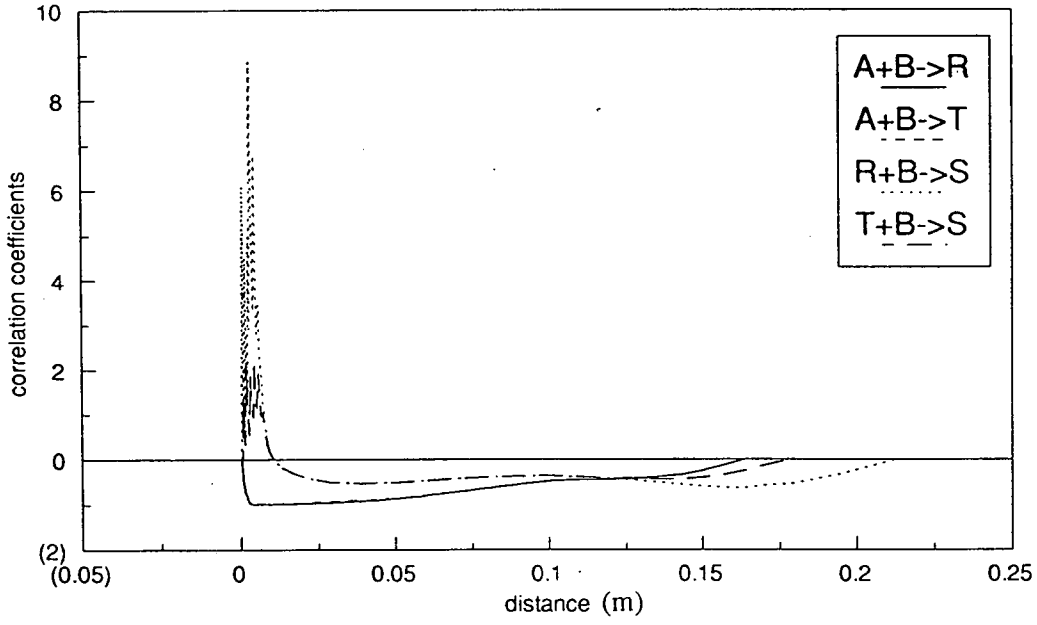

b) the entire simulated reactor length, where all R_{ij} eventually become negative, then tend to zero.

Figure 4.15 MTPDF predicted radially-averaged correlation coefficients (R_{ij}) between covariances and mean concentrations for the multiple reactions of Li & Toor (1986), plotted against distance downstream from the feed tube.

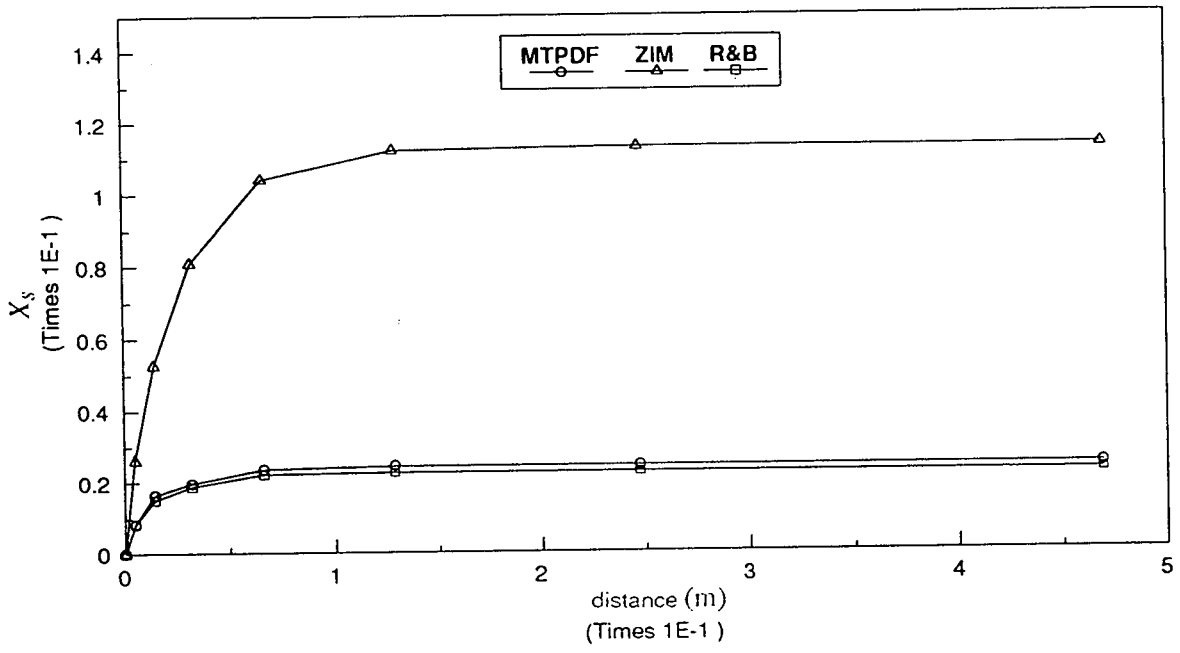

Figure 4.16 Side-product (S) formation predicted by various models for TA1. ZIM overestimates S formation, while MTPDF and R&B underestimate. The measured value was 0.065.

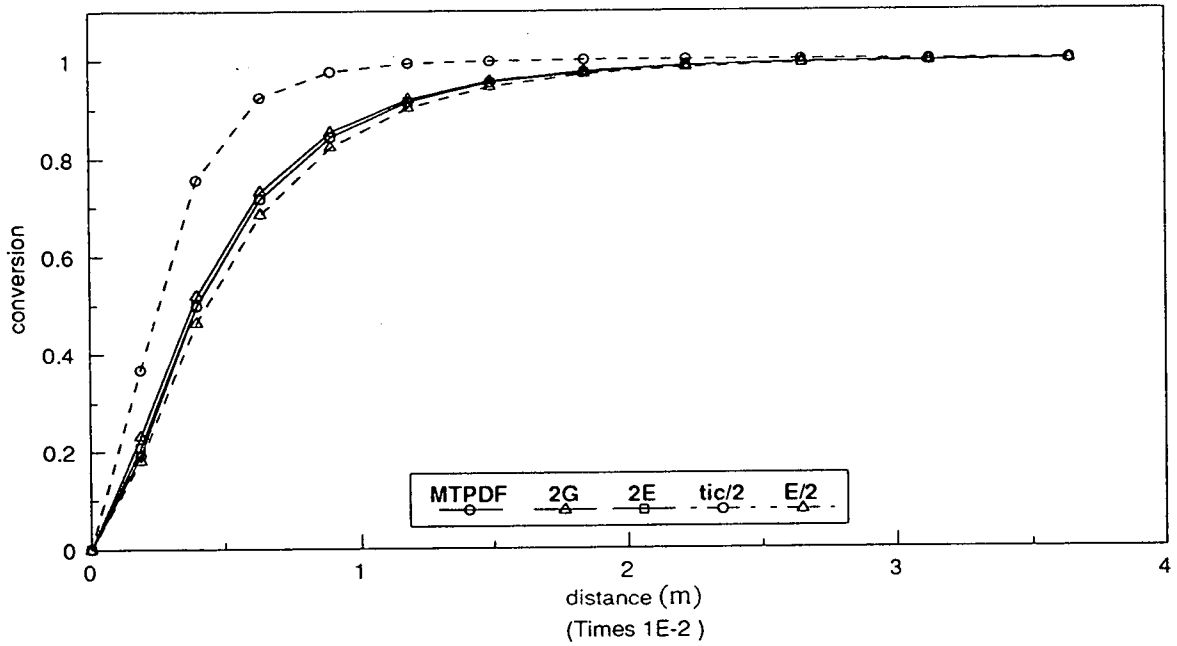

Figure 4.17 Sensitivity of MTPDF conversion-distance predictions for BN1 to values of the model constants.

The effect of viscosity was not predicted correctly above (Section 4.5) by the default MTPDF constants. Since these are theoretically based, it is not desirable to alter them simply to obtain agreement with experimental data. Valid physical reasons are needed to explain these differences.

In what follows, it is assumed that certain potential sources of error can be neglected:

- grid dependence & numerical diffusion
- deficiencies of the k-ε model
- experimental error in determining reaction length

Grid dependence was checked and was not significant. Numerical diffusion should not have been substantial (UPWIND differencing was used but the stream lines were parallel with the grid lines, which minimises errors). The k-ε model appears to have made a satisfactory prediction of the flow field. Reaction lengths should not be subject to much experimental error (Bourne & Tovstiga, 1988). In any event, all the above factors are common to all the conditions simulated.

Experimental conditions in BN led to sensitivity to viscous-diffusive mixing (Bourne & Tovstiga, 1988), which involves simultaneous deformation and molecular diffusion within thin liquid laminae. This can be well described using a one-dimensional convection diffusion equation in fluid elements of size λ_K and below, with an appropriately defined thinning velocity, such as in the EDD model of Baldyga & Bourne (1984), see Section 3.7.2. Implementation of such a model in each cell of a CFD calculation would be computationally very expensive. In its place, the rate constant G used here, which was obtained by Baldyga (1989) as an approximation to the more complex solution of the EDD model, is likely to be an over-simplification.

For similar reasons, in developing a model similar to MTPDF, Ranade & Bourne (1991) restricted its application to conditions where viscous-diffusive mixing was not limiting. To understand the limitations of these models, it is necessary to detail when diffusive mixing will limit. This requires the following two conditions to hold:

1. Turbulent dispersion, inertial-convective mixing and viscous-convective mixing must be either very rapid or unnecessary.

2. Diffusive mixing must be slower than reaction kinetics.

Condition 1 is strongly favoured by reactor operation with massive excess of the main stream reagent (in the present case, at least 109,600% excess was used). If such a small quantity of additive is introduced at a low concentration into such a large quantity of bulk fluid with a high concentration, very little long-range mixing is required for reaction to go to completion. Put another way, very small reaction zones favour short-range mixing effects, i.e. molecular diffusion.

If, on the other hand, the concentration of the additive is higher than that in the bulk and the excess is reduced, dispersion, disintegration of eddies, and engulfment are required to supply enough main stream fluid for the reaction to go to completion. These conditions are more common in practice.

If molecular diffusion is slow relative to reaction, it can limit the reaction rate. Diffusive mixing in highly turbulent flows is normally quite rapid. It is accelerated by turbulent energy dissipation which causes thinning of laminae and steepening of concentration gradients. Not all reactions are faster than diffusive mixing, but ionic reactions, such as neutralisation, tend to be.

Based on the foregoing discussion and sensitivity analysis of the BN results, it is concluded that the main source of error in the BN calculations is G. This hypothesis is supported by the drop in accuracy of MTPDF when viscosity and Schmidt number are raised at high acid-base concentration ratios - these factors both favour viscous-diffusive mixing as a limiting step. The only other parameter in MTPDF that is sensitive to viscosity is E, whose value has been established theoretically and confirmed by several applications (Baldyga & Bourne, 1989).

The above hypothesis can be tested as follows. Diffusive mixing is favoured by a high acid/base concentration ratio. As this ratio is reduced, the importance of diffusive mixing should recede. The lowest concentration ratio used by Bourne & Tovstiga was 1.0. Simulated conversion distance profiles for this and a ratio of 10 at 0.0025 Pa.s are shown in Figure 4.18. Agreement of model and experiment is much better at the lower ratio (see Table 4.5).

4.7.2 Azo-couplings

Sensitivity of the predictions of MTPDF for Li & Toor's reactor was also investigated. In this reactor the initial concentration ratio was close to one, but so were the volume ratios of the streams. This would tend to favour long-range mixing effects rather than viscous-diffusive mixing.

Doubling E and G raised yield from 97.6% to 98.6% and 98.1% respectively. Reduced t_{ic} (put equal to zero) reduced yield to 96.7%, the corresponding experimental value (for the lower concentration run) being 93.5% (Figure 4.19). Halving E gave 93.5 % exactly but for the higher concentration run gave 82.7% compared to a measured 88.3%.

For most combinations of model parameters, side-product formation X_S increases monotonically from the inlet to a constant value towards the exit. However, at the lower concentration, halving E produces an initial peak in X_S. At the higher concentration, there is also a very slight peak using the default MTPDF parameters. Such behaviour is possible if initially there is insufficient A in the reaction zone. The mechanism of addition of A is engulfment. If insufficient A is present, excess B may react further with R and T to produce a peak in X_S. No measurements of the progress of the reaction are available, so these effects cannot be confirmed. Bourne & Hilber (1990) and Ranade & Bourne (1991) have reported that X_S develops through a minimum during the batch time in some semi-batch experiments (see also predictions in Chapter 5).

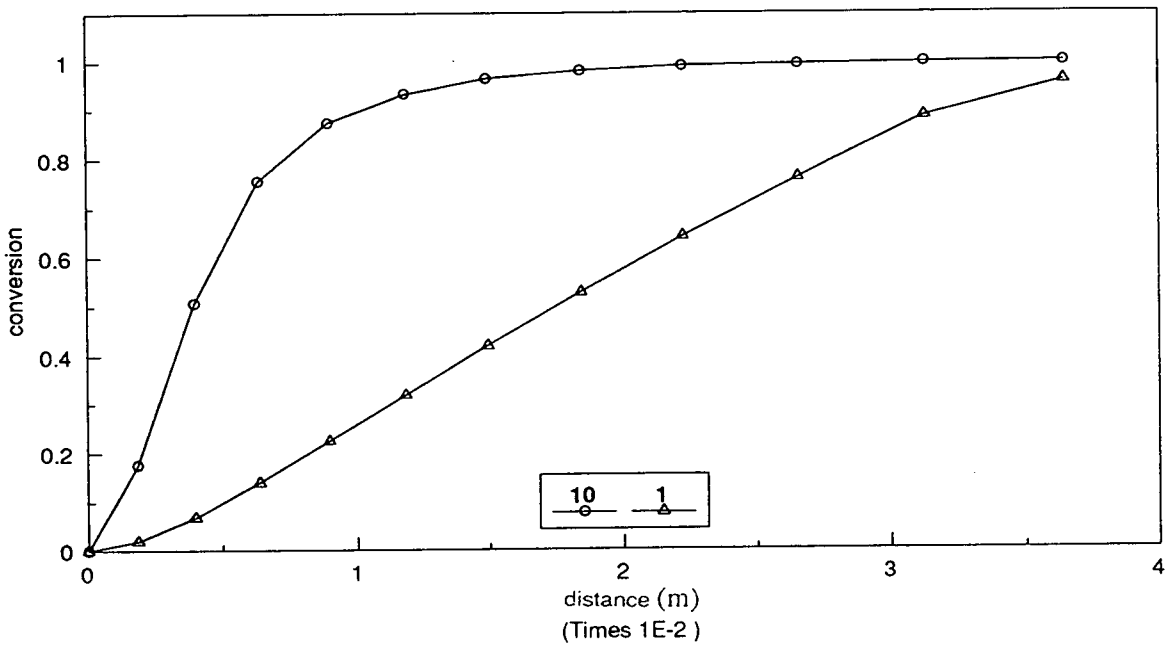

Figure 4.18 Sensitivity of MTPDF predictions to acid/base concentration ratio at raised viscosity (0.0025 Pa.s)

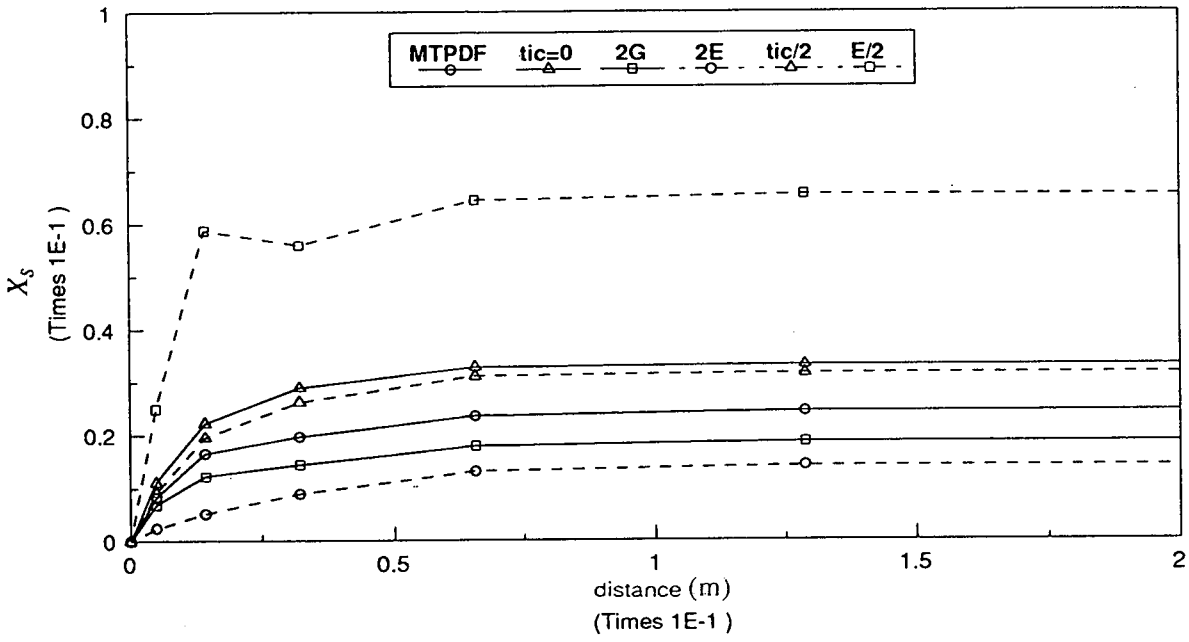

Figure 4.19 Sensitivity of MTPDF predictions of side-product formation in TA1 to model constants

Under the present mixing conditions, the R-producing and possibly the T-producing reaction are likely to be sensitive to viscous diffusive mixing, so that formation of S was jointly controlled by other mixing stages and kinetics. Over-estimation of G would produce the observed increased yield of R & T relative to experimental results and this is likely to be the main source of error, as for the neutralisations. However, agreement for TA is satisfactory, overall.

4.8 COMPARISON OF MODELS

MTPDF made reasonable predictions of both neutralisations and azo-couplings. LAM was tried for BN but did not work satisfactorily due to unphysically high reaction rates associated with neutralisation kinetics and resulting instability of the equations. Numerical simulations predicted negative concentrations of B after a very short reaction length.

ZIM was applied to both BN and TA. In the former case, it underpredicted conversion by approximately 50% (Figure 4.9). This effect is due to the inclusion of the inertial-convective and viscous-convective mixing timescales in the reaction rate calculation even when these stages are complete (see Chapter 3). In TA, ZIM predicted a yield of R & T of 88.7% for the lower concentration compared to a measured 93.5%. Almost equal amounts of R & T were produced (Figure 4.20) which indicates that ZIM predicted that all the reaction steps were equally mixing-limited.

R&B could not be directly applied to neutralisation for the same reason as LAM. However, a modified form, with reaction kinetics replaced by G, gave a shorter neutralisation length than experiments or MTPDF. Applied to TA, R&B predicted a slightly less accurate (higher) yield than MTPDF.

Both R&B & MTPDF predict that more R was formed than T, i.e. only the primary reactions were limited by viscous-diffusive mixing (Figure 4.21); this is illustrated by the calculated MTPDF correlation coefficients (Figure 4.15) which show that the S-producing steps are generally less negatively correlated than the R- & T-producing steps. Conversion length is shorter than with ZIM; however, no data on the measured length is available for comparison.

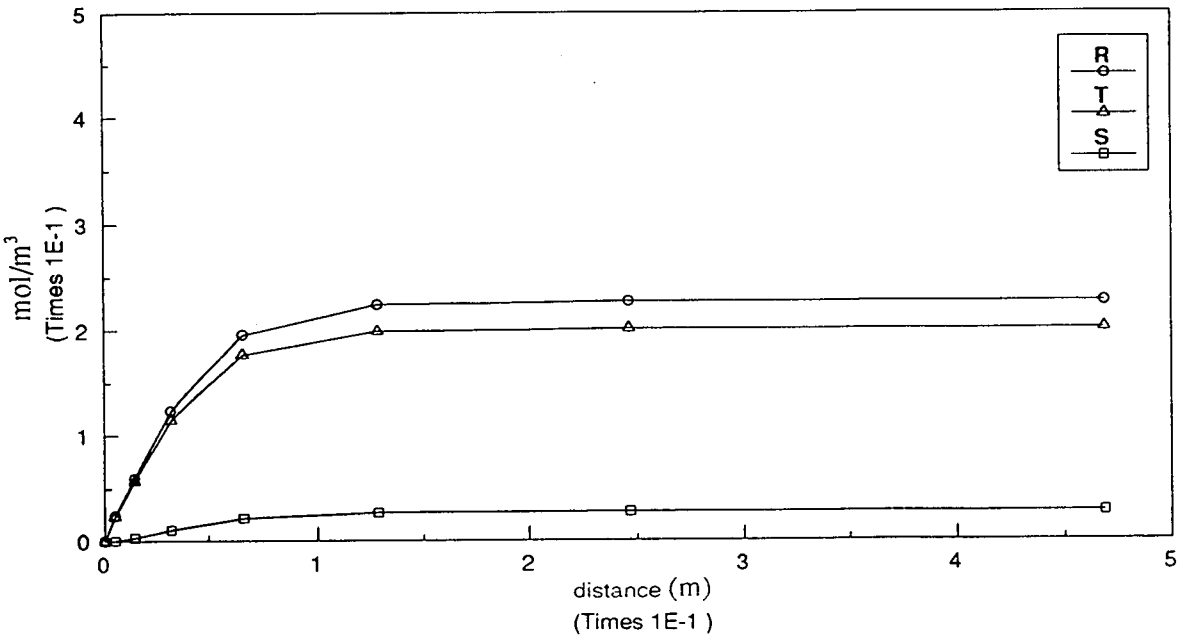

Figure 4.20 Predicted ZIM product concentrations in TA1 as a function of distance downstream from the feed tube

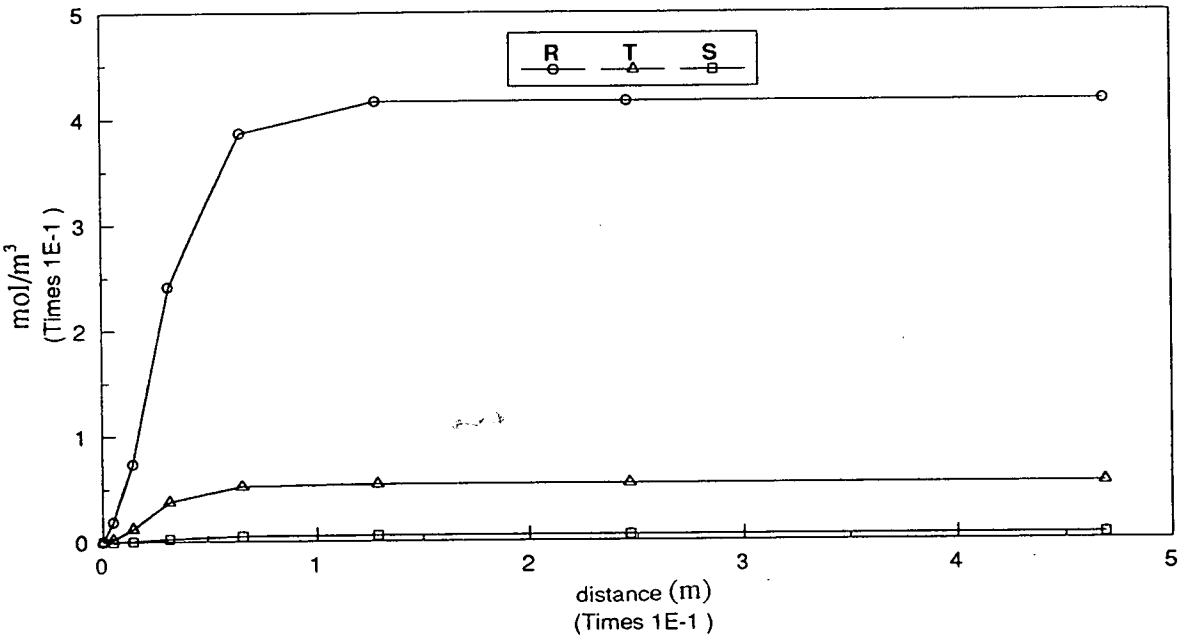

Figure 4.21 Predicted MTPDF product concentrations in TA1 as a function of distance downstream of the feed tube

4.9 CONCLUSIONS

The MTPDF model developed in Chapter 3 has been combined with the flow model described in Chapter 2 to simulate two tubular reactors under mixing-controlled conditions. Agreement between model and experiments is reasonable, and areas have been highlighted where MTPDF is unlikely to be very accurate.

Comparison of predictions for tubular reactors with other closures in the literature suggests that MTPDF is an improved approximation. Sensitivity of model predictions to changes in parameters have shown that the defaults given in Chapter 3 are acceptable under most conditions.

Some insight into the behaviour of multi-step reactions in tubes has been gained. Simulations showed that secondary reactions could have positive covariances (or correlation coefficients), in a similar way to reactions in premixed streams. Yield, plotted as a function of distance downstream from the reactor inlet, generally increased monotonically, but could exhibit a maximum or minimum under certain conditions.

Chapter 5

STIRRED TANK REACTORS

5.1 INTRODUCTION & OBJECTIVES

Fluid flow and reaction models presented in Chapters 2 and 3 and tested in simple geometries in Chapter 4 are now applied to predict flow patterns, turbulence levels and yield from a complex chemical reaction in a stirred tank reactor. The objectives of this chapter are:

1. To determine the most suitable turbulence model for stirred tanks
2. To predict and validate the flow field in a stirred tank agitated by a pitched blade turbine
3. To predict and validate reactive mixing in a stirred tank reactor

The k-ε turbulence model has been used by virtually all previous workers in this field (e.g. Harvey, 1980; Middleton et al., 1986; Hutchings et al., 1989; Brucato et al., 1990; Ranade et al., 1989; Ranade & Bourne, 1991); Bolour-Froushan (1986) modified the k-ε model to take account of curvature effects and Bakker (1992) was the first to use the Algebraic Stress Model.

The k-ε model assumes an isotropic eddy diffusivity, which is known theoretically to be inappropriate for stirred tanks (Chapter 2 of this work; Fawcett, 1992; Mahouast et al., 1989). The Boussinesq relationship between stresses and strains is of doubtful validity (Bradshaw, 1973). In many circumstances, the model is unable to predict the correct direction of swirl, particularly in the upper part of the tank.

A significant step forward would be to be able to correctly predict the direction of motion in the bulk of the tank. This would add to the realism of the simulations and enable them to be used more confidently to understand mixing processes. Bulk flow patterns, such as location and direction of swirl, are influential in determining fluid, particle and bubble trajectories and can exert a significant influence on heat and mass transfer rates. Bulk flow patterns alone are likely to be sufficient for practical design of many mixing applications, such as liquid blending and solids distribution.

For more critical and quantitative mixing applications, such as fast chemical reactions, improved predictions of turbulence levels are required in addition to the average velocities. Any turbulence model must be able to reproduce these with sufficient accuracy. In particular, the components of the turbulent (Reynolds) stress tensor are influential in determining rates of turbulent transport, and the rate of turbulent energy dissipation is responsible for intensifying fine-scale mixing processes, such as micromixing (Chapters 3 and 4) and mass and heat transfer from drops, bubbles and particles.

Both k-ε and the Differential Stress Model (DSM, see Chapter 2) have been applied here and sensitivity of predictions to boundary conditions and numerical parameters explored. This compliments and extends the recent work of Bakker (1992) using the

ASM. The MTPDF model developed in Chapter 3 is used to describe the effect of turbulence on chemical reaction. Validation is by comparison with Laser Doppler flow measurements and the results of a complex reaction conducted in the simulated tank.

5.2 DESCRIPTION OF SIMULATED STIRRED TANK

A 0.3 m diameter perspex stirred tank with a $T/3$ diameter 45 degree pitched-blade turbine impeller (details in Table 5.1) at $T/3$ clearance from the dished base was used for all the following experimental and computational work (Figure 5.1). The tank had four standard baffles of $T/12$ width at 90 degree circumferential intervals, at a spacing of $T/60$ from the tank wall. The liquid depth was equal to the tank diameter. Shaft rotational speeds were between 100 & 300 rpm. Impeller Reynolds number can be calculated from:

$$Re_i = \frac{\varrho\, N\, D^2}{\mu} = \frac{N\, D^2}{\nu} \tag{5.2.1}$$

which lay in the range 1.7×10^4 to 5.1×10^4. Fully-developed turbulent flow exists above an impeller Reynolds number of approximately 10^4 (Grenville, 1989). Power consumption can be calculated if the shaft torque is known:

$$P = 2\,\pi\, N\, M \tag{5.2.2}$$

A typical value here was 1.88 Watts at N=300 rpm. The average power input per unit mass was 0.09 W/kg under these conditions. This is compared below with power calculations from simulations.

For the chemically reacting experiments, a feed tube was placed at one of two positions (Figure 5.1). The first was just below the liquid surface in-line with a baffle and radially halfway between the axis and the wall. The second was in line with a baffle and 1 cm above the outer blade edge of the impeller. The feed tube internal diameter was 3 mm.

Table 5.1 Details of pitched blade turbine

D	W	D_H	α	t
101.5 mm	29.2 mm	19.0 mm	45 degrees	1.7 mm

5.3 FLOW FIELD MEASUREMENTS

5.3.1 Measuring system

The purpose of experimental flow measurements is twofold. Experimental data are needed as boundary conditions for the CFD model; such measurements are concentrated near the impeller. Measurements are also needed to validate model predictions. These are concentrated in the bulk of the tank.

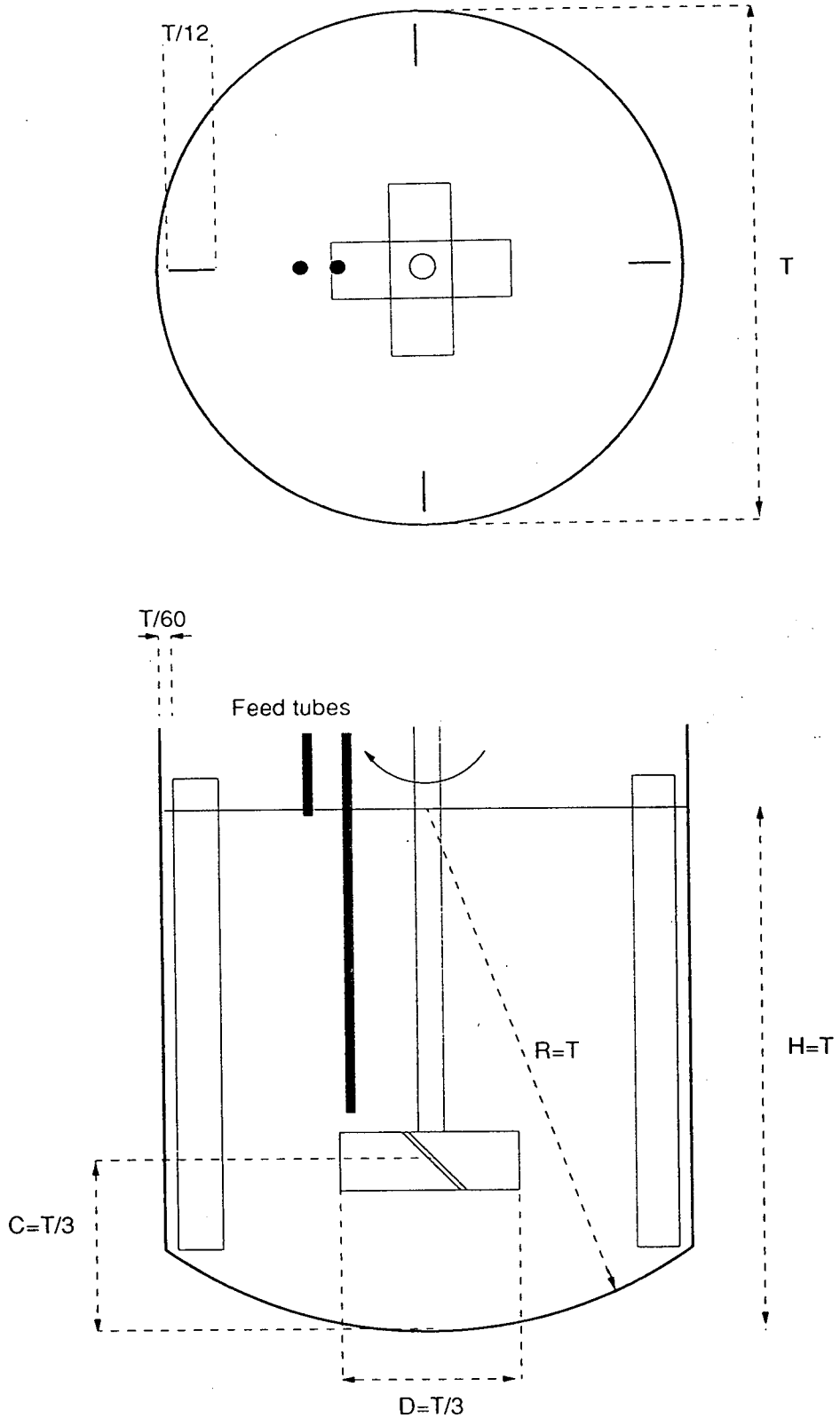

Figure 5.1 Details of stirred tank reactor used for simulations and experimental measurements

A DISA three-colour two-component Laser Doppler Anemometer (LDA, for details, see Armstrong & Ruszkowski, 1986) was used to measure average and fluctuating velocities. The LDA signal was obtained in backscatter mode and analysed using frequency counters. Six thousand samples were taken at each position, over a period typically lasting a few minutes. By varying the position where the beams entered the tank and their intersection point, it was possible to map all three components of average velocity and root mean squared fluctuating velocity as well as two components of Reynolds shear stress around the impeller region and in key positions in the bulk of the tank. Traversing was manual in the radial and circumferential directions and automatic in the axial direction. Emphasis was placed on regions where model predictions were most likely to be in error. This subjective judgement was made on the basis of preliminary simulations with the k-ε model, which for example showed reverse tangential flow near the impeller shaft in the upper part of the tank.

Flow patterns in baffled stirred tanks are time-dependent, particularly in the region of the rotating impeller, where large periodic changes in velocity occur. To model this with precision, time-dependent calculations with grids in relative motion are needed. These are prohibitively expensive at the present time. In this work, the impeller is modelled as a steady source of flow, turbulence and momentum (Section 5.4.1 below). For such a model, measurements in a stationary frame of reference are sufficient to obtain boundary conditions and for validation of predictions.

A low frequency fluctuating velocity, called pseudo-turbulence (Van't Riet et al., 1976), is induced by rotation of the impeller blades. The periodic component can be isolated using autocorrelation techniques. However for the impeller studied here, there is little difference between the total fluctuating velocities and the turbulent part (Musgrove, 1992). The total was used for boundary conditions and validation.

Measurement error for the mean velocity components is of order plus or minus 0.02 m/s. This represents a small (eg, <5%) error in the impeller discharge, which reduces as the blade edge is approached: the discharge flowrate is therefore somewhat more accurate. The percentage error is larger (eg, 20%) near the liquid surface. Errors in the velocity fluctuations are more difficult to quantify, but reproducibility is typically plus or minus ten per cent.

5.3.2 Results

Impeller Discharge

The coordinate system is shown in Figure 5.2. Measurements in the impeller discharge region (3 mm from blade) showed that magnitudes of axial (U) and tangential (W) velocities increase almost linearly along the blade before peaking near the blade edge (Figure 5.3). Radial velocity (V) is lower and passes through a maximum near the blade centre before dropping towards the axis and the blade edge. Very near the axis, the axial velocity component becomes negative, i.e. there is upward flow into the impeller discharge. This is related to a weak secondary circulation loop directly beneath the impeller.

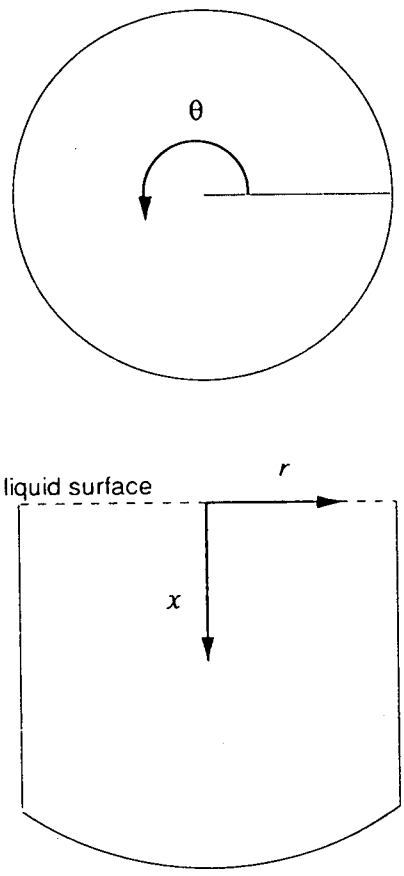

Figure 5.2 Coordinate system for stirred tank calculations

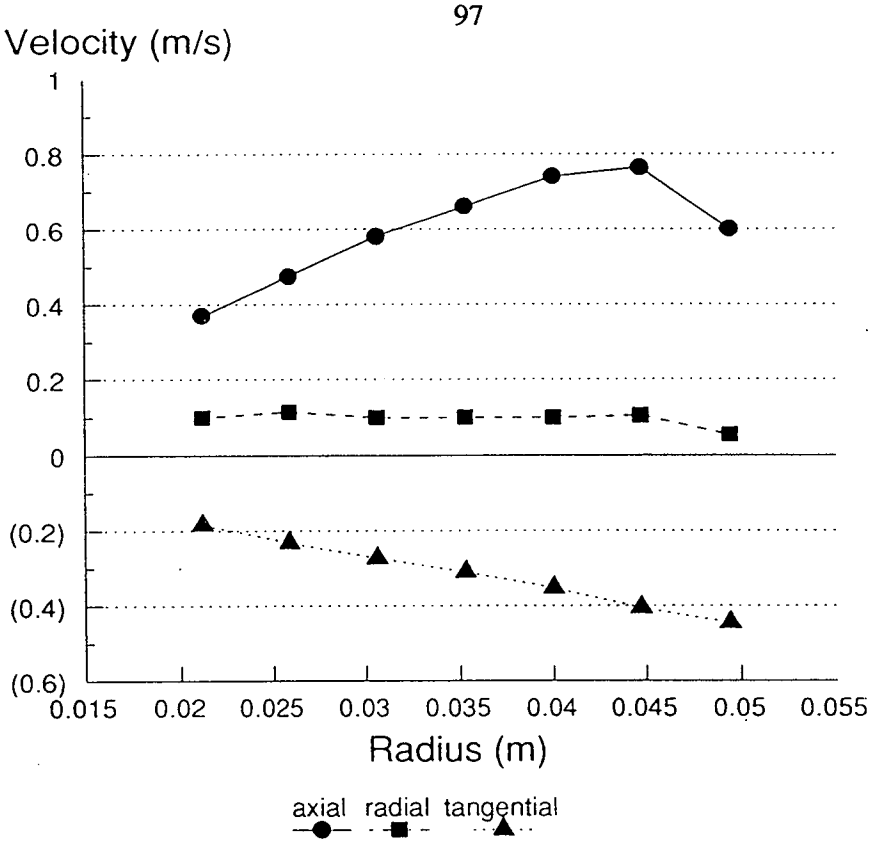

Figure 5.3 Average velocities in the impeller discharge

Root mean squared fluctuating velocities are approximately constant near the axis and increase towards the blade edge (Figure 5.4). Axial fluctuations (u) pass through a minimum also observed by Bakker (1992) for a six-bladed pitched blade impeller and by Musgrove (1992) for several other axial flow impellers. This could be related to turbulence generated by flow past the impeller hub. Radial fluctuations (v) in general exceed tangential (w) and axial fluctuations, except near the shaft, where axial values are higher. Large gradients in turbulence levels exist near the blade edge, where low-turbulence fluid is entrained into the impeller stream from the bulk.

It was not possible to directly measure the turbulent energy dissipation rate, ε. This consists of average spatial gradients of fluctuating velocity (see Chapter 2) and there is currently no fully satisfactory measurement technique. Here, it was estimated based on the turbulent kinetic energy and the integral length scale of the velocity fluctuations near the impeller (Wu & Patterson, 1989):

$$\varepsilon = A \frac{k^{3/2}}{l_e} \tag{5.3.1}$$

The constant A was taken as 1.0 and the eddy size half the projected blade width (Wu & Patterson, 1989). The resulting profile of ε in the impeller discharge is qualitatively similar to that of k, with a peak near the blade edge (Figure 5.5). The maximum value is in the region of 10 W/kg, compared to an average power dissipation level for the tank of 0.09 W/kg. This underlines the inhomogeneity of the turbulence in parts of the vessel.

Impeller suction

On the following summary plots, dashed lines indicate the measuring positions and zeros for each profile and the downward direction is positive. More detailed plots are given in Appendix D. The solid line denotes the indicated fraction of the impeller tip speed:

$$V_{TIP} = \pi ND \tag{5.3.2}$$

Measurements in the impeller suction were conducted to guide and assess subsequent modelling of the internal impeller region. Axial velocities (Figure 5.6) on the upper surface have a qualitatively similar but flatter profile compared to the discharge surface. Radial velocities on the suction side are positive (outward) near the shaft and negative (inward) near the blade edge. Tangential velocities are near zero on the suction side.

Root mean squared fluctuating velocities are substantial in the impeller suction, of order 30% of the discharge values (Figure 5.7). These are quite characteristic of bulk values in the upper part of the tank which are approximately homogeneous (independent of position) and isotropic (equal normal and zero shear components). This indicates that turbulence generation and dissipation are in balance in the bulk of the vessel, and out of balance primarily in the impeller discharge. The largest fluctuations in the suction are tangential, followed by axial, then radial. This is the reverse of the trend in the impeller discharge.

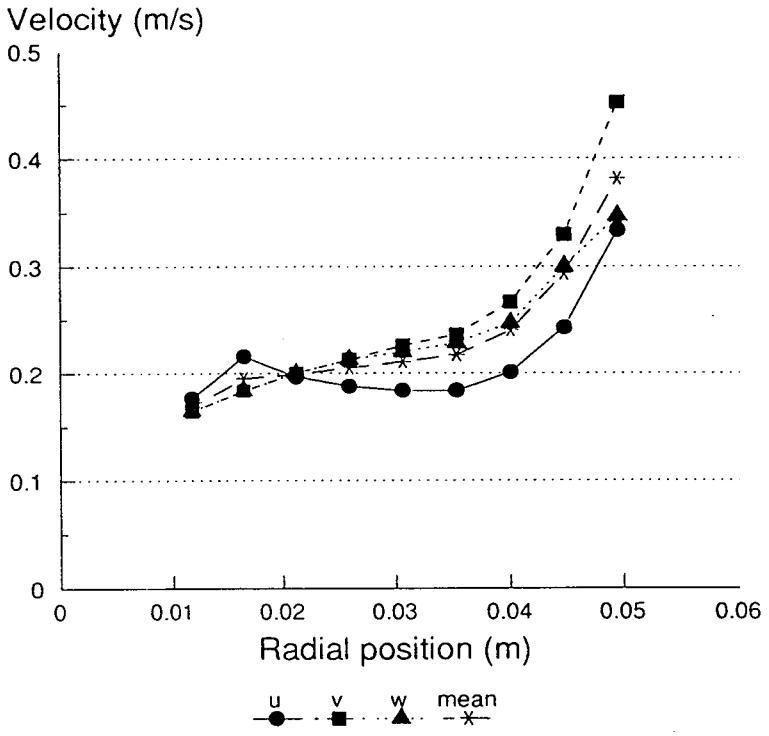

Figure 5.4 Fluctuating velocities in the impeller discharge

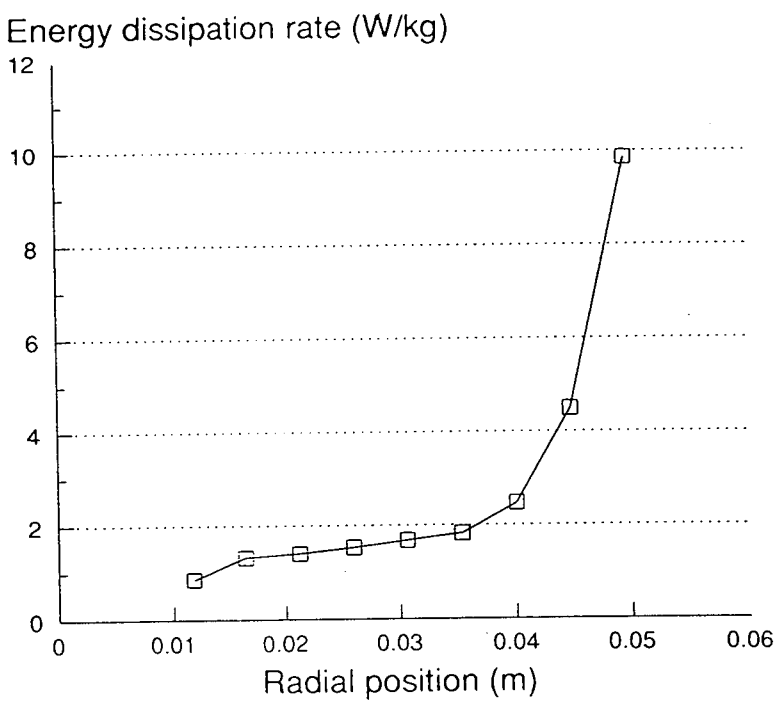

Figure 5.5 Estimated turbulent energy dissipation rate ε in the impeller discharge

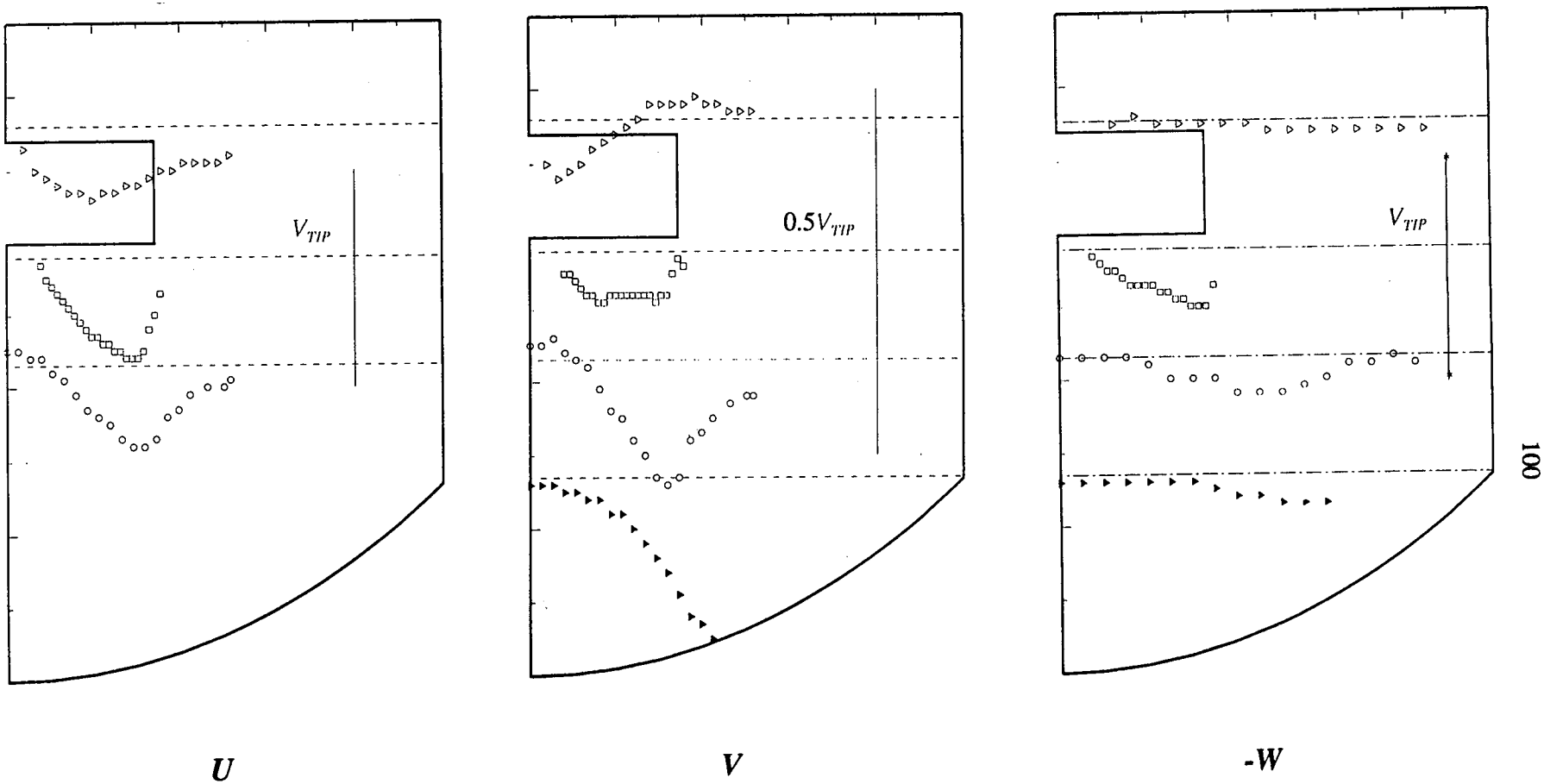

Figure 5.6 Average velocities in the impeller stream

The downward direction is positive. For more details, see Appendix D.

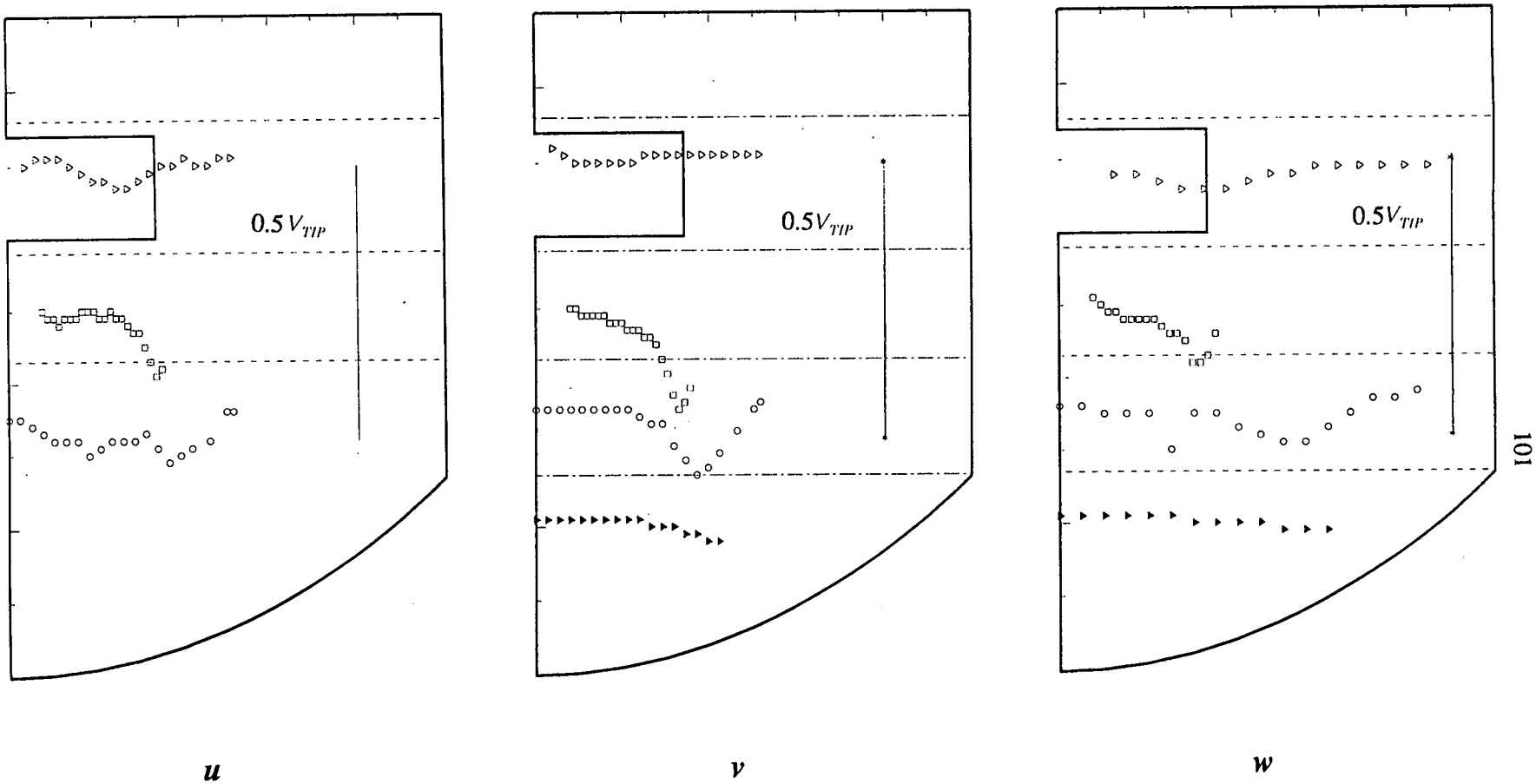

Figure 5.7 Fluctuating velocities in the impeller stream
For more details, see Appendix D.

Impeller stream and bulk of vessel

Below the impeller, there is a small region of recirculation indicated by negative (upward) axial velocities. Swirl velocities in this region are constant, indicating a free vortex with highest angular velocity along its axis. This flow structure can be experimentally observed using solid particles for flow visualisation. When these are denser than the liquid, they accumulate in the vortex and are occasionally picked up by the swirling upflow. In this region, the largest fluctuations are axial. Tangential and radial fluctuations appear to be independent of radial position inside the vortex.

Radial mean velocities inside the vortex are close to zero. Outside it, radial velocities initially increase linearly with radius before decreasing as the flow turns along the base into the main circulation loop. In the upper part of the tank, axial, radial and tangential velocities are relatively low. For more details, see Appendix D.

Below the impeller for a distance of approximately one impeller radius, turbulence inhomogeneity remains high. Thereafter, only relatively weak inhomogeneities exist.

5.4 FLOW FIELD PREDICTIONS

FLOW3D Version 2.4 was used for all the simulations which follow. The flow field was predicted using different sets of boundary conditions, turbulence models, grids and numerical parameters. Early simulations focused on the case with no baffle-wall spacing. Based on the results of these, suitable grids and turbulence models were established. Later, a baffle-wall spacing was simulated, for direct comparison with experimental data.

5.4.1 Boundary conditions

Impeller

The impeller, which drives the flow, currently requires empirical modelling (see Section 5.3.1). There are several possible approaches (Figure 5.8), including:

Model 1. Specify boundary conditions measured by LDA on the discharge surface. Solve conservation equations inside the impeller volume.

Model 2. Specify boundary conditions on all surfaces of the impeller. Do not solve conservation equations inside the impeller volume.

Model 3. Specify sources in the momentum equations inside the impeller zone.

Model 4. Model the impeller as a rotating solid-body, with all parameters taking on their measured discharge values.

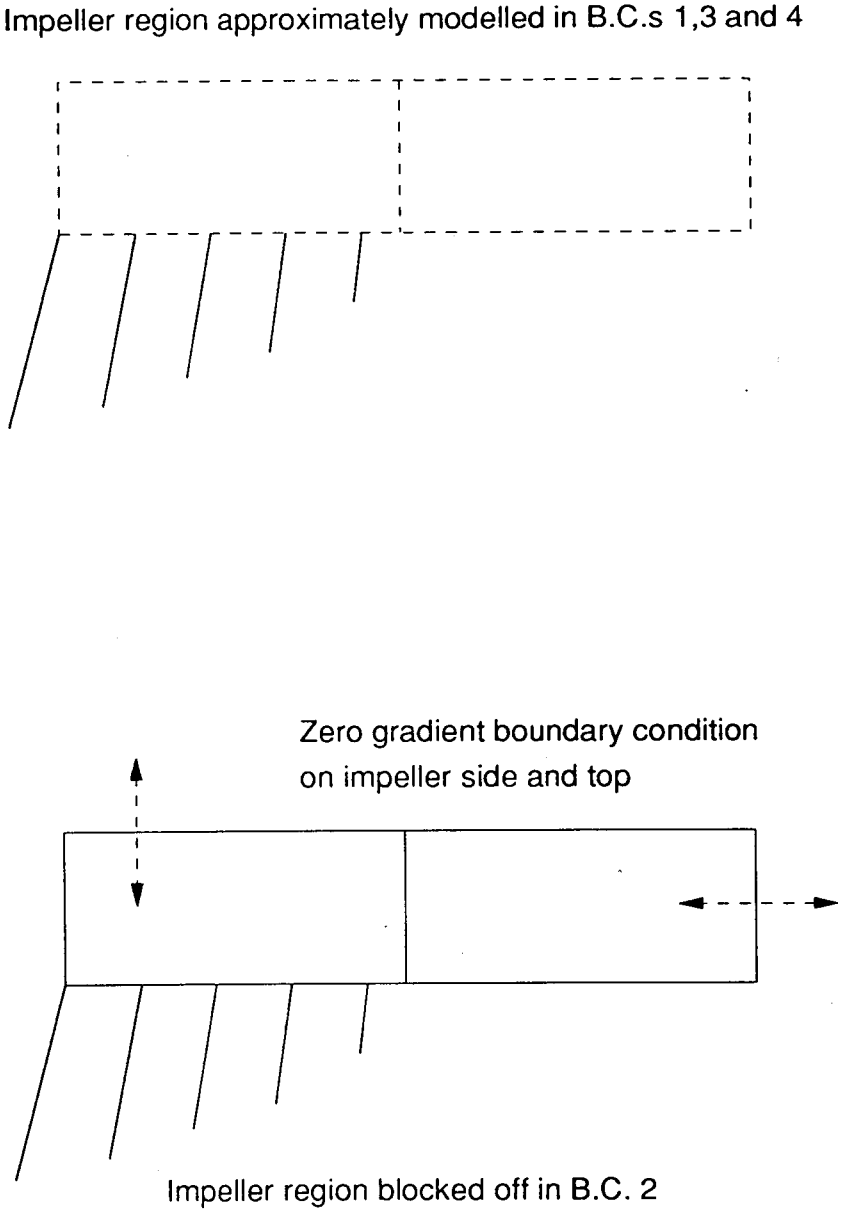

Figure 5.8 Schematic of types of approximate impeller boundary conditions

Model 2 was used in much of what follows, whereby measured LDA data (ie, three components of mean velocity, three components of turbulent normal stress and two turbulent shear stresses) were applied on the bottom discharge surface and zero gradient conditions on all variables were imposed on the side and top surfaces. The latter have the advantage of being a relatively "neutral" boundary condition, and do not fix the flow direction. Zero-gradient conditions are often applied to "outlets" from flow boundaries, and correspond to "fully developed" flow. The principal virtue of this boundary condition is that it requires relatively little input data. Fully developed conditions are not realised in practice for either the sides or top of the impeller volume, so this adds to the other approximations inherent in the current approach. Model 2 is only useful for calculation of flow patterns; if reactions are to be calculated, flow within the confines of the impeller must also be modelled.

Model 3 is potentially useful if the momentum and turbulence produced by the impeller can be quantitatively related to blade size and shape. There have been some approaches to this problem (e.g. Pericleous & Patel, 1987), but accuracy is unlikely to be as good as with LDA data.

Model 1 was used for the chemical reaction calculations presented in Section 5.8 and has previously been employed by Bakker (1992) and Ranade et al. (1989), among others. This combines the advantages of LDA data with a method for calculating the flow inside the impeller in an approximate way. Model 4 also fits this requirement.

Models 1 and 2 both require additional inputs for the turbulence equations. k was calculated directly from the root mean squared velocity fluctuations in the three coordinate directions and ε from equation 5.3.1 above.

When using the DSM, it is possible to specify all six Reynolds stresses (three normal, three shear) separately. Two possibilities exist for inputting these:

1. Only k is input and the normal stresses assumed equal and obtained from k. The shear stresses are then assumed to be either zero (boundary condition 2) or are calculated by the model (boundary condition 1).

2. All six Reynolds stresses are input directly. Five of these were available in this work from LDA measurements.

Predictions were quite insensitive to which of these options was selected. Consequently option 1 was used, for simplicity.

Baffles & Walls

The simplest model of the baffles is to treat the flow as axi-symmetric. This damps out all flow in the tangential direction, which corresponds to infinite baffling, and makes the calculations two-dimensional. However, it is not a good representation of the real situation, which is strongly three-dimensional.

In this work, the baffle is modelled as a thin plate in a three-dimensional flow domain. Wall laws are used to represent viscous damping of the turbulence very near the plate. Simulations with zero and $T/60$ baffle-wall spacing were made, which produced significant differences in flow behaviour (see Section 5.5.3). Because the impeller is treated as an axi-symmetric boundary condition and there are four baffles, it is only necessary to model one quadrant of the tank in order to calculate the flow field.

Other solid regions, such as the tank wall, base and the impeller shaft were also modelled using wall laws.

Free Surface

The liquid surface was assumed to be perfectly flat, which corresponds to a zero-gradient boundary condition for velocities parallel to the surface and all scalar quantities (e.g. k and ε), and zero flow normal to the surface. While this is an approximation, it is the intention of baffling to produce a flat surface and experimental observations suggested that this was approximately the case. At much higher impeller speeds than those used here, substantial surface disturbances would have occurred.

The shape of the liquid surface does not normally exert a strong influence on mixing in stirred tanks, but when reactants are added at the surface, the velocity vectors there can determine the initial trajectory taken. Simulations of the surface region with k-ε and Differential Stress model are compared in this light below.

5.4.2 Grid-dependence & differencing schemes

When trying to distinguish between different physical or mathematical models, it is essential for purely numerical effects to be absent from the solution. In CFD, this means testing the sensitivity of predictions to changes in grid size and other numerical parameters. In the present study, grids of 6,000 (30 axially x 20 radially x 10 tangentially), 24,000 (40 x 30 x 20) and 39,000 (50 x 30 x 26) cells were used with the k-ε model and 24,000 and 39,000 with the Differential Stress model.

All of the flow field computations used FLOW3D Version 2.4 on a Silicon Graphics 210 Server. k-ε calculations typically required 1000 iterations and DSM 3000 iterations to converge. The convergence criterion was a mass source residual of 10^{-5} times the impeller discharge flowrate and steady values of all variables. The longest run-time was 52 hours for 2000 iterations of a 39,000 cell DSM simulation.

The 24,000 cell grid is shown in Figure 5.9. A uniform fine grid was placed across the impeller discharge. Outside the impeller, the grid was made progressively coarser. Refinement in the axial direction was from the surface and the base towards the impeller, where the largest gradients were expected. In the tangential direction, cells were smallest near the baffle, in order to resolve recirculation patterns. One quadrant of the tank was modelled, with periodic boundary conditions on the first and last tangential planes.

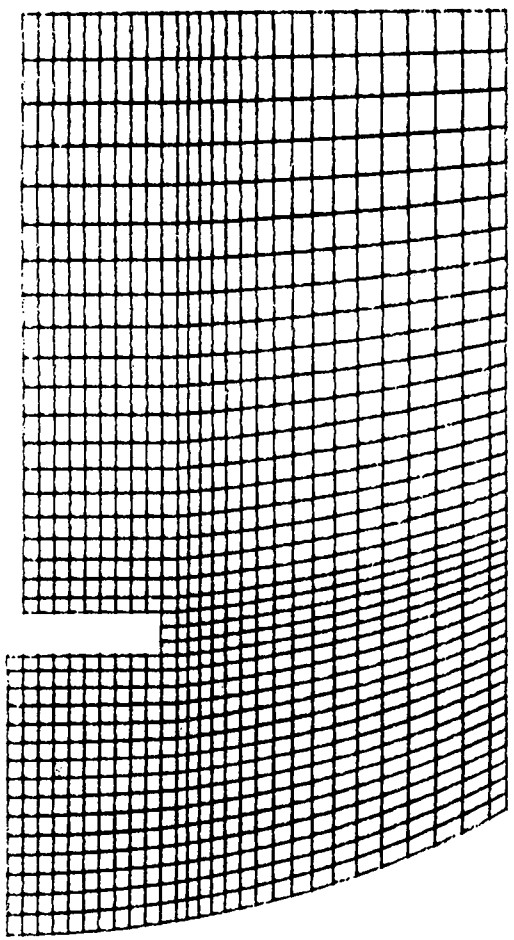

a) Vertical slice showing refinement towards the impeller

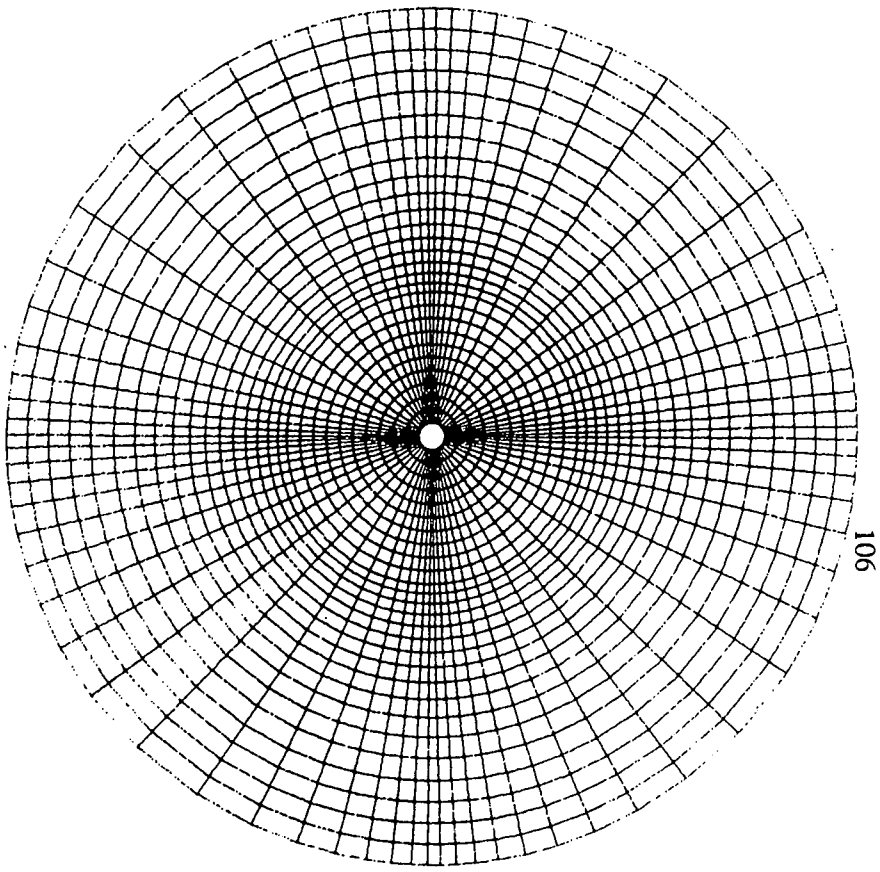

b) Horizontal slice showing refinement near the baffles. To calculate the flow field, it is sufficient to simulate one quadrant.

Figure 5.9 24,000 cell computational grid used for flow field calculations

Grid sensitivity with the DSM is shown quantitatively for mean and turbulent quantities in Figures 5.10 and 5.11 (no baffle-wall spacing). For both turbulence models, essentially grid-independent solutions were obtained with 24,000 cells. This result was the same irrespective of whether UPWIND, Higher UPWIND or CCCT differencing schemes were used for the k-ε model. For the DSM, it was difficult to obtain convergence using any scheme other than UPWIND and only UPWIND results have been included. Implications are discussed in Sections 5.8 and 5.9.

5.4.3 Turbulence model

Initial simulations used the k-ε model. Velocity vectors in the vertical section (x-r plane) between baffles (θ=0 or 90 degrees) and in the horizontal section (r-θ plane) near the liquid surface (x/T=0.025) are shown in Figure 5.12 for a tank with no baffle-wall spacing. Shading indicates flow into the page (i.e. swirl in the opposite direction to impeller rotation, or downflow). The shaded area near the impeller shaft in the vertical section is in error. This is illustrated clearly in the horizontal section where the vectors are unrealistic. Similar findings have been reported previously with this model (Middleton et al., 1986; Ranade et al., 1989). Other smaller errors include failure to predict downflow and recirculation just downstream of the baffle near the liquid surface (Bakker, 1992).

Velocity vectors predicted for this case using the DSM are shown in Figure 5.13. These reproduce the features of the flow observed in practice, particularly the correct swirl direction near the impeller shaft.

When there is no baffle-wall spacing, strong vortical structures exist near the baffle plates. Downstream of the baffle, at θ=44 degrees, a small vortex develops in the impeller plane and rises along the inside of the baffle before moving back into the bulk of the tank a short distance from the liquid surface. Above this point, a weak secondary flow develops which produces downflow at the baffle. This effect was seen by Bakker (1992) in ASM simulations of a tank with a flat bottom and validated by velocity measurements. Qualitatively similar results were obtained by Bolour-Froushan (1986) for a Rushton turbine simulated with a k-ε model modified for swirling flows.

Upstream of the baffle, at θ=46 degrees, some similar, weaker vortex structures appear, but there is no longer any downflow near the liquid surface. Sections across the vessel at various positions are shown in Figure 5.14. In these pictures, shading again indicates flow into the page (i.e. downward axial velocity). Near the liquid surface there is vortex motion near the shaft and four strong vortices, one behind each baffle. These vortices are predominantly in downflow, suggesting that they might usefully be employed for incorporation of additives or powders through the liquid surface. They persist downward into the vessel before reducing in strength and being carried into the bulk. In the impeller discharge plane, the upward flowing vortices referred to in the last paragraph are just starting to develop. Near the bottom of the tank, there is a vortex near the axis but none near the walls, as the baffles do not protrude into the dished bottom.

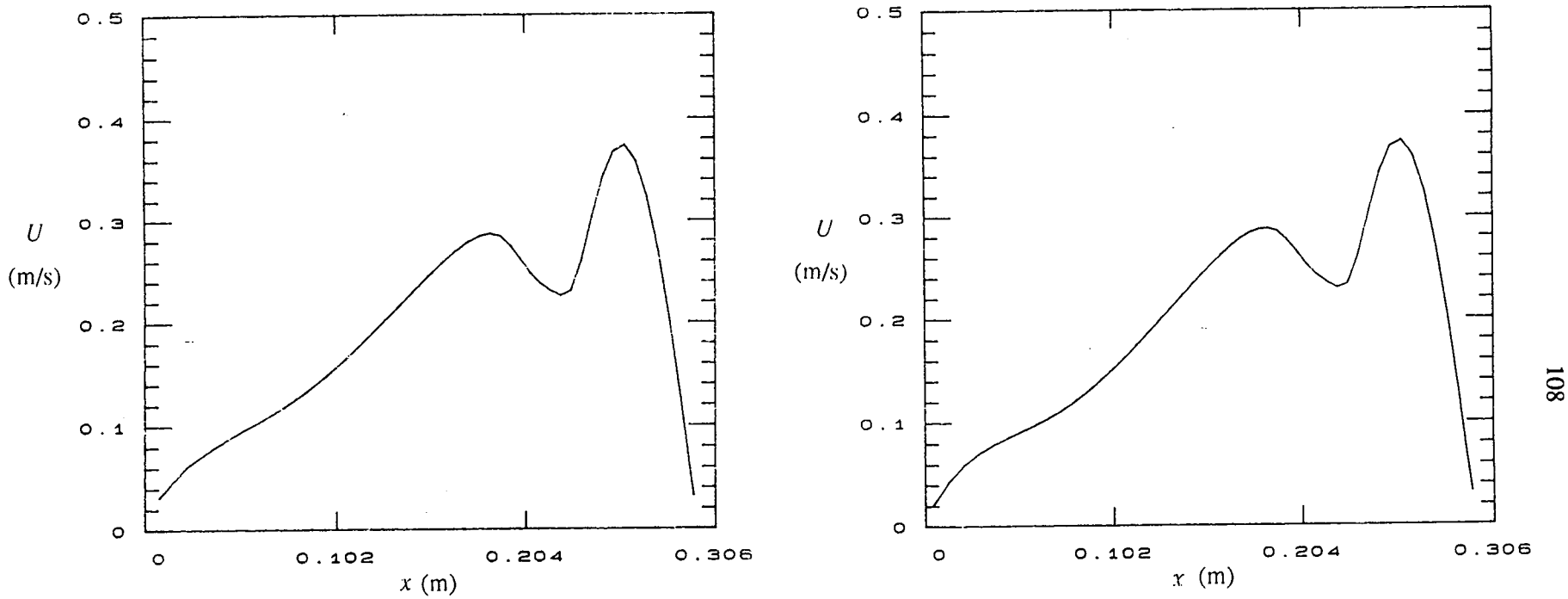

Figure 5.10 Grid sensitivity of average axial velocity at r=64 mm:

DSM turbulence model, no baffle-wall spacing, comparison between 24,000 (left) and 39,000 (right) cells

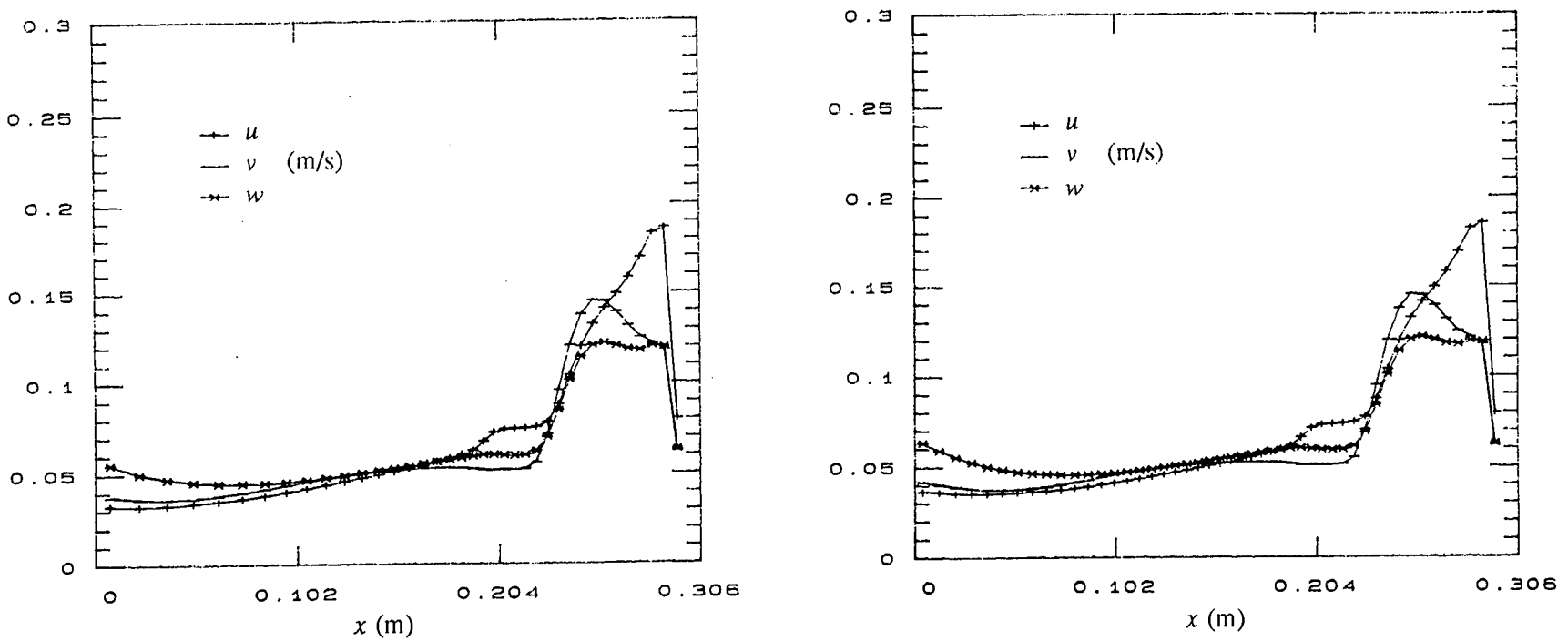

Figure 5.11 Grid sensitivity of fluctuating velocities at r=64 mm:

DSM turbulence model, no baffle-wall spacing, comparison between 24,000 (left) and 39,000 (right) cells

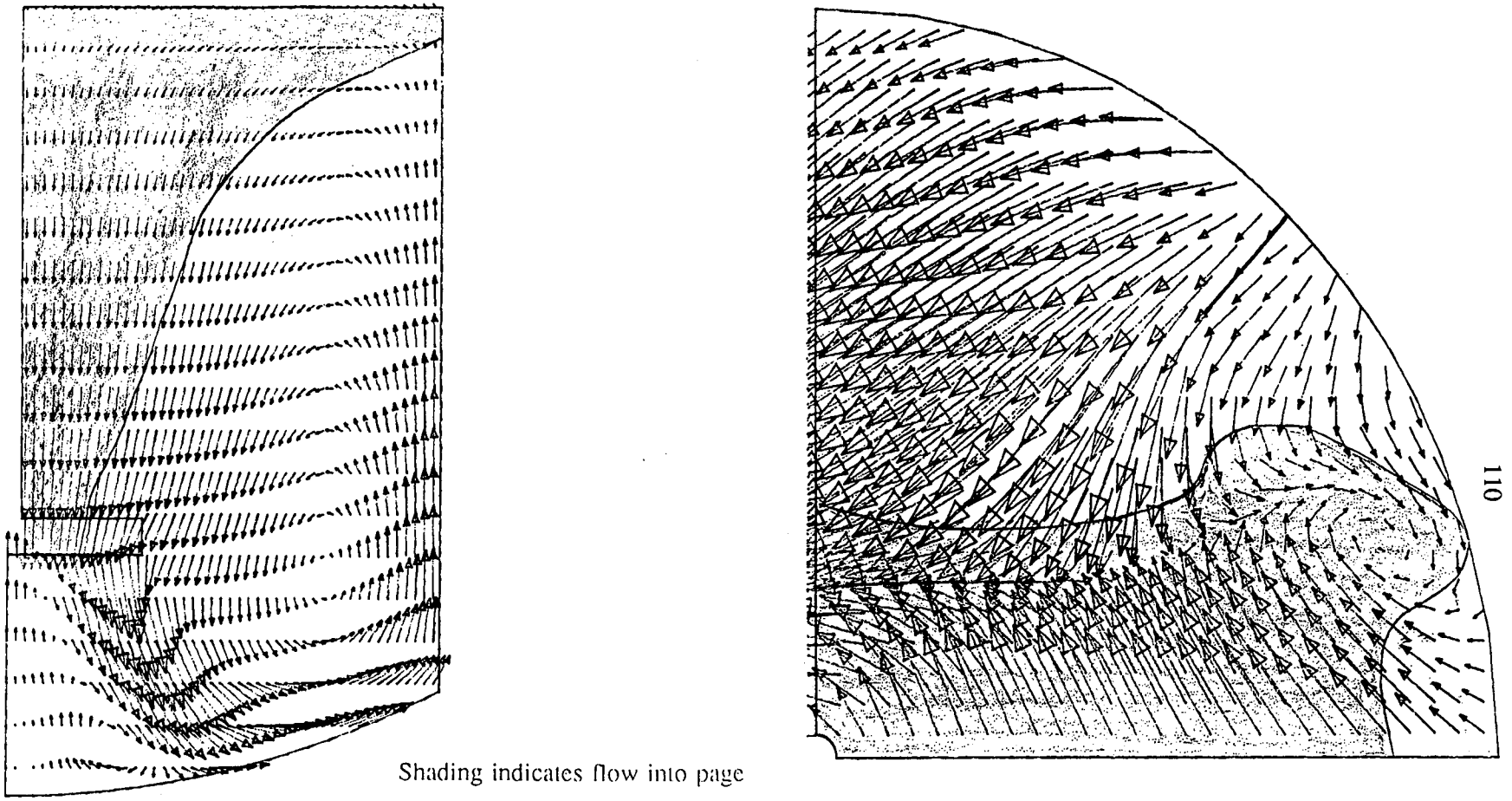

Figure 5.12 Predicted k-ε velocity vectors in a vertical slice between baffles (θ=0 degrees) and in a horizontal slice at x/T =0.025. No baffle-wall spacing

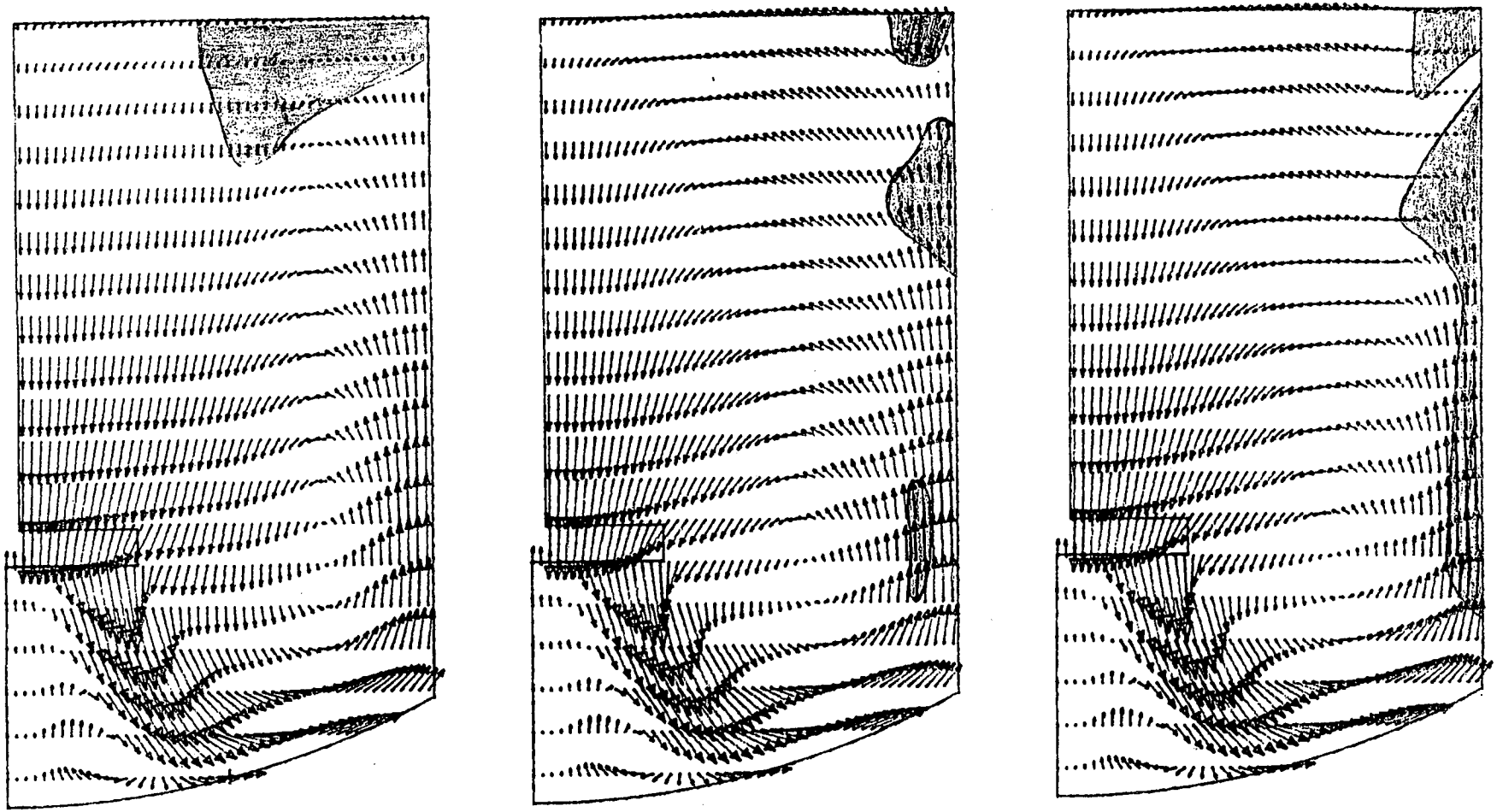

Figure 5.13 Predicted DSM velocity vectors in vertical slices at θ=0 degrees (between baffles), 46 (upstream of baffle) and 44 (downstream of baffle). No baffle-wall spacing

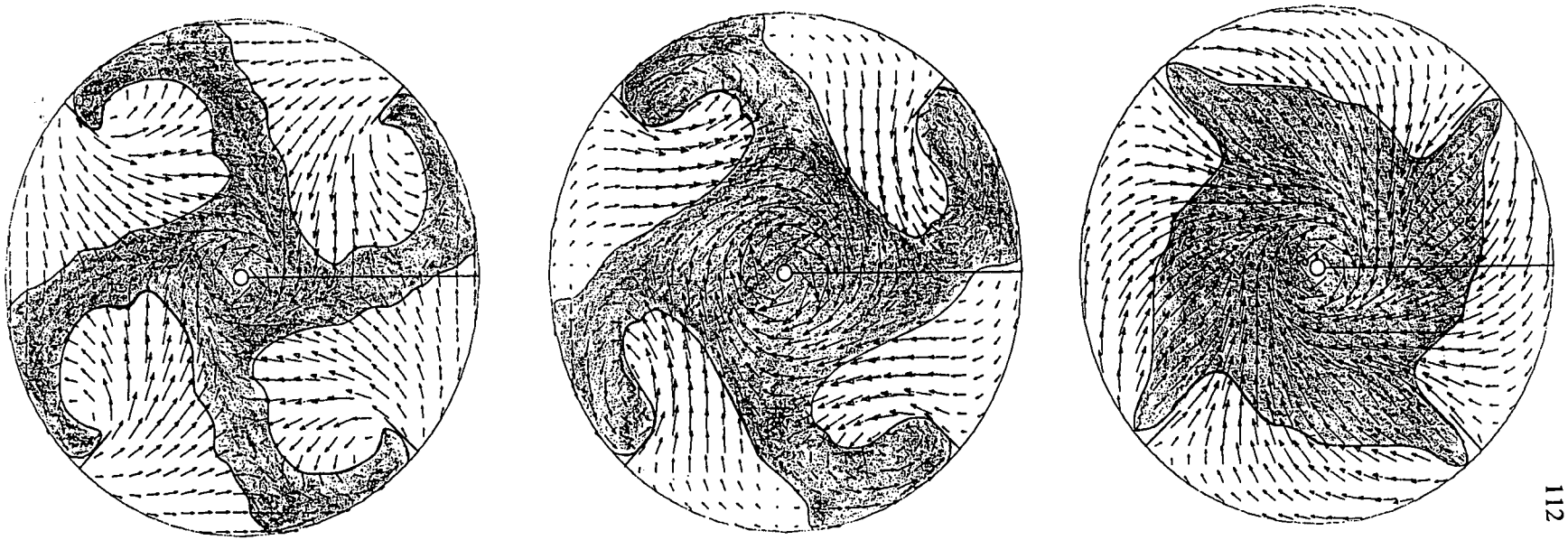

Shading indicates flow into page

Figure 5.14 Predicted DSM velocity vectors in horizontal slices at x/T=0.025, 0.167 and 0.51. No baffle-wall spacing

While these specific results without a baffle-wall spacing have not been quantitatively validated in this study, they strongly suggest that the DSM will predict stirred tank flow patterns more successfully than the k-ε model. This is examined in the next section for the case where there is a small (T/60) baffle-wall spacing, which corresponded to the geometry where LDA measurements were made.

5.5 FLOW FIELD VALIDATION

In what follows, simulations are tested using two methods, which can be described as "Integral" and "Point" Validation.

Integral validation is a global assessment. It describes qualitative measures such as intuitive judgement of flow patterns and some quantitative methods such as calculation of particle trajectories, mixing times, impeller power consumption and chemical reaction yield from simulations. An advantage of integral validation is that it can be directly related to some process result of practical interest. A disadvantage is that it tests the model as a whole and is unable to distinguish weak points in sub-models.

Point validation is more stringent, comparing predicted point values of primitive quantities (such as velocity, concentration) with experimental measurements. It can pinpoint parts of the model requiring improvement.

DSM simulations with 24,000 cells using UPWIND differencing are now compared in detail with LDA measurements. These simulations employed boundary condition 2 for the impeller.

5.5.1 Integral Validation

Predicted velocity vectors in three x-r planes are shown in Figure 5.15. At θ=0 (or 90) degrees, i.e. at the mid-point between baffles, the flow pattern consists of one large circulation loop, with a small secondary flow beneath the impeller. At θ=46 degrees, upstream of the baffle, the flow patterns are similar to 0 degrees except that the downflow region in the upper part of the vessel has a smaller diameter. There is a very small region of recirculation upstream of the baffle plate near the liquid surface. This is also in downflow.

Just downstream of the baffle, at θ=44 degrees, there is a slightly larger downflow secondary loop near the liquid surface. Otherwise, the flow patterns are similar to upstream of the baffle.

r-θ vectors predicted by the DSM are shown in Figure 5.16 at three axial positions. Near the liquid surface, flow is mainly in the same direction as impeller rotation, with weak recirculation downstream of the baffle plates. Most of the velocity vectors around the tank wall are in the same direction as impeller rotation. Strong vortex motion near the impeller shaft is evident. Upflow dominates over most of the liquid surface, both in front of and behind baffles. Downflow towards the walls is primarily in the mid-planes between baffles, extending to all planes as the impeller shaft is approached.

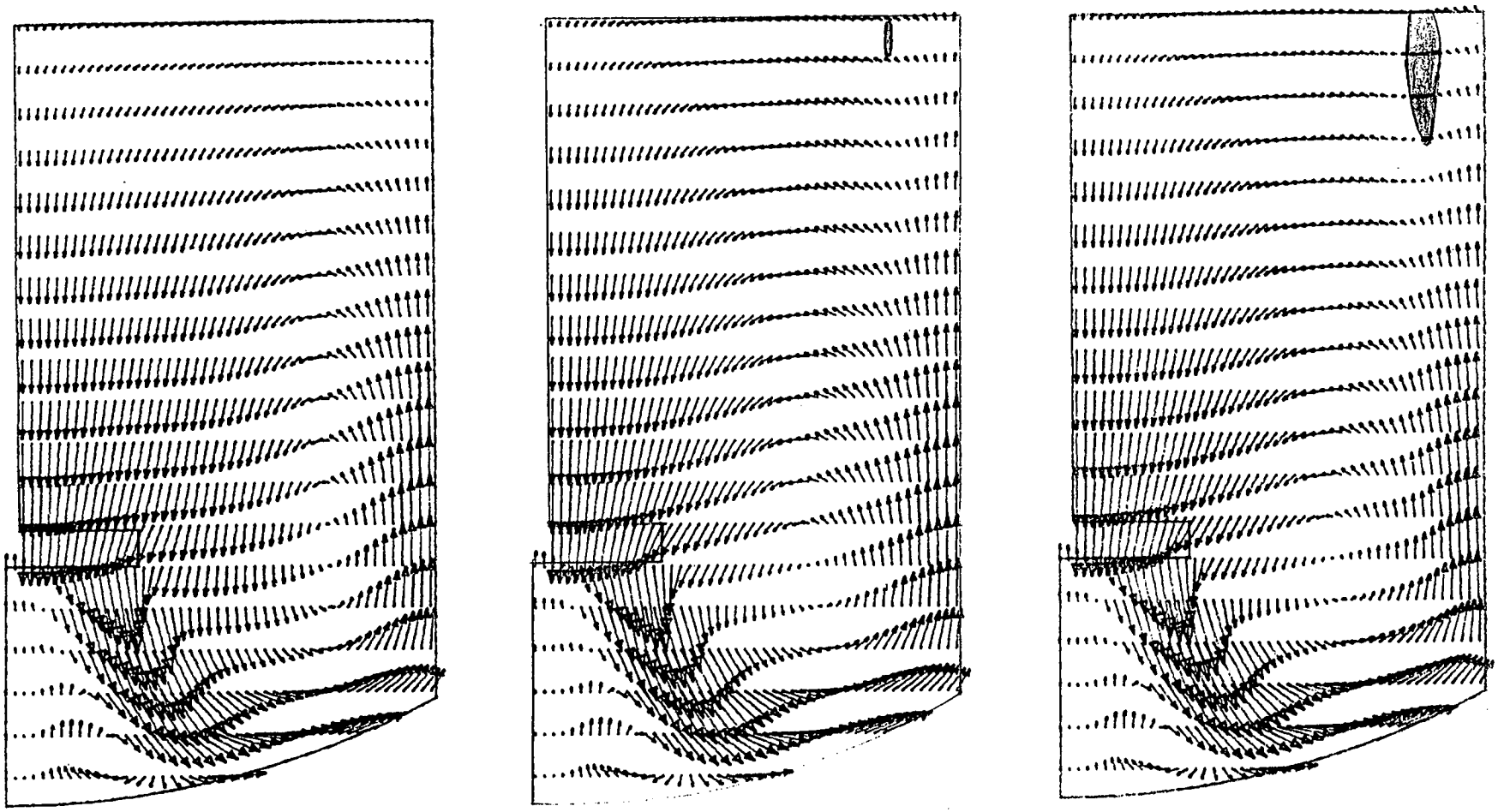

Figure 5.15 Predicted DSM velocity vectors in vertical slices at θ=0 degrees (between baffles), 46 (upstream of baffle) and 44 (downstream of baffle). *T*/60 baffle-wall spacing

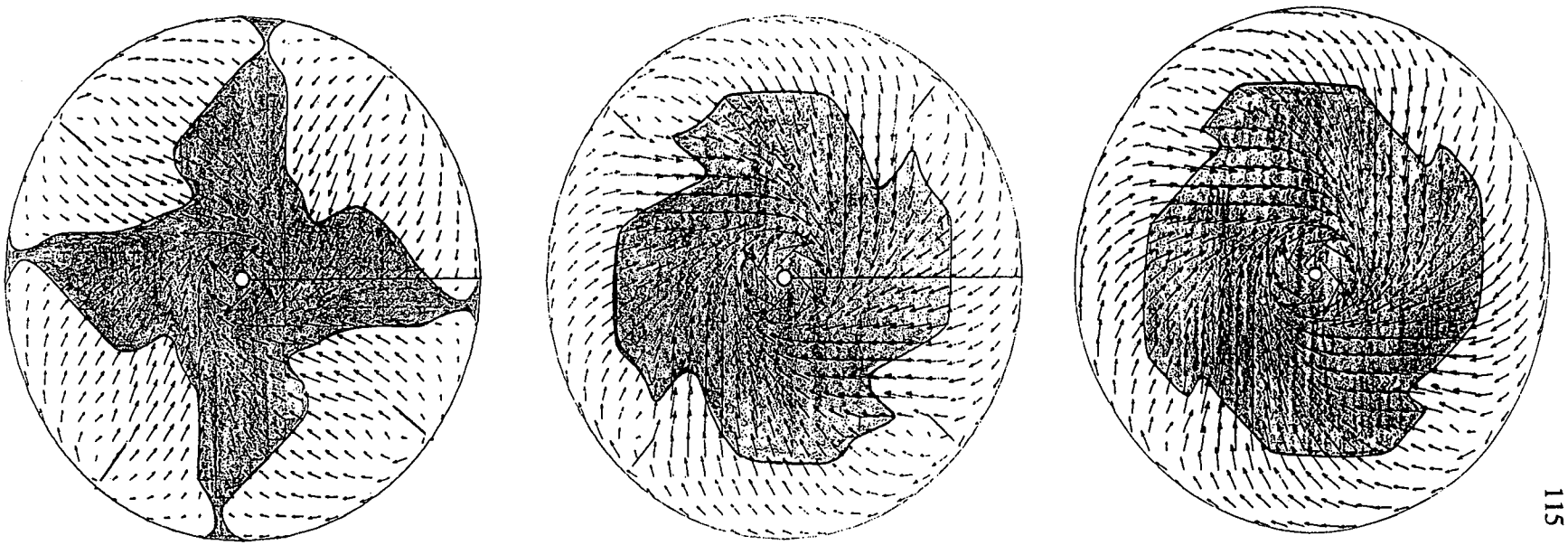

Shading indicates flow into page

Figure 5.16 Predicted DSM velocity vectors in horizontal slices at x/T=0.025 0.167 and 0.51. T/60 baffle-wall spacing

Beneath the liquid surface, at x/T=0.167, the flow pattern has changed significantly from that on the liquid surface. Now all vectors along the circumference are in the same sense as the impeller rotation. The downflow region has become more symmetric about the shaft. Very slight downflow is evident downstream of baffle plates. The pattern is similar at x/T=0.51. While the baffles evidently affect the flow pattern by reducing its swirl component near the walls, their influence is not sufficient to produce reversed flow.

Near the bottom of the tank (x/T=0.9), the flow is primarily axial and radial, except for a small region of secondary flow directly beneath the impeller. Existence of this region is confirmed by the LDA measurements above; visualisation experiments using solid particles also demonstrated this effect.

Power consumption can be calculated from CFD simulations by different methods. Some of these are reviewed by Ziman (1990) who derived a calculation method based on impeller torque. This was obtained also by Mahouast et al. (1989). Here, power has been calculated by two methods:

Method 1

$$P_\varepsilon = \int_V \varrho\, \varepsilon \, dV \tag{5.5.1}$$

Method 2

$$P_M = \int_{S_j} r \left(\varrho\, U_j\, U_\theta + \varrho\, \overline{u_j\, u_\theta} \right) dS_j \tag{5.5.2}$$

Method 1 is a volume-integrated turbulent energy dissipation rate, which in a highly turbulent flow, should approximate the impeller power input. This neglects the presumably small influence of direct dissipation due to mean velocity gradients.

Method 2 is based on a torque balance on any surface enclosing the impeller but no additional momentum sources. This method is more exact, as it accounts for both mean flow and turbulent energy input. As written above, it neglects the contribution of viscous shear, which would become significant very near the tank walls. For surfaces near the impeller, the omitted term is negligible.

Power calculations by the two methods from the above simulations are presented in Table 5.2. The power consumption obtained from torque measurements on the physical model was 1.88 W. Both methods underpredict power consumption but agreement for Method 2 is better than Method 1.

As described below, the present simulations underpredict turbulence levels (and turbulent dissipation) so that Method 1 would not be expected to give good agreement. This weakness in the model will affect predictions of turbulence-dominated processes such as micromixing. Disagreement for method 2 is also linked to poor turbulence predictions.

Power calculations are also presented in Table 5.2 for the case with no baffle-wall spacing and predict an increase of about 7% relative to the standard configuration. This is caused by a decreased level of momentum in the impeller suction, due to additional drag in the baffle region. Empirical predictions of the effect of the baffle-wall spacing suggest an increased power draw of about 10%. This trend is quite well predicted.

Table 5.2 Power calculations from simulations

	T/60 spacing	No spacing
P_ε	1.0 W	1.0 W
P_M	1.48 W	1.58 W
Actual	1.88 W	2.07 W

5.5.2 Point validation

Radial profiles

Simulations and LDA data are quantitatively compared in Figure 5.17, which shows the axial, radial and tangential mean velocities at various axial positions. Further details of the magnitudes of all velocities are given in Appendix D. Agreement between model and experiments is very reasonable, but there are detailed differences.

In the impeller suction (x=0.19 m), axial velocities are reasonably predicted, which is expected since the predominant motion is axial and mass conservation must be satisfied between the suction and discharge sides of the impeller. Near the shaft, the model expects the axial velocity to remain approximately constant, whereas measurements show that it is reduced. Measured radial velocities showed outflow near the shaft and inflow near the blade edge. Simulations predict inflow across the entire blade length. Tangential velocities in the suction are small and simulations agree reasonably with experiments. For more details, see Appendix D.

Results for the impeller discharge (x=0.216 m) are not used for validation as the LDA measurements formed boundary conditions for the CFD model. Below the impeller, at x=0.238 m the model slightly underpredicts the strength of upflow near the axis and the peak in axial velocity below the impeller blade edge. Radial velocities along the axis and below the blade edge are also underpredicted by the model and the agreement appears to worsen moving radially into the bulk liquid. Significantly, the radial gradients of radial velocity, which contribute to turbulence generation, are also underpredicted. Tangential velocities are overpredicted by 50-100% in some places beneath the impeller and appear to be underpredicted in the bulk of the tank base.

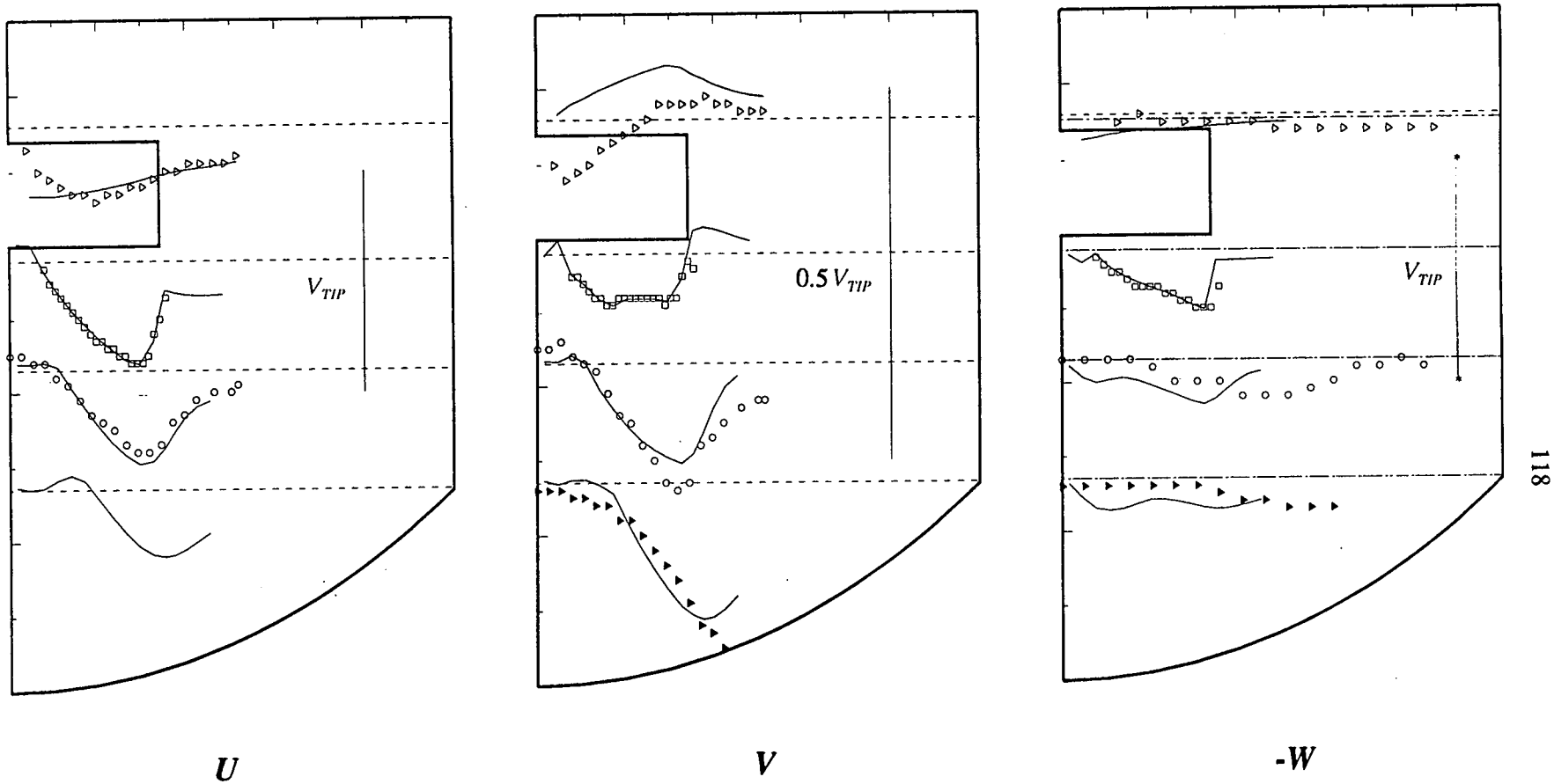

Figure 5.17 DSM predictions compared to LDA measurements in the impeller stream.

Axial, radial and tangential average velocities. Dashed lines indicate measuring position and zero for curves (DSM) and points (LDA). Bars indicate impeller tip speed. The downward direction is positive.
For more details, see Appendix D.

At x=0.263 m, the shape of the impeller discharge is incorrect because measurements show a monotonic increase in radial velocity from the axis outward, whereas simulations produced a maximum velocity just outside the blade edge. Tangential velocities show the same trend as at x=0.238 m in the vortex region but agreement appears to improve moving radially outwards.

At all axial positions apart from the impeller discharge (boundary condition), the root mean squared fluctuating velocities are under-predicted by the simulations (Figure 5.18), as are their spatial gradients. This is characteristic of simulations using UPWIND differencing, which tends to smooth out spatial gradients. A similar effect on average velocity gradients causes turbulence generation rates and hence prevailing turbulence levels to be under-predicted. These results are consistent with those of Bakker (1992) and are discussed further in Section 5.9.1.

Simulations also predict a more rapid and greater decay of fluctuations away from the impeller discharge. Errors below the impeller are of order 25-50% and appear to reduce as the base is approached. In the impeller suction, all predicted fluctuations are approximately equal, below the impeller the radial fluctuations temporarily exceed the others and in the base the axial fluctuations are highest. These qualitative observations are in accord with LDA data.

Boundary condition 1 was used to simulate the same vessel and operating conditions as above and results compared with boundary condition 2. Apart from a very slightly improved prediction of axial velocity profiles, there were no significant differences between traverses for the two cases.

Axial profiles

The main axial profile of interest is at r=64 mm. This traverse passes from the top to the bottom of the tank and near the impeller shaft. It passes through the region where the k-ε model failed to predict the correct swirl direction (Figure 5.11).

Measurements of mean velocities are compared with simulations in Figure 5.19. A few measurements were also made along the impeller side. Axial velocities along these traverses agree quantitatively very well with measurements from the mid-height of the vessel to the bottom of the impeller. Elsewhere, agreement is less quantitative, with largest errors where velocities are lowest. Similar remarks apply to both radial and tangential velocities. Greater detail is available in Appendix D.

The most significant result is that the tangential velocity retains the correct sign for the entire height of the vessel, including the region above the impeller where the k-ε model fails. Agreement is excellent for this component all the way to the liquid surface, which is heartening in view of the flat surface boundary condition assumed. This is often regarded as a poor approximation (e.g. Launder, 1989) when surface effects are to be predicted in great detail, but it appears sufficiently accurate for the present purposes.

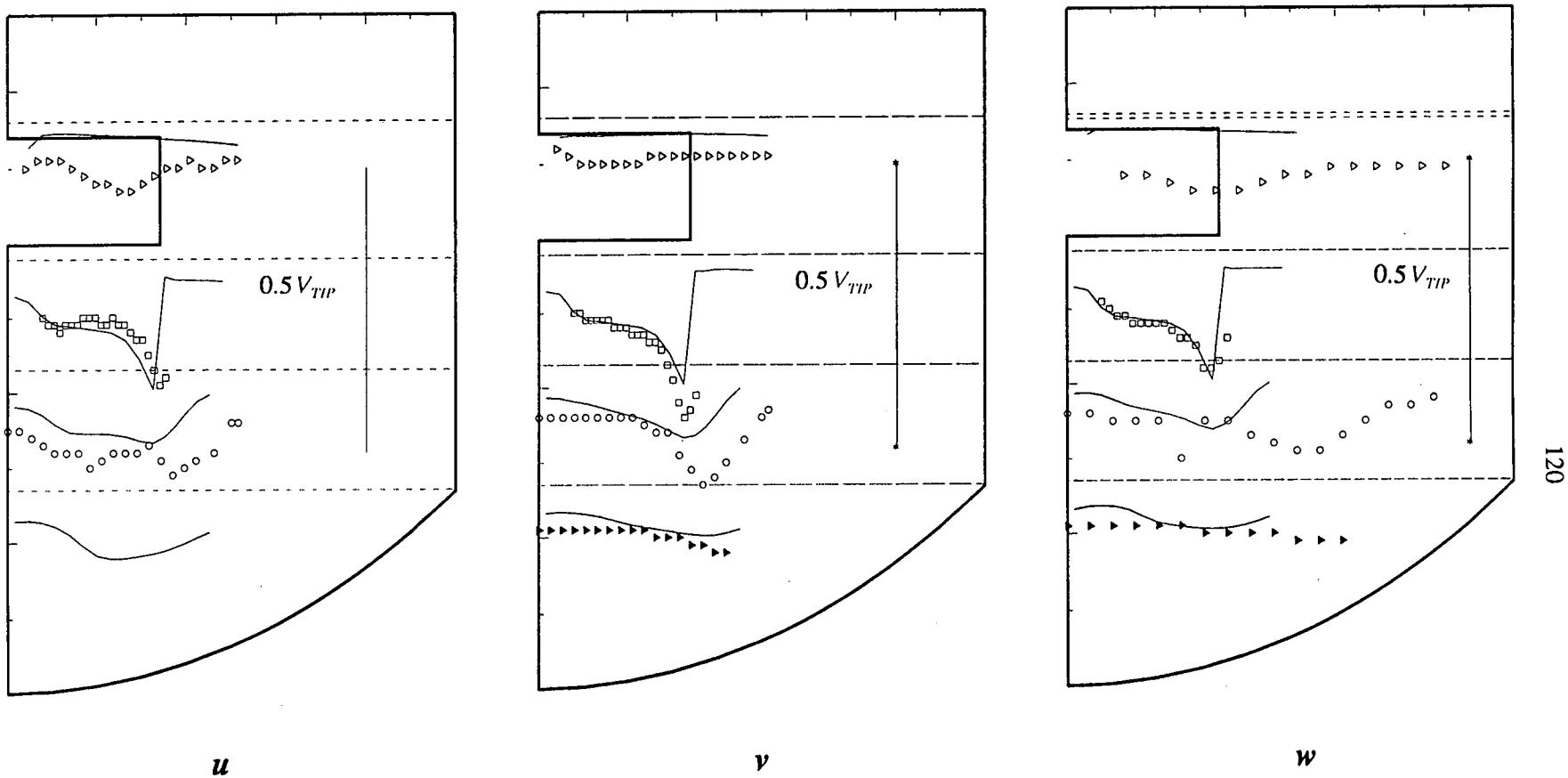

Figure 5.18 DSM predictions compared to LDA measurements in the impeller stream.

Axial, radial and tangential fluctuating velocities. Dashed lines indicate measuring position and zero for curves (DSM) and points (LDA). Bars indicate impeller tip speed.
For more details, see Appendix D.

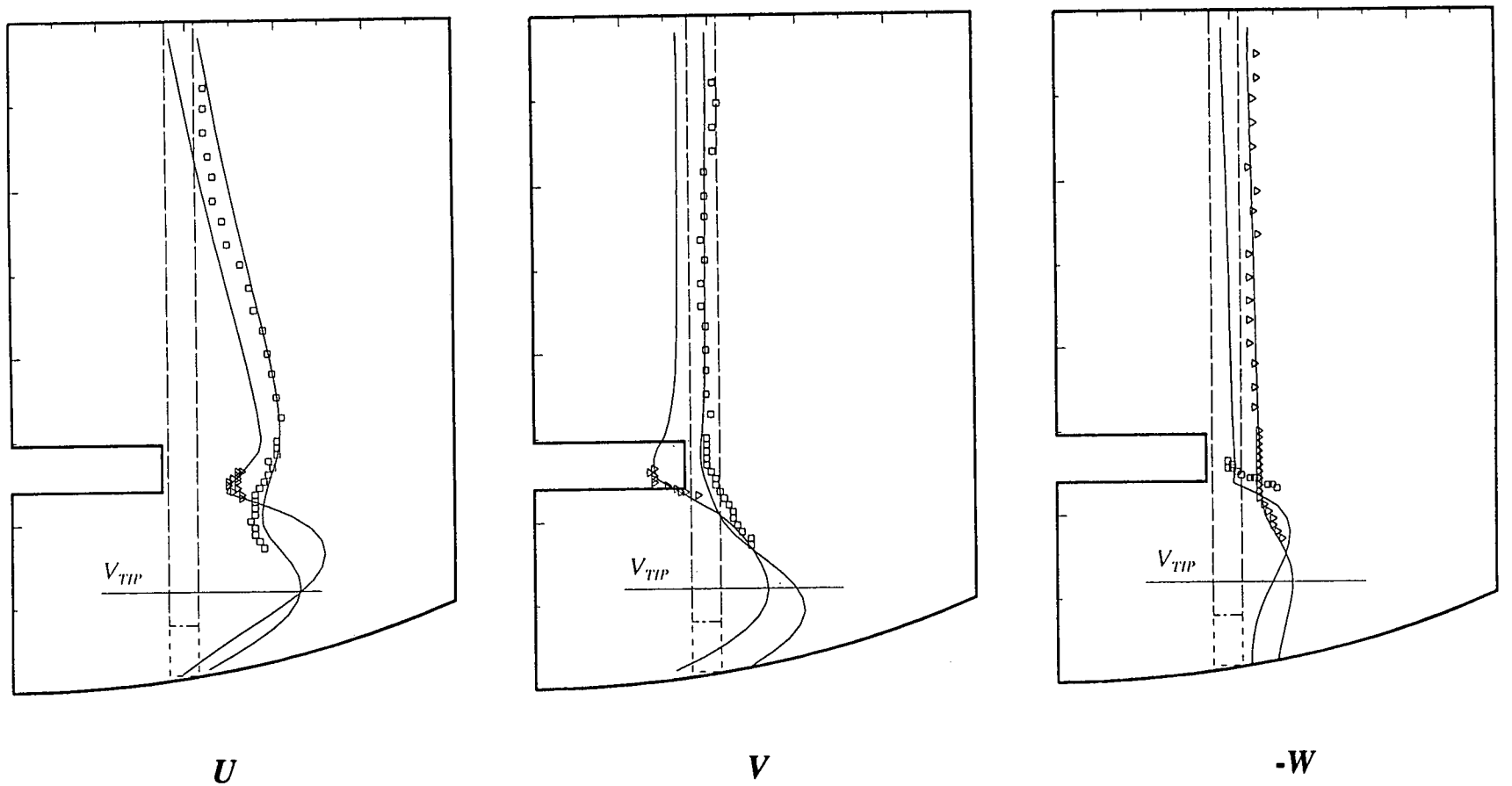

Figure 5.19 DSM predictions compared to LDA measurements at r=64 mm.

Axial, radial and tangential average velocities. Dashed lines indicate measuring position and zero for curves (DSM) and points (LDA). Bars indicate impeller tip speed. The radially outward direction is positive.
For more details, see Appendix D.

Turbulence predictions along these traverses are in poorer agreement with experimental data (Figure 5.20). Errors vary from about 50% to 80% low, accuracy being best near and below the impeller. This applies to all three sets of fluctuations. Agreement towards the liquid surface is best for the tangential fluctuations, which appear only in the tangential momentum equation. This could contribute to the improved prediction of average swirl velocity compared to k-ε.

Reynolds shear stresses showed similar trends to normal stresses, i.e. were underestimated. These have a relatively smaller effect on the momentum equations than the normal stresses and experimental values are less certain, in view of their magnitudes.

5.6 CHEMICAL REACTION MEASUREMENTS

5.6.1 Details of Test Reaction

A homogeneous liquid-phase chemical reaction scheme with a mixing-sensitive yield was conducted in aqueous solution to measure reactive mixing performance of the same stirred vessel used for the flow computations and LDA measurements. This involved the azo-coupling between 1- and 2-naphthol (A and C) and diazotised sulfanilic acid (B). The reaction pathway and kinetics have been determined by Bourne et al. (1992) and are as follows (T=298 K):

A + B $\rightarrow$ R	k_1=12238 m^3/mol.s
A + B $\rightarrow$ T	k_2=921 m^3/mol.s
R + B $\rightarrow$ S	k_3=1.835 m^3/mol.s
T + B $\rightarrow$ S	k_4=22.25 m^3/mol.s
C + B $\rightarrow$ Q	k_5=125 m^3/mol.s

Rate constants vary over five orders of magnitude. When mixing is rapid, formation of R and T is favoured. When mixing is very slow, formation of S is favoured. At intermediate levels of mixing, formation of Q is favoured. The system exhibits many degrees of freedom and its sensitivity to mixing depends on experimental conditions.

All reactions compete for B. The yield of products and by-products can be expressed as a ratio to the original B concentration. Two such ratios are used:

$$X_Q = \frac{C_Q}{C_B + C_Q + C_R + C_T + 2C_S} \tag{5.6.1}$$

$$X_S = \frac{2C_S}{C_B + C_R + C_Q + C_T + 2C_S} \tag{5.6.2}$$

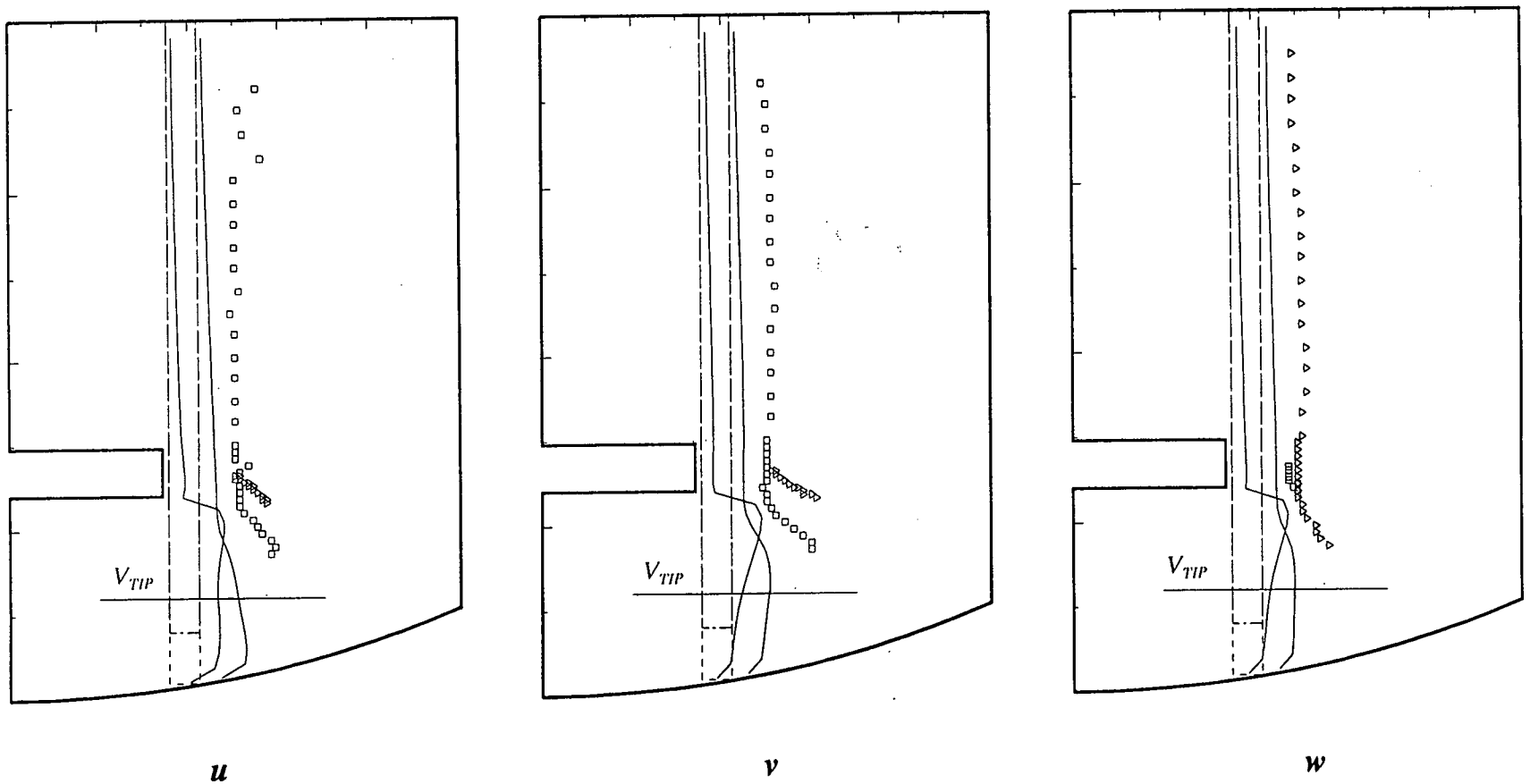

Figure 5.20 DSM predictions compared to LDA measurements at r=64 mm.

Axial, radial and tangential fluctuating velocities. Dashed lines indicate measuring position and zero for curves (DSM) and points (LDA). Bars indicate impeller tip speed.
For more details, see Appendix D.

X_Q and X_S express the fractions of by-products Q and S formed from reacted B. They are related to the following dimensionless groups describing mixing and reaction:

$$X_Q \, , \, X_S = f \left(\frac{N_{A0+C0}}{N_{B0}} \, , \, \frac{C_{A0}}{C_{C0}} \, , \, \frac{V_{A+C}}{V_B} \, , \, Sc \, , \, k_3 C_{B0} \, t_{mi} \right) \qquad (5.6.3)$$

In the most general situation, the characteristic mixing timescales t_{mi} depend on bulk convection, turbulent diffusion, inertial-convective, viscous-convective and viscous-diffusive mixing (Chapter 3). The first two stages are described by convection and diffusion terms in the species transport equations. The latter three contribute to the source and sink terms in those equations which can be calculated from the MTPDF model (Chapter 3).

5.6.2 Experimental design

Using Baldyga & Bourne's (1989) model of viscous-convective micromixing, experimental conditions where the reaction system was likely to show mixing-sensitivity in aqueous solution (Sc=1425, Tovstiga, 1986) were determined approximately. The results of this analysis were not all quantitatively valid, being limited to conditions where this mixing step or kinetics are controlling, but were useful for experimental design.

Simulation required concentrations of A, C and B, a volume ratio V_{A+C}/V_B and an energy dissipation rate ε to be selected. Typical values of the latter were obtained from the above three-dimensional computations for surface and impeller addition of B. Results from the model calculations are shown in Table 5.3. Mixing-sensitivity was expected at A and C concentrations of 0.1 mol/m^3 with B at 50 mol/m^3 and a volume ratio of 500. This amounts to an excess of A and C of 100%. Experimental values of X_S and X_Q were expected to lie in a similar range to those predicted by the micromixing model.

An important feature of the MTPDF model for reactive mixing is its ability to predict reaction yield when either bulk or fine-scale mixing is controlling. Thus, experiments in both categories were needed. In semi-batch chemical reactors, it is possible to vary which mixing stage is limiting by varying the feed time. Fast feeding favours bulk mixing control. Slow feeding favours fine-scale mixing. To quantify "fast" and "slow", the bulk mixing time was calculated from the FMP empirical correlation for turbulent flow in a standard tank (Grenville, 1989):

$$t_{95} = 5.4 \, \frac{T^2}{Po^{\frac{1}{3}} \, N \, D^2} \qquad (5.6.4)$$

which gives 8.8 seconds at N=300 rpm for the present geometry. This suggests a bulk circulation time of 2-3 seconds. Feed times comparable to or shorter than t_{95} are fast. Feed times much longer than t_{95} are slow.

It was also of interest to investigate the effect of impeller speed on yield at a constant feed time and repetitions were desirable to reduce uncertainty. However, the number of possible experiments was limited to the period for which the reagents remained fresh. This was estimated to be 3 hours (Hearn, 1992).

The selected experimental conditions, including ratios of feed time to bulk mixing time, are given in Table 5.4, together with resulting values of X_Q and X_S.

Table 5.3 Micromixing model calculations for experimental design

$C_{A0}=C_{C0}=0.1$ mol/m^3; $C_{B0}=50$ mol/m^3; $V_{A+C}/V_B=500$

	impeller	surface
ε * (W/kg)	9.86	2.07 x 10^{-4}
X_S	0.014	0.3
X_Q	0.139	0.38

* based on maximum and minimum ε values taken from flow simulations

Table 5.4 Results of complex reaction measurements

$C_{A0}=C_{C0}=0.1$ mol/m^3; $C_{B0}=50$ mol/m^3; $V_{A+C}/V_B=500$

Run #	Q_B (l/min)	Feed Point	N (rpm)	t_B (s)	Mass of B added (g)	X_S	X_Q	t_B/t_{95}	MB timed	MB weighed
1	5.0	surface	300	0.5	39.52	0.091	0.376	0.06	0.88	0.93
2	0.45	surface	300	5.32	41.67	0.099	0.366	0.6	1.01	0.97
3	0.3	surface	300	8.34	43.5	0.094	0.366	0.95	1.01	0.97
4	0.15	surface	300	16.77	44.2	0.114	0.386	1.91	0.81	0.77
5	0.45	impeller	300	5.66	47.2	0.071	0.407	0.64	1.09	0.98
6	0.15	impeller	300	19.05	49.4	0.031	0.358	2.16	1.03	0.99
7	0.15	surface	300	16.67	43.2	0.107	0.383	1.89	0.96	0.93
8	0.15	surface	100	16.63	42.9	0.155	0.411	0.63	0.93	0.90
9	0.15	surface	200	16.74	43.1	0.134	0.404	1.27	0.92	0.90
10	0.06	surface	300	41.55	42.8	0.102	0.385	4.72	0.96	0.93
11	0.03	surface	300	83.24	42.8	0.076	0.314	9.46	1.15	1.12
12	0.03	impeller	300	83.38	42.7	0.019	0.259	9.48	1.01	0.98

5.6.3 Experimental procedure

500 litres of 1- and 2-naphthol (A and C) solution was made in a supply tank using de-ionised water and buffered to pH=9.9. The sulfanilic acid (B) was made in a 4.0 litre beaker just prior to starting experiments. These conditions avoid undesirable chemical degradation of the reagents (Bourne et al., 1981) and pH gradients in the reaction zone. The nominal reaction temperature was 298 K (μ=0.89 Pa.s).

Figure 5.21 shows the flowsheet for the reactor, which was operated in semi-batch mode. B was added to A and C over a period using a gear pump. Initially 20.84 litres of A and C were added to the tank. The impeller speed was selected and the feed tube assembly placed in the desired position. The mass in the B reservoir was noted before starting the gear pump. Pumping (or feed) time was also monitored by stopwatch. When the desired quantity (nominally 41.67 ml) of B had been added, the gear pump was stopped. Agitation continued for about a minute to ensure complete consumption of B (the intrinsic reaction time of the slowest reaction is of order 0.01 s under these conditions).

After each run was completed, a 25 ml sample was taken from the tank contents and immediately diluted with buffer solution. The contents of the tank were pumped to storage and the tank washed with de-ionised water before proceeding with the next batch. Samples were analyzed using a spectrophotometer, which directly gives the concentrations of R,T, S and Q. Experimental error associated with the analysis is less than 3% (Bourne et al., 1992).

12 experiments were carried out in this way. The feed time was varied in order to ensure that the reactions proceeded under both macromixing- and micromixing-controlled conditions.

The volume of B added was measured gravimetrically and by timing the period of operation of the gear-pump. Results from both techniques agreed reasonably (Figure 5.22). When feed times are short compared to bulk mixing time, the reaction is controlled by bulk mixing, but under these conditions, experimental difficulties are greater than for long feed times: small errors in feed time have a large effect on the overall stoichiometry. The nominal B charge was more accurately attained with low feed velocities (Figure 5.22).

Following analysis of the product solution, it is possible to carry out a mass balance as follows:

$$MB = \frac{V_B C_{B0}}{(V_{A+C}+V_B)(C_R+C_T+2C_S+C_Q)} \qquad (5.6.5)$$

MB should have a value of 1.0 assuming no experimental errors (e.g. in measurements or analysis) and no side-reactions which might produce other products not accounted for in equation 5.6.3. Most mass balances for the runs above came out within 10% of closure (see Table 5.4). Where this was not the case, the principal error probably resulted from an inaccurate B volume. The impact of this on X_S and X_Q values does not appear to have been too large: for example, results from runs 4 and 7, which were

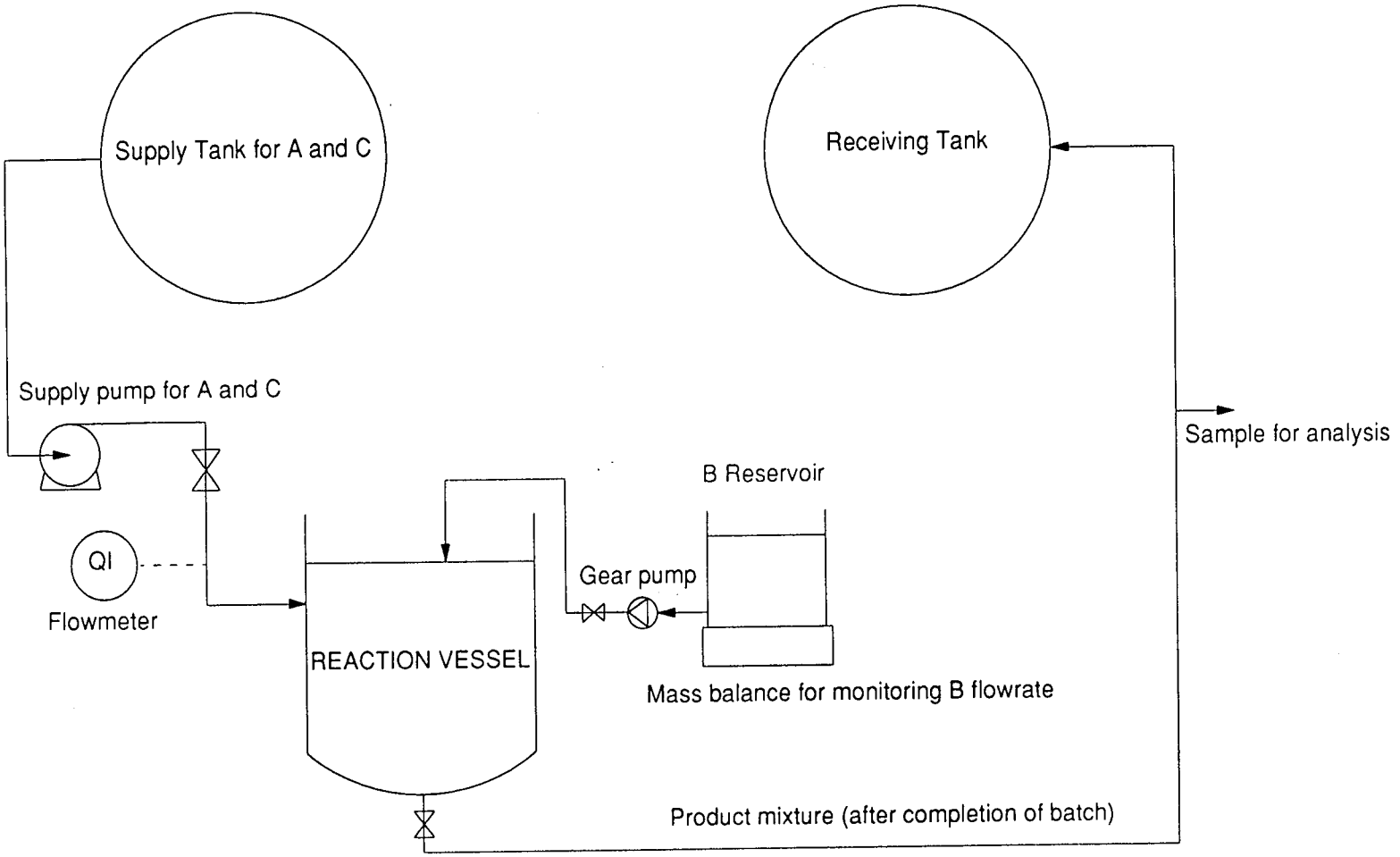

Figure 5.21 Flowsheet for chemical reaction experiments

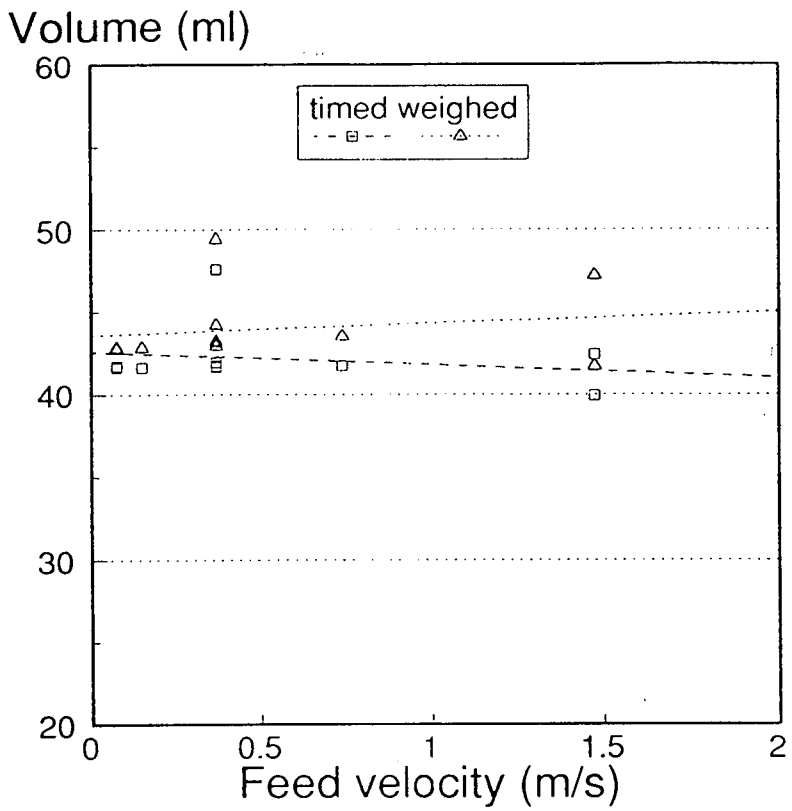

Figure 5.22 Comparison of timed and weighed B volumes as a function of B velocity.

nominally identical experiments, produced very similar yields despite a low *MB* for run 4. Incomplete closure of the mass balance is not uncommon (Hearn, 1992).

5.6.4 Results

Effect of feed time

Feed time has a complex effect on the yield of this reaction scheme. Two competing factors cause the yield of side-products to reach maximum values as feed time increases before decreasing towards the kinetically-controlled values.

Firstly, when the volume of B added is constant but the time of addition is reduced, the feed velocity and kinetic energy are increased:

$$U_B \propto \frac{V_B}{t_B} \tag{5.6.6}$$

This causes increased local mixing as the feed jet enters the vessel. It also causes feed fluid to penetrate further into the vessel than at longer feed times. Secondly, when feed times are short, the reaction zone can quickly become locally depleted of A, so that formation of side-products Q and S is favoured. As the feed time is increased, bulk circulation of fluid reduces this effect, so that at longer feed times, reduced Q and S would be expected.

These effects are illustrated by the results of experiments at a given set of agitation conditions (e.g. N=300 rpm, surface addition) when the feed time is varied (Figure 5.23). For feed times shorter than a certain value, t_{min}, X_Q and X_S increase with increasing feed time. This is attributed to the increased kinetic energy of the feed jet at short feed times. When the feed time exceeds t_{min}, increasing feed time reduces X_Q and X_S. This effect is attributed to improved bulk circulation relative to the feed rate. Similar results were obtained with a simpler form of this reaction by Bourne & Hilber (1990).

The precise value of t_{min} depends on the balance between bulk mixing and local mixing near the feed point (inertial-convective, viscous-convective and viscous-diffusive). The rates will in general vary at different points in the tank. This is illustrated by the impeller addition data at N=300 rpm (Figure 5.24), which shows a monotonic decrease in X_Q and X_S when feed time is increased. Due to the relatively higher turbulence in the impeller region, t_{min} at this location is very much shorter than at the liquid surface.

Effect of impeller speed

For a given feed time, increasing impeller speed (and hence agitation intensity) reduces X_Q and X_S (Figure 5.25). This can again be explained by two contributing factors: increased turbulence levels throughout the tank, hence increased local mixing intensity and enhanced bulk circulation rates, leading to reduced macroscopic concentration gradients.

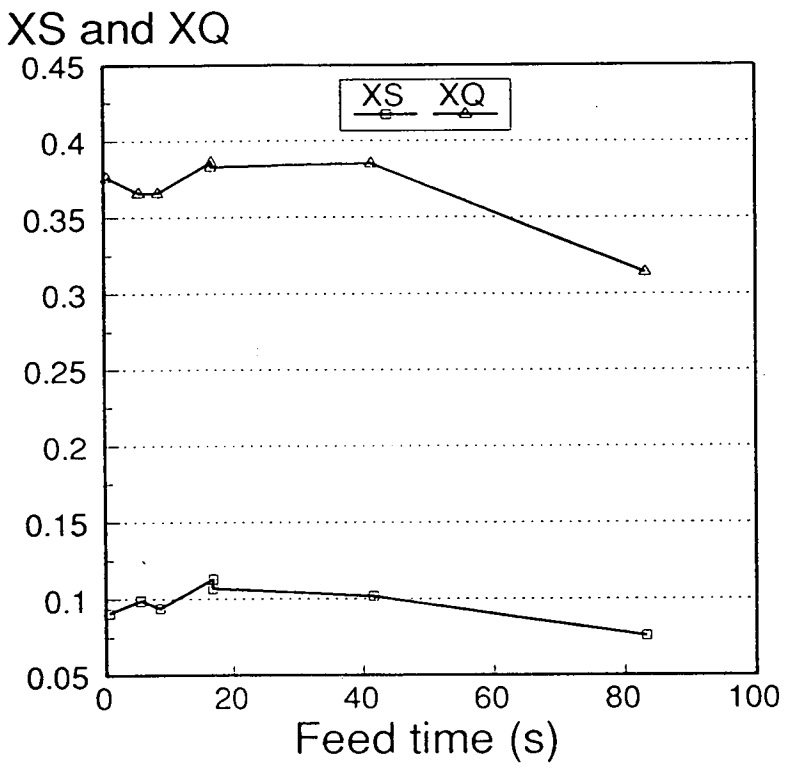

Figure 5.23 Effect of feed time on side-product (Q and S) formation. Feed point at liquid surface.

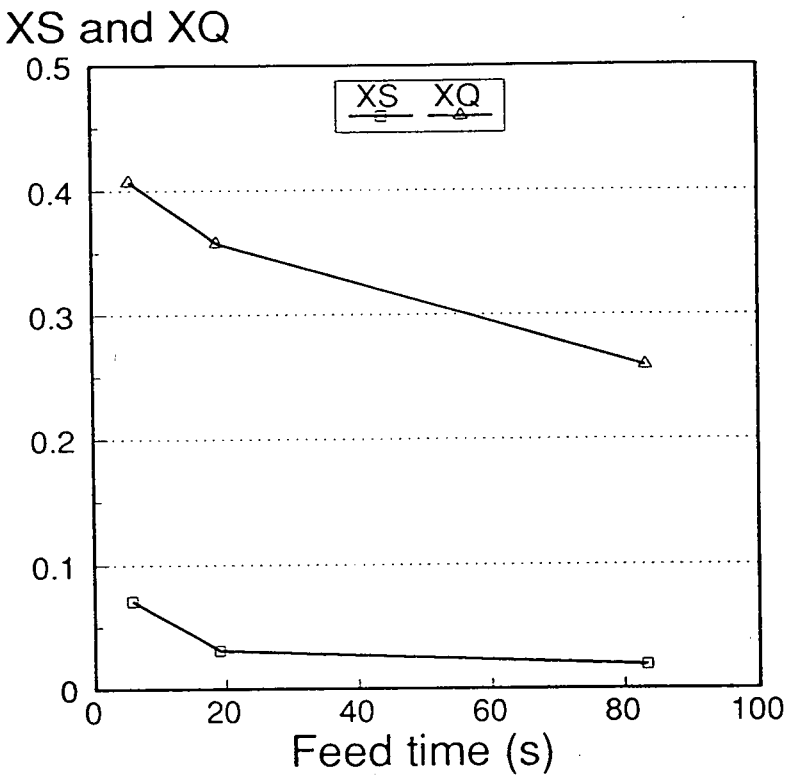

Figure 5.24 Effect of feed time on side-product (Q and S) formation. Feed point in impeller suction.

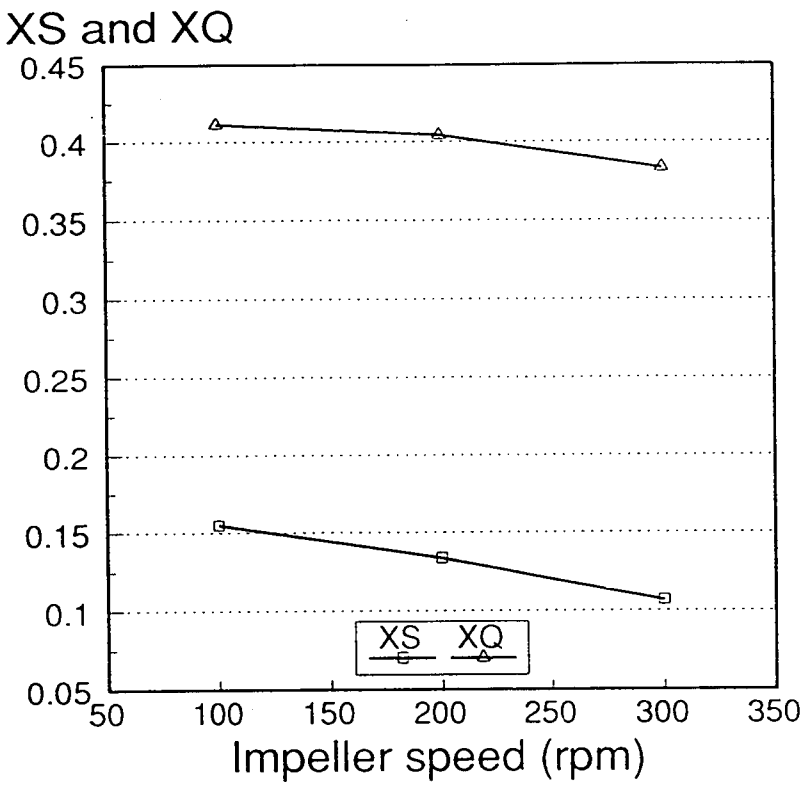

Figure 5.25 Effect of impeller speed on side-product (Q and S) formation. Feed point at liquid surface.

Effect of feed position

For a given impeller speed and feed time, feeding into the impeller region rather than at the liquid surface generally reduces X_Q and X_S (Figure 5.26). This effect is particularly clear at longer feed times, where the reaction zone tends to be more highly localised than at short feed times, and reflects differences in local mixing rates and levels of turbulence.

More detailed discussion of results follows below.

5.7 CHEMICAL REACTION PREDICTION

5.7.1 Assumptions

The reactions were carried out under isothermal conditions and with the exception of the small intrusive effect of the feed tube, had no other effect on the flow field. The flow field, on the other hand, has a strong effect on the reaction rates.

The flow field calculated above assumes that the impeller is a steady source of flow and momentum. This assumption is partly justified if the simulated process takes place on a timescale long in comparison with the time for one impeller rotation (0.2 s at 300 rpm). In other words, long feed times will tend to average out effects of the periodicity of the impeller motion on the mixing rates. The shortest feed time simulated here was 5.5 seconds, which is probably sufficient to meet this criterion.

The way forward then appears to be to use the previously calculated 3-d flow fields as input and solve the additional equations for species transport and reaction rate determination. However, initial axi-symmetric simulations with the MTPDF model required more than 30 hours of computer time on a Silicon Graphics 210 Server, which was roughly equivalent to the time required for the three-dimensional DSM flow-field calculation. The corresponding three-dimensional time-dependent MTPDF run would therefore require about 800 hours, which was not feasible. Although the reactive mixing model is conceptually simple, when applied to complex reactions in three-dimensional time-dependent flows with fine grids, it is extremely compute-intensive, by today's standards. Estimates of the required CPU time on a Cray 2 supercomputer came out at a minimum of 50 hours, which is punitively expensive for one run.

To render the model equations computationally tractable, two simplifying assumptions could be made:

1. Simulate the reactions using a two-dimensional flow field
2. Reduce the resolution (i.e. number of cells) in the three-dimensional problem

Option 2 is not feasible for two reasons. Firstly, even a much coarser 3-d mesh would still be extremely compute-intensive. Secondly, coarser meshes than 24,000 cells would not give an acceptable representation of the flow field with the DSM.

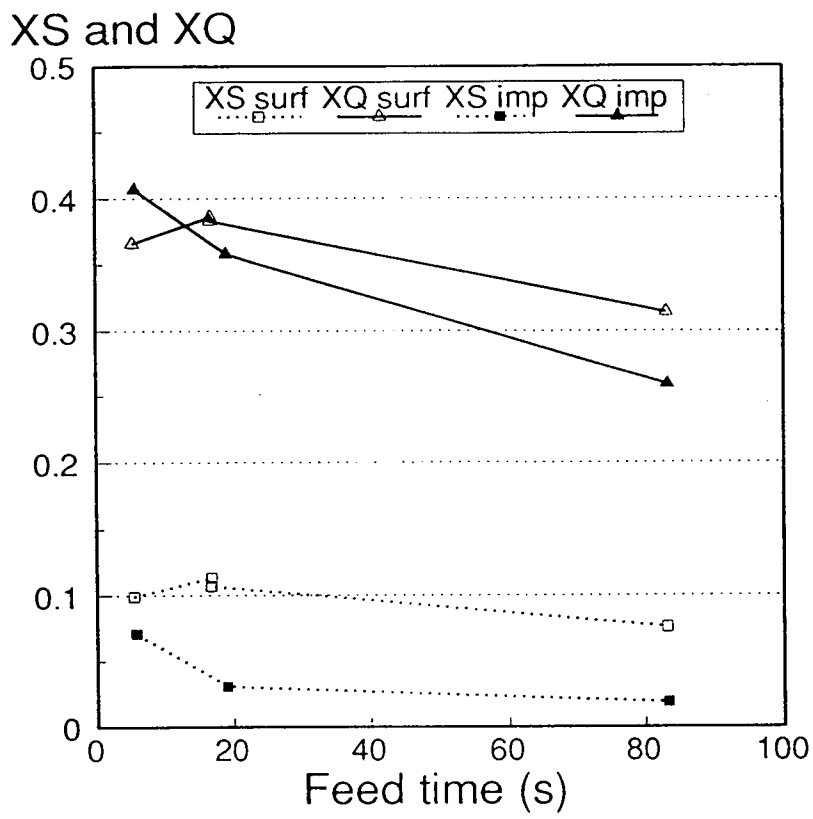

Figure 5.26 Effect of feed position on side-product (Q and S) formation for various feed times.

Option 1 requires further examination to establish its limitations. A two-dimensional model would average in the tangential direction, setting all gradients to zero. This would change the following parameters relative to the experiments:

1. Some details of the flow field
2. The feed trajectory
3. The environment concentration
4. The feed position
5. The local feed concentration

Axi-symmetric simulation on a 40 X 30 grid using the DSM produces the x-r vector plot in Figure 5.27. Axial and radial velocities are quantitatively similar to those of the three-dimensional runs in all but the planes near the baffle plate. Upflow in the vortex beneath the impeller is also somewhat stronger than in the 3-d case. There is no tangential flow in axi-symmetric simulations and computed volume averaged ε values dropped by 15% compared to the 3-d run.

The environment for reaction in axi-symmetric simulation is tangentially homogeneous, whereas in the 3-d experiment, it is not. Axi-symmetric simulation effectively assumes that the tangential mixing time is much less than the feed time. The tangential circulation time at 300 rpm is of order 3 seconds. Thus this condition should be approximately fulfilled for all but the shortest feed times.

The feed position in axi-symmetric simulation is in the shape of a narrow annulus (Figure 5.28), again tangentially averaged, whereas the experiments used point addition. The former has a better initial feed distribution, which means better mixing and reduces the likelihood of side-product formation.

Finally, local feed concentration is much lower in axi-symmetric simulations than in the point-addition experiment. This is because of tangential averaging, which spreads the feed addition over a much larger annular area (or into a larger volume). This would also tend to depress side-product formation, by lowering the intrinsic speed of all the reactions.

Factors 3 and 4 probably constitute the most serious differences between axi-symmetric simulations and three-dimensional reactive mixing experiments. The effect of factor 4 can be estimated by increasing all initial concentrations and hence reaction speeds. It is not possible to quantify the effect of factor 3 via axi-symmetric simulation.

Despite the inadequacies of axi-symmetric simulations, it appears that they should still give an indication of whether the MTPDF model can predict the correct trends in selectivity when experimental conditions are changed. It would be useful to carry out their three-dimensional counterparts when sufficient computer power becomes available economically. Axi-symmetric simulations were used for all the reactive mixing simulations that follow. These were conducted on the Cray 2 supercomputer at Harwell Laboratory and seven simulations required in total approximately 40 CPU hours.

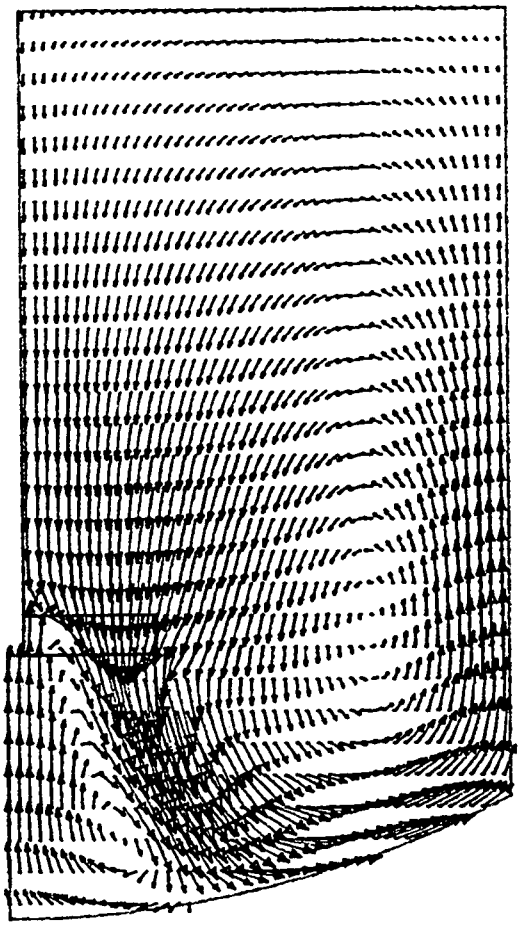

Figure 5.27 Predicted DSM velocity vectors from a two-dimensional flow field simulation.

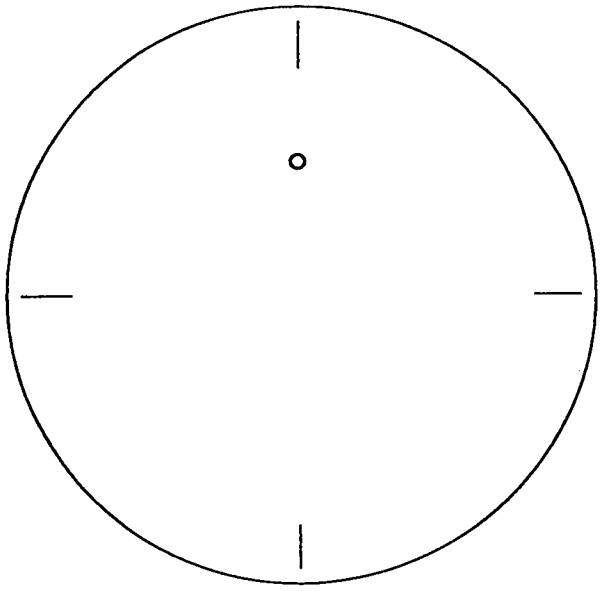

Three-dimensional feeding at a single point

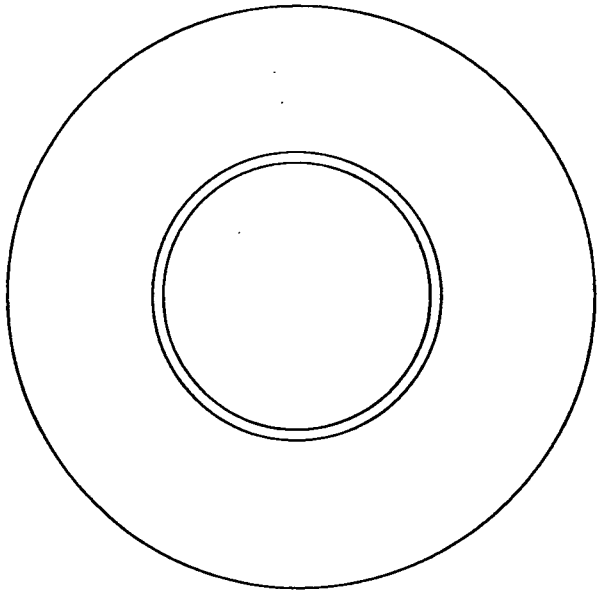

Axi-symmetric feeding in the shape of an annulus

Figure 5.28 Comparison between feed pipe geometries in three- and two-dimensional situations.

5.7.2 Boundary & Initial Conditions

To apply the MTPDF model, boundary conditions were needed for α_s, α_r, reaction zone concentrations and volume-averaged concentrations. For all these parameters, zero flux conditions applied along walls and the liquid surface. At the inlet (feed tube) only α_s (1.0) and C_B (50 mol/m^3) had non-zero values.

Initial conditions for all variables in the bulk were zero except for volume-averaged A and C concentrations, which were set to their initial values of 0.1 mol/m^3.

The experimental volume ratio of B to A and C was 1/500, so that addition of B caused a negligible (0.2 %) increase in the reactor contents. In the computations, the reactor volume was assumed to be constant throughout the feed time. Feeding was modelled via "volumeless" source terms applied to the α_s and C_B equations in the cell nearest to the experimental feed point. The source terms have the following functional form:

$$S_B = \varrho\, Q_B\, \phi_B \tag{5.7.1}$$

where ϕ_B denotes either α_s or C_B and Q_B denotes the feed volumetric flow rate. Since the volume of B was kept constant in experiments, while the feed time changed, the velocity of feed addition also varied, between 0.07 and 1.47 m/s. When the feed stream has a significant velocity of its own, it affects the flow field locally, which can affect the reaction rate. A high-velocity feed can travel further and faster than a low velocity feed, transporting reaction into regions of different mixing intensity.

In the above experiments, the ratio $(C_{A0}+C_{C0})/C_{B0}$ was very low (0.004), i.e. the feed stream was much more highly concentrated than the bulk. The Schmidt number (Sc=1425) was <<4000. For short feed times, bulk convection would be expected to be rate-controlling; for medium feed times, inertial-convective mixing would play a role. For long feed times, viscous-convective engulfment should be rate-controlling (see Chapter 3).

5.7.3 Timestep selection

The criterion for choosing the timestep size is that it should be small compared to the timescale over which the concentrations change significantly. The choice of timestep can affect the accuracy of the simulations in the same way as the grid size. When dealing with multiple reactions with widely-varying ("stiff") rate-constants, or any phenomenon involving a range of timescales, it would be useful to employ different timesteps for each equation or each transport process. Rapidly-changing concentrations require short steps, while slowly-changing concentrations do not.

In FLOW3D Version 2.4, all transport processes and all equations in MTPDF were constrained by the program to use the same time steps and under-relaxation factors. This meant that steps had to be small enough and iterations sufficiently numerous to resolve the fastest-changing and most slowly converging variables. Such restrictions are unnecessary and undesirable in simulations of this type. These considerations meant than a disproportionate amount of computational work was needed at each timestep.

From a practical point of view, timestep size is limited by computer power. Use of very small steps in these calculations would have been prohibitive. Therefore a standard step size of 0.5 s was selected and used for most of the computations. Sensitivity to this parameter was evaluated, see Section 5.8.4 below.

5.7.4 Special considerations for complex geometry simulations

In Chapter 4, MTPDF was applied to tubular (plug flow) reactors. MTPDF uses Lagrangian concepts to describe the effects of mixing and reaction on identifiable fluid elements as they flow around the reactor. In plug flow systems, each packet of feed is associated with a unique environment which passes the feed point only once. The reaction zone therefore grows downstream of the feed point at the expense of segregated and bulk volume fractions.

In a recirculating flow, the reaction zone at one instant can subsequently form part of the environment. Therefore reaction zone volume is sometimes dissipated as well as generated. For example, fluid passing the feed point at time t_0 passes from the environment into the reaction zone. Subsequently, after time t_1, when all B in the moving reaction zone has been consumed, that portion of reaction zone disappears. Bulk flow patterns ultimately carry the same fluid elements back to the feed point, where at time t_2 they once again pass from the (new) environment into the (new) reaction zone.

In the present simulations, this effect was modelled as follows. At the end of each timestep, local values of α_r and all reaction zone concentrations, $\alpha_r C_{ir}$ were set to zero unless C_B was greater than zero. This approach is valid as long as the timesteps are much shorter than the circulation time. It prevents old reaction zone fluid from influencing events in the new reaction zone. This condition was met by all timestep sizes used.

5.8 CHEMICAL REACTION VALIDATION

Seven simulations were conducted comprising four complete batches at different experimental conditions and three shorter runs to estimate mainly numerical parametric effects. Details are given in Table 5.5. Three full batch simulations considered addition of B in the impeller region with variable batch time and one considered addition at the liquid surface. Development of X_Q and X_S during the batch time was monitored by calculating vessel-averaged values at the end of each time step. Due to computer storage restrictions, data on spatial variation of variables is only available for the final timesteps of each run.

Qualitative behaviour is shown in Figure 5.29. When feeding begins, a reaction zone develops near the feed tube. This is convected into other regions of the vessel, growing all the time, until it is depleted of B. Meanwhile, A and C are engulfed into and consumed within this reaction zone and R,T, Q and S produced. When feeding stops, reaction continues for a short period until B is fully consumed, after which the contents of the tank continue blending without further reaction.

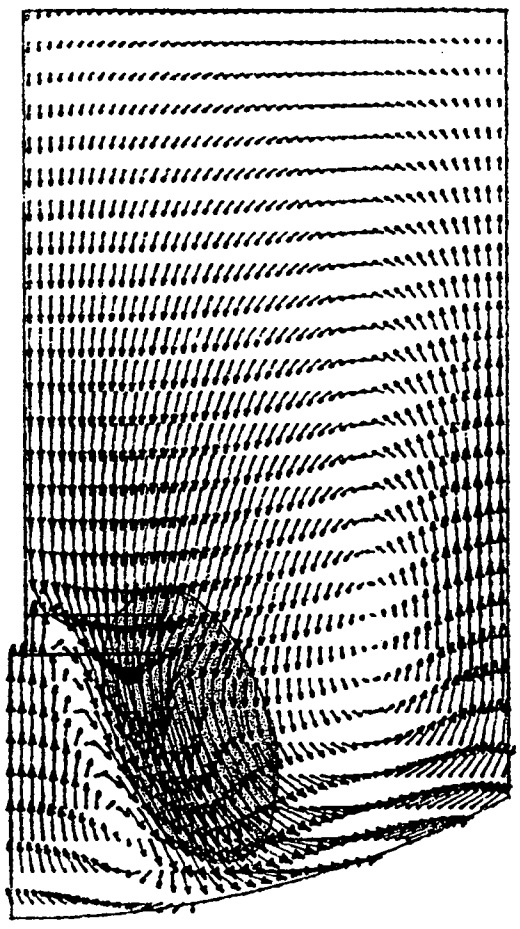

Figure 5.29 Predicted development of the reaction plume in the impeller discharge (t_B=5.5s). Picture shows regions where α_r exceeds 0.5.

Table 5.5 Results of reaction simulations

Chemical conditions as in Table 5.4, except run 6324, where all concentrations are raised by a factor 70.

Run #	Q_B (l/min)	Feed Point	N (rpm)	t_B (s)	Timestep (s)	X_S	X_Q
88940 *	0.45	impeller discharge	300	5.5	0.5	0.0406	0.1938
16100 *	0.15	impeller suction	300	19.0	0.5	0.0506	0.1634
30549 *	0.03	impeller suction	300	83.0	0.5	0.0466	0.1560
26182 *	0.15	surface	300	16.5	0.5	0.2526	0.3731
91607	0.45	impeller discharge	300	2.5	0.25	0.0161	0.142
9258	0.45	impeller discharge	300	0.5	0.025	0.0132	0.1565
6324	0.45	impeller discharge	300	1.0	0.1	0.245	0.3483

* denotes simulations which covered the complete corresponding experimental feed time

5.8.1 Effect of feed time

Three feed times were simulated for impeller addition at 300 rpm. Results are shown in Figure 5.30 with experimental values for comparison. Quantitative accuracy is poor, but major trends are correct.

X_S is close to zero for all three cases. Experiments show a monotonic decrease as feed time increases, whereas simulations show a slight hump. This may be due to slightly different initial conditions for the 5.5 s feed time. In this case, the feed had a higher velocity than the surrounding bulk liquid so its computational position was moved down from the impeller suction into the discharge. Turbulence levels were therefore initially higher than for the other two cases, which could explain the reduced X_S at this condition. A similar measure was used by Ranade & Bourne (1991) to simulate non-isokinetic feeding.

X_Q decreases monotonically as feed time increases, in accord with experiments. Quantitative agreement improves as the feed time is increased, suggesting that under this condition an axi-symmetric model becomes a better approximation (see Section

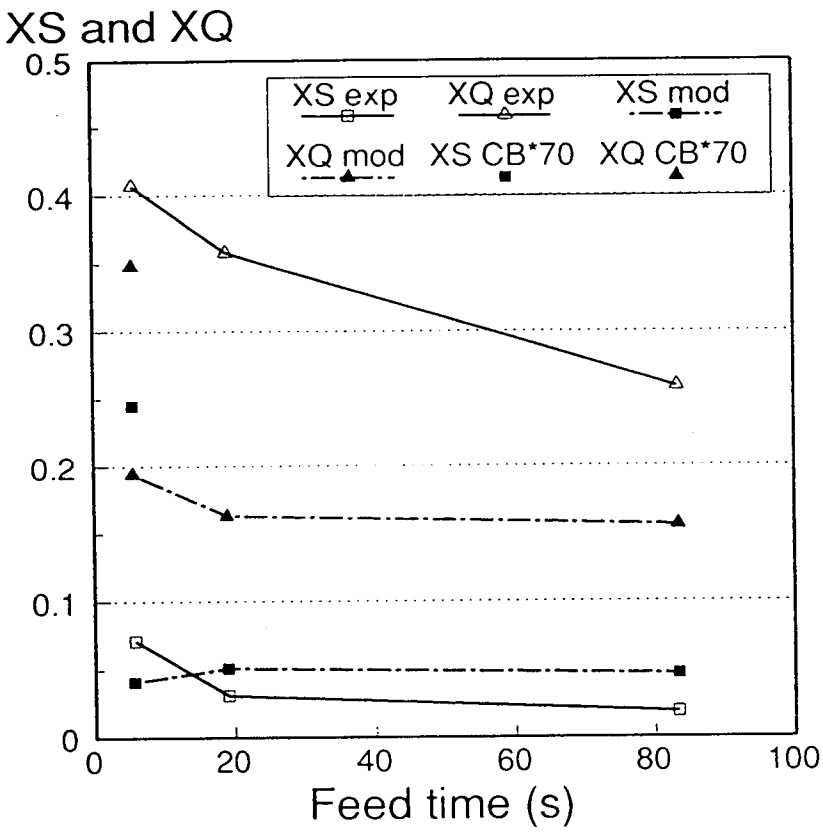

Figure 5.30 DSM and MTPDF two-dimensional model predictions of the effect of feed time on side-product formation compared with measurements.

5.7.1 above). Improved agreement at longer feed times also suggests that the details of fine-scale mixing are being accurately modelled.

Improved bulk mixing at longer feed times can also be seen from maximum and minimum deviations of species concentrations from their vessel-averaged values. This is shown in Table 5.6. At t_B=5.5 s after feeding is complete the maximum deviation of local A concentration from the vessel mean value is 77.5%. When t_B=83.0 s, this is reduced to 8.2%. Peak A concentrations occur in relatively dead regions, such as beside the impeller shaft near the liquid surface.

Table 5.6 Simulated macroscopic homogeneity of A versus feed time (all concentrations in mol/m^3)

t_B (s)	minimum	average	maximum	% deviation
5.5	1.86×10^{-2}	2.31×10^{-2}	4.1×10^{-2}	77.5
83.0	1.9×10^{-2}	1.94×10^{-2}	2.1×10^{-2}	8.2

Computed X_Q and X_S values are 30-70% low compared to experiments. This may be due to errors in the MTPDF approximations but more likely to the 3-d nature of the experiments. Simulations had better initial feed distribution and lower effective initial concentrations of B, which tend to depress Q and S formation.

The magnitude of the latter effect was explored as follows. Point addition used a 3.0 mm feed pipe with a B concentration of 50 mol/m^3. Simulations used a 3.0 mm annulus. The effective initial concentration in simulations was reduced in proportion to the discharge area of the annulus, i.e.

$$C_{B0,\,2\text{-}d} \approx C_{B0,\,3\text{-}d}\,\frac{\pi\, D_B^{\,2}}{\pi\, R_B\, D_B} \tag{5.8.1}$$

giving a value of approximately 0.7 mol/m^3. Intrinsic reaction speed determined by the B concentration was thus substantially reduced. A more representative situation would be obtained if the feed concentration was raised so that its initial value was similar to point addition. In an additional simulation, all concentrations were raised by a factor 70 whilst maintaining the same overall stoichiometry. Results after the initial period of this batch are shown in Figure 5.30. X_Q and X_S are both substantially increased. This result has no particular quantitative significance but demonstrates that the MTPDF predictions move in the right direction as the axi-symmetric model is made more representative of the 3-d experiments.

5.8.2 Effect of feed position

Two runs considered the effect of feed position. At $t_B=1.9t_{95}$, addition at the impeller gave reduced X_Q and X_S compared to addition at the surface (Table 5.7). The magnitude of the difference is much greater than that seen experimentally.

Apart from the axi-symmetric approximation, another potential reason for this is the under-prediction of turbulence quantities by the flow model. As described in Section 5.5.1, volume-integrated ε values accounted for only 53% of the power input by the stirrer blades. Naturally, better turbulence predictions were obtained in the bottom of the vessel, where measured boundary conditions were used as input. Predictions are likely to be least accurate in the upper part of the tank, where root mean squared velocities are underpredicted by as much as 80%.

Furthermore, simulation of surface addition did not account for turbulence and mixing induced by the feed jet, which would also depress X_Q and X_S.

Table 5.7 Simulated effect of feed position on yield compared with measurements ($t_B=1.9t_{95}$)

	Simulated X_Q	Simulated X_S	Measured X_Q	Measured X_S
Surface	0.37	0.25	0.38	0.11
Impeller	0.16	0.05	0.36	0.03

5.8.3 X_Q and X_S during batch time

It was not possible experimentally to measure the time-evolution of X_Q and X_S, but this is easy to accomplish from computations. There do not appear to be any published measurements of these parameters, although Ranade (1992) comments that in a simpler version of this reaction scheme, X_S develops through a minimum during the batch time.

In the present reaction system, even more complicated behaviour might be expected, due to extra degrees of freedom introduced by the Q-producing parallel reaction. Development of X_Q and X_S was monitored in all of the computations presented here.

Results for X_S are shown in Figure 5.31. In general, this develops through a minimum. Such behaviour might be explained as follows. Initial feed fluid consumes most of the A and some C in its local environment forming R,T and Q, but an excess of B remains. This reacts to form S. Subsequently, fresh A and C enter the local environment forming more R,T and Q. The overall A concentration reduces quickly and the C concentration remains quite high. R formation is thus depressed and so also is S formation. Later, as reacted fluid is pumped back into the reaction zone, S formation increases again, due to the presence of R and T.

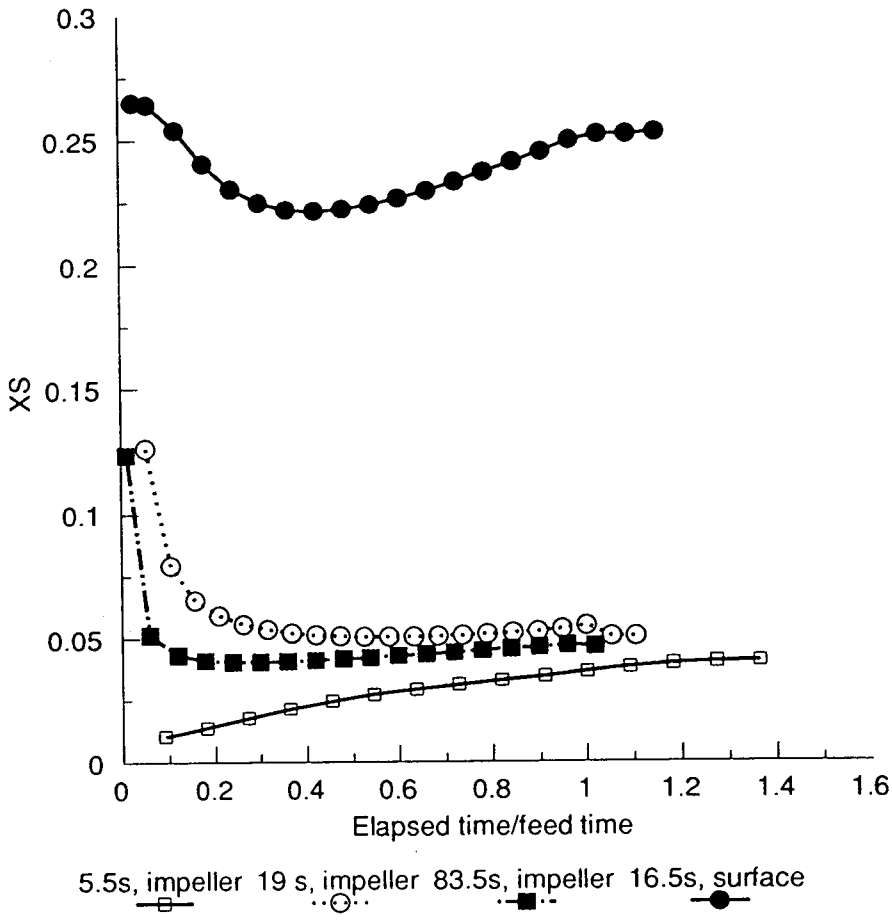

Figure 5.31 DSM and MTPDF two-dimensional model predictions of the development of X_S during the batch time.

The minimum in X_S might reasonably be expected to correlate with the bulk circulation time. However, no direct correlation is evident from the simulations. For example, at t_B=1.9t_{95}, the minimum occurs later for impeller addition than surface addition, whereas the circulation time should be shorter in the latter case. This emphasises that data of this type is difficult to interpret, much less predict, using rules of thumb.

X_Q tends to a monotonic increase during the batch time (Figure 5.32), consistent with the above behaviour of X_S. Initially, while A competes for B more successfully than Q, S formation is favoured. Later, when A is depleted, C competes more effectively and Q is formed.

Discontinuities evident in Figures 5.31 and 5.32 occur when feeding is stopped. These are most obvious for short feed times, where feed rates are higher; the end of the experiment is then more keenly felt by the flow. The magnitude of the discontinuity decreases as the feed rate is reduced relative to the bulk circulation rate in the vessel (i.e. at longer feed times).

Even before feeding stops, the gradients in the curves appear to depend on feed time. Faster feeding leads to larger gradients, so that the ultimate yield is only attained near the end of the batch. When feeding is slower, the ultimate yield is attained earlier. This is probably due to increased levels of dilution (and macroscopic homogeneity) of products during longer batch times.

The above effects appear to be rational, but are not supported directly by any experimental data. Such complex behaviour is intuitively to be expected with complex reactions of this type.

5.8.4 Effect of time-step size

Time-step dependence was evaluated by varying the number of steps for a fixed feed time (Figure 5.33). Time steps varied from 0.025 to 0.5 s. Independence was not achieved over this range, and could not be without excessive cost. The magnitude of the effect is significant, with shorter steps increasing X_Q.

At t_B=5.5 s, after 0.5 s has elapsed, X_Q increases from 0.11 through 0.13 to 0.16 as timesteps are reduced from 0.5 through 0.25 to 0.025 s. X_S is less affected by timestep size. The trend is encouraging insofar as it suggests that numerical errors contribute substantially to deviations between experimental results and simulations and reducing these sends X_Q in the right direction.

The shapes of the X_Q and X_S profiles during the early stages of the batch are also affected by timestep size, but are qualitatively similar to those discussed above. An initial maximum in X_S for t_B=5.5 s is resolved by the shortest step, which also produces an initial maximum in X_Q. It is uncertain whether these are real effects but there is some support for their existence in the literature (Ranade, 1992).

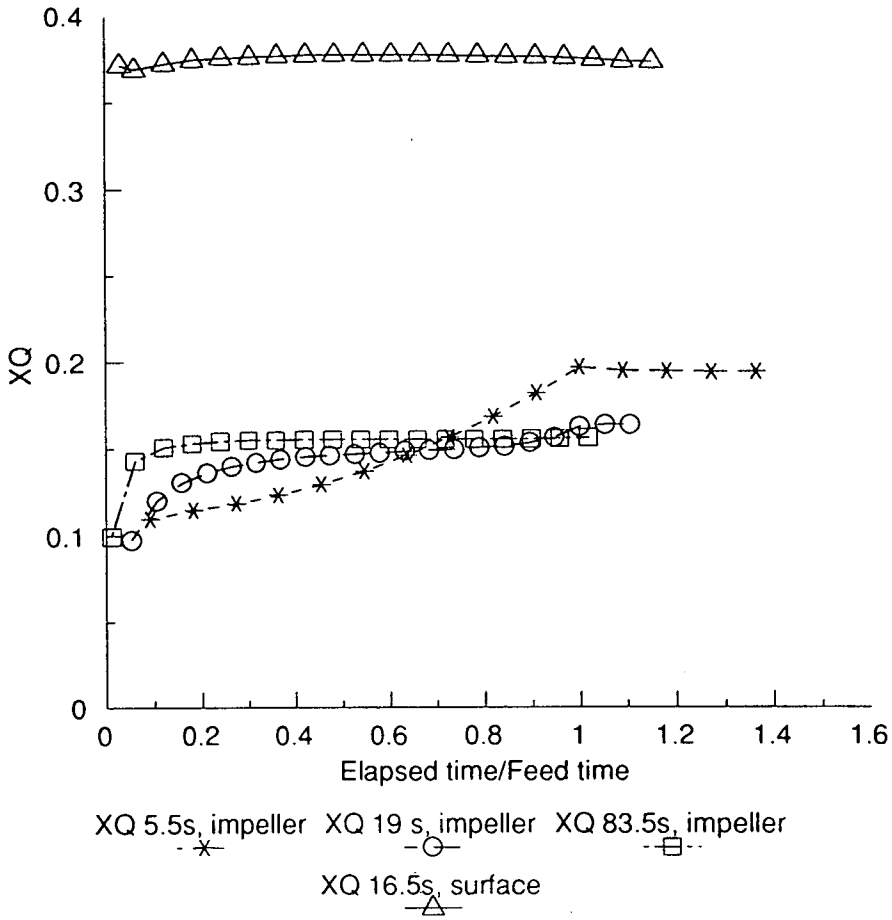

Figure 5.32 DSM and MTPDF two-dimensional model predictions of the development of X_Q during the batch time.

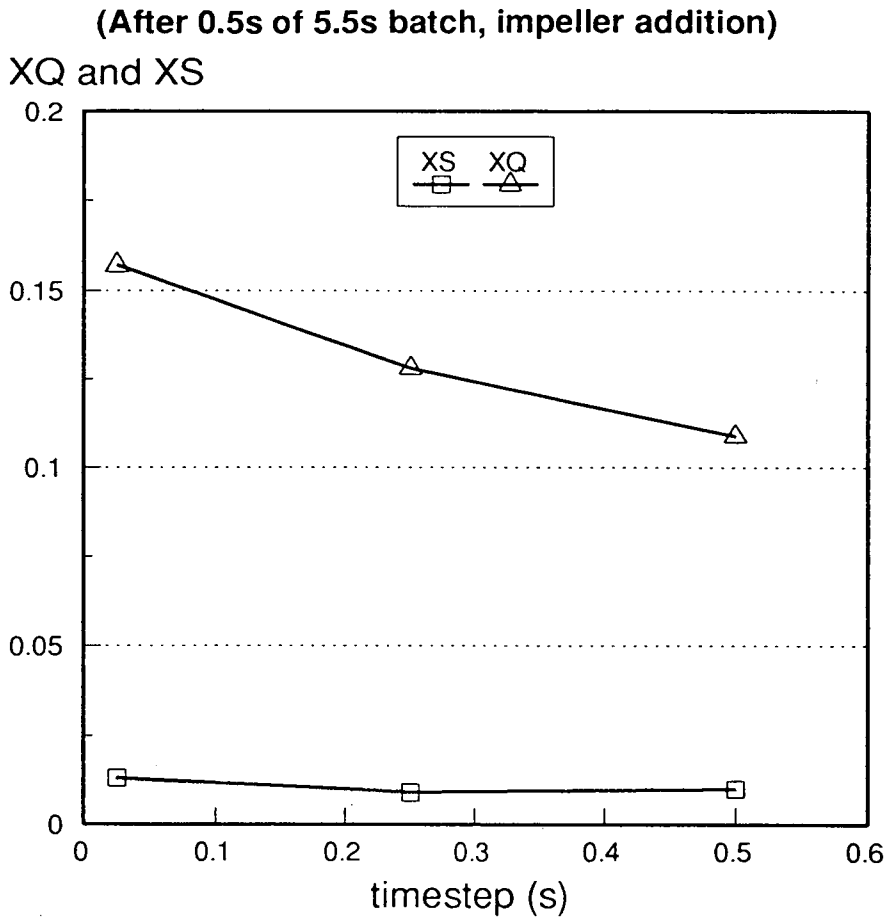

Figure 5.33 Effect of computational timestep on predicted X_Q and X_S

5.9 DISCUSSION OF RESULTS

5.9.1 Flow field

The Differential Stress turbulence model has been shown above to give better predictions than k-ε for average velocities in three-dimensional mixing processes. It represents more accurately the influence of turbulent stresses on the flow field. There are two possible reasons for this:

1. Relaxation of the linear (Boussinesq) relationship between turbulent stresses and velocity gradients

2. More accurate transport of turbulent stress

As described in Chapter 2, both reasons are likely to apply in a stirred vessel, where turbulent normal stresses are unequal in the impeller discharge and eddy diffusivities measured using LDA are not isotropic (e.g. Fawcett, 1992; Mahouast et al., 1989). The k-ε model does not account for these effects.

Details of the turbulence distribution predicted here with the standard Differential Stress model and boundary condition 2 are less accurate than mean velocities. For example, volume-integrated ε values account for only 53% of the energy input by the stirrer (calculated from the measured torque, equation 5.2.2). Fluctuating velocities are low by as much as 80% in some parts of the tank, although agreement is better in the impeller region.

Some processes are insensitive to local turbulence. For example, coarse-scale liquid blending in simple geometries (e.g. flow patterns with one major circulation loop) and distribution of solid particles are influenced mainly by average velocities. On the other hand, if turbulent diffusion is a controlling mixing parameter, inaccurate turbulence predictions can have a very significant effect. Furthermore, if fast chemical reactions are conducted under conditions where inertial-convective, viscous-convective or viscous-diffusive mixing are controlling, predictions of ε in particular should be as accurate as possible:

$$t_{ic} \propto \varepsilon^{-1/3} \tag{5.9.1}$$

$$E \propto \varepsilon^{1/2} \tag{5.9.2}$$

$$G \propto \varepsilon^{1/2} \tag{5.9.3}$$

Some consequences of these factors are discussed in Section 5.8.2 above. The relatively poor turbulence predictions can be attributed to:

1. Unmodelled energy input by the impeller
2. Transient nature of the real flow
3. UPWIND differencing

Taking these in turn, the impeller is assumed in present models to be a steady source of flow, momentum and energy. However, in reality, the blades move through the fluid in a time-dependent way. Modelling the impeller axi-symmetrically leads to zero gradients of all variables in the direction of rotation. Vortices shed by the real impeller are not modelled. These are responsible for substantial turbulence generation outside the impeller region. To improve on this aspect of the simulations requires time-dependent calculations with two grids, one for the impeller and one for the bulk flow, in relative motion.

Flow patterns in stirred tanks are transient due to the rotation of the impeller, but also show fluctuations of lower frequencies than the impeller rotation. The assumption of a fully time-averaged flow treats these low frequency oscillations as turbulence. For example, the LDA measurements would interpret these as a contribution to turbulent fluctuations. To resolve the details of these structures would also require transient simulation.

UPWIND differencing, as pointed out in Chapter 2, tends to flatten profiles by introducing false or "numerical" diffusion. It was necessary to use UPWIND for the DSM calculations presented here, because higher order schemes led to oscillating solutions. Higher order schemes were used for the k-ε runs and had little or no effect on predictions with that model. However, these capture velocity gradients more accurately, which leads to increased turbulence generation. Unconverged higher-order DSM calculations predicted volume-integrated ε values typically 80% of those measured by shaft torque, indicating that this route of improvement holds some promise.

Nevertheless the flow predictions above represent a substantial improvement over what has previously been standard modelling practise for stirred vessels. Computational cost increases with the DSM by a factor of about 3 compared to k-ε. However, using UPWIND differencing, quite accurate results were obtained on a relatively coarse grid (24,000 cells). Flow pattern predictions are sufficient for many practical design problems.

Apart from the validation studies, these simulations provide some quantitative insight into detailed geometric effects in mixing tanks. The effect of baffle-wall spacing has implications for blending of miscible fluids, drawdown of air, immiscible liquids and solid particles from the liquid surface and impeller power draw.

It is reassuring that the simulations predict intensified vortex motion on the liquid surface and increased power draw when there is no baffle-wall spacing. These results could be extended by simulating dip pipes or coils which are frequently immersed in stirred reactors. With complicated geometries, intuition and experience may be unable to predict the consequences for mixing performance. Solution of such problems via the k-ε model would almost certainly be incorrect, but the DSM is likely to succeed at least qualitatively.

5.9.2 Chemical reactions

Experimental studies with a complex reaction have underlined its sensitivity to mixing, with yield of primary products R & T varying from 44% to 73% when only agitation conditions are changed. Sensitivity to feed time illustrated the existence of a regime ($t_B<t_{min}$) in which increasing feed time can reduce yield of desired products, which occurs for very short feed times. Sensitivity to feed position was greatest for long feed times, since these conditions produce smaller reaction zones whose behaviour reflects local rather than global mixing rates. Addition of limiting reactant into the impeller region gave higher selectivity for desired products than surface addition, due to more intense local turbulence.

Flow computations have been used to test application of the MTPDF model developed in Chapter 3 to predict rates and yield of the reactions in a stirred tank reactor. Severe computational demands of time-dependent three-dimensional stiff equations meant that complete quantitative assessment of the model was not possible. A simplified two-dimensional flow field predicted using the DSM was used to provide a qualitative test of MTPDF in regimes controlled by both bulk- and fine-scale mixing.

When bulk mixing controlled (i.e. short feed times) the two-dimensional approximation was also least appropriate and agreement between model and experiment was poor. As feed time increased, agreement improved. This was interpreted as due to an improvement in the two-dimensional approximation and accurate modelling of fine-scale (e.g. inertial-convective and viscous-convective) mixing. Effects of feed time and feed position are qualitatively correct. In view of the accuracy of the tubular reactor simulations in Chapter 4, it seems reasonable to conclude that the principal sources of error are due to the simplified flow model.

UPWIND differencing would have tended to produce more rapid mixing than was actually present. Two-dimensionality also led to more rapid homogenisation, particularly in the tangential direction. Feed injection, trajectory and concentration were all affected in such a way as to ease the mixing problem. Taken together, these influences would cause the predicted side-product yields to be lower than measured. This was the case.

Acting against these influences, turbulence levels in the reactor were under-predicted, which would tend to retard turbulent diffusion, inertial-convective, viscous-convective and viscous-diffusive mixing rates. Turbulent diffusion tends not to limit bulk mixing in vessels with a single main circulation loop. The other three mixing stages are quite insensitive to turbulence errors: e.g. for a 50% error in ε, these change by not more than 25% (equations 5.9.1 to 5.9.3 above). The overall effect was therefore still to reduce side-product yield.

Some useful insights into the nature of complex reaction systems was obtained from the simplified simulations. The computed behaviour of the mixture during the batch time suggests that its behaviour is very complex, with time-dependent yields of some compounds exhibiting maxima and minima during the batch time. Unfortunately, no experimental data are available to test the validity of the transient profiles.

The shell program employed for these calculations, FLOW3D Version 2.4, was not optimal for problems with widely-varying timescales. The MTPDF model requires under-relaxation of most variables to secure convergence. However, the same under-relaxation factors and time step sizes had to be used for all variables and transport processes, which meant that an excessive number of iterations were required at each timestep. This caused CPU time to increase dramatically.

Under certain conditions, the MTPDF equations can be simplified to ease the computational task without much loss of generality, see Appendix A. Simplified versions are applicable, for example, to complex reactions of arbitrary speed in one-dimensional reactors. These versions are faster to compute but less general than the full 3-d version. They may give good estimates of performance of reactors with simplified flow patterns without excessive computational cost.

5.10 CONCLUSIONS

The MTPDF model developed in Chapter 3 has been combined with the flow model described in Chapter 2 and applied to the complex, three-dimensional, recirculating flow field in a stirred tank reactor. The average velocity distribution for a $T/3$ diameter pitched-blade turbine at $T/3$ clearance is well-predicted by the Differential Stress model. This is superior to the much-used k-ε, particularly in the upper part of the vessel. Insight into some subtle geometric effects on flow patterns and power consumption was gained with the aid of the improved model.

Chemical reactions conducted in the tank exhibited strong sensitivity to mixing, including feed rate, feed position and impeller speed. Simulation of the semi-batch experiments in three-dimensions required excessive CPU time (estimated 50 hours per run on a Cray 2 supercomputer). Mixing effects were qualitatively reproduced by a simplified (two-dimensional) flow field and chemical reaction model. Non-monotonic development of yield as a function of time during a batch run was predicted, which has been reported in practice. Reasons are given for discrepancies, which can be resolved when sufficient computer power becomes available.

Chapter 6

COST BENEFIT ANALYSIS OF CFD IN REACTOR SCALE-UP

6.1 INTRODUCTION & OBJECTIVES

The objective of this chapter is to determine under what conditions a CFD model should be used for scale-up of new chemical processes. Costs of traditional pilot-plant studies are compared with those of CFD using investment appraisal techniques.

6.2 BACKGROUND

Figure 6.1 shows a typical chemical production process layout. Raw materials enter the process from storage, are pre-treated before entering a reactor, where they react to form products and waste. Following the reactor, separation and purification take place, the product is pumped to storage and the waste recycled or treated before discharge.

Although very often taken for granted, the means by which fluids are mixed in chemical reactors can have a dramatic effect on the profitability of a chemical process. A recent survey of industrial needs in mixing research (AIChE, 1989; Smith, 1990) revealed that inadequate mixing costs the U.S. chemical industry between 0.5 and 3% of turnover, i.e. between 1 and 10 billion dollars per annum.

In what follows, attention is focused on development of new products and scale-up from laboratory to production scale. Other types of analysis could have been carried out, such as the cost benefits of troubleshooting existing processes with CFD. Scale-up of a new process was selected because it is a critical and often high-value activity.

Commercialisation of new chemical processes requires scale-up from chemical laboratory to full-scale production facility. Mixing behaviour always changes on scale-up, with the result that plant often under-performs. Two methods suggest themselves for solving this problem. One is to undertake process development at intermediate scales before constructing the large plant. This is the traditional chemical industry practice. The other is a new method based on CFD (Computational Fluid Dynamics). A cost benefit analysis is now used to evaluate these process development routes.

6.3 INVESTMENT APPRAISAL METHODS

There are several quantitative analysis methods available (e.g. Allen, 1980) to help discriminate between investment (process development) options., including:

- Net Present Value (*NPV*)
- Internal Rate of Return (*IRR*)

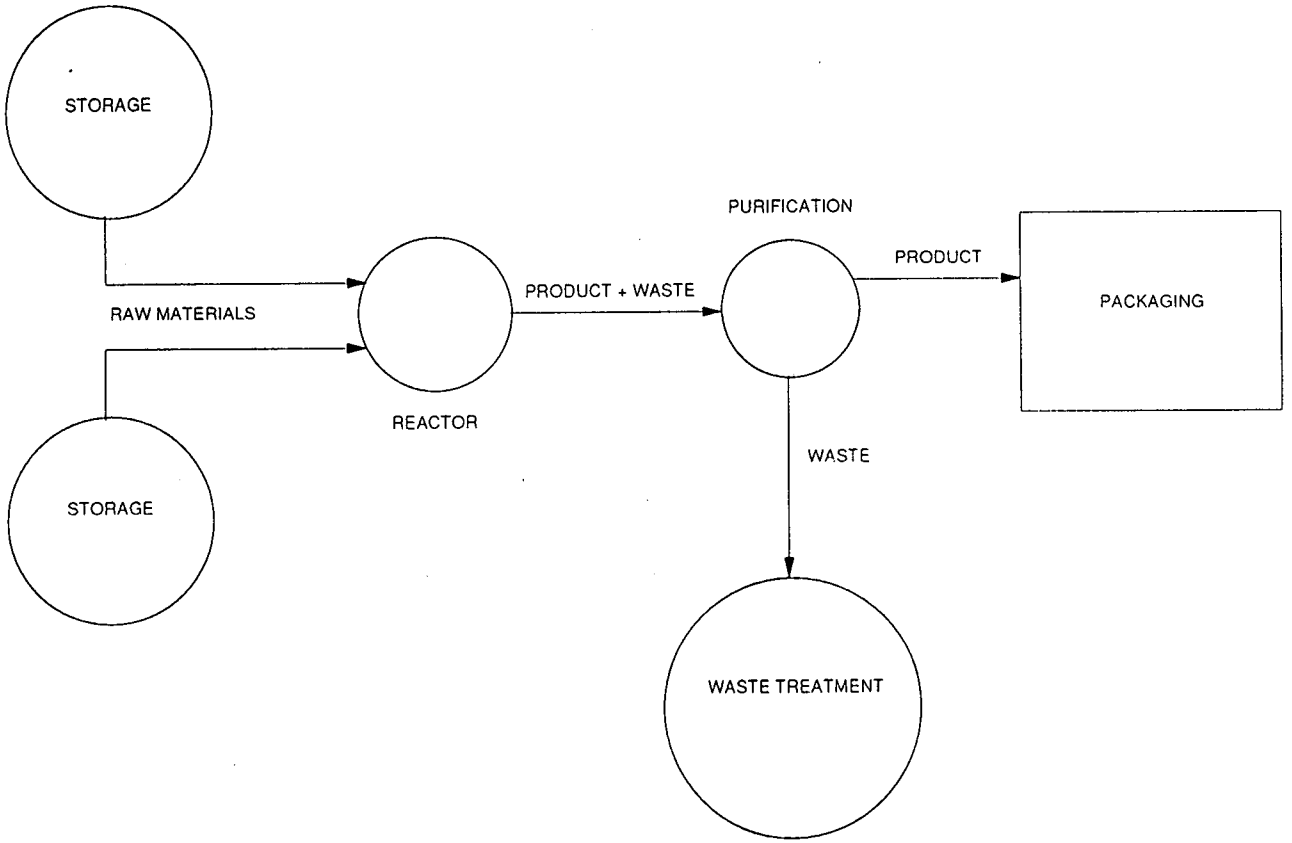

Figure 6.1 Schematic of stages in typical chemical production process

In practice, investment decisions are not always subjected to quantitative criteria, and choices are frequently made more for strategic or emotional reasons. However, even in the presence of such factors, the above methods are useful tools.

6.3.1 Net present value

Investments are made with the intention of exchanging cash now for future cash. Net Present Value (*NPV*) is the sum of the discounted cash flows over the life of the investment. Discounting means that future cash flows are discounted to their value based on the value of money at the time of the investment decision. The value of money changes with time as follows:

$$PV = \frac{C_n}{(1 + R)^n} \tag{6.3.1}$$

where *PV* denotes the present value of a cash flow *C* taking place *n* years from now. *R* is the discount rate. When *R* is positive, the value of a fixed number of money units (e.g. pounds) decreases with time.

NPV is given by:

$$NPV = \sum_1^n PV \tag{6.3.2}$$

Cash flows taken into account include capital investment, cost of raw materials, labour, revenue from sales and tax on profits. When *NPV* is positive, the investment results in a net positive cash flow for the company. If it is sufficiently positive, this may justify the investment. When selecting from a range of possible investments, the one with the highest *NPV* is the most valuable. If *NPV* is negative, the investment is unwise.

To apply *NPV* requires advance knowledge of the discount rate, *R*. There are no definite rules for selecting a suitable value of *R*. It should reflect the rate of interest which cash flows from the project would earn if invested wisely as soon as they arose. This is known as the "opportunity rate". It should also reflect the "cost of capital", i.e. the effective interest rate which has to be paid in order for any capital required to be raised from banks, shareholders or elsewhere. If predicted future cash flows take account of inflation, the discount rate should also reflect this. All three factors are difficult to predict at the outset of a project and it is wise to conduct a sensitivity analysis to the rate selected.

NPV analysis also requires that future cash flows are known in advance. These are rarely known with sufficient accuracy, reflecting the inherent uncertainty and risk in undertaking the project. All quantitative investment analysis techniques require this information.

Sensitivity of predictions to inaccurate forecasts is investigated in Section 6.4.4.

6.3.2 Internal rate of return

The Internal Rate of Return (*IRR*) is the discount rate which makes *NPV* equal to zero. If the investment has a higher *IRR* than a certain "hurdle rate", the project is acceptable. The hurdle rate generally equals *R*, the discount rate described above. Discriminating between projects, that with the highest *IRR* is the most valuable.

Application of *IRR* is similar to *NPV* except that *IRR* must be calculated iteratively by successive *NPV* calculations with different discount rates.

6.4 COST-BENEFIT ANALYSIS OF CFD

6.4.1 Factors taken into account

CFD as an alternative to pilot-plant (experimental) trials at several scales can shorten the time taken from product identification to commercialisation (scale-up). This will normally result in a significant cost benefit, roughly in proportion to the time saved.

The approach taken here is to compare a development project using traditional scale-up procedures with one using CFD. To simplify matters, the following assumptions have initially been made:

1. All the scale-up routes considered ultimately lead to the same design. This allows factors common to both designs to be eliminated from the differential cost benefit analysis. Only factors specific to each scale-up procedure are taken into account.

2. CFD is applicable to the design problem. In other words, the complexities of the problem fall within the limits of the capability of CFD. Models are assumed to require low to moderate CPU times (such as those in Chapter 4, for example). Approximate reaction kinetics data are available.

3. The investing organisation possesses or has easy access to a CFD facility (computer, software, trained personnel).

4. An existing pilot-plant can be modified to accommodate the new process by replacing its agitator and some minor auxiliaries.

5. Personnel are available to operate the pilot plant and analyze the results of experiments.

6. Future cash flows resulting from expenditure on process development and profits from sales of product can be reliably estimated.

7. Three stages of pilot-plant studies are required. Duration of each stage of pilot-trials is 1 year. Duration of the CFD stage is 1 year. This simplifies the *NPV* calculations.

8. Tax implications for the decision-making process can be ignored.

9. The appropriate discount factor, R, is 20%.

Some of these assumptions, particularly 1, 2, 6, 7 and 9, are later relaxed. The *NPV* analysis carried out focuses on Costs associated with each process development route. The *NPV* calculated here is therefore negative as it does not account for revenues; these are assumed to be sufficient to make the overall project attractive. The differential cost benefit analysis therefore compares relative costs of different options. This is quantified through ratios, e.g.:

$$R_c = \frac{NPV_{3,c}}{NPV_{CFD,c}} \tag{6.4.1}$$

where R_c denotes the ratio under conditions of complete certainty. If this is greater than 1.0, the CFD route is the better investment.

Cash flows taken into account for the base case are as follows:

- Labour and materials costs of pilot-plant studies
- Labour cost of CFD simulations
- Potential profits lost during development time
- Penalty for lateness into market

Labour costs have been estimated at £40 per man-hour. The number of man-hours required depends on such factors as the complexity of the work, the number of runs required in the pilot-plant and the number of alternatives considered in CFD. Materials and lost profits depend heavily on the type of product. For high end-value products, both labour and pilot-plant raw materials costs are likely to be insignificant compared to lost profits during development time.

There is a further potential cost related to the delayed arrival of product in the market-place. This is estimated here by a market penalty factor (*MPF*), which is applied as a multiple to the present value of profits lost in Year 1:

$$C_{MP,n} = MPF_n \, PV_{PR,1} \tag{6.4.2}$$

It varies from 0.0 (no delay) upwards and increases as the level of process development increases (because of increased development time). This choice is rather arbitrary, but there does not appear to be a better basis for estimation for a general process. Sensitivity of the decision to *MPF* is investigated in Section 6.4.4 below.

All of the above data were entered into a Lotus 123 spreadsheet. A sample input is shown in Table 6.1. The spreadsheet calculated cash flows using equations given in Appendix C. A sample output is shown in Table 6.2.

PARAMETERS		one stage	two stage	three stage	CFD			
Uncertainty of pilot-plant		0.80	0.40	0.20	0.20			
	Years late	0.00	1.00	2.00	3.00	4.00		
Put-right factor	PRF	0.00	1.60	1.20	1.00	0.90		
Market penalty	MPF	0.00	0.50	1.00	1.50	2.00		
Cost of man hour		40.00						
Production rate		1.00	m3/day					
Cost of raw mats.		100.00	per m3					
Cost waste t'ment		100.00	per m3					
Product profit		1000.00	per m3					
Disc. Rate (1+R)		1.20						
Inflation rate (1+I)		1.00						
Pilot Study	Scale	Build	No. runs	Probes	Man-hours	Duration	Raw Mats	Waste
Stage 1	0.15	1000.00	20.00	1000.00	80.00	365.00	0.05	0.05
Stage 2	0.60	10000.00	15.00	5000.00	200.00	365.00	2.55	2.55
Stage 3	1.83	30000.00	10.00	10000.00	800.00	365.00	48.14	48.14
CFD Study								
Full-scale	0.00	5000.00	10.00	0.00	80.00	365.00	0.00	0.00

Table 6.1 Lotus 123 input datasheet for cost-benefit analysis

CASH FLOWS							
Pilot Plant	Year 1	Year 2	Year 3	Year 4		CFD	Year 1
Build	1000.00	10000.00	30000.00			Grid	5000.00
Experiments	4200.00	13000.00	42000.00			Tests	3200.00
Raw mats.	5.30	254.50	4813.93				
Waste	5.30	254.50	2400.00				
Lost profits	365000.00	365000.00	365000.00	365000.00		Lost profits	365000.00
Total	370210.60	388509.00	444213.93			Total	373200.00
Discount	0.83	0.69	0.58	0.48		Discount	0.83
PV	308508.84	269797.92	257068.24			PV	311000.00
PV lost profits	304166.67	253472.22	211226.85			PV lost prf	304166.67
NPV (3 stage, certain)	1139541.67					NPV	311000.00
includes MPF							
NPV in uncertain conditions (MPF & PRF)							
Uncertainty	0.80	0.40	0.20			Uncertainty	0.20
NPV 1 stage	1022286.61					NPV CFD	551939.91
NPV 2 stage		1021714.16					
NPV 3 stage			1326829.48				
SUMMARY OF RESULTS							
Ratio (certain)	3.66						
Ratio (unc. 1 stage)	1.85						
Ratio (unc. 2 stage)	1.85						
Ratio (unc. 3 stage)	2.40						

Table 6.2 Lotus 123 worksheet output for cost-benefit analysis

6.4.2 Results for base case

The base case deals with a proposed development producing an average of 1 m^3 per day of a medium-value chemical product (such as paint, for example) with a profit (PR_V) of £1,000 per cubic metre (or approximately £1 per kilogramme). As a result, the cost of potential profits lost tends to dominate other factors in the calculation. For this calculation, it is assumed (see above) that all relevant parameters can be predicted without uncertainty.

From Table 6.3, row 1, column 3, it is clear that the CFD route is more cost-effective for the base case than three stages of pilot-plant trials. At a discount factor of 20% equation 6.4.1 gives a ratio R_c of 3.66. Under conditions of complete certainty the CFD route would be the appropriate choice for this particular project.

6.4.3 Effect of scale-up uncertainty

The above analysis assumes that the outcome is certain, but in practise, this will not be the case. A major source of uncertainty is confidence in scale-up procedures. The following assumptions are made for the purposes of calculating the effect of this parameter:

1. Uncertainties of successful scale-up (or probabilities of failure) after 1, 2 and 3 stages of pilot-plant work (U_1, U_2, U_3) are 0.8, 0.4 and 0.2, respectively. Uncertainty for scale-up after CFD (U_{CFD}) is 0.2.

2. Failure of the commercial scale plant to meet product specification will result in a delay of 1 year.

3. Failure of the plant if designed by CFD will be followed by three stages of pilot-plant development.

Assumption 7 above is thus relaxed, so it becomes possible to select one of four investment decisions: 1, 2 or 3 stages of pilot-plant, or CFD.

If the commercial scale plant does not perform to specification, costs will be incurred in putting it right. These will consist of further potential profits lost and the cost of any modifications required. The put-right cost is likely to vary depending on the amount of process development carried out in the scale-up procedure. If the procedure is thorough, the plant will require the minimum of modification. If not, replacement of complete items of equipment may be required. To estimate this effect, a Put Right Factor (*PRF*) has been used here which varies from 0.0 upwards (row 1 of Table 6.3), depending on the level of process development. Like *MPF*, this factor is used as a multiplier for the present value of lost profits in Year 1. Because one increases and one decreases with development time, *MPF* and *PRF* have opposite effects on *NPV*.

This increasingly complex picture is taken into account by calculating the *NPV* of costs assuming both success and failure and weighting these with their probabilities (*U*, see Appendix C). Note that the *NPV* of costs for both pilot-plant trials and CFD increases

significantly as soon as uncertainty is introduced (Table 6.2). The resulting ratio calculations for the base case are shown in the last three columns of row 1 in Table 6.3. Ratios for one, two and three stages of pilot-plant (R_1, R_2, R_3) all exceed 1.0, so CFD remains cheaper than pilot-plant work. However, the difference is less than before (R_c=3.66), due to uncertainty of success with CFD and the consequences of assumption 3 above. Sensitivity to these subjective probabilities is explored below.

6.4.4 Sensitivity analysis

Uncertainty enters the calculations through several factors which in practice are difficult to predict in advance. These include:

- discount rate, R
- confidence in scale-up procedures (U)
- production capacity (Q_P)
- profit per unit volume sold (PR_V)
- penalty for late arrival of product in the market-place (MPF)
- put-right cost of full-scale plant, in case of failure (PRF)

Put-right cost and penalty for lateness to market are likely to vary over orders of magnitude. The appropriate investment strategy can depend on the balance between these factors, which will depend in turn on the type of industry. For example, in pharmaceuticals MPF and PRF may be very high whereas in bulk chemicals they may be low. If both are low, sensitivity is also low.

Default values of all the above parameters are shown in row 1 of Table 6.2. In the following analysis, each parameter has the default value in row 1, unless sensitivity to that parameter is being investigated, i.e. normally only one parameter type is changed at a time. The parameter to which sensitivity is calculated is underlined.

Discount Factor, R

The simplest way to deal with uncertainty in the discount factor is to calculate NPV for upper and lower limits of R. Practical limits are 10% and 30%. Sensitivity to these is shown in Table 6.3 (rows 2 and 3). The above conclusion is not changed by varying R between these limits.

Scale-up Uncertainty

Subjective probabilities have been assigned to successful scale-up using any of the process development routes. 80%, 40% and 20% chances of failure were initially assigned to one, two or three stages of pilot studies and 20% to the CFD study. This suggests that there may be an optimum level of pilot-scale testing at which uncertainty is sufficiently reduced for further pilot tests to be unnecessary. This is reflected in almost equal costs under some circumstances for one and two stages of pilot-plant respectively. Changing these probabilities to 20%, 5% and 1% causes one stage of pilot-plant work to become cheaper than CFD (row 4 of Table 6.3).

TABLE 6.3 COST-BENEFIT ANALYSIS RESULTS

Parameters varied are shown underlined
Cost-benefit ratios are shown in **bold**

PR_V (£/m^3)	R %	R_c	U_1	U_2	U_3	U_{CFD}	PRF_1	PRF_2	PRF_3	PRF_4	MPF_1	MPF_2	MPF_3	MPF_4	R_1	R_2	R_3
1000	20	**3.66**	0.8	0.4	0.2	0.2	1.6	1.2	1.0	0.9	0.5	1.0	1.5	2.0	**1.85**	**1.85**	**2.40**
1000	10	**3.9**	0.8	0.4	0.2	0.2	1.6	1.2	1.0	0.9	0.5	1.0	1.5	2.0	**1.79**	**1.83**	**2.43**
1000	30	**3.48**	0.8	0.4	0.2	0.2	1.6	1.2	1.0	0.9	0.5	1.0	1.5	2.0	**1.9**	**1.86**	**2.38**
1000	20	**3.66**	0.2	0.05	0.01	0.2	1.6	1.2	1.0	0.9	0.5	1.0	1.5	2.0	**0.9**	**1.41**	**2.12**
1000	20	**3.66**	0.8	0.4	0.2	0.4	1.6	1.2	1.0	0.9	0.5	1.0	1.5	2.0	**1.29**	**1.29**	**1.67**
1000	20	**3.66**	0.8	0.4	0.2	0.6	1.6	1.2	1.0	0.9	0.5	1.0	1.5	2.0	**0.99**	**0.99**	**1.28**
10	20	**7.82**	0.8	0.4	0.2	0.2	1.6	1.2	1.0	0.9	0.5	1.0	1.5	2.0	**0.63**	**1.33**	**3.44**
10^5	20	**4.53**	0.8	0.4	0.2	0.2	1.6	1.2	1.0	0.9	0.5	1.0	1.5	2.0	**1.9**	**1.87**	**2.36**
1000	20	**3.66**	0.8	0.4	0.2	0.2	1.6	1.2	1.0	0.9	1.0	2.0	4.0	8.0	**1.53**	**1.65**	**2.39**
1000	20	**3.66**	0.8	0.4	0.2	0.2	1.6	1.2	1.0	0.9	0.0	0.0	0.0	0.0	**1.98**	**1.78**	**2.05**
10	20	**7.51**	0.8	0.4	0.2	0.2	1.6	1.2	1.0	0.9	0.0	0.0	0.0	0.0	**0.6**	**1.3**	**3.41**
10^5	20	**4.53**	0.8	0.4	0.2	0.2	1.6	1.2	1.0	0.9	1.0	2.0	4.0	8.0	**1.56**	**1.67**	**2.36**

The value of CFD uncertainty depends heavily on the technical details of the scale-up problem. For example, 20% is a fair estimate for a single-phase liquid application but in multi-phase processes, for example, an 80% chance of failure would be more likely. Calculations are sensitive to this parameter (rows 1,5 and 6 of Table 6.3). Increasing from 20% through 40% to 60% causes the ratio for one stage of pilot testing to drop from 1.85 through 1.29 to 0.99. For the present case study, 60% uncertainty is the maximum value at which any cost benefit could be expected from CFD calculations.

Production rate and profit per unit volume

Sensitivity to production rate and profit per unit volume have the same effect in this particular calculation, as the cost of lost profits is proportional to their product. In rows 7 and 8 of Table 6.3, profit is varied from £10 to £100000 per m^3. For a low profit item, one stage of pilot-plant is more economical than CFD. For a high profit good, the opposite is the case.

Lateness to Market

The cost of lateness to market is product- or market-specific, as pointed out above. Three sets of values for *MPF* have been used. The default is a linear increase from 0.0 (on-time) to 2.0 (4 years late) and is row 1 of Table 6.3. The second is an exponential increase from 1.0 (1 year late) to 8.0 (four years late) which might correspond to the situation with a new drug (row 9). The third is a zero penalty irrespective of lateness (row 10), which might correspond to a bulk chemical. Conclusions are not greatly affected by these variations and CFD remains the best alternative.

This unexpected result is obtained because the profit per unit volume is not varied at the same time as *MPF*. For a bulk chemical, both would be low, giving the values in row 11. For a new drug, both would be high, yielding row 12. These are more realistic values and reinforce the conclusions in the above sub-section.

6.5 CONCLUSIONS

A cost benefit analysis has been carried out on alternative routes of scale-up of new chemical processes. This shows that CFD, when technically applicable, tends to be more cost-effective than pilot-plant trials, particularly for high end-value goods.

However, CFD is not yet applicable to many types of scale-up problem, such as those involving multi-phase chemical reactions. Even for single-phase reactions, although the appropriate equations can be written down, realistic, quantitative, three-dimensional modelling remains computationally expensive (see Chapter 5). For these cases, pilot-plant trials are probably still more cost-effective.

Chapter 7

CONCLUSIONS AND RECOMMENDATIONS

7.1 ADVANCES IN PREDICTIVE MODELS AND VALIDATION

This thesis has concerned modelling fluid mixing in tubular reactors and stirred tanks, with and without homogeneous chemical reactions. Chemical process performance can depend strongly on these factors. Computational Fluid Dynamics has been used to predict localised effects in reactors and results have been validated by comparison with experimental measurements of velocities, impeller power consumption, chemical reaction rates and yields.

To compute the fluid flow patterns and turbulence levels, both k-ε and Differential Stress models (DSM) for the required Reynolds stress components have been used. A literature review in Chapter 2 suggested and simulations in Chapter 5 subsequently confirmed that in swirling flows, DSM makes better predictions of flow patterns, notably tangential velocities, than was previously possible with the widely used k-ε model. This is because effects such as anisotropy of the turbulent normal stresses and transport of turbulent shear stresses, which are present in stirred tanks, are allowed by the DSM model.

The turbulence levels predicted by the DSM are low compared to experimental measurements, similarly to k-ε, in the present study. This is attributed partly to use of UPWIND interpolation (see Chapter 2) in the calculation of convective fluxes.

A new closure model for turbulent chemically reacting flows has been developed, following an extensive literature review (Chapter 3). The MTPDF model provides a method of specifying chemical production and consumption terms in species transport equations, incorporating both effects of chemical kinetics and fluid flow and is quite easy to program into three-dimensional CFD programs. It is based on the concept of a multiple timescale decay of concentration fluctuations, which accounts for inertial-convective, viscous-convective and viscous-diffusive mixing.

The new closure model has been applied in conjunction with the above flow field predictions to tubular reactors and stirred tanks. Both simple and complex (multi-step) reactions have been considered, with different rate-controlling steps. Predictions in tubular reactors give good quantitative agreement, superior to models previously used in the literature. In stirred tanks, the model gives at least qualitative agreement: quantitative testing required an excessive amount of computer (Cray 2) time and was not possible at this stage. Useful experimental data for testing closure models has been gathered from a stirred tank in semi-batch operating mode.

7.2 INSIGHTS GAINED

The fluid flow (DSM) model was used to gain insight into the detailed flow patterns in stirred vessels. Three-dimensional simulations of a pitched-blade turbine agitator pumping downwards revealed some subtle, but important, flow structures. A small secondary flow loop exists under the impeller, in which velocities are lower than on the rest of the tank bottom. Experimentally, it is found that solid particles (denser than the liquid) accumulate in this region, despite being suspended in other parts of the vessel. When there is no baffle-wall spacing, intensified vortex motion is caused at the liquid surface, creating a flow pattern which appears well suited to incorporation of additives or powders. This also causes the impeller power draw to increase relative to the case with a $T/60$ baffle-wall spacing.

Measured (and predicted) large-scale turbulent velocity fluctuations are nearly homogeneous and nearly isotropic in the bulk of the stirred vessel. Both turbulence generation and dissipation are greatest near the impeller, where the large-scale turbulence is inhomogeneous and non-isotropic.

The chemical reaction (MTPDF) model was applied to single- and multi-step reactions in continuous-flow tubular reactors (Chapter 4). Using the flow fields predicted by the flow model as input, the coarse- and fine-scale distributions of reactants and products were calculated. The effect of the feed tube on local turbulence levels was illustrated. Positive correlation coefficients (or covariances of concentration fluctuations) for primary products of multi-step reactions, which subsequently reacted further, were predicted by the model. Furthermore, it appears that under certain conditions, yield from multi-step reactions does not increase monotonically from the inlet to the outlet.

In semi-batch operated stirred tanks (Chapter 5), several mixing-controlled regimes appear to exist, depending primarily on the feed time. With competitive-consecutive reactions, over a certain range of feed times, increasing feed time leads to increased yield of primary products. When feed time is very long, further increases do not affect yield. When feed time is very short, another regime appears to exist, whereby jet mixing by the feed itself causes yield to increase. These results are supported by findings in the literature.

The effect of feed position on yield from multi-step reactions was illustrated by both experiments and simulations with a five-step azo-coupling reaction scheme. Yield of primary products was much higher when limiting reactant was fed directly into the impeller region than on the liquid surface. This was due to more rapid initial mixing experienced by the feed jet.

The chemical reaction model applied to semi-batch reactors predicted a non-monotonic variation of yield as a function of time during the batch. This is partly explained by bulk circulation effects and is too complicated for a lumped parameter model to predict. It is also supported by literature data.

A cost-benefit analysis was carried on the use of CFD for scale-up of new chemical reaction processes (Chapter 6). This used investment appraisal techniques to evaluate CFD against several stages of pilot-plant development. The analysis showed that when CFD was technically applicable to the design problem, it was more cost-effective than pilot-plant trials, particularly for high end-value products. However, if the technical uncertainty associated with the CFD calculation was too great, pilot-plant trials were more cost-effective.

7.3 RECOMMENDATIONS FOR FUTURE WORK

Flow field

There is still much room for improvement of flow field simulations. A first step would be to use more accurate differencing schemes (e.g. QUICK) for the convection terms in all the transport equations. This would lead in particular to improved (higher) turbulence predictions.

A further improvement would be to develop a better model of the impeller region in stirred tanks. LDA measurements show that flow within the impeller is highly turbulent, but the boundary conditions used here do not reflect this. A model which treats the entire impeller zone as a boundary condition with specified velocities and turbulence quantities could be more successful. Such a method was employed by Ziman (1990) for a Rushton disc turbine.

Treating the impeller as a steady source of flow and turbulence in the present approach sets tangential gradients of all velocities to zero. This inhibits turbulence generation. To avoid this requires simulating the motion of the impeller blades through the fluid time-dependently. This would also remove the need to specify LDA data as input.

The above measures should significantly close the gap between simulations and reality, without having to change any of the DSM model constants.

Single-phase models provide vital understanding of basic processes but multi-phase reactors are of more practical interest. Extension of fluid flow models to predict effects such as bubble and drop size and local dispersed phase holdup would constitute an important next step.

Chemical reactions

Experimental data for testing chemical reaction closure models is lacking, especially for multi-step reactions in well-defined flow fields. Data are needed which span the entire range of mixing-controlled regimes. Measurements of reaction yield as a function of time in semi-batch reactors and position in continuous reactors would also be useful. These data, combined with more accurate flow field predictions, will provide more stringent tests of closure models.

The concepts used in the MTPDF model could be extended to non-isothermal reactions by solving extra equations for the temperature field inside and outside the reaction zone. The approach to this extension is summarised in Appendix B. If valid, this would bring non-isothermal reactions within the grasp of the method, which would be useful for reactions where heat release (exothermic) or absorption (endothermic) are significant. Once again, data to validate non-isothermal closure models is required.

Once reliable multi-phase flow models are available, single-phase chemical reaction models such as MTPDF should provide a good basis for developing multi-phase models. This development would make a whole range of important industrial reactions amenable to optimisation using CFD.

Numerical modelling

To describe complex processes, such as multi-step reactions, simultaneous heat and mass transfer and multi-phase flows, requires a large number of transport equations to be solved simultaneously. This thesis has revealed a persistent limitation of practical Computational Fluid Dynamics in complex flows to steady-state conditions with relatively coarse grids.

Complete and thorough simulation of for instance a semi-batch liquid-phase reactor would typically require up to 25 transport equations and at least 100,000 cells. To achieve timestep-independence might require several thousand timesteps. More efficient numerical algorithms and faster, cheaper computers will be required if these problems are to be tackled routinely using CFD.

REFERENCES

AIChE, Report of the Mixing 3A Workshop on Industrial Needs for Mixing Research, held at University of Maryland, U.S.A., March 22-23, 1989

Allen, D. H., 'A Guide to the Economic Evaluation of Projects', 2ed., Institution of Chemical Engineers, Rugby, England, 1980

Armstrong, S. G. & S. Ruszkowski, 'Measurement and comparison of flows generated by different types of impeller in a stirred tank', FMP Report 024, BHR Group Limited, Cranfield, Bedford, England, April 1986.

Bakker, A., 'Hydrodynamics of stirred gas-liquid dispersions', PhD Thesis, Delft University of Technology, The Netherlands, 1992

Baldyga, J. 'Turbulent mixer model with application to homogeneous instantaneous chemical reactions', Chem. Eng. Sci., 44, p.1175, 1989

Baldyga J. & J. R. Bourne, 'A fluid mechanical approach to turbulent mixing and chemical reaction', Chem. Eng. Comm, 28, p.259, 1984

Baldyga, J. & J. R. Bourne, 'Simplification of micromixing calculations', Chem. Eng. J., 42, p.83, 1989

Baldyga, J. & J. R. Bourne, 'Interactions between mixing on various scales in stirred tank reactors', Chem. Eng. Sci., 47, p.1839, 1992

Bird, R. B., W. E. Stewart & E. N. Lightfoot, Transport Phenomena, John Wiley & Sons, New York, 1960

Bolour-Froushan, A. H. 'Prediction of single-phase turbulent flow in agitated mixing vessels', PhD Thesis, University of London, 1986

Bourne, J. R. & H. L. Toor, 'Simple criteria for mixing effects in complex reactions', AIChEJ., 23, p.602, 1977

Bourne, J. R., U. Morgelli & P. Rys, 'Mixing and fast chemical reaction: effect of viscosity on product distribution', Proc. 2nd Euro. Conf. on Mixing, paper B3, p.41, BHRA Fluid Engineering, Cranfield, Bedford, England, 1977

Bourne, J. R., F. Kozicki, & P. Rys, 'Mixing and fast chemical reaction I', Chem. Eng. Sci., 10, p.1043, 1981

Bourne, J. R. & G. T. Tovstiga, 'Micromixing and fast chemical reactions in a turbulent tubular reactor', Chem. Eng. Res. Des., 66, p.26, 1988

Bourne, J. R. & C. P Hilber, 'The productivity of micromixing-controlled reactions: Effect of feed distribution in stirred tanks', Trans. I. Chem. E., 68, Part A, p.51, 1990

Bourne, J. R., O. Kut & J. Lenzner, 'An improved reaction system to investigate micromixing in high intensity mixers', Ind. Eng. Chem. Res., 31, p.949, 1992

Bradshaw, P., 'Effects of streamline curvature on turbulent flow' AGARDograph, 169, 1973

Brucato, A., M. Ciofalo, F. Grisafi & L. Rizzuti, 'Computer simulation of turbulent fluid flow in baffled and unbaffled tanks stirred by radial impellers', Computer Applications to Batch Processes, Cengio, Italy, March 1990

Chella, R. & J. Ottino, 'Conversion and selectivity modifications due to mixing in unpremixed reactors', Chem. Eng. Sci., 39, p.551, 1984

Chou, P. Y., 'On velocity correlations and the solutions of the equations of turbulent fluctuation', Quart. J. App. Math. 3, p.38, 1945

Clarke, D. S. & N. S. Wilkes, 'The calculation of turbulent flows in complex geometries using a Differential Stress Model', AERE R13428, Harwell Laboratory, Oxfordshire, U.K., 1989

Clarke, D. S., J. R. Moore & N. S. Wilkes, 'Prediction of turbulent swirling flows through quarled burners using Reynolds Stress turbulence models', AERE R13726, Harwell Laboratory, Oxfordshire, U.K., 1990

Corrsin, S. 'The isotropic turbulent mixer: Part II Arbitrary Schmidt Number', AIChEJ., 10, p.870, 1964

Daly, B. J. & F. H. Harlow, 'Transport equations in turbulence', Phys. Fluids, 13, p.2634, 1970

Donaldson, C. Du P., in 'Turbulent Mixing in Nonreactive and Reactive Flows', ed. S.N.B. Murthy, Plenum Press, New York, p.131, 1975

Dutta, A. & Tarbell, J. M., 'Closure models for turbulent reacting flows', AIChEJ., 35, p.2013, 1989

Eswaran, V. & S. B. Pope, 'Direct Numerical Simulations of the turbulent mixing of a passive scalar', Phys. Fluids, 31, p.506, 1988

Fawcett, N., 'Estimation of the turbulent energy dissipation rate at the discharge of pitched blade turbines from LDA data: a preliminary study', FMP Interim Report 1066, BHR Group Limited, Cranfield, Bedford, England, February 1992

Gibson, M. M., W. P. Jones, J. J. McGuirk & J. H. Whitelaw, Lecture notes for Turbulence Models in Computational Fluid Dynamics, Imperial College London, 1990

Grenville, R. K., 'Calculation procedures and database for mixing times: Proposed format', FMP Interim Report, 1043, BHR Group Limited, Cranfield, Bedford, England, August 1989

Guiraud, P., J. Bertrand, & J. Costes, 'Laser measurements of local velocity and concentration in a turbulent jet-stirred tubular reactor', Chem. Eng. Sci., 46, p.1289, 1991

Hanjalic, K. & B. E. Launder, 'A Reynolds stress model of turbulence and its application to thin shear flows', J. Fluid Mech., 52, p.609, 1972

Harada, M., K. Arima, W. Eguchi & S. Nagata, 'Micromixing in a continuous flow reactor', Mem. Fac. Eng. Kyoto Univ., 24, p.431, 1962

Harvey, P. S., 'The modelling and prediction of turbulent flow in an agitated vessel', PhD Thesis, University of Bath, U.K., 1980

Hearn, S., Private Communication to J. Hannon, 1992

Hutchings, B. J., R. J. Weetman & B. R. Patel, 'Computation of flow fields in mixing tanks with experimental verification', ASME Annual Meeting, San Francisco, Dec. 10-15, 1989

Jaworski, Z., A. W. Nienow, E. Koutsakos, K. Dyster & W. Bujalski, 'An LDA study of turbulent flow in a baffled vessel agitated with a pitched blade turbine', Trans. I. Chem. E., 69, Part A, p.313, 1991

Jones, W. P. & J. H. Whitelaw, 'Calculation methods for reacting turbulent flows: a review', Combustion & Flame, 48, p.1, 1981

Kresta, S. & P. E. Wood, 'Prediction of the three-dimensional turbulent flow in stirred tanks', AIChEJ., 37, p.448, 1991

Kolmogoroff, A. N., 'The local structure of turbulence in incompressible viscous fluid for very large Reynolds numbers', Compt. Rend. Acad. Sci. URSS, 30, p.301, 1941

Launder, B. E., G. T. Reece & W. Rodi, 'Progress in the development of a Reynolds stress turbulence closure', J. Fluid Mech., 68, p.537, 1975

Launder, B. E., 'Second moment closure and its use in modelling turbulent industrial flows', Int. J. Num. Meth. in Fluids, 9, p.963, 1989

Leonard, A. D. & J. C. Hill, 'Direct numerical simulations and simple closure theory for a chemical reaction in homogeneous turbulence', in Turbulent Reactive Flows, R. Borghi, S.N.B Murthy, eds., Springer-Verlag, New York, 1989

Li, K. T. & H. L. Toor, 'Turbulent reactive mixing with a series-parallel reaction: Effect of mixing on yield', AIChEJ., 32, p.1312, 1986

Liu, C. H. & C. H. Barkelew, 'Numerical analysis of jet stirred reactors with turbulent flows and homogeneous reactions', AIChEJ., 32, p.1813, 1986

Mahouast, M., G. Cognet & R. David, 'Two-component LDV measurements in a stirred tank', AIChEJ., 35, p.1770, 1989

Mao, K.W., & H. L. Toor, 'A diffusion model for reactions with turbulent mixing', AIChEJ., 16, p.49, 1970

Mao, K.W. & H. L. Toor, 'Second order reactions with turbulent mixing', Ind. Eng. Chem. Fund., 10, p.192, 1971

McKelvey, K. N., H. Yieh, S. Zakanycz & R. S. Brodkey, 'Turbulent motion, mixing and kinetics in a chemical reactor configuration', AIChEJ., 21, p.1165, 1975

Mehta, R.V. & J. M. Tarbell, 'Four-environment model of mixing and chemical reaction' AIChEJ., 29, p.320, 1983

Middleton, J. C., F. Pierce & P.M. Lynch, 'Computation of flow fields and complex reaction yield in a turbulent stirred reactor and comparison with experimental data', Chem. Eng. Res. Des., 64, p. 18, 1988

Musgrove, M., Private Communication to J. Hannon, 1992

Oosthuizen, P. H. & M. C. Wu, 'Experimental and numerical study of constant diameter ducted jet mixing', Turbulent Shear Flows I, Durst, F. et al., eds., Springer-Verlag, 1979

Patterson, G. K. 'Application of turbulence fundamentals in reactor modelling and scale-up', Chem. Eng. Comm., 8, p.25, 1981

Pericleous, K. A. & M. K. Patel, 'The modelling of tangential and axial agitators in chemical reactors', Physicochemical Hydrodynamics, 8, p.105, 1987

Placek, J., L. L. Tavlarides, G. W. Smith & I. Fort, 'Turbulent flow in stirred tanks, Part 2: A two-scale model of turbulence', AIChEJ., 32, p.1771, 1986

Pohorecki, R. & J. Baldyga, 'New model of micromixing in chemical reactors', Ind. Eng. Chem. Fund., 22, p.392, 1983

Ranade, V. V., J. B. Joshi & A. G. Marathe, 'Flow generated by pitched blade turbines, 2' Simulation using k-ε model', Chem Eng. Comm., 81, p.225, 1989

Ranade, V. V. & J. R,. Bourne, 'Reactive mixing in agitated tanks', Chem. Eng. Comm., 99, p.33, 1991

Ranade, V. V. 'Decoupling of micro- and macromixing in turbulent reactive flow', AIChEJ., 38, p.467, 1992

Ritchie, B. W. & A. H. Tobgy, 'A three environment micromixing model for chemical reactors with arbitrary separate feed streams', Chem. Eng. J., 17, p.173, 1979

Rosensweig, R. E. 'Idealised theory for turbulent mixing in vessels', AIChEJ., 10, p.91, 1964

Schetz, J. A. 'Injection & Mixing in Turbulent Flow', AIAA, New York, 1980

Smith, J. M., 'Industrial Needs for Mixing Research', Trans. I Chem. E., 68, Part A, p.3, 1990

Spalding, D. B. 'Concentration fluctuations in a round turbulent free jet', Chem., Eng. Sci., 26, p.95, 1971

Studer, M., 'Ablauf schneller Reaktionen in Rotor-Stator-Mischern verschiedener Grosse', Dissertation ETH No. 9037, ETH Zurich, 1990.

Tennekes, H. & J. L. Lumley, 'A first course in turbulence', MIT Press, Cambridge, Ma., 1972

Toor, H. L., 'Turbulent mixing of two species with and without chemical reactions', Ind. Eng. Chem. Fund. 8, p.655, 1969

Tovstiga, G. T., 'Micromixing & fast chemical reactions in a turbulent tubular reactor', Dissertation ETH No. 8111, ETH Zurich, 1986

Van't Riet, K., W. Brujin & J. M. Smith, 'Real and pseudo-turbulence in the discharge stream from a Rushton turbine', Chem. Eng. Sci., 31, p.407, 1976

Vassilatos, G. & H. L. Toor, 'Second order chemical reactions in a nonhomogeneous turbulent fluid', AIChEJ., 11, p.666, 1965

Villermaux, J. & J. C. Devillon, Represetation de la coalescence et la redispersion des domaines de segregation dans un fluide pars un model d'interaction phenomenologique', Symp. Chem. React. Eng., paper B1-13, Elsevier, 1972

Warhaft, Z. & J. L. Lumley, 'An experimental study of the decay of temperature fluctuations in grid-generated turbulence', J. Fluid Mech., 88, p.659, 1978

Warhaft, Z. 'The interference of thermal fields from line sources in grid turbulence', J. Fluid Mech., 144, p.363, 1984

Wu, H. & G. K. Patterson, 'Laser Doppler measurements of turbulent flow parameters in a stirred mixer', Chem. Eng. Sci., 44, p.2207, 1989

Younis, B. A., 'On modelling the effects of streamline curvature on turbulent shear flows', PhD Thesis, University of London, 1984

Ziman, H. J., 'A computer prediction of chemically reacting flows in stirred tanks', PhD Thesis, Imperial College London, 1990

APPENDIX A: SIMPLIFIED VERSIONS OF MTPDF

Simplified versions of MTPDF can be derived for application to particular sets of reaction conditions. Some examples include:

Rapid inertial-convective and viscous-diffusive mixing

When viscous-diffusive and inertial-convective mixing are rapid relative to reaction and other mixing steps, MTPDF reduces to the two subgroup model of Ranade & Bourne (1991). A possible scenario is slow feeding of concentrated reactant into the bulk of a low viscosity semi-batch reaction process. This requires one less equation than MTPDF.

Rapid inertial-convective, viscous-convective and viscous-diffusive mixing

Under these conditions, MTPDF reduces to the Laminar model. A possible scenario is rapid feeding, such as in a batch reactor. Equations are then only required for volume-averaged species concentrations.

Rapid radial mixing

When coarse-scale concentration gradients can be ignored, e.g. in a turbulent pipeline fitted with motionless mixing elements, a one-dimensional version of MTPDF could be used. This would require equations for segregated and reaction zone volume fractions and reaction zone concentrations only.

APPENDIX B: MTPDF IN NON-ISOTHERMAL FLOWS

The MTPDF model developed in this work for isothermal flows can be extended to non-isothermal situations as follows. A transport equation for the volume-averaged enthalpy can be written in the same way as one for concentration of a chemical species:

$$\frac{DH}{Dt} = S_H \tag{B.1}$$

where:

$$H = \rho C_p T \tag{B.2}$$

and S_H denotes a source of enthalpy, such as heat generated or absorbed by a chemical reaction. Enthalpy in the reaction zone is given by an energy balance between the segregated, reaction and environment zones:

$$\frac{D\alpha_r H_r}{Dt} = \frac{1}{t_{ic}}\alpha_s(1-\alpha_s)H_s + E^*\alpha_r H_e + \Omega_i \Delta H_r \alpha_r \tag{B.3}$$

where ΔH_r denotes the heat of reaction, which can be either positive (exothermic) or negative (endothermic). Both B.1 and B.3 can be rearranged into equations for temperature using B.2, from which the dependence of the reaction velocity constant on temperature can be obtained using Arrhenius parameters:

$$k = A\exp-\frac{E}{RT_r} \tag{B.4}$$

In the most general case, material properties in each zone, such as density, viscosity, diffusion coefficient and specific heat capacity can also take on local temperature-dependent values, if the appropriate functions are supplied as input. Enthalpies in the three zones are related to volume-averaged enthalpy by:

$$H = \alpha_s H_s + \alpha_r H_r + \alpha_e H_e \tag{B.5}$$

If H_s is assumed to retain a constant value (as the MTPDF model assumes for feed concentration), equations B.3 & B.5 can be used to obtain enthalpies in all three zones. The micromixing model of Baldyga & Bourne can be adapted similarly (e.g. Studer, 1990) and non-isothermal reaction models are widespread in combustion. The latter, however, do not account for the influence of viscosity and diffusion coefficient, which can be significant in liquids.

APPENDIX C: EQUATIONS USED IN COST BENEFIT ANALYSIS

The following procedure was used for the cost benefit analyses presented in Chapter 6.

Inputs

Uncertainties, U_1, U_2, U_3, U_{CFD}
Put-right factors, PRF_1, PRF_2, PRF_3, PRF_4
Market Penalty Factors, MPF_1, MPF_2, MPF_3, MPF_4
Cost of a man-hour C_{MH}
Production Rate Q_P
Cost of raw materials per unit volume, C_{RMV}
Cost of waste treatment per unit volume C_{WV}
Product profit per unit volume, PR_V
Discount Rate, R
Scale of pilot plants, T_1, T_2, T_3
Construction costs, C_{CON1}, C_{CON2}, C_{CON3}
Number of runs, N_{RP1}, N_{RP2}, N_{RP3}
Cost of instrumentation, C_{INST1}, C_{INST2}, C_{INST3}
Number of man-hours required, N_{MH1}, N_{MH2}, N_{MH3}
Duration of studies, 365 days each

See, for example, Table 6.1.

Equations

Raw materials volume is given by:

$$V_{RM} = \pi \frac{T^3}{4} N_{RP} \tag{C.1}$$

where T is the pilot scale vessel diameter and N_{RP} is the number of pilot scale runs carried out. The volume of waste V_W is equal to the volume of raw materials. The running costs of experiments in the pilot plant or CFD simulations are obtained from:

$$C_{EX} = N_{MH}\, C_{MH} + C_{INST} \tag{C.2}$$

where N_{MH} and C_{MH} denotes the number and cost of man-hours respectively. C_{INST} is the cost of any instrumentation required, which was entered separately into the worksheet (see Table 6.1). The cost of raw materials is then obtained from:

$$C_{RM} = V_{RM}\, C_{RMV} \tag{C.3}$$

where C_{RMV} denotes the cost per unit volume.

Waste treatment costs for the pilot plant are obtained from:

$$C_W = V_W \, C_{WV} \tag{C.4}$$

where C_{WV} is the cost of treating one cubic metre of waste. The cost of lost profits is obtained from:

$$C_{PR} = 365 \, Q_P \, PR_V \tag{C.5}$$

where Q_P denotes production rate and PR_V profit per unit volume.

The discount multiplier for a cash flow in year n is obtained from:

$$D_n = \frac{1}{(1+R)^n} \tag{C.6}$$

The present value of a cash flow in year n is then:

$$PV_n = D_n \, C_n \tag{C.7}$$

This was applied to all the cash flows above and some others entered directly as inputs (see Table 6.2). *NPV* is obtained from:

$$NPV_n = \sum_1^n PV_n \tag{C.8}$$

The present value of profits arising in year n is:

$$PV_{PR,n} = C_{PR} \, D_n \tag{C.9}$$

The market penalty cost of arriving n years late is:

$$C_{MP,n} = MPF_n \, PV_{PR,1} \tag{C.10}$$

The above equations apply under conditions of certainty, i.e. when the full-scale plant is guaranteed to work properly. More realistically, probabilities were assigned to failure, depending on the amount of development carried out. Fault trees were used to work out the resulting *NPV*, with subjective probabilities applied to each possible outcome. The *NPV* of n stages of pilot plant is then given by:

$$\begin{aligned} NPV_{n,uc} &= NPV_{n,c} \, (1-U_n) \\ &+ U_n \, (MPF_{n-1} \, PV_{PR,1} + PRF_{n-1} \, PV_{PR,1} + NPV_{n,c} + PV_{PR,n+1}) \end{aligned} \tag{C.11}$$

For CFD, when failure is followed by three stages of pilot-plant work:

$$NPV_{CFD,uc} = NPV_{CFD,c}\,(1-U_{CFD}) + U_{CFD}\,U_3\left(NPV_{CFD,c} + MPF_3PV_{PR,1} + \frac{NPV_{3,c}}{1+R}\right) + U_{CFD}\,(1-U_3)\left(NPV_{CFD,c} + \frac{NPV_{3,c} + PV_{PR,A}}{1+R} + PRF_4PV_{PR,1} + MPF_4PV_{PR,1}\right) \quad \text{(C.12)}$$

APPENDIX D: COMPARATIVE PLOTS FROM LDA AND CFD

The following set of twelve graphs displays the same data as Figures 5.6, 5.7, 5.17, 5.18, 5.19 and 5.20, but in greater detail. In particular, absolute values of velocities and positions can be quantitatively read.

On each graph, LDA measurements and CFD predictions of all three components of either mean or fluctuating velocities are given. LDA data are denoted by symbols and CFD by curves.

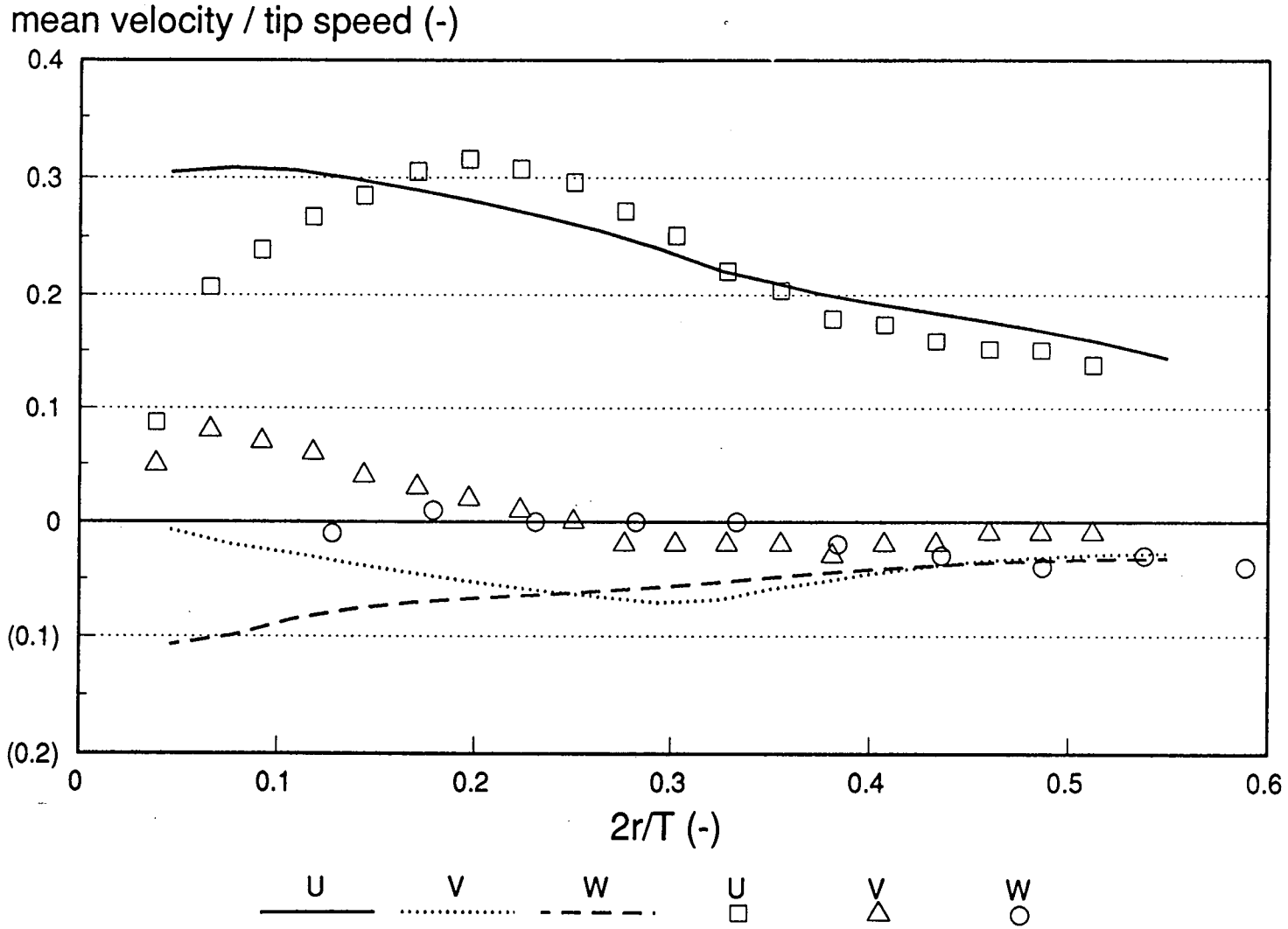

Figure D.1 Mean velocities on the impeller top surface (x=0.190 m)

Curves denote CFD and symbols LDA data.

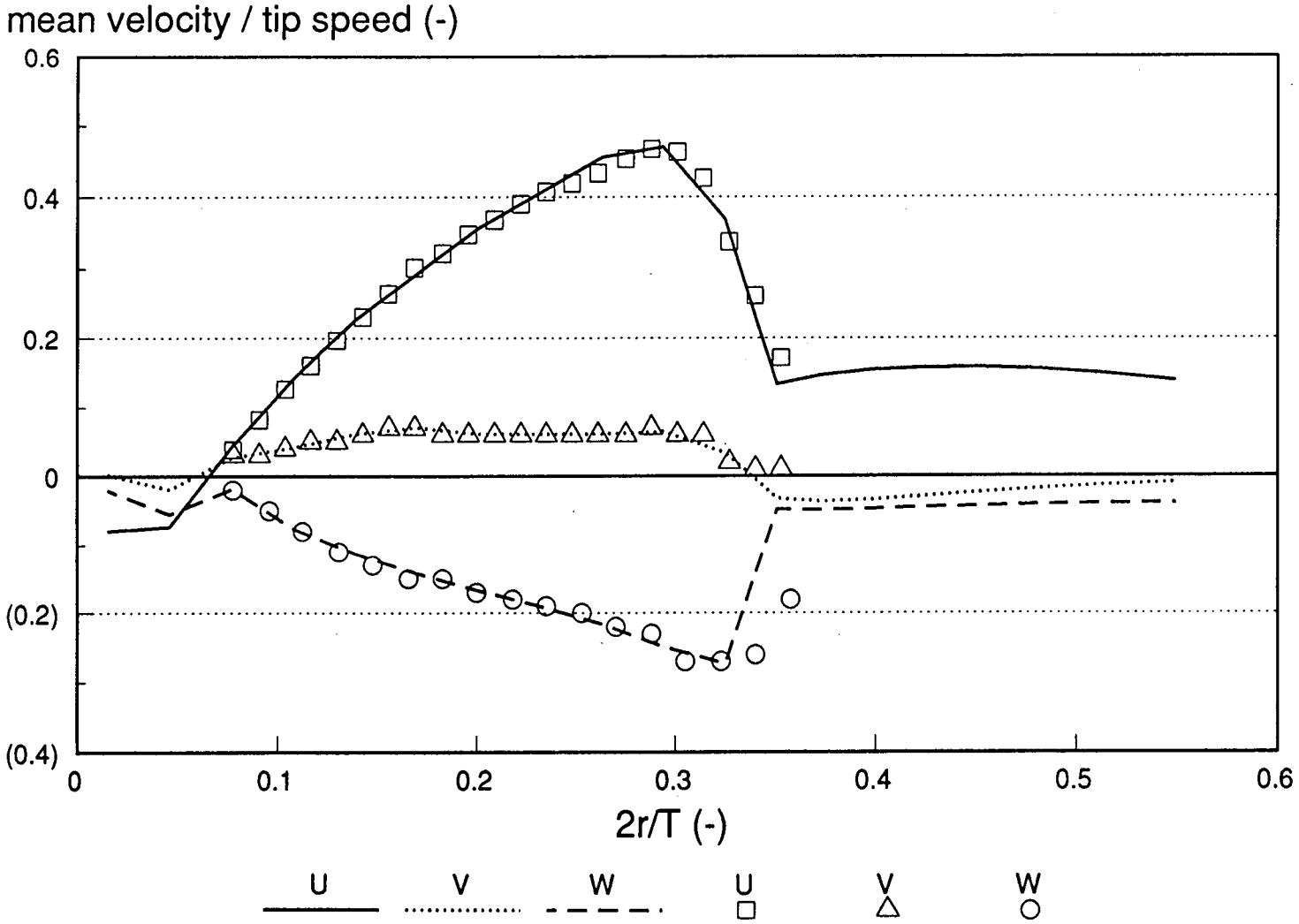

Figure D.2 Mean velocities on the impeller bottom surface (x=0.203 m)

Curves denote CFD and symbols LDA data.

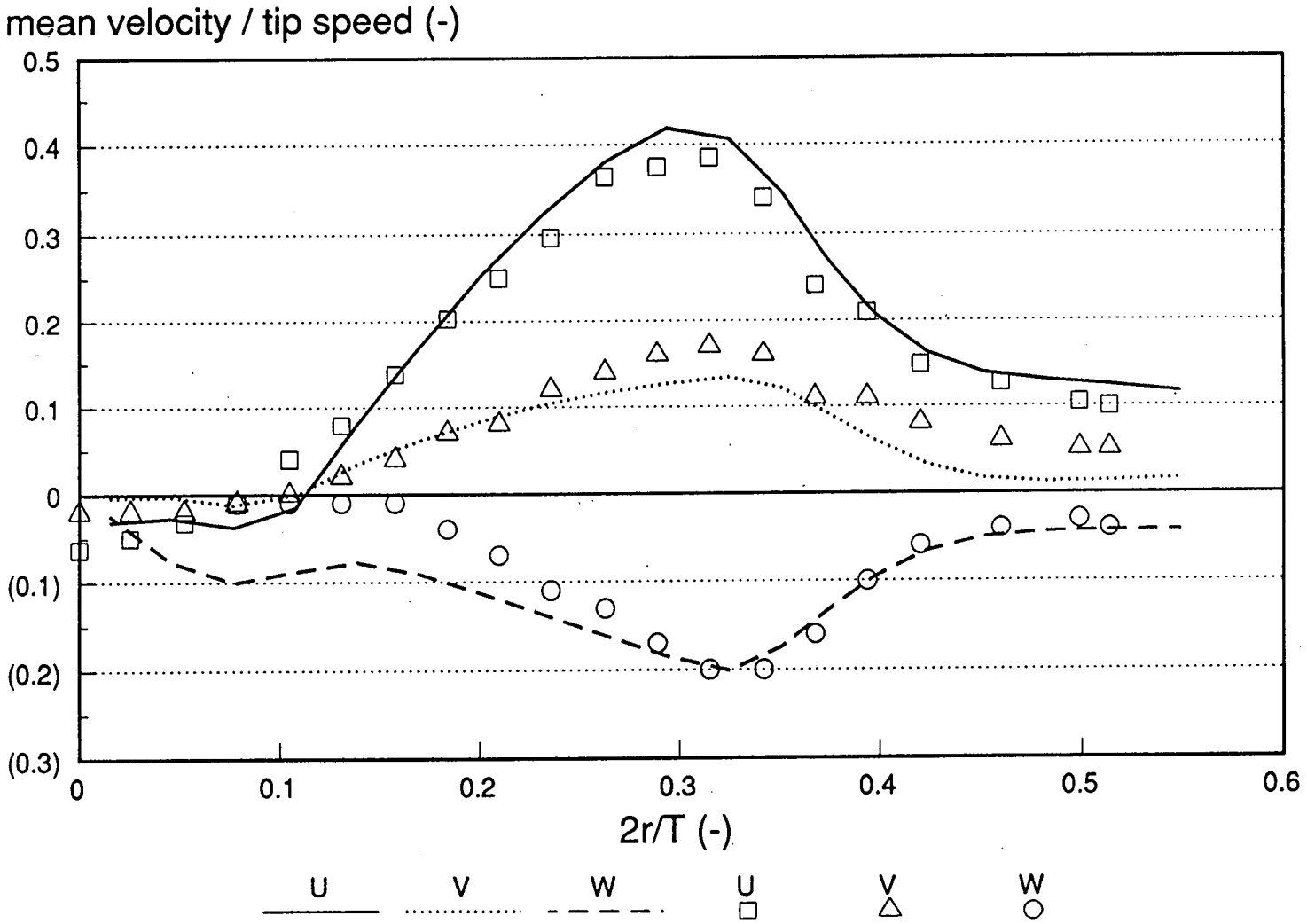

Figure D.3 Mean velocities at x=0.238 m

Curves denote CFD and symbols LDA data.

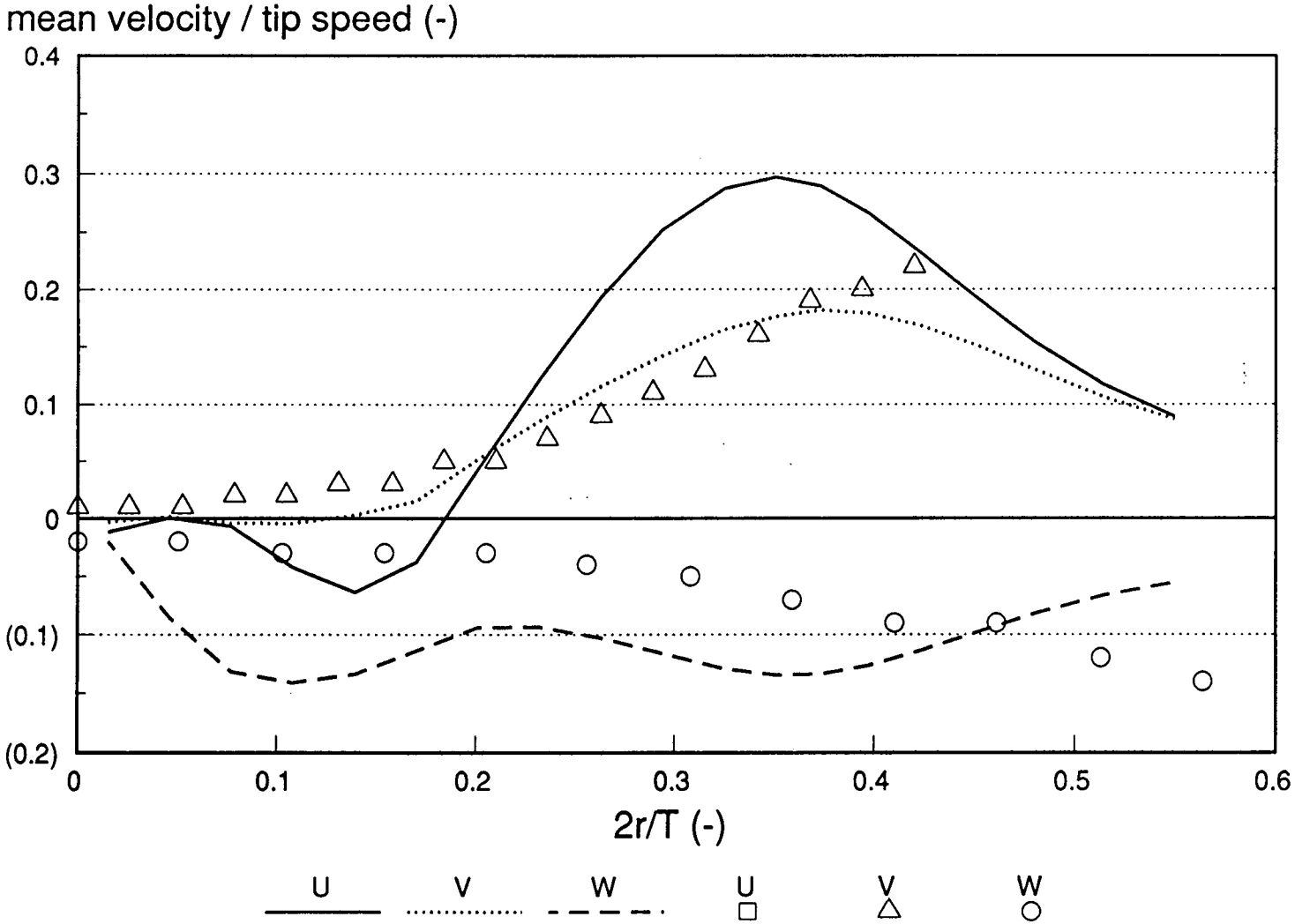

Figure D.4 Mean velocities at x=0.263 m

Curves denote CFD and symbols LDA data.

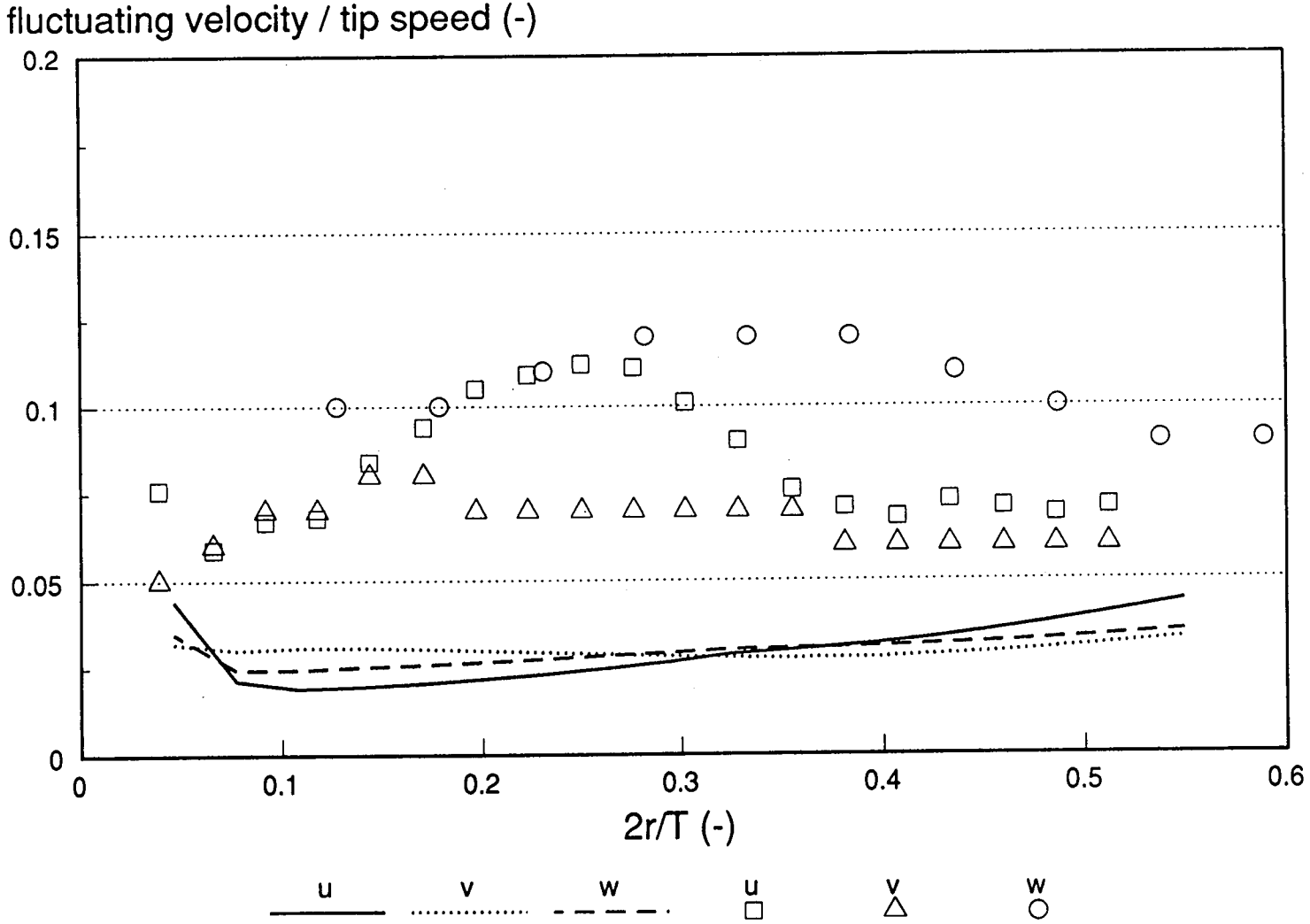

Figure D.5 Fluctuating velocities on the impeller top surface (x=0.190 m)

Curves denote CFD and symbols LDA data.

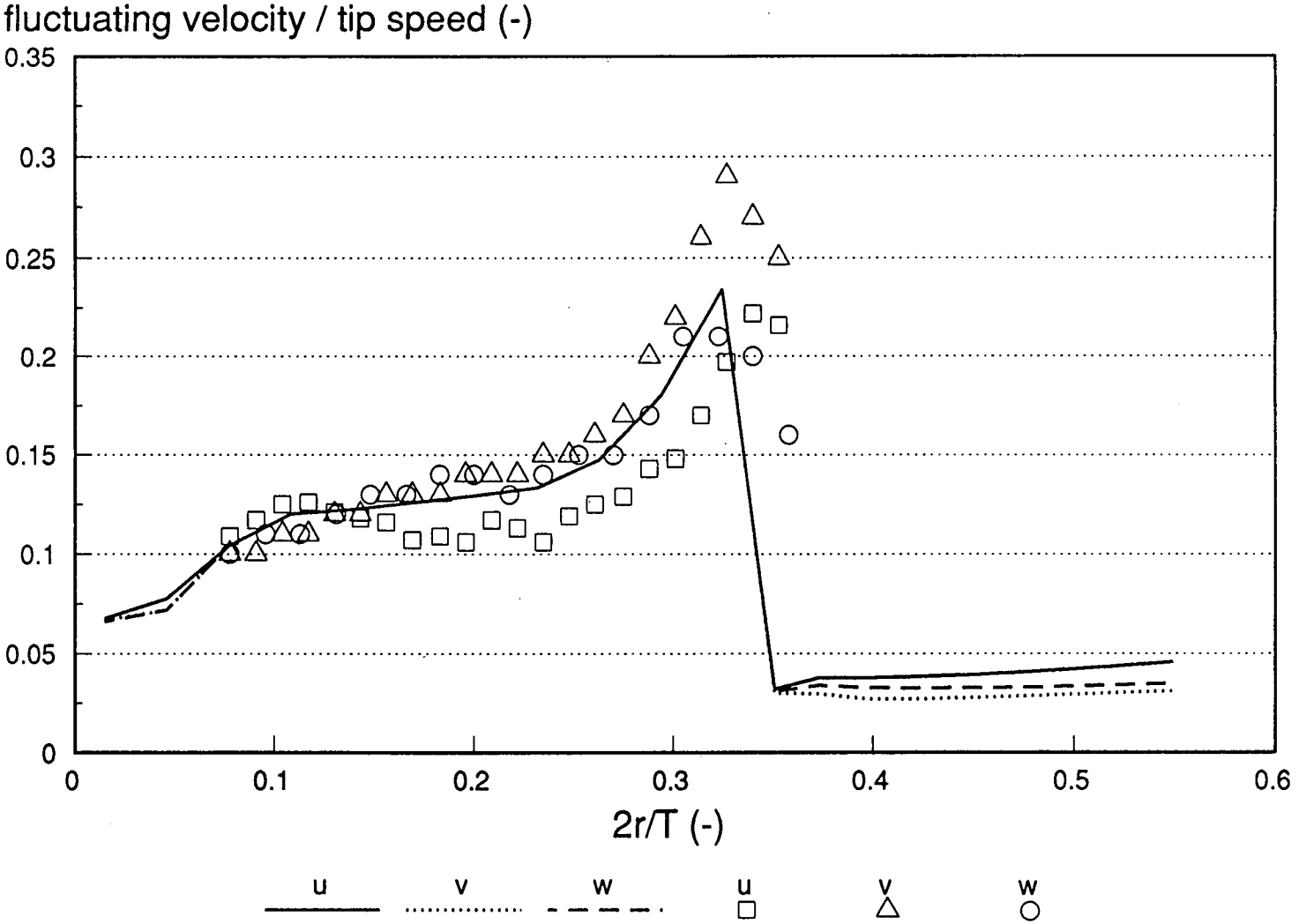

Figure D.6 Fluctuating velocities on the impeller bottom surface (x=0.203 m)

Curves denote CFD and symbols LDA data.

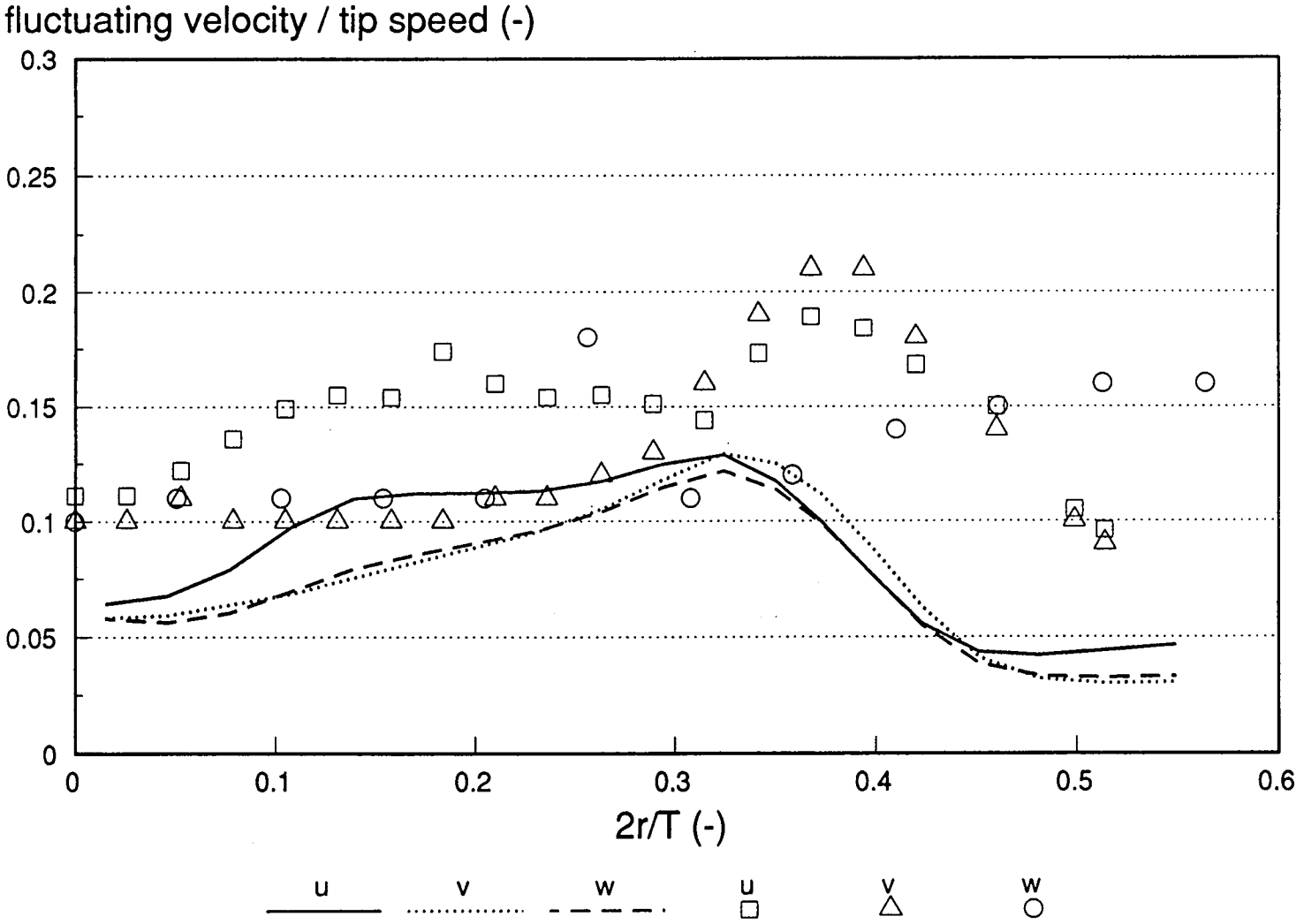

Figure D.7 Fluctuating velocities at x=0.238 m

Curves denote CFD and symbols LDA data.

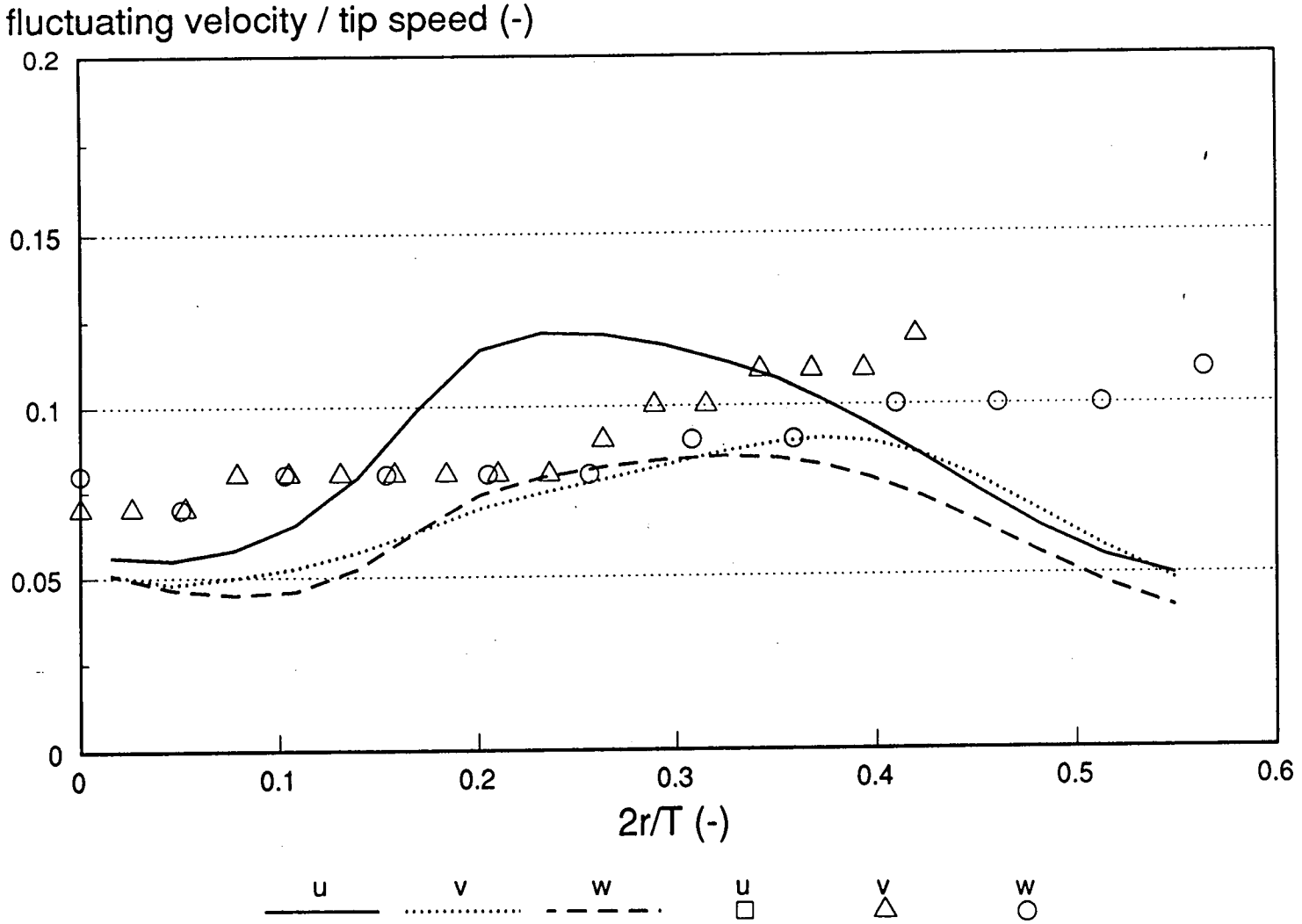

Figure D.8 Fluctuating velocities at x=0.263 m

Curves denote CFD and symbols LDA data.

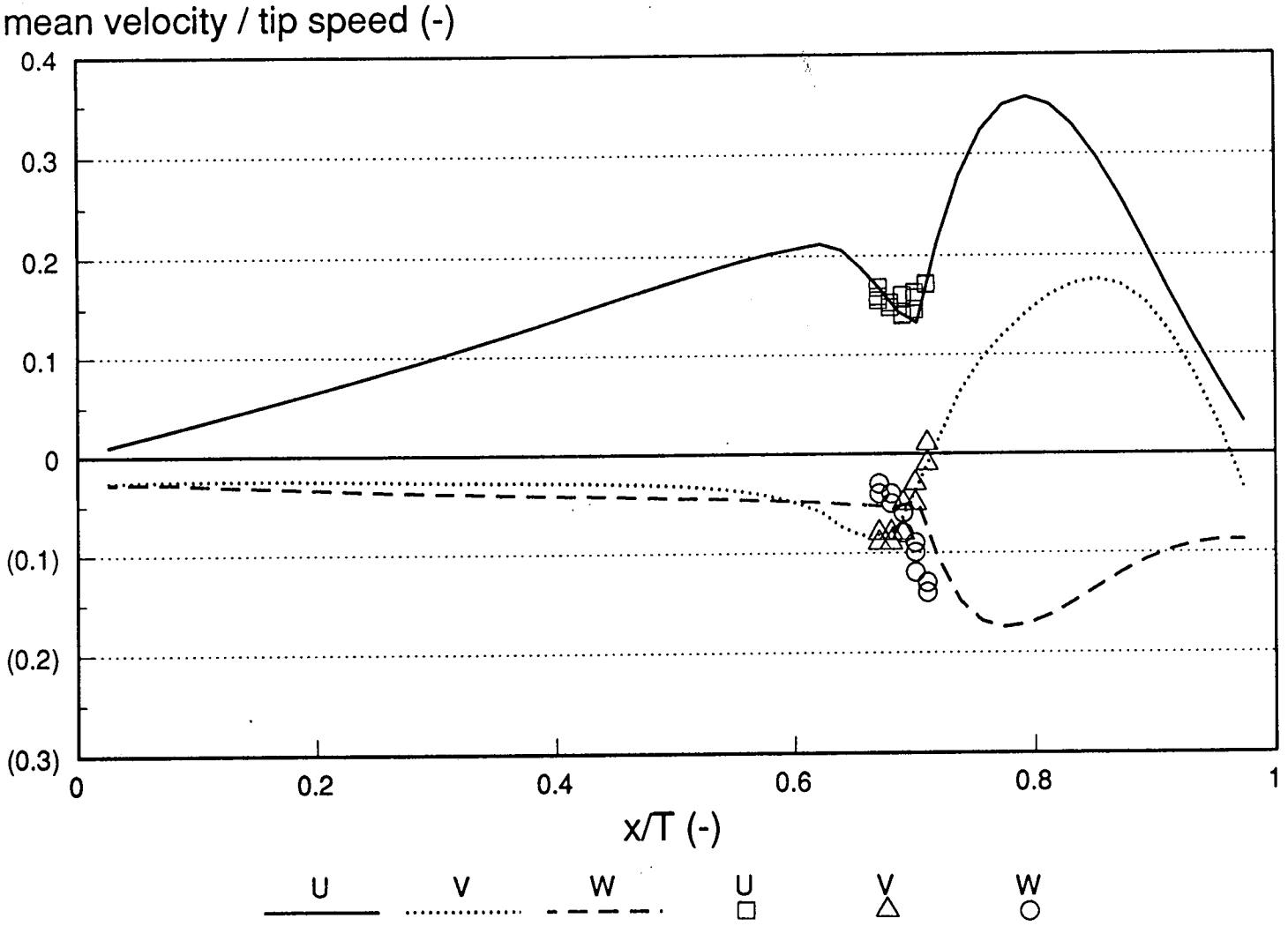

Figure D.9 Mean velocities at r=0.054 m

Curves denote CFD and symbols LDA data.

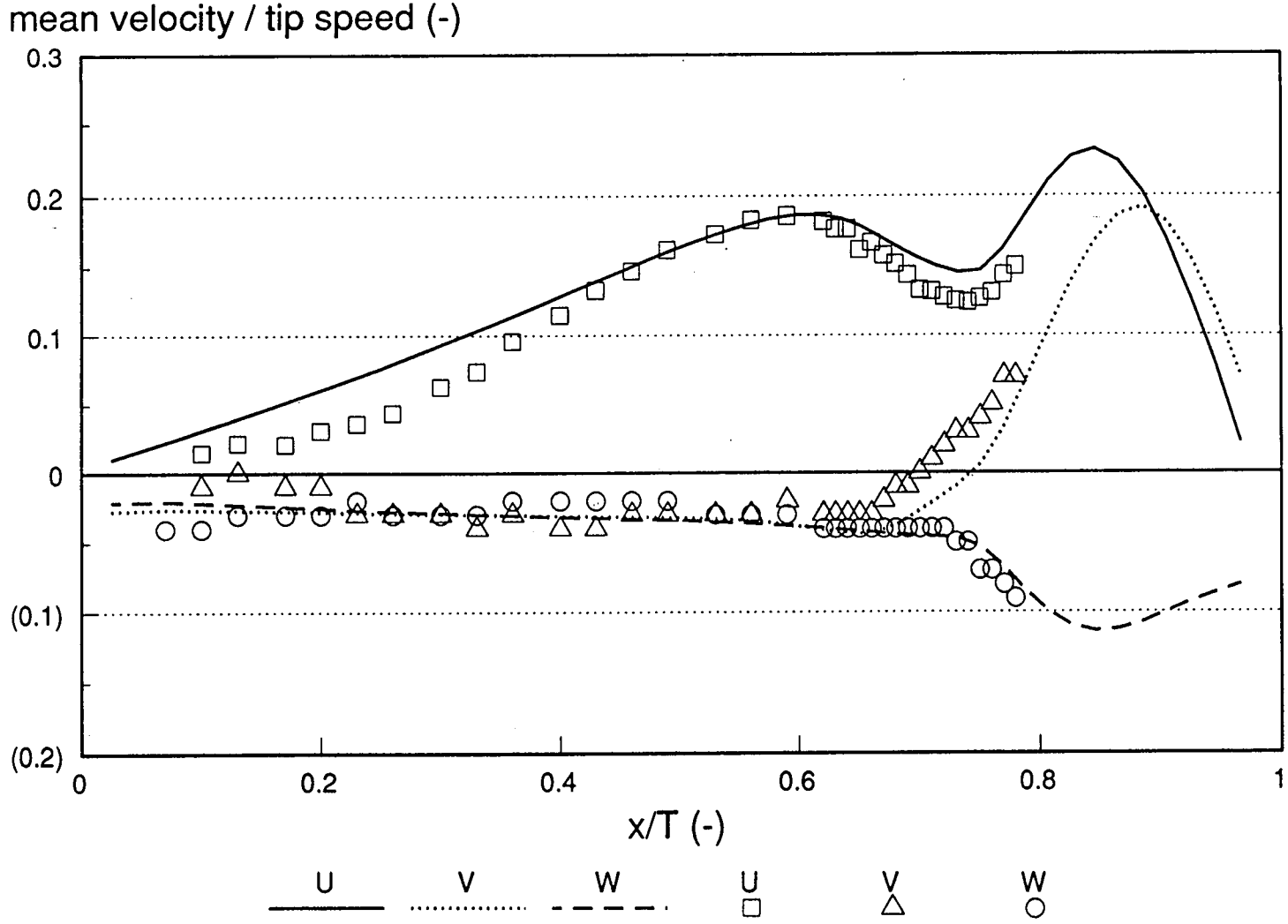

Figure D.10 Mean velocities at r=0.064 m

Curves denote CFD and symbols LDA data.

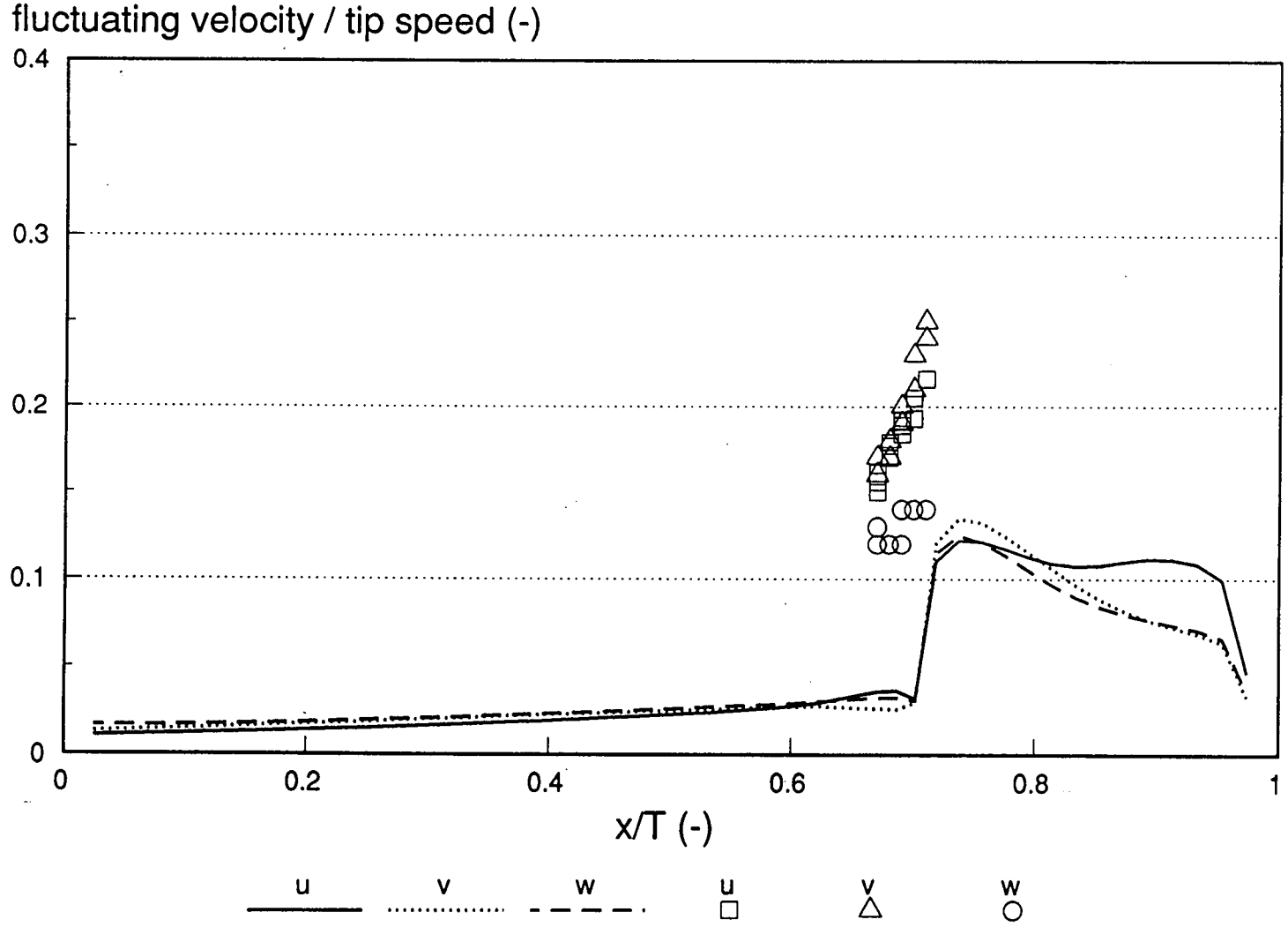

Figure D.11 Fluctuating velocities at r=0.054 m

Curves denote CFD and symbols LDA data.

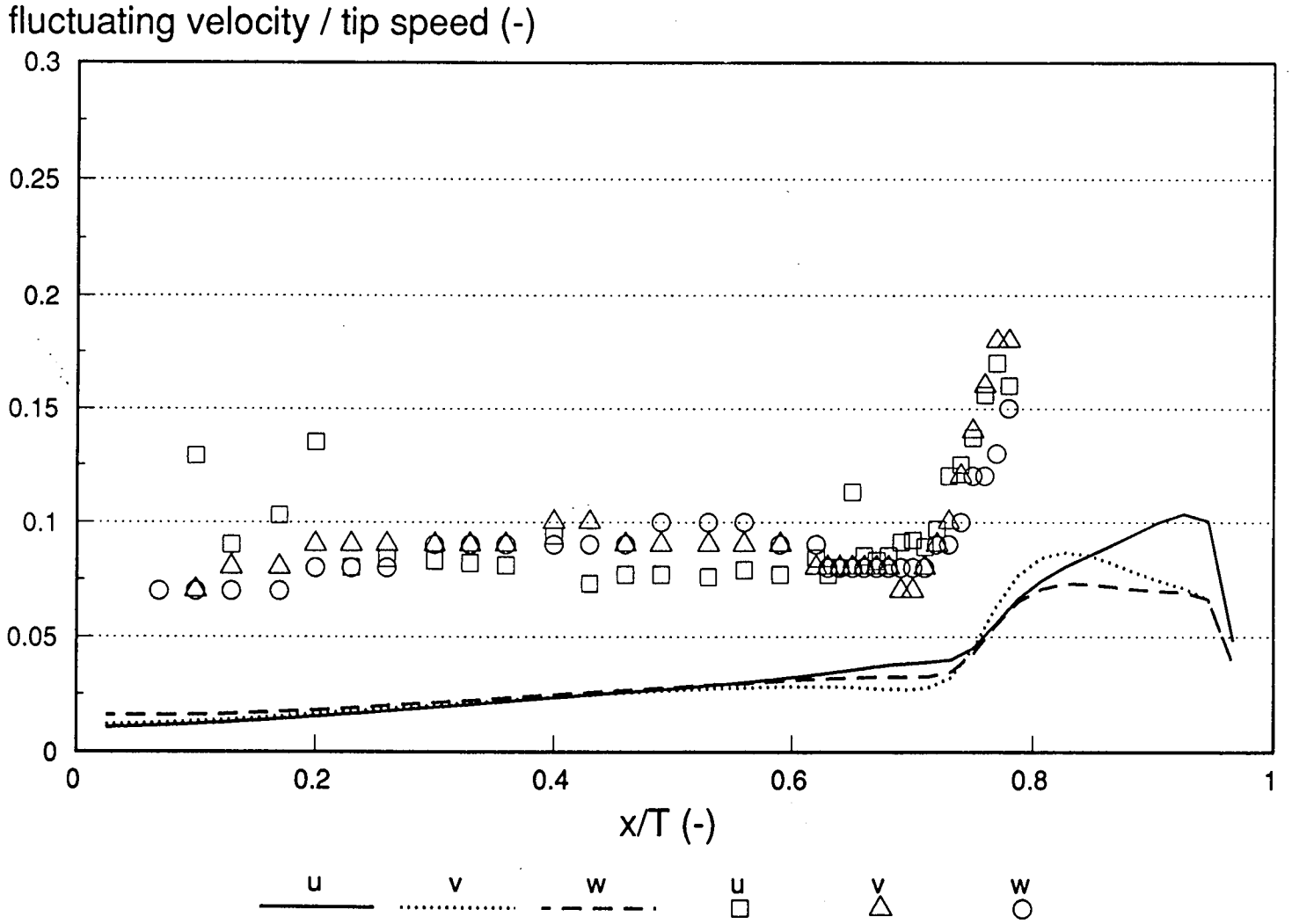

Figure D.12 Fluctuating velocities at r=0.064 m

Curves denote CFD and symbols LDA data.